Julius-Maximilians-Universität Würzburg
Graduate School of Science and Technology

Doctoral thesis / *Dissertation*
for the doctoral degree / *zur Erlangung des Doktorgrads*
Doctor rerum naturalium (Dr. rer. nat.)

Locally driven complex plasmonic nanoantenna systems

Lokal angetriebene komplexe plasmonische Nanoantennen-Systeme

Submitted by / *Vorgelegt von*
Philipp Martin Grimm
from / aus
Aschaffenburg
Würzburg, 2022

Submitted on / *Eingereicht am:* ....

Stamp / *Stempel* Graduate School

Members of thesis committee / *Mitglieder des Promotionskomitees*

Chairperson / Vorsitz: ....

1. Reviewer and Examiner / 1. Gutachter und Prüfer: Prof. Dr. Bert Hecht

2. Reviewer and Examiner / 2. Gutachter und Prüfer: Prof. Dr. Jens Pflaum

3. Examiner / 3. Prüfer: Prof. Dr. Tobias Hertel

Additional Examiners / Weitere Prüfer: ....

....

Day of thesis defense / *Tag des Promotionskolloquiums:* ....

To my family.

List of publications

Parts of this dissertation are based on the following peer-reviewed journal articles:

René Kullock, Maximilian Ochs, **Philipp Grimm**, Monika Emmerling & Bert Hecht.
Electrically-driven Yagi-Uda antennas for light.
Nature Communications **11**, 115 (2020) https://doi.org/10.1038/s41467-019-14011-6
Licensed under the Creative Commons Attribution 4.0 International (CC BY 4.0).
The content is reproduced and modified with permission in Chap. 5.
Author contributions:
R. K. conceived and set up the experiments. M. E. fabricated the electrode structures and transferred the platelets. M. O. and R. K. optimized the FIB milling. M. O. conducted the DEP, WL and EL measurements. P. G. set up the analytical model and performed the BEM and FDTD simulations. R. K., M. O., P. G. and B. H. analyzed the data and co-wrote the manuscript. B. H. supervised the work.

Philipp Grimm, Stefan Zeißner, Maximilian Rödel, Simon Wiegand, Sebastian Hammer, Monika Emmerling, Enno Schatz, René Kullock, Jens Pflaum, and Bert Hecht.
Color-Switchable Subwavelength Organic Light-Emitting Antennas.
Nano Letters **22** (3), 1032-1038 (2022) https://doi.org/10.1021/acs.nanolett.1c03994
Copyright © 2022 American Chemical Society.
The content is reproduced and modified with permission in Chap. 6.
Author contributions:
P. G. and S. Z. contributed equally to this work. B. H., J. P., and R. K. conceived the idea. P. G., R. K., and E. S. analyzed and evaluated measurement data. P. G. performed numerical simulations. S. Z., R. K., M. E., and E. S. fabricated electrodes and plasmonic nanostructures. S. Z., R. K., and E. S. performed optical precharacterization and electro-optical measurements. ZnPc thin films were grown and optically analyzed by M. R., S. W., and S. H.. R. K., B. H., and J. P. supervised the work. All authors contri-

buted to the discussion of the data and the writing of the manuscript.

Philipp Grimm, Gary Razinskas, Jer-Shing Huang and Bert Hecht.
Driving plasmonic nanoantennas at perfect impedance matching using generalized coherent perfect absorption.
Nanophotonics **10**, 1879-1887 (2021) https://doi.org/10.1515/nanoph-2021-0048
Licensed under the Creative Commons Attribution 4.0 International (CC BY 4.0).
The content is reproduced and modified with permission in Chap. 7.
Author contributions:
G. R. simulated the inset near-field maps of Figs. 7.2 a, 7.8 a and the FDTD data points in Fig. 7.4 e. P. G. performed all other calculations, simulations, and data evaluations. All the authors have accepted responsibility for the entire content of this submitted manuscript and approved submission.

Credits to published figures within the dissertation and copyright information are indicated at the end of the respective figure captions.

Further articles by the author (not part of this dissertation):

René Kullock, **Philipp Grimm**, Maximilian Ochs, and Bert Hecht.
Directed emission by electrically driven optical antennas.
Proc. SPIE 10540, Quantum Sensing and Nano Electronics and Photonics XV, 1054012 (2018). https://doi.org/10.1117/12.2289647

Matthias Hensen, Bernhard Huber, Daniel Friedrich, Enno Krauss, Sebastian Pres, **Philipp Grimm**, Daniel Fersch, Julian Lüttig, Victor Lisinetskii, Bert Hecht, and Tobias Brixner.
Spatial Variations in Femtosecond Field Dynamics within a Plasmonic Nanoresonator Mode.
Nano Letters **19** (7), 4651-4658 (2019) https://doi.org/10.1021/acs.nanolett.9b01672

Bert Hecht, René Kullock, Max Ochs, **Philipp Grimm**, Luka Zurak, Patrick Pertsch, Daniel Friedrich, Jessica Meier, Benedikt Schurr, and Monika Emmerling.
Electrically-driven Plasmonics.
Proc. SPIE 11462; Plasmonics: Design, Materials, Fabrication, Characterization, and Applications XVIII; 114620Q (2020). https://doi.org/10.1117/12.2568370

Contributions on conferences and seminars:

Posters

Philipp Grimm, René Kullock and Bert Hecht.
Optimizing Yagi-Uda Antennas for High Directivity and Electrical Driving in the Visible Regime.
DPG spring meeting, Dresden, Germany (2017).

Philipp Grimm, René Kullock, Maximilian Ochs and Bert Hecht.
Optimizing Yagi-Uda Antennas for directional light emission.
NFO15, Troyes, France (2018).

Benedikt Schurr, **Philipp Grimm**, Tobias Helbig, Tobias Hofmann, Thorsten Feichtner, Lukas Wehmeier, Felix G. Kaps, Susanne C. Kehr, Lukas M. Eng, Ronny Thomale and Bert Hecht.
Nanoscale plasmonic Su-Schrieffer-Heeger chain.
ct.qmat virtual cluster retreat, online (2021).

Talks

Philipp Grimm.
Optical antennas for novel nanoscale light-emitting devices.
GSST retreat, Kloster Schöntal, Schöntal, Germany (2019).

Philipp Grimm, Gary Razinskas, Jer-Shing Huang, and Bert Hecht.
Coherent perfect absorption in plasmonic nanocircuitry.
NFO16 online conference (2020).

Abstract

Metallic nanostructures possess the ability to support resonances in the visible wavelength regime which are related to localized surface plasmons. These create highly enhanced electric fields in the immediate vicinity of metal surfaces. Nanoparticles with dipolar resonance also radiate efficiently into the far-field and hence serve as antennas for light. Such optical antennas have been explored during the last two decades, however, mainly as standalone units illuminated by external laser beams and more recently as electrically driven point sources, yet merely with basic antenna properties. This work advances the state of the art of locally driven optical antenna systems. As a first instance, the electric driving scheme including inelastic electron tunneling over a nanometer gap is merged with Yagi-Uda theory. The resulting antenna system consists of a suitably wired feed antenna, incorporating a tunnel junction, as well as several nearby parasitic elements whose geometry is optimized using analytical and numerical methods. Experimental evidence of unprecedented directionality of light emission from a nanoantenna is provided. Parallels in the performance between radiofrequency and optical Yagi-Uda arrays are drawn. Secondly, a pair of electrically connected antennas with dissimilar resonances is harnessed as electrodes in an organic light emitting nanodiode prototype. The organic material zinc phthalocyanine, exhibiting asymmetric injection barriers for electrons and holes, in conjunction with the electrode resonances, allows switching and controlling the emitted peak wavelength and directionality as the polarity of the applied voltage is inverted. In a final study, the near-field based transmission-line driving of rod antenna systems is thoroughly explored. Perfect impedance matching, corresponding to zero back-reflection, is achieved when the antenna acts as a generalized coherent perfect absorber at a specific frequency. It thus collects all guided, surface-plasmon mediated input power and transduces it to other nonradiative and radiative dissipation channels. The coherent interplay of losses and interference effects turns out to be of paramount importance for this delicate scenario, which is systematically obtained for various antenna resonances. By means of the here developed semi-analytical toolbox, even more complex nanorod chains, supporting topologically nontrivial localized edge states, are studied. The results presented in this work facilitate the design of complex locally driven antenna systems for optical wireless on-chip communication, subwavelength pixels, and loss-compensated integrated plasmonic nanocircuitry which extends to the realm of topological plasmonics.

Zusammenfassung

Metallische Nanostrukturen besitzen die Fähigkeit, Resonanzen im sichtbaren Wellenlängenbereich zu unterstützen, die mit lokalisierten Oberflächenplasmonen in Verbindung stehen. Diese erzeugen hochverstärkte elektrische Felder in der unmittelbaren Nähe von Metalloberflächen. Nanopartikel mit dipolarer Resonanz strahlen zudem effizient in das Fernfeld ab und dienen somit als Antennen für Licht. Solche optischen Antennen wurden in den letzten zwei Jahrzehnten erforscht, allerdings hauptsächlich als eigenständige Einheiten, welche von externen Laserstrahlen angeregt werden, und in jüngerer Zeit als elektrisch getriebene Punktquellen, die jedoch lediglich über grundlegende Antenneneigenschaften verfügen. Diese Arbeit erweitert den aktuellen Stand von lokal getriebenen optischen Antennensystemen. In einem ersten Fallbeispiel wird das elektrische Antriebsschema einschließlich inelastischem Elektronentunneln über einen Nanometer-Spalt mit der Yagi-Uda-Theorie zusammengeführt. Das resultierende Antennensystem besteht aus einer passend verdrahteten, gespeisten Antenne, die einen Tunnelübergang enthält, sowie mehreren nahe gelegenen parasitären Elementen, deren Geometrie mit analytischen und numerischen Methoden optimiert wird. Experimentelle Befunde für eine ungeahnte Direktionalität der Lichtemission von einer Nanoantenne werden erbracht. Es werden Parallelen im Leistungsverhalten zwischen Radiofrequenz- und optischen Yagi-Uda-Anordnungen gezogen. Als zweites wird ein Paar elektrisch kontaktierter Antennen mit unterschiedlichen Resonanzen als Elektroden in einem Prototyp einer organischen lichtemittierenden nanoskaligen Diode eingesetzt. Das organische Material Zinkphthalocyanin, welches asymmetrische Injektionsbarrieren für Elektronen und Löcher aufweist, ermöglicht in Verbindung mit den Elektrodenresonanzen die Schaltbarkeit und Kontrolle der emittierten Wellenlänge und der Direktionalität bei Umkehr der Polarität der angelegten Spannung. In einer abschließenden Studie wird der nahfeldbasierte Antrieb von stäbchenförmigen Antennsystemen mittels eines Wellenleiters detailliert untersucht. Perfekte Impedanzanpassung, entsprechend einer verschwindenden Rückreflexion, wird erreicht, wenn die Antenne bei einer spezifischen Frequenz als verallgemeinerter kohärenter perfekter Absorber agiert. Hierbei nimmt sie die gesamte wellenleitergeführte Eingangsleistung, vermittelt durch ein Oberflächenplasmon, auf, und überträgt sie auf andere nichtstrahlende und strahlende Dissipationskanäle. Das kohärente Zusammenspiel von Verlusten und Interferenzeffekten erweist sich für dieses empfindliche Szenario, das systematisch für verschiedene Antennenmoden erzeugt wird, als äußerst wichtig. Mit Hilfe des hier entwickelten semi-analytischen Werkzeugsets werden auch komplexere Ketten aus Nanostäbchen untersucht, bei denen topologisch nichttriviale lokalisierte Randzustände auftreten. Die in dieser Arbeit vorgestellten Ergebnisse erleichtern die Entwicklung komplexer lokal angetriebener Antennensysteme für optische drahtlose Kommunikation auf einem Computerchip, Subwellenlängenpixel und verlustkompensierte integrierte plasmonische Nanoschaltkreise, welche sich bis auf das Gebiet der topologischen Plasmonik erstrecken.

Contents

1

Introduction

Antennas, whether for television broadcasting, mobile phones, or, as investigated in this thesis, for light emission, convert electric signals to free-space electromagnetic radiation and vice versa. Historically, they have played an essential role in wireless data exchange since the end of the 19^{th} century. After H. Hertz's pioneering demonstration of a dipole-like antenna, the first experimental series of long-distance wireless telegraphy outside the lab was carried out by G. Marconi who received the Nobel Prize in Physics in 1909, together with F. Braun [1]. Naturally, the prototype antennas Marconi used had a simplistic design – grounded metal sheets – acting as monopoles [2]. In the 1940s, antenna theory and engineering evolved more rapidly and various radio antenna concepts were launched, comprising rods, horns, reflectors, and apertures [3]. Applying a small aperture was also the key step in optics beyond the diffraction limit, *viz.* scanning near-field optical microscopy (SNOM) [4, 5], developed in the 1980s. Here the main goal is to collect radiation from single fluorescent molecules on a sample surface using an aperture tip. Since the fluorophore's electronic confinement, typically on the order of 1 nm, is considerably smaller than its absorption and emission wavelengths, the absorption and radiation efficiencies are very low and the molecule can be interpreted as a dipolar emitter that faces a large impedance mismatch to the free vacuum [6]. Consequently, it is of interest to better match the electronic transition to an external light field. At this point, antenna theory provides an interesting solution [7]. A metal structure of suitable size and shape, featuring high input impedance at the fluorophore's position, is needed to boost the coupling to free-space modes and thereby increase the radiation efficiency. High impedance means that the ratio of electric field strength to magnetic field strength is large. A metallic nanorod acting as resonant optical antenna fulfills this prerequisite, with the molecule being placed at the end of the rod. This example shows that antenna theory not only stimulates radiofrequency communication, but also near-field optics, where some kind of nanoscopic structure interacts with visible and near-infrared light. Indeed, optical antennas have become a multifaceted research area branching out into fundamental analysis as well as interdisciplinary studies [8–12].

In addition to the antenna effect, small metallic structures support free-electron oscillations against their ionic background that couple with evanescent optical fields – a quasiparticle known as plasmon [13]. Due to these collective excitations, which are an integral aspect of this dissertation, fields at the surface of subwavelength sized metal particles can be resonantly enhanced and squeezed far below the diffraction limit. The ultrahigh field confinement inside gaps and at sharp features enables record small effective mode volumes occupied by a photon, approaching the spatial realm where electronic transitions in active matter take place. Thereby it was possible to demonstrate strong light-matter interaction between a plasmonic mode and a single emitter at room temperature [14, 15].

Producing near-field hot spots requires suitable antenna excitation schemes. A well established method to drive plasmonic nanoantennas is illuminating the specimen with a beam from the far-field, providing a versatile platform for scattering experiments with applications in single molecule sensing [16], surface-enhanced Raman spectroscopy [17, 18], metasurfaces [19], higher harmonic generation [20–23], and other fields. Nevertheless, optical antennas can also be directly connected to a voltage source via attaching metal nanowire leads and thus be driven locally, which will be a focus of this work. The possibility of electrical driving constitutes a clear asset over purely isolated structures, opening the possibility to record electroluminescence. The antenna then acts as a true transmitter for light by converting localized electric energy into free-space photons, in contrast to a mere isolated scatterer.

Said electro-optical interconnects therefore bridge two branches of modern technology: nanoelectronics with its tiny circuit elements, e. g. sub-10 nm transistors [24] that are densely integrated in state-of-the-art computer chip architectures, and photonics, benefiting from ultrahigh bandwidths, i. e. data processing rates [25, 26]. Moreover, electrical feeding of optical antennas adds new degrees of freedom in the realm of nonlinear photonics. Zero-frequency waves, corresponding to DC signals, can be injected or probed which is not possible from the far-field. This is relevant, e. g., in optical rectification [27] or electric-field-induced second harmonic generation [28].

Supported by numerical simulations and continuously improving nanofabrication methods, electrical driving of optical antennas has been developed in the last decade. One challenge is the non-negligible size of electrical leads compared to the antenna building blocks themselves. The antenna performance is thus prone to suffer from the nearby wires. Hence, the question of an optimal placement of the latter was addressed [29]. Afterwards, an electron tunnel junction was created in the gap of a nanorod dimer, yielding the first electrically driven optical antenna [30]. This milestone triggered the development of related schemes [31]. A twisted dimer yielded improved directivities of the emitted light [32]. Out of plane antenna systems with electrical access were reported as well [33–35]. Common to all cited studies is the use of inelastic electron tunneling across a biased nanometer sized gap, generating a broadband light spectrum from tunnel current fluctuations [31]. This is necessary because conventional function generators suitable for feeding RF antennas are not able to operate at terahertz and optical frequencies [36]. The overall antenna designs, however, remained rather simple.

Chap. 5 of this thesis demonstrates that local driving of nanoantenna systems via inelastic electron tunneling can be combined with more sophisticated in-plane antenna geometries. Parasitic reflector and director elements are placed in the vicinity of the actively driven feed antenna, in compliance with the Yagi-Uda principle that has turned out quite successful in radiofrequency (RF) communication by virtue of its pronounced directional emission/reception [3]. An artistic view is displayed in Fig. 1.1 a. Under the constraints of fabrication accuracy and the local driving subsystem itself, the optical Yagi-Uda geometry is analytically and numerically optimized for high forward-to-backward emission ratio, yielding unprecedented values for electrically driven nanoantennas [32]. Numerical simulations further investigate how the director number influences the forward gain. The impacts of the dielectric environment and Ohmic dissipation inherent to optical Yagi-Uda antennas are explored.

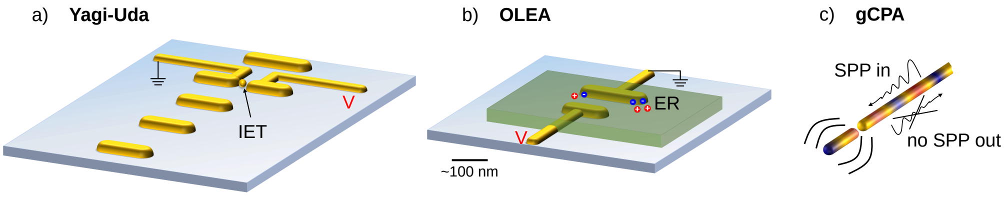

Figure 1.1 – Locally driven antenna concepts explored in this dissertation. a) Optical Yagi-Uda antenna with a DC voltage applied at the feed element. Light generation by inelastic electron tunneling (IET) across the nanogap is enhanced by the plasmon resonance and the emission is directed by parasitic elements. **b)** Organic light-emitting antenna (OLEA) device with a DC voltage applied between resonant antenna electrodes. Exciton recombination (ER) in the organic thin film (green) prevails near the cathode. **c)** All-plasmonic wire-rod nanocircuit where the rod antenna is near-field driven by an incoming surface plasmon polariton (SPP) on the wire. At the generalized coherent perfect absorption (gCPA) condition, the outgoing SPP is completely suppressed, corresponding to perfect impedance matching. The approximate scale bar is valid for all three panels. Panel b) adapted with permission from [37]. © 2022 American Chemical Society.

While inelastic tunneling bypasses the need of any optically active matter, hybrid devices of such materials encompassing e. g. single-photon emitting nitrogen vacancy centers in diamond [38, 39] or monolayers of transition metal dichalcogenides [40, 41], and optical antennas have been reported. Organic semiconductors represent a particularly versatile emitter class in this context [42–44], owing to low-cost production, mechanical flexibility, and great spectral diversity via chemical engineering [45]. For no lesser reason they are indispensable for novel energy-saving lighting solutions and state-of-the art organic light-emitting diode (OLED) displays [46]. Nonetheless, the steeply growing internet of things aims to integrate computational modules, network access and miniaturized human-computer interfaces into everyday life products, e. g. smart textiles [47]. This goes in hand with a major demand of advanced display technology and ultrasmall pixel dimensions. Therefore, future OLED cells require further downscaling where at the same time nonradiative exciton decay, e. g. quenching or coupling to waveguide modes near the electrodes, must be avoided. In Chap. 6, a novel OLED concept based on organo-plasmonic subwavelength diodes, whose plasmonic subsystem consists of electrically connected nanoantennas, is introduced. Fig. 1.1 b shows a sketch of the device. Radiative exciton recombination (ER) locally drives the antenna system. Assisted by numerical simulations, we conceive a gold-organic-gold prototype with antenna-shaped electrodes supporting spectrally dissimilar plasmon resonances. Switchable emission of two colors is accomplished by steering the ER zone via the applied bias. Yet, the light is emanating from the same diffraction-limited spot of the device. Using a qualitative model, an explanation for the color selectivity is given. This model is further corroborated by bias-dependent far-field radiation patterns.

Recalling macroscopic broadcasting systems, power transfer is accomplished via transmission line cables attached to the antenna at a specific feed point. As mentioned above, a key design rule for antenna engineers is the matching of impedance between feeder and antenna [48]. Detrimental reflections back to the transmission line that would generate reactive power are then canceled out and all power is transferred onto the radiator. A nano-optical transmission line consists of a thin metal wire that supports a propagating surface plasmon polariton (SPP) [49]. Via a small gap, a nanorod antenna can be attached to form an all-plasmonic nanocircuit, as depicted in Fig. 1.1 c. Here, the local driving mechanism relies on the coherent power transfer of the guided SPP into a localized plasmon resonance of the nanorod. The concept of impedance has been reformulated for optical structures, yielding circuit analogs for quantum emitters, nanocavities, and nanoantennas [6, 50]. Impedance matching has been sought after in plasmonic nanocircuitry [51], yet largely addressed with parameter sweeps using time-consuming numerical simulations. Chap. 7 demonstrates perfect impedance matching of several simple and complex optical antenna configurations. The idea of impedance matching is embedded into the more abstract framework of coherent perfect absorbers [52]. Generalizing the perfect absorber idea allows us to grasp radiation from antennas as a subset of loss channels, enabling the description of plasmonic nanoresonators. Instead of brute-force simulation efforts, a semi-analytical toolbox is established and validated against full numerical results. This speeds up the entire analysis and the tracking of perfect absorption conditions in the antenna systems. Such conditions are found for several superradiant and subradiant resonances, so that the eventual dissipation mechanism can be chosen. Even chains of coupled plasmonic nanoresonators are studied, where topological edge modes can be detected. Notably, losses are regarded mostly as an undesirable property in plasmonics. More and more efforts are recently undertaken to explore their beneficial sides in various technological fields [53]. Here, the naturally occurring loss is leveraged to accomplish perfect impedance matching of optical antenna systems in an all-plasmonic nanocircuit.

The dissertation is structured as follows: Chap. 2 outlines the central aspects of electromagnetic theory necessary for understanding the physics of plasmons and the numerical simulation algorithm. Chap. 3 proceeds with the optical properties of noble metals and the concomitant emergence of plasmons at planar metal-dielectric interfaces as well as closed metallic nanoparticles. The numerical simulation method applied in this thesis is introduced in Chap. 4. Afterwards, the results are manifested in the three aforementioned project chapters 5, 6, and 7. Each of these is completed by a summary and outlook section. Finally, Chap. 8 conveys generic conclusion and outlook notes concerning locally driven complex optical antenna structures.

2

Electromagnetic theory: An overview

The science of light is based on classical electromagnetism, a fundamental pillar in today's physics besides mechanics, quantum mechanics, and statistics. While Newton's axioms had manifested a closed picture of classical mechanics in the late 17^{th} century [54], key discoveries in electrostatics started 100 years later by groundbreaking works of Cavendish and Coulomb. They initiated a rapid development which peaked in J. C. Maxwell's dynamical theory of the electromagnetic field in 1865 [55]. This consistent formulation in a set of partial differential equations was crucial for understanding the interplay between electricity, magnetism, and optics. In 1888, H. Hertz's experimental observation of electromagnetic waves propagating at the speed of light corroborated Maxwell's theory [56]. As opposed to Newtonian mechanics, Maxwell's equations show covariant behavior under Lorentz transformations, assuring validity in any inertial system. Triggered by this invariance, A. Einstein developed the special relativity theory which revolutionized the scientific conception of space and time [57]. Nowadays classical electromagnetism still plays an important role in research as well as in engineering.

This chapter gives an overview of classical electromagnetic theory to an extent necessary for the understanding of the following chapters. Beginning with Maxwell's equations in vacuum and some derivations, we arrive at electromagnetic fields in matter and the vectorial Helmholtz equation. For a more profound reading about the entire theory, various textbooks are available [56, 58, 59], as is the case for particular treatise on nano-optical aspects [13, 60].

2.1 Maxwell's equations in vacuum

Maxwell's equations are a set of partial differential equations connecting the temporal dynamics of the electric field $\vec{E}$, magnetic field $\vec{H}$, electric displacement $\vec{D}$, and magnetic induction $\vec{B}$ with the associated external charge density ρ and current density

$\vec{j}$ [56]. In differential form they read[1]:

$$\vec{\nabla}\cdot\vec{D}(\vec{r},t) = \rho(\vec{r},t), \tag{2.1a}$$

$$\vec{\nabla}\times\vec{E}(\vec{r},t) = -\frac{\partial\vec{B}(\vec{r},t)}{\partial t}, \tag{2.1b}$$

$$\vec{\nabla}\times\vec{H}(\vec{r},t) = \frac{\partial\vec{D}(\vec{r},t)}{\partial t} + \vec{j}(\vec{r},t), \tag{2.1c}$$

$$\vec{\nabla}\cdot\vec{B}(\vec{r},t) = 0. \tag{2.1d}$$

Using vector calculus, an equivalent integral form can be found [61]. This equation system has axiomatic character. Qualitatively, Eq. (2.1a) establishes the charge density as the source of electric fields (Coulomb's law), Eq. (2.1b) relates temporal changes of the magnetic induction with electric vortex fields (Faraday's law of induction). In Eq. (2.1c), magnetic vortex fields are generated by electric displacement fields varying in time (i. e. Maxwell's displacement current) and external currents (Ampère's law). The magnetic induction is source-free according to Eq. (2.1d), i. e. magnetic monopoles do not exist.

An important property of Maxwell's equations is their linearity. This allows decomposing a solution to this equation system into an (infinite) sum, in particular it is possible to apply a Fourier transform to all the quantities,

$$\vec{E}(\vec{r},t) = \int\limits_{-\infty}^{+\infty} \vec{E}(\vec{r},\omega)e^{-\mathrm{i}\omega t}\mathrm{d}\omega, \tag{2.2}$$

here shown for the electric field, yielding single-frequency contributions $\vec{E}(\vec{r},\omega)$ in the integrand. The inverse Fourier series of the time-dependent quantity yields the respective quantity in the spectral domain, e. g.

$$\vec{E}(\vec{r},\omega) = \frac{1}{2\pi}\int\limits_{-\infty}^{+\infty} \vec{E}(\vec{r},t)e^{\mathrm{i}\omega t}\mathrm{d}t. \tag{2.3}$$

The partial time derivatives in Eqs. (2.1) can thus be resolved:

$$\vec{\nabla}\cdot\vec{D}(\vec{r},\omega) = \rho(\vec{r},\omega), \tag{2.4a}$$

$$\vec{\nabla}\times\vec{E}(\vec{r},\omega) = \mathrm{i}\omega\vec{B}(\vec{r},\omega), \tag{2.4b}$$

$$\vec{\nabla}\times\vec{H}(\vec{r},\omega) = -\mathrm{i}\omega\vec{D}(\vec{r},\omega) + \vec{j}(\vec{r},\omega), \tag{2.4c}$$

$$\vec{\nabla}\cdot\vec{B}(\vec{r},\omega) = 0. \tag{2.4d}$$

---

[1] SI units are used throughout this thesis.

2.2 Poynting vector and conservation laws

In this section we note down some laws concerning the conservation of energy and electric charge. Assuming fields with harmonic time dependence $e^{-\mathrm{i}\omega t}$ such that

$$\vec{E}(\vec{r},t) = \Re\left[\vec{E}(\vec{r})e^{-\mathrm{i}\omega t}\right] \equiv \frac{1}{2}\left[\vec{E}(\vec{r})e^{-\mathrm{i}\omega t} + \vec{E}^*(\vec{r})e^{\mathrm{i}\omega t}\right], \tag{2.5}$$

the energy flux density is given by the complex Poynting vector $\vec{S}$, defined as [56]

$$\vec{S} = \vec{E} \times \vec{H}^*. \tag{2.6}$$

The electromagnetic energy density can be expressed by

$$W_{em} = \frac{1}{2}(\vec{E}\cdot\vec{D}^* - \vec{B}\cdot\vec{H}^*). \tag{2.7}$$

Its averaged time-variation depends on the rate of work done by the fields and the Poynting vector [56]:

$$-\left\langle \frac{\partial W_{em}}{\partial t} \right\rangle = \frac{1}{2}\Re(\vec{j}^*\cdot\vec{E}) + \vec{\nabla}\cdot\langle\vec{S}\rangle. \tag{2.8}$$

Eq. (2.8) is called Poynting's theorem and ensures energy conservation. Considering a closed surface A with outward pointing unit normal vector $\vec{n}$ surrounding a radiation source, one obtains the time-averaged power flow $\langle P\rangle$ by integrating the Poynting vector over the surface:

$$\langle P\rangle = \frac{1}{2}\oint_A \Re(\vec{S})\cdot\vec{n}\,\mathrm{d}A \tag{2.9}$$

A relation similar to Eq. (2.8) can be deduced directly by the time derivative of Eq. (2.1a) and the divergence of Eq. (2.1c),

$$-\frac{\partial\rho(\vec{r},t)}{\partial t} = \vec{\nabla}\cdot\vec{j}(\vec{r},t), \tag{2.10}$$

which expresses conservation of electrical charge. It is referred to as continuity equation.

2.3 Electromagnetic fields in matter

All physical objects consist of atoms. These in turn are assembled of neutrons and protons in the nucleus, and electrons in orbitals surrounding the nucleus. Although, on the macroscopic scale, a body is electrically neutral, an applied electric field displaces electron clouds from the nuclei. Due to the displacement an effective dipole moment is created in each atom, which leads to a macroscopic polarization throughout the body. Likewise, a magnetic field can give rise to the magnetization of a substance. These perturbations act back on the electromagnetic field distribution inside the material. A complete description of the fields on the microscopic level is practically impossible as electrons and even entire atoms exhibit motion all the time, thereby altering the local field dramatically. Moreover, such a field description would possess a singularity at each particle position. Therefore, a macroscopic model dealing with average fields over a region much larger than the atom diameter is the appropriate way to describe the influence of matter on electromagnetic fields. The macroscopic polarization $\vec{P}$ and magnetization $\vec{M}$ are defined by the following relations [56]:

$$\vec{D}(\vec{r},\omega) = \varepsilon_0 \vec{E}(\vec{r},\omega) + \vec{P}(\vec{r},\omega), \tag{2.11a}$$

$$\vec{B}(\vec{r},\omega) = \mu_0 \vec{H}(\vec{r},\omega) + \mu_0 \vec{M}(\vec{r},\omega). \tag{2.11b}$$

$\vec{P}$ connects the electric and $\vec{M}$ the magnetic field quantities. Both $\vec{P}$ and $\vec{M}$ vanish in free space. ε_0 and μ_0 are the electric permittivity and magnetic permeability of vacuum, which have a direct connection to the speed of light in vacuum via $c = 1/\sqrt{\varepsilon_0 \mu_0}$. In general, the macroscopic response of matter can be a function of the intensity of the incident field and the crystallographic direction. In this thesis, however, a simpler description, valid for linear and isotropic materials, such as noble metals and glass, is sufficient[2]. The connections between $\vec{P}$ ($\vec{M}$) and $\vec{E}$ ($\vec{H}$) read in this case [59]:

$$\vec{P}(\vec{r},\omega) = \varepsilon_0 \chi_e(\vec{r},\omega) \vec{E}(\vec{r},\omega) \tag{2.12a}$$

$$\vec{M}(\vec{r},\omega) = \chi_m(\vec{r},\omega) \vec{H}(\vec{r},\omega). \tag{2.12b}$$

χ_e and χ_m denote the electric and magnetic susceptibility, respectively. Their dependence on the angular frequency ω indicates that they show dispersive behavior, i. e. the strength and phase shift of the material response to an incident electromagnetic field varies with its frequency. Inserting Eqs. (2.12) into Eqs. (2.11) and reformulating $\varepsilon = 1 + \chi_e$ and $\mu = 1 + \chi_m$ yields the so-called constitutive relations [59],

$$\vec{D}(\vec{r},\omega) = \varepsilon_0 \varepsilon(\vec{r},\omega) \vec{E}(\vec{r},\omega), \tag{2.13a}$$

$$\vec{B}(\vec{r},\omega) = \mu_0 \mu(\vec{r},\omega) \vec{H}(\vec{r},\omega), \tag{2.13b}$$

where ε and μ are called relative permittivity and permeability. They inherit the dispersive properties from the susceptibilities. While for the media investigated in this work magnetizations can be neglected ($\vec{M} = \vec{0},\ \mu = 1$), the dispersion of the relative permittivity of metals in the visible wavelength regime has a crucial impact on nano-optical effects and is one of the central aspects of the entire research field. The permittivity $\varepsilon(\vec{r},\omega)$, including the frequency dependence, is referred to as dielectric function in the following chapters. For gold and silver the dielectric functions along with implications are thoroughly investigated in Chap. 3. Besides bound electron clouds, free electrons are also influenced by electromagnetic fields in metals. With the conductivity σ, Ohm's law expresses the connection between electric field and current density, reading

$$\vec{j}(\vec{r},\omega) = \sigma(\vec{r},\omega) \vec{E}(\vec{r},\omega). \tag{2.14}$$

---

[2] In Chap. 6 the organic semiconductor zinc phthalocyanine is used as active material which exhibits anisotropic dielectric behavior, requiring a tensor for highly accurate modeling. In this work we simplify it to a frequency-dependent isotropic dielectric function. In spite of a resulting systematic deviation the isotropic model is sufficient for design optimization via numerical simulations.

All these relations complement the Maxwell equations (2.4) so that a consistent solution can be found, e. g. by the finite-difference time-domain algorithm introduced in Chap. 4.

If more than one material is involved, the physical conditions change abruptly across the interface. Since Maxwell's equations are valid in the entire space, certain boundary conditions are imposed on the fields to retain a meaningful solution. The situation can be treated elegantly by dividing space into subdomains and formulating separate solutions for the subdomains. Let us assume two material domains D_i and D_j with the interface ∂D_{ij}. On ∂D_{ij} a surface current density $\vec{j}_s$ and a surface charge density ρ_s can emerge. The global solution requires the subsolutions to be connected consistently, i. e. obeying Maxwell's equations. It can be shown that the tangential field components fulfill [13]

$$\vec{n}\times(\vec{E}_i-\vec{E}_j)=\vec{0} \quad \text{at } \partial D_{ij}, \tag{2.15a}$$

$$\vec{n}\times(\vec{H}_i-\vec{H}_j)=\vec{j}_s \quad \text{at } \partial D_{ij}, \tag{2.15b}$$

where $\vec{n}$ denotes the unit normal vector on the boundary. Hence, while the tangential electric field components are continuous at the boundary those of the magnetic field jump by an amount determined by surface currents. Analogously, the normal field components satisfy

$$\vec{n}\cdot(\vec{D}_i-\vec{D}_j)=\rho_s \quad \text{at } \partial D_{ij}, \tag{2.16a}$$

$$\vec{n}\cdot(\vec{B}_i-\vec{B}_j)=0 \quad \text{at } \partial D_{ij}, \tag{2.16b}$$

which means that the normal component of the magnetic field is conserved, whereas the displacement fields exhibit a jump defined by the surface charge density. In the case of source-free domains $\vec{j}_s$ and ρ_s vanish.

2.4 Vector Helmholtz equation and plane waves

In this section a simple solution of Maxwell's equations is discussed. For the case of a source-free dielectric ($\mu=1, \sigma=0, \rho=0, \vec{j}=\vec{0}$), combining Eqs. (2.4) with the constitutive relations (2.13) yields the equation system

$$\vec{\nabla}\cdot[\varepsilon_0\varepsilon(\vec{r},\omega)\vec{E}(\vec{r},\omega)]=0, \tag{2.17a}$$

$$\vec{\nabla}\times\vec{E}(\vec{r},\omega)=\mathrm{i}\omega\mu_0\vec{H}(\vec{r},\omega), \tag{2.17b}$$

$$\vec{\nabla}\times\vec{H}(\vec{r},\omega)=-\mathrm{i}\omega\varepsilon_0\varepsilon(\vec{r},\omega)\vec{E}(\vec{r},\omega), \tag{2.17c}$$

$$\vec{\nabla}\cdot[\mu_0\vec{H}(\vec{r},\omega)]=0. \tag{2.17d}$$

An equation for the electric field can be found by the curl of Eq. (2.17b) substituted into Eq. (2.17c),

$$\vec{\nabla}^2\vec{E}+\frac{\omega^2}{c^2}\varepsilon\vec{E}=\vec{\nabla}(\vec{\nabla}\cdot\vec{E}), \tag{2.18}$$

where the vector calculus identity $\vec{\nabla}\times\vec{\nabla}\times = -\vec{\nabla}^2 + \vec{\nabla}\vec{\nabla}\cdot$ is employed. Eq. (2.17a) can be written as

$$\vec{\nabla}\cdot\vec{E} = -\vec{E}\cdot\vec{\nabla}\ln(\varepsilon) \tag{2.19}$$

and put into Eq. (2.18) to obtain the wave equation

$$\vec{\nabla}^2\vec{E} + \frac{\omega^2}{c^2}\varepsilon\vec{E} = -\vec{\nabla}[\vec{E}\cdot\vec{\nabla}\ln(\varepsilon)]. \tag{2.20}$$

Using Eqs. (2.17b) - (2.17d) the wave equation for the magnetic field reads

$$\vec{\nabla}^2\vec{H} + \frac{\omega^2}{c^2}\varepsilon\vec{H} = \vec{\nabla}\times\vec{H}\times\vec{\nabla}\ln(\varepsilon). \tag{2.21}$$

In the case of a homogeneous, isotropic dielectric environment ($\varepsilon(\vec{r}) = \varepsilon = \text{const.}$) the wave equations simplify to the Helmholtz equations

$$(\vec{\nabla}^2 + \vec{k}^2)\vec{E} = \vec{0}, \tag{2.22a}$$

$$(\vec{\nabla}^2 + \vec{k}^2)\vec{H} = \vec{0}, \tag{2.22b}$$

with $|\vec{k}| = k = \frac{\omega}{c}\sqrt{\varepsilon}$ being the wave number. A solution to Eqs. (2.22) is provided by propagating plane waves defined as

$$\vec{E}(\vec{r},t) = \vec{E}_0\, e^{\mathrm{i}(\vec{k}\cdot\vec{r}-\omega t)}, \tag{2.23a}$$

$$\vec{H}(\vec{r},t) = \vec{H}_0\, e^{\mathrm{i}(\vec{k}\cdot\vec{r}-\omega t)}, \tag{2.23b}$$

where the wave vector $\vec{k}$ points into the direction of propagation. From Eqs. (2.17a), (2.17d) it follows that $\vec{k}\perp\vec{E}$ and $\vec{k}\perp\vec{H}$, i. e. the waves are transversal. In addition, the curl equations (2.17b), (2.17c) imply $\vec{E}\perp\vec{H}$ such that for a source-free dielectric or vacuum the vector orientations are given by

$$\vec{k}\perp\vec{E}\perp\vec{H}. \tag{2.24}$$

The dispersion relation connects the wave number k to the angular frequency ω. Considering electromagnetic plane waves in vacuum, the relation reads

$$\omega = c\cdot k = \frac{2\pi c}{\lambda} \tag{2.25}$$

with λ the vacuum wavelength. Ideal plane waves do not exist in nature because they would carry an infinite amount of energy. Nevertheless, they allow for a good approximation to real waves in the far-field. Due to the linearity of Maxwell's equations any linear combination of plane waves provides a solution as well.

When focusing a light beam through e. g. a microscope objective, the minimum focal size s is governed by the diffraction limit,

$$s \simeq \frac{\lambda}{2}, \tag{2.26}$$

a fundamental law discovered by E. Abbe [62] which dictates the minimal "volume" of light with conventional focusing methods like lenses. In the following chapter, a way to considerably reduce the volume occupied by an electromagnetic mode, down to the deep subwavelength regime, is introduced.

3

Principles of plasmonics

Squeezing of light down to subwavelength dimensions happens when metallic nano objects interact with incident electromagnetic radiation. This astonishing effect is caused firstly by the object's geometry and is well established in waveguiding designs as well as subdiffraction sized cavities [63, 64]. Secondly, the optical properties of metals are key as they offer a large number of quasi-free electrons which form a charge density wave, known as plasmon, creating evanescent optical fields at the object's surface. Particular interest lies in noble metals, mainly gold, being chemically inert and having favorable optical properties on the red side of the optical spectrum. Moreover, the possibility to chemically synthesize monocrystalline gold platelets allows to fabricate high-quality gold nanostructures for sophisticated nano-optical experiments [65–67]. The physics of plasmons is crucial for the effects shown in this work. In the present chapter, beginning with an analysis of the dielectric function of noble metals, the conditions and properties of surface plasmons at basic planar geometries and particles are investigated.

3.1 Optical properties of noble metals

As stated in Sec. 2.3, electromagnetic fields in matter are dramatically influenced by the electronic and atomic configuration, i. e. for a solid the electronic band structure largely determines the optical response, quantified by the complex-valued frequency-dependent dielectric function $\varepsilon(\omega) = \varepsilon'(\omega) + i\varepsilon''(\omega)$. When a metal is illuminated by an electromagnetic wave the conduction electrons collectively oscillate 180° out of phase, giving rise to the well observable high reflectivity. Consequently, $\varepsilon'(\omega)$ is negative for the spectral regime of interest. Indeed, this condition turns out to be a requirement for the occurrence of plasmons, cf. Sec. 3.2.1 below. While at radio frequencies noble metals can be treated as perfect conductors this simple picture breaks down at optical frequencies. The excitation field now changes so rapidly in time that the finite effective electron mass m^* cannot be neglected anymore. It prevents the charge density from an instantaneous response to the source field. Thus, the shielding becomes imperfect and some portion of the field penetrates into the bulk. The (positive) imaginary part $\varepsilon''(\omega)$ accounts for the damping of electron motion, e. g. due to scattering at phonons or impurities.

The simplest approach to model the dielectric function of noble metals is known as Drude-Sommerfeld theory. It accounts for the polarization of the free electron gas, obeying the equation of motion for the electron displacement vector $\vec{r}$ [13]

$$m_e \frac{\partial^2 \vec{r}}{\partial t^2} + m_e \Gamma \frac{\partial \vec{r}}{\partial t} = e\vec{E}_0 e^{-\mathrm{i}\omega t}, \tag{3.1}$$

where a time-harmonic driving field with angular frequency ω and amplitude $\vec{E}_0$ is assumed. m_e and e are the effective electron mass and elementary charge. The velocity-dependent damping term contains $\Gamma = v_F/l$ with v_F being the Fermi velocity and l the electron mean free path between scattering events. Since only unbound electrons are treated, Eq. (3.1) lacks a restoring force term. The ansatz $\vec{r}(t) = \vec{r}_0 e^{-\mathrm{i}\omega t}$ leads to the Drude dielectric function,

$$\varepsilon_D(\omega) = 1 - \frac{\omega_p^2}{\omega^2 + \mathrm{i}\Gamma\omega}. \tag{3.2}$$

The expression $\omega_p = \sqrt{ne^2/(m_e\varepsilon_0)}$ is known as plasma frequency. n denotes the density of free electrons.

Fig. 3.1 a shows the measured dielectric function of single-crystalline gold [68] together with a fit of Eq. (3.2). The fit parameters are $\hbar\omega_p = 8.95\,\mathrm{eV}$ and $\hbar\Gamma = 47\,\mathrm{meV}$. As is clearly seen, Drude-Sommerfeld theory only approximates the long wavelength part reasonably and becomes inaccurate below 800 nm, especially in the imaginary part. For shorter wavelengths, the response of bound electrons needs to be included [13, 69]. In gold, valence electrons from the d-band exhibit interband transitions into the sp conduction band if excited by a photon with sufficient energy. This absorption process manifests as a drastic increase of ε'' below 550 nm. Classically the bound electron response can be approximated by a driven, damped harmonic oscillator whose equation of motion reads

$$m \frac{\partial^2 \vec{r}}{\partial t^2} + m\gamma \frac{\partial \vec{r}}{\partial t} + \alpha \vec{r} = e\vec{E}_0 e^{-\mathrm{i}\omega t}, \tag{3.3}$$

where m is the effective mass of bound electrons, γ is their damping rate, and α plays the role of a spring constant in the restoring atomic potential. With the above ansatz an interband transition adds a Lorentzian term

$$\varepsilon_{\mathrm{Interband}}(\omega) = 1 + \frac{\tilde{\omega}_p^2}{(\omega_0^2 - \omega^2) - \mathrm{i}\gamma\omega} \tag{3.4}$$

to the dielectric function such that the Drude-Lorentz model reads

$$\varepsilon_{DL}(\omega) = \varepsilon_D(\omega) + \varepsilon_{\mathrm{Interband}}(\omega). \tag{3.5}$$

The shorthand expression $\tilde{\omega}_p = \sqrt{\tilde{n}e^2/(m\varepsilon_0)}$ is defined analogously to the plasma frequency in Eq. (3.2), however, with a different physical meaning. $\tilde{n}$ is the density of bound electrons and $\omega_0 = \sqrt{\alpha/m}$ is the interband transition frequency. In

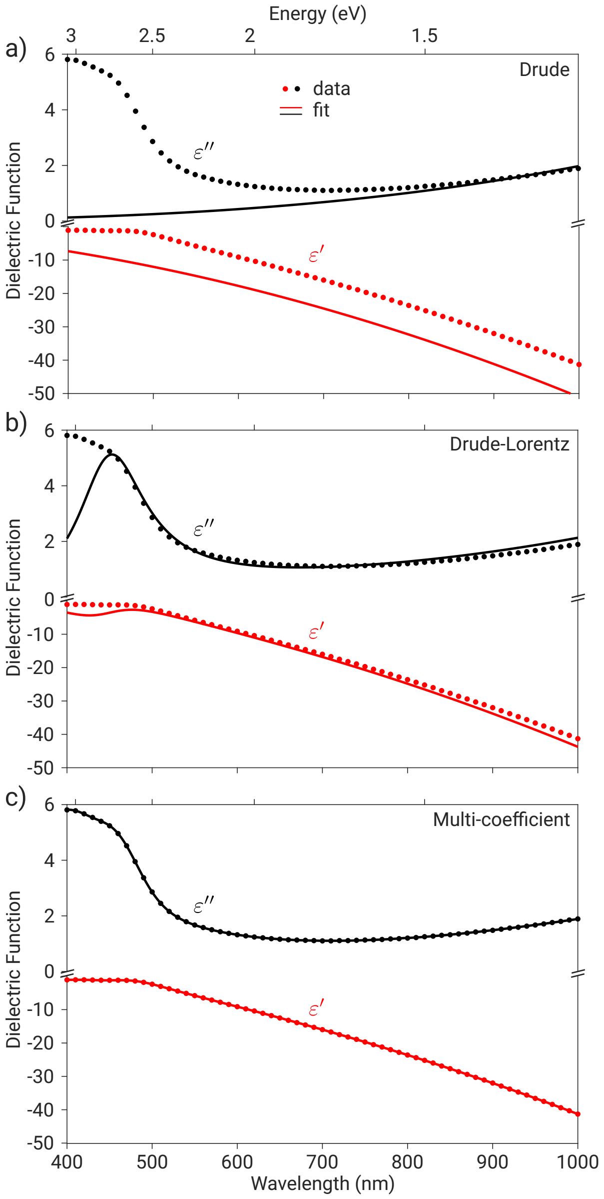

Figure 3.1 – Dielectric function of gold in the visible and near infrared (NIR). The real part ε' is plotted in red, the imaginary part ε'' in black. Measured values (dots) are single crystal data taken from Olmon *et al.* [68]. The solid lines show different model fits. **a)** Drude model. **b)** Drude-Lorentz model. **c)** Multi-coefficient material (MCM) model. The fit parameters are given in the text. Note the different scale of positive and negative ordinates.

order to account for further interband transitions a cumulative offset ε_∞ can be employed. Fig. 3.1 b displays a Drude-Lorentz fit to the experimental dielectric function. The solid lines show that including one interband transition improves the model significantly, down to $\lambda = 500\,\text{nm}$. As fit parameters, $\hbar\tilde{\omega}_p = 2.83\,\text{eV}$, $\hbar\gamma = 0.59\,\text{eV}$, $\omega_0 = 2\pi c/\lambda_0$ with $\lambda_0 = 450\,\text{nm}$, and $\varepsilon_\infty = 5$ are used. Adding more Lorentz-oscillators allows modeling the dielectric function with arbitrary precision, however, this adds a large number of unphysical parameters. A more physical path to the problem is a so-called critical point analysis which uses modified Lorentz oscillators to better reproduce asymmetric lineshapes. Resulting fits have a small set of physically meaningful parameters and comply very well with the experimental dielectric function [70–72].

In finite-difference time-domain (FDTD) simulations, explained in more detail in Chap. 4, it is essential to accurately model each material's dielectric function in the spectral region of interest. The FDTD software package contains a proprietary multi-coefficient material (MCM) fit which calculates a polynomial fit for $\varepsilon'(\omega)$ and $\varepsilon''(\omega)$ obeying the Kramers-Kronig relations [73]. In Fig. 3.1 c the MCM fit is applied to the experimental data, yielding an excellent fit over the entire bandwidth. It is worth mentioning that the MCM method is not developed from a physically meaningful picture, such as a critical point analysis, but rather offers a computationally efficient calculation of the optical properties of noble metals.

The majority of metallic structures discussed in this thesis are made of gold. Some structures are also simulated with silver as material. The dielectric function of template stripped polycrystalline silver [74], together with MCM fit is presented in Fig. 3.2. It can be inferred from the monotonous behavior of ε' and ε'' that silver behaves as a pure Drude metal in the visible and near infrared (NIR). Indeed, the first interband transition occurs around $\lambda = 300\,\mathrm{nm}$. Simultaneously, the imaginary part is smaller than that of gold, in particular for the green and blue spectral region, which makes silver an interesting candidate for nano-optics at shorter wavelengths [75–77]. The chemical reactivity of silver, however, is higher than of gold, making it more challenging to handle under ambient conditions.

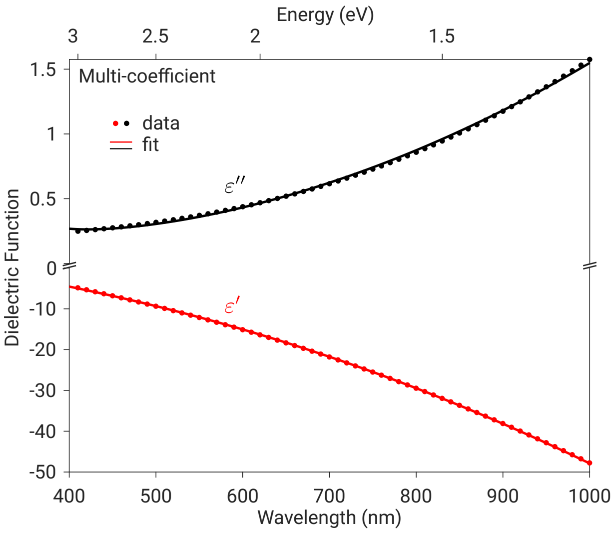

Figure 3.2 – Dielectric function of silver in the visible and NIR. The real part ε' is plotted in red, the imaginary part ε'' in black. Measured values (dots) are template stripped polycrystalline data taken from Yang *et al.* [74]. The solid lines show a MCM model fit. Note the different scale of positive and negative ordinates.

3.2 Surface plasmon polaritons

In the last section the dielectric function of noble metals is shown to have a negative real part and a positive imaginary part at optical wavelengths. In contrast, a dielectric material is characterized by a real-valued positive dielectric constant. At a metal-dielectric interface, solutions of the homogeneous Helmholtz equation (2.22) are composed of electromagnetic fields propagating in-plane, while the out-of-plane field is evanescent. The fields are coherently coupled to surface charge density waves at the metallic surface, resulting in a surface plasmon polariton (SPP). Such coupled excitations are described as quasiparticles in condensed matter physics so that an SPP can be regarded as a coupled light-plasma quantum. In the following, the condition for the existence of SPPs and their basic properties are discussed.

3.2.1 Single interface

The simplest model system is a single interface in a Cartesian coordinate system, located at $z = 0$ without loss of generality. The lower halfspace $z < 0$ is occupied by the noble metal with $\varepsilon_1(\omega) = \varepsilon_1'(\omega) + \mathrm{i}\varepsilon_1''(\omega)$ and the upper halfspace $z > 0$ is filled with a dielectric, see Fig. 3.3 a, where a gold-air boundary ($\varepsilon_2 = 1$) is assumed. Only a p-polarized eigensolution exists for the SPP because the electric field vector has to possess a component parallel to the plasmon's dipole moment, i. e. in x-direction, which is exactly zero in the case of s-polarization. Thus the electric field vector can be written as [13]

$$\vec{E}_j = \begin{pmatrix} E_{j,x} \\ 0 \\ E_{j,z} \end{pmatrix} e^{\mathrm{i}k_x x - \mathrm{i}\omega t} e^{\mathrm{i}k_{j,z} z}, \quad j = 1,2. \tag{3.6}$$

The two halfspaces are labeled by j, the SPP wave number by k_x, and the out-of-plane wave number for the halfspaces by $k_{j,z}$. Due to its polarization ($E_x \neq 0$, $E_z \neq 0$, $H_y \neq 0$) Eq. (3.6) is also known as transverse magnetic (TM) mode.

Exploiting the conservation of the parallel wave vector k_x and the boundary conditions (2.15a) and (2.16a) (with $\sigma_s = 0$), a dispersion relation connecting the wave vector with the angular frequency can be formulated,

$$k_x(\omega) = \sqrt{\frac{\varepsilon_1(\omega)\,\varepsilon_2}{\varepsilon_1(\omega) + \varepsilon_2}}\,\frac{\omega}{c} \tag{3.7a}$$

$$k_{j,z}(\omega) = \sqrt{\frac{\varepsilon_j^2}{\varepsilon_1(\omega) + \varepsilon_2}}\,\frac{\omega}{c}, \quad j = 1,2 \tag{3.7b}$$

for parallel and normal wave vector components. Contrary to free-space light (Eq. (2.25)) the SPP dispersion relation is nonlinear. From $\varepsilon_1(\omega) \in \mathbb{C}$ it follows that $k_x, k_{j,z} \in \mathbb{C}$. The mostly imaginary $k_{j,z}$ (compare the values of $\varepsilon_1(\omega)$ of Fig. 3.1 with $\varepsilon_2 = 1$) give rise to the evanescent nature of the SPP in z-direction, as plotted in Fig. 3.3 b for an exemplary wavelength of 830 nm. It can be seen that the penetration depth into the gold is much smaller than into the air halfspace. For k_x both its real and imaginary part

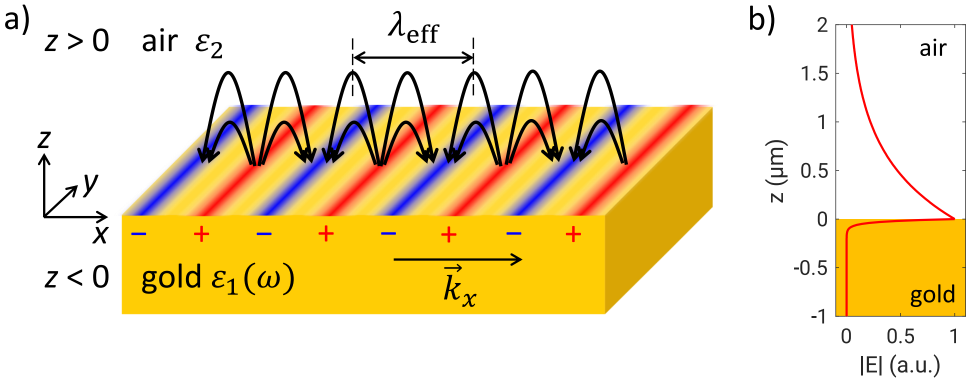

Figure 3.3 – **Surface plasmon polariton at a gold-air interface.** **a)** Sketch of the interface at $z = 0$ with illustrated charge density wave and coupled field (curved arrows). The bound SPP propagates in forward x-direction, indicated by $\vec{k}_x$. The definition of the effective wavelength $\lambda_{\rm eff}$ is also visible. **b)** Electric field as a function of z-coordinate at vacuum wavelength $\lambda_0 = 830\,\text{nm}$, showing the exponential decay away from the interface. Figure design inspired from [78].

play an important role. Thus it is common to represent the complex SPP wave number as

$$k_x(\omega) = \beta(\omega) + \mathrm{i}\alpha(\omega), \tag{3.8}$$

where $\beta \equiv \Re(k_x)$ is the propagation constant and $\alpha \equiv \Im(k_x)$ the field attenuation constant of the SPP due to Ohmic losses. From Eqs. (3.7a) and (3.7b) one is able to find necessary conditions for the existence of a bound interface mode. First, imaginary perpendicular components of k occur if the dielectric functions forming the interface fulfill $\Re\left[\varepsilon_1(\omega) + \varepsilon_2\right] < 0$. Second, the parallel component k_x needs to have a real part, i. e. nonzero β which is realized if $\Re\left[\varepsilon_1(\omega) \cdot \varepsilon_2\right] < 0$. Recalling the dielectric functions of gold and silver, Figs. 3.1 and 3.2, it is evident that both metals, interfacing a dielectric such as air ($\varepsilon_{\rm air} = 1$) or glass ($\varepsilon_{\rm glass} \approx 2.3$) meet these conditions and therefore are able to support bound SPPs.

The dispersion relation of an SPP at a gold-air interface is shown in Fig. 3.4 a for the optical regime. The MCM fit to the measured dielectric function of gold [68] is used for $\varepsilon_1(\omega)$, as displayed in Fig. 3.1 c. Indeed, two connected branches are visible in the dispersion relation. The higher-frequency branch below $\lambda = 510\,\text{nm}$ describes propagation inside the metal (Brewster mode) [13] and is not of interest here. The low frequency branch describes the bound SPP mode. For increasing frequency it bends further away from the light line and assumes increasing wave numbers. As there is no intersection point between the lines, SPPs on ideal smooth surfaces do not decay into far-field radiation. Likewise, excitation is impossible by far-field illumination from air. To overcome this momentum mismatch one can apply the Otto [79] or Kretschmann configuration [80] where the light beam is guided through a glass prism coupler. With the light line in glass lying below that of air (not shown) the required momentum can be delivered to excite SPPs on a metal film. Figure 3.4 b depicts the attenuation constant α as a function of frequency and vacuum wavelength, revealing a drastic increase as

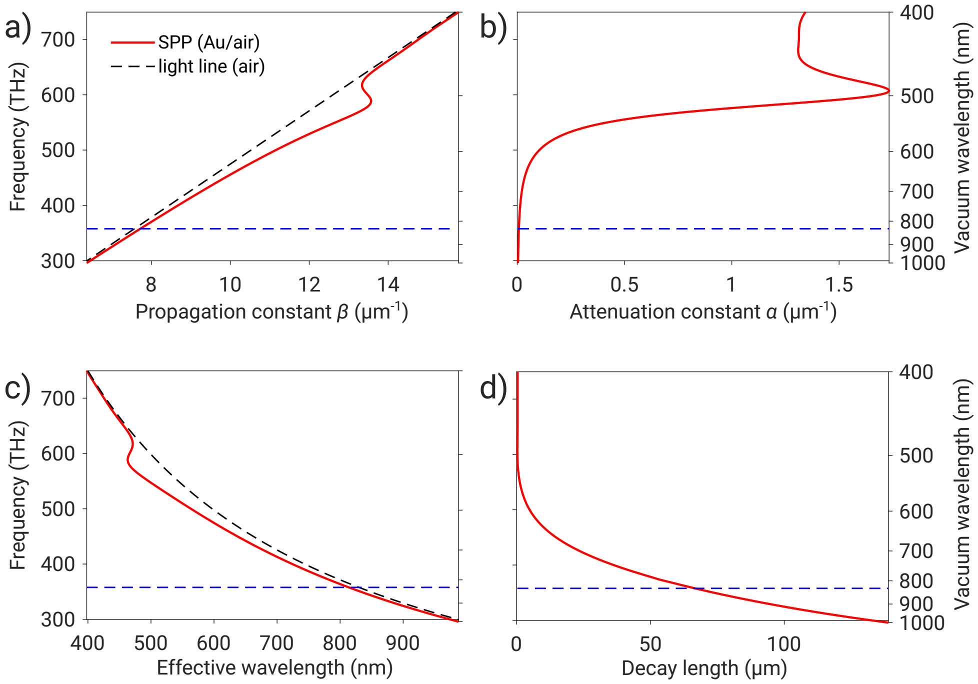

Figure 3.4 – Dispersive properties of SPPs. a) Dispersion of propagation constant β of a gold-air interface (red solid line) plotted against frequency $\nu = \omega/2\pi$, along with the light line in air (black dashed line). Dielectric properties are modeled after Fig. 3.1 c. **b)** Dispersion of attenuation constant α. On the right axis, vacuum wavelengths corresponding to the frequencies are added. **c)** Effective wavelength λ_{eff} of the SPP (red solid line) as a function of frequency, in comparison to the well established relation $\lambda = c/\nu$ in air (black dashed line). **d)** Decay length l_{decay} of the SPP as a function of frequency. The blue dashed lines mark the vacuum wavelength of 830 nm.

the propagation constant β moves away from the light line. In other words, the SPP is governed by the damped surface charge oscillations in this spectral regime. At lower frequencies where β lies close to the light line the SPP behavior rather resembles a plane wave oscillation found in free-space radiation. Correspondingly, the damping constant is very small. In plasmonics the general trade-off is found that increased light localization comes at the price of higher dissipation.

To provide a more intuitive picture of the SPP properties, length quantities are derived from β and α. The effective wavelength of a SPP mode is defined as

$$\lambda_{\text{eff}} = \frac{2\pi}{\beta}. \tag{3.9}$$

It turns out to be always shorter than the free-space wavelength at the respective frequency. From the attenuation constant the decay length l_{decay} is deduced after which $1/e$ of the initial SPP intensity upon propagation is left:

$$l_{\text{decay}} = \frac{1}{2\alpha}. \tag{3.10}$$

λ_{eff} and l_{decay} are plotted in Fig. 3.4 c and d, respectively. In agreement to the above observations, large decay lengths are identified in the region where the effective wavelength nearly coincides with the vacuum wavelength. A more reduced effective wavelength is accompanied by short decay lengths.

3.2.2 Double interface

According to the previous section each metal-dielectric interface is able to support a bound SPP mode under the considered circumstances. A metallic film is thus expected to host two such modes, one at each interface [81, 82]. Here we study a symmetric insulator-metal-insulator (IMI) system, air-gold-air, with varying gold film thickness t (Fig. 3.5 a). For films much thicker than the SPP penetration depth the two SPPs behave like individual states. Reducing the thickness below that length scale gives rise to a mutual Coulomb coupling between the SPPs at the double interface which creates new hybrid states comparable to strongly interacting electron orbitals in molecules [83].

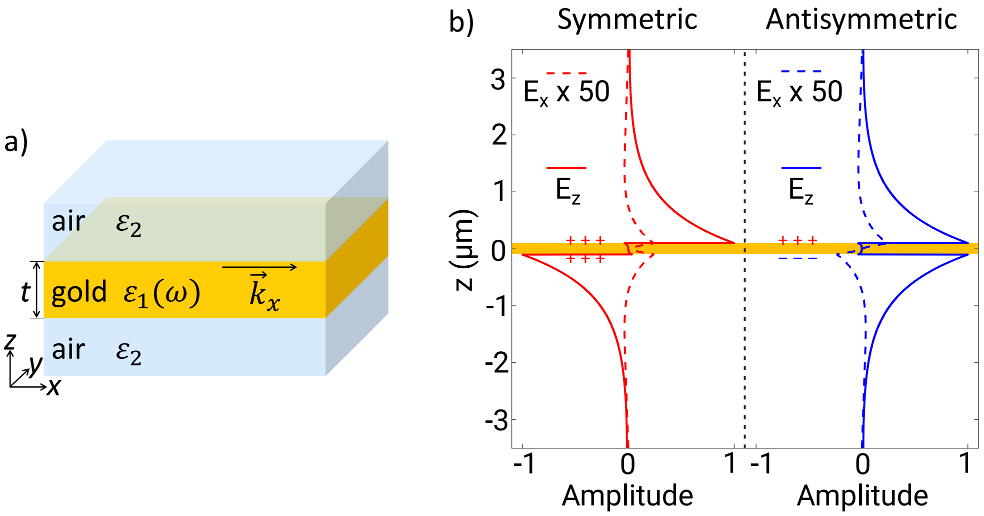

Figure 3.5 – SPP hybrid modes at an air-gold-air interface. a) Sketch of the IMI structure. **b)** Electric field components E_x (dashed lines) and E_z (solid lines) for the symmetric (red) and antisymmetric (blue) mode as a function of z at a vacuum wavelength of 830 nm. The film thickness is $t = 200$ nm. Corresponding charge distributions are indicated. Note the scaling of E_x for better visibility. Figure design inspired from [78].

The dispersion relation for a double layer system yields a transcendental equation between k_x and ω and can therefore not be solved algebraically [84]. Instead, we numerically determine the modal properties for the air-gold-air structure by means of a finite-difference frequency domain solver (cf. Sec. 4.3). The hybrid states are classified according to the symmetry of surface charge distributions on the metal surface. Fig. 3.5 b displays the electric field components for a 200 nm thick gold film surrounded by air. The symmetric mode (quasi TM mode) is characterized by a symmetric

E_x field w. r. t. the z-axis whereas E_z changes its sign. Surface charges at the metal surfaces are arranged symmetrically. In the antisymmetric case (quasi transverse-electric (TE) mode) E_x passes through zero at $z = 0$, with charges of opposite sign gathering at the surfaces, while E_z is symmetrically distributed.

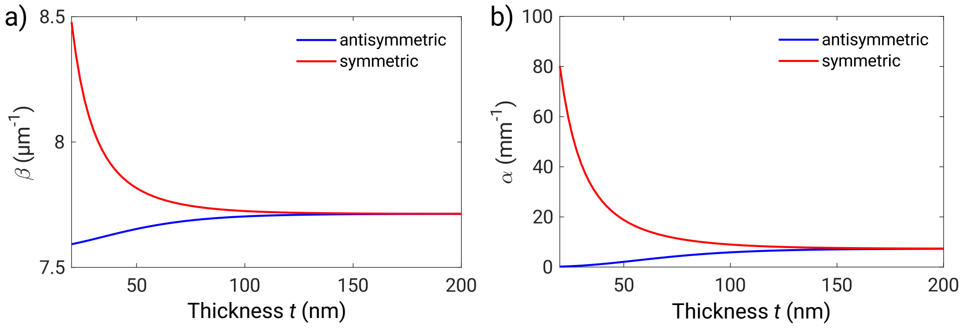

Figure 3.6 – Dispersive properties of hybrid modes at the air-gold-air double interface. a) Propagation constant β of the symmetric (red) and antisymmetric (blue) mode for varying film thickness t. **b)** Attenuation constant α of the symmetric (red) and antisymmetric (blue) mode. All values are taken for a vacuum wavelength of 830 nm.

Figure 3.6 compares the propagation and attenuation constants of symmetric and antisymmetric mode at 830 nm. Large film thicknesses yield degenerate modes. Below $t = 150$ nm a splitting is observed for both β and α. The symmetric mode experiences a strong increase in both constants for decreasing t. Physically, the mode assumes large wave numbers, i. e. it is highly confined, in conjunction with high losses. The antisymmetric mode shows rather opposite behavior. Its propagation constant approaches a value of 7.6 µm^{-1}. This coincides surprisingly well with the free-space value of β at $\lambda = 830$ nm (see the intersection point of the blue dashed line and the light line in Fig. 3.4 a), meaning that the antisymmetric mode resembles a plane wave propagating along the thin gold film. At the same time the mode's damping becomes small, as observed in α, which agrees with the aforementioned trade-off in plasmonics. Due to the long decay lengths of this class of SPPs, they are termed long-range SPPs [85–87] and qualify for applications in plasmonic circuitry [88, 89]. IMI structures with dissimilar dielectric layers bear more complex hybrid solutions [90] which are not discussed here. The inverse design, a metal-insulator-metal stack, also supports (anti)symmetric hybrid modes for small insulating gaps [91–93].

3.3 Plasmon resonances of nanoparticles

In the previous section propagating plasmons at smooth interfaces, largely determined by the involved dielectric functions, were explored. We now draw our attention to the interaction of light with small metallic particles. These are able to sustain resonant surface plasmons with the potential of high localization (i. e. small mode volume) and strong resonant enhancement of electromagnetic fields which also boost the interaction cross sections. Hence, besides the material properties the particle's geometry and size are of utmost importance in plasmonics. To understand why a resonance builds up in closed particles we illustrate an analogy to classical mechanics in Fig. 3.7. Upon excitation by an external electric field the electron plasma in the gold nanosphere oscillates against the positively charged lattice background. Electrons are pushed towards the boundaries and the motion is counteracted by the restoring Coulomb force from the ionic background. The mechanical analog contains a mass with a spring attached. The mass resembles the electron gas as both are subject to inertia. The spring delivers a backdriving force linear to the displacement, representing Coulomb interaction. This driven (damped) oscillator picture captures the resonant behavior of the plasma oscillation amplitude and the related phase shift around the resonance frequency. Another access to the resonant nature of plasmons on closed particles is provided by considering the particle as a Fabry-Pérot cavity. Several particle shapes are studied in the following subsections with regard to their plasmon resonances, starting with the case of highest symmetry.

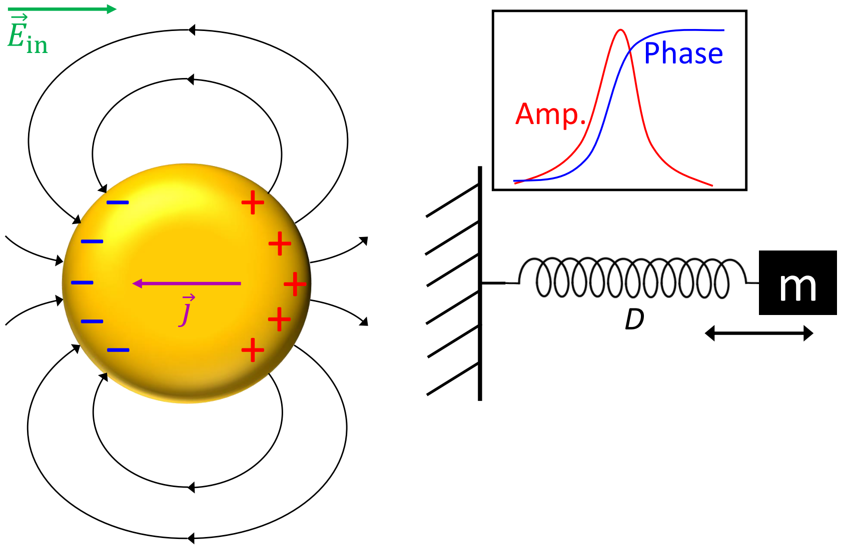

Figure 3.7 – **Plasmon resonance and mass-spring model.** Left: Sketch of nanosphere with momentary charge distribution, electric field lines and current density $\vec{j}$ upon excitation with $\vec{E}_{\text{in}}$. Inspired from [13]. Right: Mass attached to a spring with spring constant D, exhibiting a harmonic oscillation similar to the charge density on the sphere. The resonant behavior gives rise to a Lorentz-shaped peak amplitude in conjunction with a phase jump at resonance.

3.3.1 Single sphere

Mathematically, the basic task is to solve the vector Helmholtz equation (2.22) for a multiple domain setup under the correct boundary conditions. The most symmetric situation, a sphere embedded in a homogeneous environment, where a plane wave is impinging, can be solved analytically and is widely known as Mie theory [60, 94]. G. Mie wrote incoming and scattered electromagnetic fields as an infinite series of vector spherical harmonics, a special class of mathematical functions obeying orthogonality [58, 60]. Each scattered mode is weighed by a Mie coefficient. The most fundamental modes are denoted as electric dipole mode and electric quadrupole mode. The former is illustrated in Fig. 3.7. As can be seen from the charge distribution it is associated with a dipole moment.

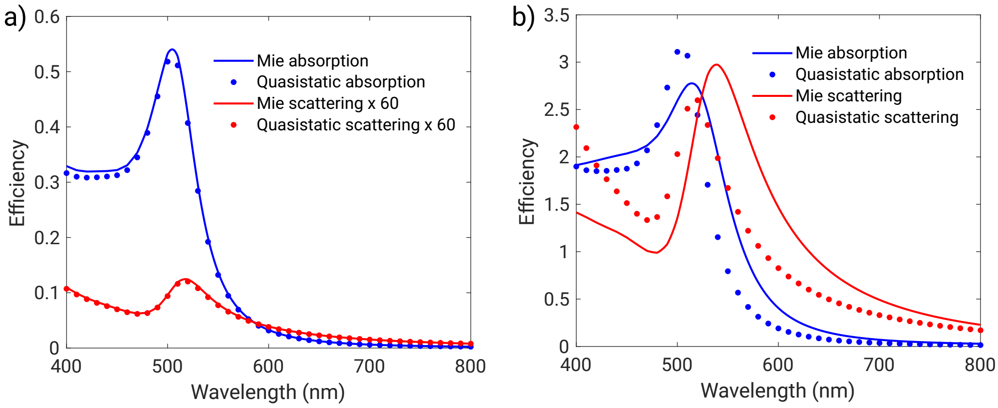

Figure 3.8 – Absorption and scattering efficiencies of gold nanospheres. a) Absorption (blue) and scattering (red) of a sphere with 10 nm radius in air. The quasi-static approximation (dots) reproduces full Mie calculations (solid lines) remarkably well. Note the distinct scaling of scattering curves for better visibility. **b)** Same as in a) for a sphere radius of 60 nm. With increasing particle size deviations between quasi-static approximation and Mie theory become evident. Figure design inspired from [95].

A well-established simplification is the quasi-static approximation, valid for particle radii a much smaller than the wavelength of the applied field ($ka \ll 1$). One can then assume that the entire particle is exposed to a uniform excitation phase. It has been demonstrated that the resulting field around a sphere is identical to the electromagnetic field of a static point dipole residing at the center of the sphere [60]. From this correspondence, the induced dipole moment is proportional to the field, similar to Eq. (2.12a),

$$\vec{p} = \varepsilon_0 \varepsilon_2 \xi \vec{E}_{\text{in}}, \tag{3.11}$$

with the polarizability ξ[1],

$$\xi = 4\pi a^3 \, \frac{\varepsilon_1 - \varepsilon_2}{\varepsilon_1 + 2\varepsilon_2}. \tag{3.12}$$

Here, ε_1 and ε_2 are the dielectric functions of the sphere and the surrounding, respectively. A vanishing denominator implies a resonance condition for $\Re(\varepsilon_1) = -2\varepsilon_2$ occurring at green wavelengths for a gold nanosphere in air (cf. Fig. 3.8). The particle's response to an applied field is referred to as its interaction cross section where different mechanisms are considered. The absorption cross section C_{abs} accounts for the light absorbed by the particle and transferred to nonradiative channels such as heat, phonons etc. (Re-)scattered fields, i. e. radiative channels are included in the scattering cross

---

[1] In the literature, the polarizability is usually denoted as α. To avoid confusion with the field attenuation constant α defined in Sec. 3.2.1, in this work we denote the polarizability as ξ.

section C_{scat}. The sum of both is called extinction cross section $C_{\text{ext}} = C_{\text{abs}} + C_{\text{scat}}$. In the framework of the quasi-static approximation, the polarizability (3.12) allows to express the cross sections in a simple closed form [60]:

$$C_{\text{abs}} = k \cdot \Im(\xi) \,\propto a^3 \tag{3.13a}$$

$$C_{\text{scat}} = \frac{k^4 |\xi|^2}{6\pi} \,\propto a^6 \tag{3.13b}$$

A strong dependence on the particle size is obtained. While particles with small volume mostly absorb incoming light the response of larger particles is governed by scattering. Figure 3.8 illustrates a comparison between full Mie theory and quasi-static approximation as well as the limitation of the latter. Panel a) depicts scattering and absorption efficiency (interaction cross section divided by geometric cross section) for a gold nanosphere of radius 10 nm in air. As expected, the scattering efficiency is weak compared to absorption. Resonance features for the former and latter are obtained at 518 nm and 505 nm wavelength. Both calculation methods agree very well. A different situation is found for a larger gold sphere with radius 60 nm in Fig. 3.8 b. Here both cross sections have a similar efficiency. Strikingly, the approximative method blue-shifts the resonances w. r. t. full Mie calculations which demonstrates the limited applicability for bigger particles. In such a case retardation effects, e. g. non-uniform excitation phase and polarization vectors across the particle dimension have to be taken into account [96]. This is the point where fully vectorial numerical simulations enter and become the method of choice when modeling the optical response of such non quasi-static objects. Chap. 4 is dedicated to the finite-difference time-domain algorithm, one of the most popular numerical approaches.

To conclude this section, we take a brief look at the case of ellipsoidal particles within the quasi-static approximation. We assume two minor semiaxes a, b and one major semiaxis $c > a, b$ (prolate ellipsoid). The geometric generalization of the spherical shape manifests itself as a generalization of the polarizability expression into a tensor whose long axis component ξ_c reads as [60]

$$\xi_c = 4\pi abc \frac{\varepsilon_1 - \varepsilon_2}{3\varepsilon_2 + 3L_c\,(\varepsilon_1 - \varepsilon_2)}, \tag{3.14}$$

where L_c is the geometrical factor for polarization along the major axis. L_c depends on the eccentricity and thus on the aspect ratio of the ellipsoid [60, 97–99]. For a sphere $L_c = 1/3$ holds, which reduces Eq. (3.14) to the aforementioned polarizability Eq. (3.12).

3.3.2 Single rod

In the previous section gold nanospheres embedded in air turned out to have a (dipolar) plasmon resonance at 510 nm that weakly depends on particle size. However, a myriad of applications involving plasmonics, e. g. strong light-matter interaction [14, 15, 100–102], metasurfaces [19], surface-enhanced Raman scattering (SERS) [103, 104] even down to the single-molecule level [105, 106], photodetection via hot electrons [107] and biosensing [108, 109], to name a few, calls for resonances at well-defined frequencies across the entire visible and NIR spectrum. Various particle shapes, reaching from shells, triangles, slits and more have been harnessed in these cited works to achieve spectral tunability of plasmonic resonances. Likewise, the ellipsoid's polarizability Eq. (3.14) already hints towards the most intuitive way towards resonance tuning, namely by using elongated nanoparticles.

Rods are among the simplest elongated particle designs, consisting of a cylindrical wire section terminated by two hemispherical end caps. As nanorods are a fundamental building block for several structures throughout this work, it is highly instructive to understand their resonant behavior within a "lightweight" model. Here we treat the rod as a Fabry-Pérot resonator [11, 75, 110, 111] in which a guided SPP exists on the cylindrical section, similar to an IMI structure discussed in Sec. 3.2.2. One can imagine that by rotating the IMI layer around its longitudinal symmetry axis, it becomes a cylindrical metal wire and that their modal properties are thus related. Moreover, in the limit of infinite cylinder radius the SPP solution of a single interface (cf. Sec. 3.2.1) is attained [112], corroborating the strong connection between propagating and particle plasmons. On the continuous piece of wire waveguide the SPP propagates back and forth. According to the mass-spring model (cf. Fig. 3.7) the plasmon feels a restoring force at the end caps, resulting in a reflection. Another point of view is conveyed by impedance matching [6, 50, 51]. The abrupt structural change from the uniform waveguide across the end cap towards vacuum induces discontinuities in the guided mode's impedance which is accompanied by high reflectivities. Not only the amplitude is affected by each reflection at the end cap, also the phase of the SPP experiences a shift which depends on the exact termination geometry and must be taken into account [110, 111].

Figure 3.9 a illustrates the rod as Fabry-Pérot resonator with net length, total length, and phase jumps associated with the end caps. Altogether a standing wave is able to build up on the rod by constructive interference if the phase accumulated upon an entire round-trip equals an integer multiple of 2π. Thus a Fabry-Pérot resonance emerges if the net rod length L_{net} fulfills the condition

$$\beta L_{\text{net}} + \phi_e = n\pi, \quad n \in \mathbb{N} \tag{3.15}$$

with β the propagation constant of the guided SPP and ϕ_e the reflection phase at the end cap adjacent to vacuum. Note that to compute the propagation phase one must use the net length of the uniform cylindrical section L_{net} instead of the total rod length L because the guided mode is not an eigenmode on the end caps. Together with Eq. 3.9 a linear relation is established between effective wavelength and net rod length at which a resonance arises. In addition, a linear effective wavelength scaling with vacuum wavelength has been derived for metallic rods at optical frequencies as long as the material behaves like a Drude metal [113, 114]. If the dispersion relation of the guided mode and the reflection phase are known, resonance wavelengths of nanorods of lengths L can be calculated by Eq. (3.15). Results for the first three resonance orders on gold nanorods are visualized in Fig. 3.9 b. The rod diameter is fixed to 30 nm. As expected, the resonance wavelength scales almost linearly with the rod length since the

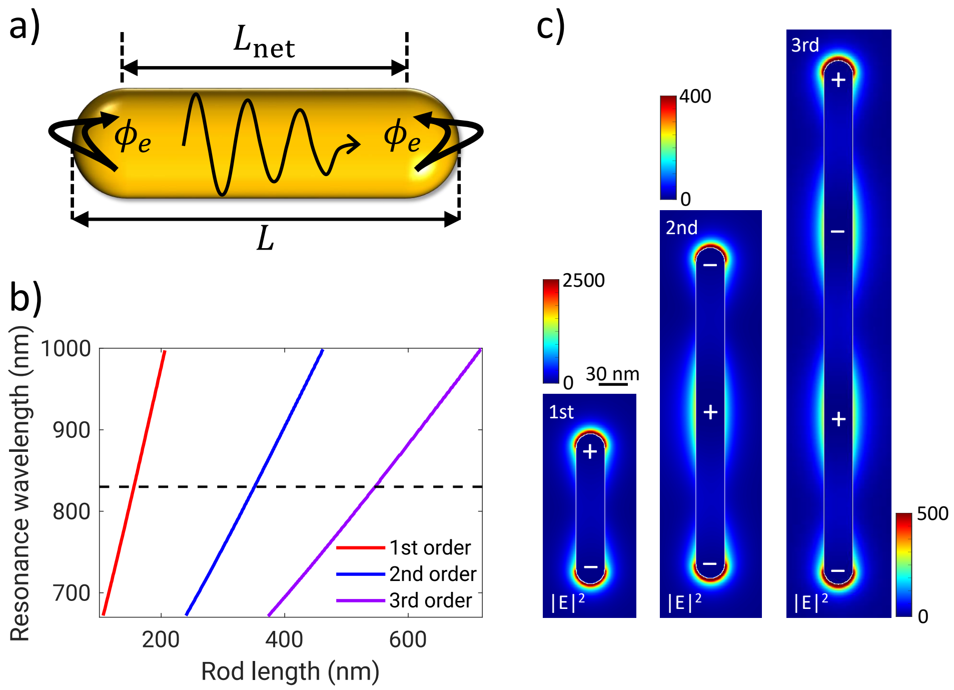

Figure 3.9 – **Fabry-Pérot resonances of nanorods.** **a)** Schematics of the Fabry-Pérot model. A guided wire mode propagates along the cylindrical part (L_{net}) of the rod. At the hemispherical end caps and open vacuum ends, the mode is subject to a reflection phase shift ϕ_e. The entire rod length is denoted L. **b)** Calculated resonance wavelengths for rod length L at a fixed rod diameter of 30 nm. The lowest three Fabry-Pérot resonances are shown in red, blue, and violet. The black dashed line marks 830 nm resonance wavelength. **c)** Near-field intensity ($|E|^2$) enhancement maps for first, second, and third resonance order at 830 nm simulated by the FDTD method (cf. Chap. 4). Rod lengths are 157 nm, 346 nm, and 548 nm, respectively. Momentary charge distributions are indicated on the rods. Note the different color scale for each mode. Figure design inspired from [95].

free electron gas in gold mainly contributes to the plasmonic response between 670 nm and 1000 nm (cf. Sec. 3.1). This scaling represents a useful design rule for resonance tuning of rods. It is worth mentioning that the dispersion relation and reflection phase have been obtained numerically as a function of vacuum wavelength such that the overall calculation is semi-analytical. In Secs. 4.3 and 4.4.2, the numerical methodology is explained in detail. Later, the Fabry-Pérot model is revisited in Sec. 7.3.1 where plasmonic nanorod resonances are investigated under the viewpoint of generalized coherent perfect absorption (gCPA).

At vacuum wavelength 830 nm we obtain the resonance rod lengths $L = 156$ nm, 351 nm, 546 nm for first, second, and third Fabry-Pérot orders. Each resonance is associated with highly enhanced and confined near-fields at the rod terminations, rendering these structures an attractive building block for various applications as mentioned above. Fig. 3.9 c presents simulated near-field intensity ($|E|^2$) enhancement maps for each resonance. Albeit with slightly deviating rod lengths the Fabry-Pérot condition is still well fulfilled. The fundamental resonance is of dipolar nature, as indicated by the asymmetric momentary charge distribution. Subsequent higher orders of degree *n* are characterized by *n* charge nodes along the rod. The third resonance order again possesses a net dipole moment that can couple to far-field radiation. Hence, first and third order are superradiant modes. In contrast, the second order has vanishing net dipole moment due to its symmetric charge distribution. This mode only weakly couples to the far-field and is therefore termed subradiant. Its damping over time is dominated by Ohmic losses. According to the reciprocity theorem [13] it cannot be excited with an impinging plane wave at normal incidence. A symmetry break must be introduced into the system [115]. Here the nanorod is illuminated by a Gaussian beam at an angle of 45° w. r. t. the normal direction. Also the enhancement factors differ for the three modes. Maximum intensity enhancement is observed for the fundamental dipolar resonance. With increasing rod length the Ohmic dissipation upon propagation becomes more and more pronounced and diminishes the enhancement factor for higher orders. One more aspect determining the enhancement shown here is the difference in excitation efficiency between the modes. Superradiant modes are ideally far-field excited with a normal incidence beam. However, the subradiant second order resonance is driven less efficiently by the grazing incidence. Therefore its enhancement factor cannot be compared directly with those of the superradiant modes.

Besides longitudinal resonances, also transverse resonances exist on a nanorod where charges oscillate perpendicular to the long axis [116, 117]. Transverse resonances are only weakly tunable by changing the rod diameter. Compared to the longitudinal counterparts their near-field intensity enhancement factors remain relatively weak.

3.3.3 Double rod

Combining two nanorods in close proximity to a rod dimer opens a new class of plasmonic resonances which is of particular interest because of even higher field enhancement and confinement in hotspot regions. Here we discuss end-to-end aligned nanorods separated by a narrow gap. Coulomb interactions couple the individual plasmon oscillations across the gap, giving rise to hybrid modes of a rod dimer, similar as observed for SPPs in thin IMI stacks (cf. Sec. 3.2.2). Drawing the analog to classical mechanics, two mass-spring systems coupled by a third spring intuitively explain the modal symmetries [118–121].

In the so-called antibonding mode, Fig. 3.10 a, the two masses oscillate out of phase, i. e. undergo a symmetric motion w. r. t. the center of the structure. The same is true for the charge oscillations on the gold nanorod dimer. This implies that charges of equal sign appear at the gap and create a field minimum at the center. At the far ends, however, enhanced near-fields close to the metal are visible. Quite the opposite happens for the mode where the masses move in-phase so that the coupling spring is at constant length all the time (cf. Fig. 3.10 b). Also the charges on the plasmonic particles oscillate with the same phase which leads to an antisymmetric charge distribution. Attractive Coulomb interactions across the gap accumulate an increasing number of

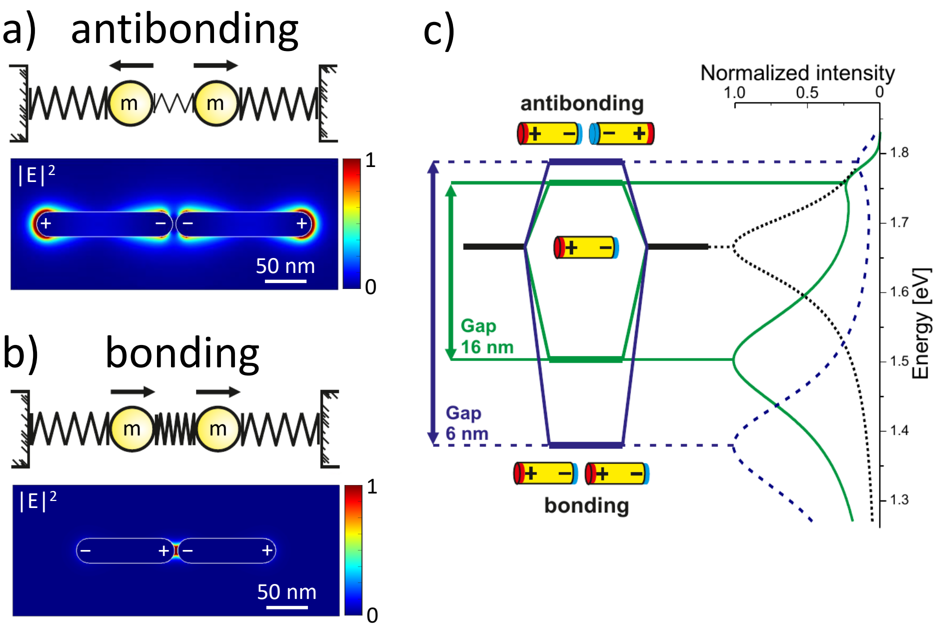

Figure 3.10 – **Hybrid modes and energy splitting in rod dimers.** **a)** Mechanical mass-spring model and plasmonic double rod structure showing out of phase oscillations (antibonding mode). The near-field intensity map is simulated for rod diameter 30 nm, rod length 166 nm, and gap width 4 nm at $\lambda = 818$ nm. **b)** Same as in a) but for the bonding mode. The simulated rod length is 120 nm. **c)** Energy splitting of rod dimer modes for two different gap sizes, in comparison to a single rod. Reprinted and adapted with permission from [115]. © 2010 American Chemical Society.

charges in this so-called bonding mode. Therefore the electric near-field is considerably enhanced and localized to the gap region. A similar symmetry argument as for the longitudinal modes of a single nanorod holds here regarding excitation mechanisms. The bonding mode can be excited from the far-field by a plane wave propagating perpendicular to the dimer axis. In order to drive the antibonding mode an asymmetric excitation is needed, e. g. an offset Gaussian beam or a point dipole source near the rod ends. The latter scheme is used to obtain the near-field intensity map in Fig. 3.10 a.

The formation of the hybrid modes is accompanied by an energy splitting as depicted in Fig. 3.10 c. One may well imagine that the out of phase motion happens at a higher frequency than the plasmon oscillation on an isolated rod since the coupling spring adds to the total restoring force. The energy of the antibonding mode is thus increased. In the classical picture the resonance frequency of the in-phase coupled masses is equal to a single mass-spring system [122]. Considering the electromagnetic nature of plasmons, however, the attractive Coulomb interaction lowers the energy so that the bonding plasmon mode appears energetically below the single rod resonance. The total energy splitting and the maximum field enhancement depend critically on the gap width between the particles, with narrow gaps causing larger resonance shifts and higher enhancement factors.

Aligning two nanorods side by side, longitudinal and transverse modes on single rods hybridize and offer a variety of coupled modes with different symmetries, resonance shifts and line widths [123]. Using a bottom-up self-assembly approach of chemically synthesized gold nanorods ultra-narrow gaps can be produced, giving rise to resonant near-fields confined down to atomic length scales [124].

3.4 Dipole coupled to plasmonic nanoantenna

Upon illumination by a light beam metallic nanospheres and nanorods exhibit highly confined and resonantly enhanced near-fields, as demonstrated in the last sections. With this feature they serve as an interconnect between free-space light and localized electromagnetic energy and are therefore termed optical antennas [8–12]. They are often combined with various optically active nano-objects, e. g. semiconductor quantum dots, atoms, dye molecules, nitrogen-vacancy centers in diamond, defects in transition-metal dichalcogenides (TMDCs), or, alternatively, tunnel currents (cf. Chap. 5). The antenna's task is to couple these nano-objects efficiently to the far-field and enhance both transmitting and receiving processes.

It is therefore interesting to study the characteristics of such a quantum emitter in close proximity to a plasmonic nanostructure. Originally, the increase of molecular quantum efficiency (QE) upon changes of the local environment, e. g. by adding nearby silver islands, was discovered by Wokaun *et al.* [125]. Here we consider a two-level emitter with ground state $|g\rangle$, excited state $|e\rangle$, and transition frequency ω weakly coupled to an antenna. In the perturbation limit the emitter can be described as a classical dipole [9]. According to the multipole expansion of the current density $\vec{j}$ at the origin $\vec{r}_0$, the lowest order term of the Taylor series is proportional to the dipole moment $\vec{p}$ [13]:

$$\vec{j}(\vec{r}) = -\mathrm{i}\omega\vec{p}\delta(\vec{r}-\vec{r}_0). \tag{3.16}$$

The Dirac delta function is denoted by δ. The above equation states that a current density can be approximately modeled by an electric dipole, an important step for modeling tunneling currents (see Chap. 5). Inserting Eq. (3.16) into Poynting's theorem Eq. (2.8) and integrating over a closed surface according to Eq. (2.9) the radiated power P from the emitter reads

$$P = \frac{\omega}{2}\Im[\vec{p}^{*}\cdot\vec{E}(\vec{r}_0)]. \tag{3.17}$$

The dot product requires the dipole moment to be aligned with the local electric field in order for the emitter to be influenced by the antenna. As the field value at $\vec{r}_0$ enters Eq. (3.17) the outgoing power is determined by the interaction of the emitter with its own back-scattered field. Splitting $\vec{E}$ at the origin into primary and scattered field contributions,

$$\vec{E}(\vec{r}_0) = \vec{E}_0(\vec{r}_0) + \vec{E}_s(\vec{r}_0), \tag{3.18}$$

the normalized rate of energy dissipation can be written as [13]

$$\frac{P}{P_0} = 1 + \frac{6\pi\varepsilon_0\varepsilon}{|\vec{p}|^2k^3}\Im[\vec{p}^{*}\cdot\vec{E}_s(\vec{r}_0)] \tag{3.19}$$

with P_0 the power dissipated in a homogeneous vacuum environment. The scattered field $\vec{E}_s$ solely stems from inhomogeneities which thus are responsible for changes in the radiation rate.

Excited quantum emitters embedded in free space are subject to spontaneous emission after a lifetime τ, a process triggered by fluctuations of a quantized vacuum field. A quantitative description has been developed in the framework of quantum electrodynamics (QED) using Fermi's golden rule. The rate of spontaneous decay γ is given by [9]

$$\gamma = \frac{1}{\tau} = \frac{\pi\omega}{3\hbar\varepsilon_0} \left| \left\langle g \middle| \hat{\vec{p}} \middle| e \right\rangle \right|^2 \rho_p(\vec{r}_0, \omega), \tag{3.20}$$

where $\left\langle g \middle| \hat{\vec{p}} \middle| e \right\rangle$ is the matrix element for a dipole transition between $|e\rangle$ and $|g\rangle$ with dipole operator $\hat{\vec{p}}$ and ρ_p the partial photonic local density of states (LDOS), a measure for the number of optical modes available per unit volume and unit frequency. The photonic LDOS can be expressed by the dyadic Green function of the system the quantum emitter is embedded in. The LDOS is therefore highly dependent on the environment, first discovered by Purcell in 1946 for atoms in a resonant electric circuit [126]. Importantly, an analogy between classical and quantum mechanical pictures can be drawn. It is found that the normalized decay rate of a quantum emitter equals the normalized dissipated power of a classical dipole [13]:

$$\frac{\gamma}{\gamma_0} = \frac{P}{P_0}. \tag{3.21}$$

This relation implies that changes in the decay rate of a quantum emitter can be safely predicted by putting a classical point dipole in the same environment and observing its emitted power analytically or in numerical simulations (cf. Chap. 4).

Analytical solutions to calculate dipolar decay rates close to small spherical particles have been reported decades ago [128]. As an optical antenna in form of a double rod (cf. Sec. 3.3.3) provides highly enhanced fields in the gap it also provides significant LDOS enhancement and reduces quantum emitter lifetimes drastically. We illustrate the influence of an antenna by simulating the decay rate of a quantum emitter[2] placed in the gap of a gold rod dimer with the numerical boundary element method (BEM) [127] (see also Sec. 5.2.2). First we assume the internal quantum efficiency (IQE) of the emitter to be 1, i. e. all deexcitation processes result in a photon and no internal loss is present. However, since the emitter is coupled to a metallic nanostructure the total decay γ is determined by radiative decay γ_{rad} and nonradiative decay γ_{nrad}. The latter contains Ohmic losses in the metal and coupling to higher-order dark modes. Hence, the external quantum efficiency (EQE) can be written

$$\mathrm{EQE} = \frac{\gamma_{\mathrm{rad}}}{\gamma_{\mathrm{rad}} + \gamma_{\mathrm{nrad}}}. \tag{3.22}$$

Simulated values for γ_{rad} and γ_{nrad} are plotted in Fig. 3.11 a. The inset shows the double rod structure with the x-polarized emitter placed centrally in the gap. Each rod

---

[2] We restrict ourselves to the weak excitation limit where the emitter resides mostly in the ground state $|g\rangle$ and no saturation effects are present.

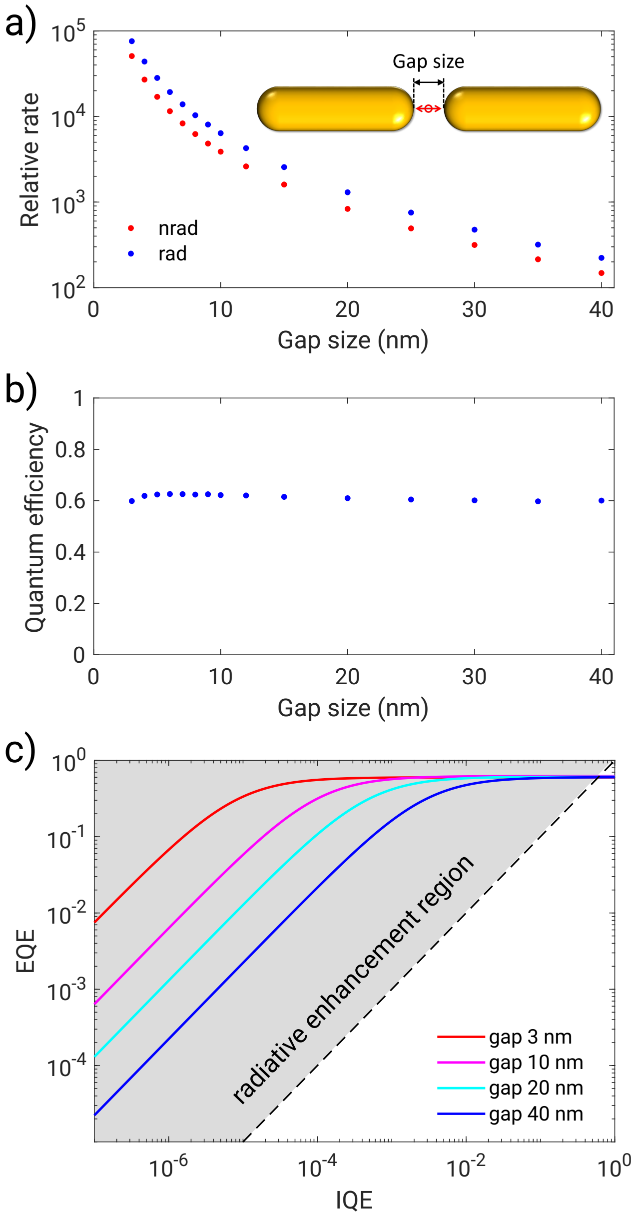

Figure 3.11 – **Dipole in a gap antenna.** **a)** Normalized radiative and nonradiative decay rates as a function of antenna gap size, simulated by the boundary element method (BEM) [127]. The inset visualizes the simulated structure. **b)** (External) quantum efficiency of the dipole-antenna system for an emitter with internal quantum efficiency IQE=1 as the gap size varies. **c)** External quantum efficiency (EQE) as a function of IQE for selected gap sizes. Within the gray shaded area radiative enhancement is achieved. Figure design inspired from [95].

has a length of 120 nm and diameter 30 nm. We use the bonding plasmon resonance with field hotspot in the gap (field aligned with dipole moment) to show the strong dependency of the gap width on the LDOS enhancement. According to Sec. 3.3.3 a varying gap size is associated with a shift of resonance wavelength. Thus the decay rates for different gap sizes are evaluated at the corresponding resonance wavelengths between $\lambda = 740\,\mathrm{nm}$ (gap 40 nm) and $\lambda = 820\,\mathrm{nm}$ (gap 3 nm). Both decay rates are highly enhanced for decreasing gaps. In each case the radiative decay exceeds the nonradiative decay. From these numbers the EQE is evaluated via Eq. (3.22) and visualized in Fig. 3.11 b. It assumes stable values around 0.6 for a broad range of gap widths. Shrinking the gap below 3 nm a breakdown of the EQE is indicated. If a dipolar emitter resides very close to a metallic surface it is largely coupled to highly confined nonradiative modes and a strong image dipole inside the gold generates heat, giving rise to fluorescence quenching [129]. An EQE of 0.6 indeed means that the radiation efficiency of the quantum emitter is reduced by the presence of the antenna. An intrinsically 100 % efficient emitter simply cannot be improved in efficiency. The lossy nature of the gold antenna decreases the overall QE.

The situation changes drastically if an intrinsically inefficient emitter is put in the gap of the rod dimer. Now $\mathrm{IQE} = \gamma^0_{\mathrm{rad}}/(\gamma^0_{\mathrm{rad}} + \gamma^0_{\mathrm{nrad}})$ with the free-space decay rates γ^0_{rad} and γ^0_{nrad}. Eq. (3.22) is then generalized to

$$\mathrm{EQE} = \frac{\gamma_{\mathrm{rad}}/\gamma^0_{\mathrm{rad}}}{\gamma_{\mathrm{rad}}/\gamma^0_{\mathrm{rad}} + \gamma_{\mathrm{nrad}}/\gamma^0_{\mathrm{rad}} + (1-\mathrm{IQE})/\mathrm{IQE}}. \tag{3.23}$$

Small values of IQE can be enhanced by several orders of magnitude as illustrated in Fig. 3.11 c. The gray shaded area left of the dashed black line shows the region of radiative enhancement of the EQE. The smaller the antenna gap the higher the enhancement factor can be. This is an important finding because a variety of quantum emitters available on the nanoscale is intrinsically quite inefficient such as photon generation from inelastic tunneling (cf. Chap. 5) or radiative recombination of charge carriers in zinc phthalocyanine (cf. Chap. 6).

4

Numerical simulations

Ultimately, physics is an experimental science. New knowledge is generated by real-world observations under repeatable, reproducible, and in the best case controllable environmental conditions. Observations must coincide with a theoretical model to be properly interpreted. Theoretical foundations also have the task to predict novel, unexplored effects that in turn reinforce efforts in experimental design and measurement techniques. This way a mutual triggering of milestones between experiment and theory is established which may e. g. also lead to previous models being proven false and replaced by a corrected framework. In the field of nanophotonics, theoretical modeling and numerical simulations play a paramount role for several reasons. First, closed analytical solutions to Maxwell's equations exist only for simplistic particle geometries (spheres) embedded in homogeneous surroundings [94]. More sophisticated shapes and environments require thorough numerical modeling. Second, state-of-the-art nanofabrication techniques such as top-down electron beam lithography (EBL) and focused ion beam (FIB) milling are cost drivers. Consequently, launching brute-force fabrication series to obtain complex antenna designs with desired resonances and other functionalities by trial and error goes beyond any financial scope and timeline. Third, the experimental observation of a certain physical effect can be overshadowed by environmental influences or imperfections of the sample under study. Thus the relation between specimen properties, external influences and measured results remains elusive and it would be of interest to consider a "neat" specimen under "ideal" circumstances. In view of all these aspects, numerical simulations represent an essential and versatile tool in nowadays' nanoscience with their ability to not only forecast optical resonances, near- and far-field distributions, among other physical quantities. Moreover, they allow studies on idealized materials and "clean" systems, where the effect of interest can be better explored and understood, in close relation to theoretical models. The possibility to employ increasing computational resources allows comprehensive design optimization.

Two major classes of algorithms to numerically solve Maxwell's equations are in use, *viz.* differential and integral methods. Depending on the problem at hand, a certain algorithm may be better suited to find accurate solutions than the other approaches [130]. Among differential methods the finite-difference time-domain (FDTD) and the finite element (FE) are widespread because they are able to tackle a large variety of nanophotonic problems. It is necessary to discretize the entire space, either with a Cartesian grid or tetrahedrons, and to solve for electromagnetic fields in each cell. Integral methods solve Maxwell's equations in integral formulation via Green function techniques in the frequency-domain. The dyadic Green tensor describes the full vectorial fields originating from a source dipole with arbitrary orientation. Here it is sufficient to subdivide the scatterer's volume into small cells each of which carries a dipole polarizability, as in the discrete dipole approximation (DDA) method. A second popular implementation is the boundary element method (BEM) where only surfaces between piecewise homogeneous objects are discretized, reducing the calculation of desired fields to a surface integral expression [127, 131]. To the majority of numerical problems addressed in this thesis the FDTD method is applied. Hence, this chapter introduces the most important aspects of the underlying algorithm, methodology, and postprocessing steps necessary for data evaluation. For in-depth information about the FDTD technique the reader is referred to the comprehensive textbook of Taflove and Hagness [132]. A brief description of the closely related finite-difference frequency-domain (FDFD) method for waveguide eigenmode calculation is given, too.

4.1 The finite-difference time-domain algorithm

The main goal of the FDTD technique is to obtain electromagnetic fields on a discretized spatial lattice with iterative stepping through discrete time intervals. To better illustrate how an elaborate discretization strategy leads to robust numerical operations we rewrite Maxwell's curl equations (2.1b), (2.1c) in components, assuming time-independent ε, μ, and σ:

$$\frac{\partial E_i}{\partial t} = \frac{1}{\varepsilon}\left(\frac{\partial H_k}{\partial j} - \frac{\partial H_j}{\partial k} - \sigma E_i\right), \tag{4.1a}$$

$$\frac{\partial H_i}{\partial t} = \frac{1}{\mu}\left(\frac{\partial E_j}{\partial k} - \frac{\partial E_k}{\partial j}\right). \tag{4.1b}$$

Using Cartesian coordinates, $\{i, j, k\}$ denote $\{x, y, z\}$ and its cyclic permutations so that Eqs. (4.1) establish a system of six coupled partial differential equations. We declare the notation of a field component F at a grid point as

$$F(u\Delta x, v\Delta y, w\Delta z, n\Delta t) = F^n(u, v, w). \tag{4.2}$$

The indices (u, v, w) mark the discrete position in (x, y, z)-direction in the Cartesian grid and n is the discrete time step.

In 1966 Kane Yee introduced a discretization scheme which is nowadays known as Yee cell [133]. One of its key ideas is that both electric and magnetic fields are explicitly calculated instead of merely one field quantity, making the algorithm more robust and versatile in computational electrodynamics [132]. Temporal updates of the field components are arranged in a way such that electric and magnetic fields are calculated alternately in increments of $\Delta t/2$. Following this leapfrog scheme visible in

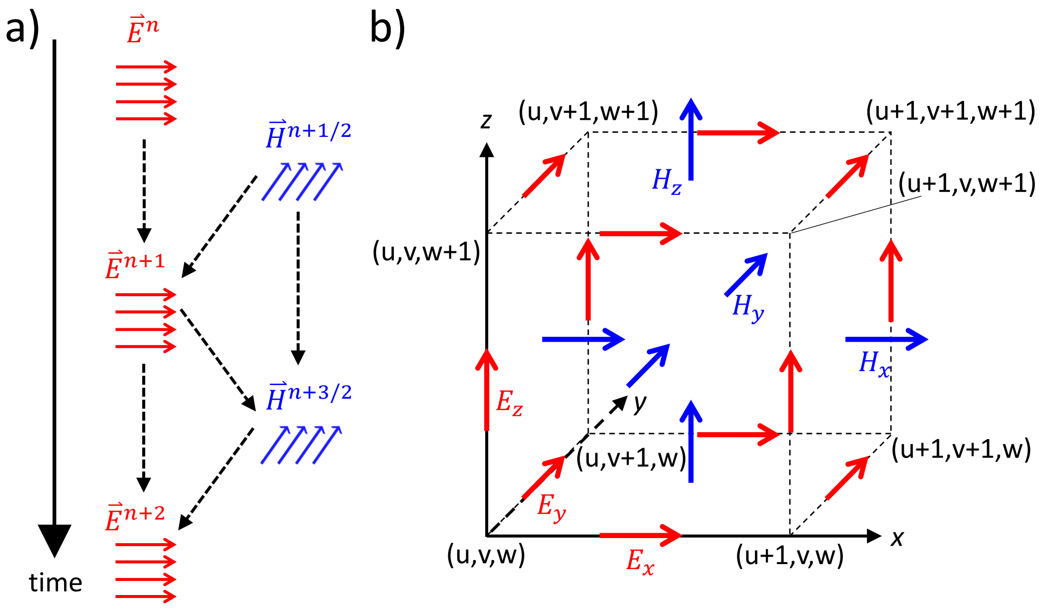

Figure 4.1 – Temporal and spatial discretization methods in the FDTD algorithm according to Yee's proposal. a) Leapfrog stepping with alternating $\vec{E}$ and $\vec{H}$ computations in increments of $\Delta t/2$. **b)** Cubic Yee cell embedded in Cartesian coordinate system with vertices labeld by (u,v,w) indices. Electric field components (red) are centered at the cube edges. Magnetic field components (blue) are calculated at the face centers of the Yee cube. Inspired from [133].

Fig. 4.1 a, e. g. previously stored $\vec{E}$ data together with the magnetic curl of the past half time step are used to construct new $\vec{E}$ data. Partial time derivatives are approximated with central-difference terms

$$\frac{\partial F^{n}(u,v,w)}{\partial t} = \frac{F^{n+1/2}(u,v,w) - F^{n-1/2}(u,v,w)}{\Delta t} + \mathcal{O}(\Delta t^{2}), \tag{4.3}$$

being second-order accurate.

Another important feature of the Yee algorithm is the spatial distribution of field components, as sketched in Fig. 4.1 b. Internally it uses an interleaved double lattice on whose edge centers the components of $\vec{E}$ and $\vec{H}$ are allocated. The two grids are offset by half a lattice constant in each dimension. Thus, the curl operations in Eqs. (4.1) are naturally implemented because each $\vec{E}$ component is enclosed by four circulating $\vec{H}$ components and vice versa. Spatial distributions of ε, μ and σ are fed into the Yee lattice so that physical structures are properly placed in the simulation volume. The central-difference terms originating from the partial derivatives in x-direction read

$$\frac{\partial F^{n}(u,v,w)}{\partial x} = \frac{F^{n}(u+1/2,v,w) - F^{n}(u-1/2,v,w)}{\Delta x} + \mathcal{O}(\Delta x^{2}), \tag{4.4}$$

and equivalently for derivatives in y- and z-direction by lowering/raising v,w on the r. h. s., respectively. These approximations are again second-order accurate. Moreover, the chosen arrangement of $\vec{E}$ and $\vec{H}$ components in conjunction with the central-difference formulas implicitly enforce the remaining two Maxwell equations (2.1a), (2.1d) [132].

As a ramification of the discretized spacetime, errors are introduced in numerical wave properties such as speed of light $\tilde{c}$ and wave number $\tilde{k}$. Discrepancies vanish if the step sizes tend to zero, as illustrated in the numerical dispersion relation [132] becoming "analytical" in the aforementioned limit:

$$\left[\frac{1}{\tilde{c}\Delta t}\sin\left(\frac{\omega\Delta t}{2}\right)\right]^2 = \sum_{i=\{x,y,z\}}\left[\frac{1}{\Delta i}\sin\left(\frac{\tilde{k}_i\Delta i}{2}\right)\right]^2 \tag{4.5a}$$

$$\xrightarrow{\Delta t\to 0,\ \Delta i\to 0} \left(\frac{\omega}{c}\right)^2 = \sum_{i=\{x,y,z\}} k_i^2\ . \tag{4.5b}$$

Numerical stability in the temporal evolution imposes an upper limit on the time step Δt for given Δi, which is known as Courant criterion [132],

$$\Delta t \le \frac{1}{v_{\max}\sqrt{\frac{1}{(\Delta x)^2}+\frac{1}{(\Delta y)^2}+\frac{1}{(\Delta z)^2}}}, \tag{4.6}$$

where $v_{\max}$ denotes the maximum possible phase velocity in the simulation region.

4.2 Simulation software and setup

In this thesis FDTD simulations are carried out with the commercial software package Lumerical Solutions (Lumerical Inc., Vancouver, CA; since April 2020 ANSYS Lumerical Software ULC, Vancouver, CA), versions 8.15 to 8.24.2502. A detailed documentation is available online [134]. Based on a graphical user interface, physical structures can be intuitively composed from fundamental building blocks (spheres, cylinders, polygons etc.) or via computer-aided design. As an example we consider an electrically connected side-by-side aligned nanorod dimer with dissimilar rod lengths in Fig. 4.2 a.

All elements are embedded inside the simulation volume where a solution of electromagnetic fields is sought. Since the entire space has to be discretized in the FDTD algorithm, only a finite simulation volume can be considered (cf. Fig. 4.2 a). Boundary conditions assure that solutions take on a form compatible with the laws of electromagnetism. A special way of mimicking an infinite domain is to only allow outgoing waves in the far field (Sommerfeld radiation condition). This can be realized by employing perfectly matched layers (PML) at the boundaries. Initialized by Berenger's seminal work on a split-field PML concept [135], several modifications and improvements have been published. Prominent extensions are stretched-coordinate PML [136, 137] relying on complex frequency shifts to achieve absorption and uniaxial anisotropic PML [138] that use a physical anisotropic perfectly matched medium. Here we mostly use the stretched-coordinate PML as boundary condition spanning a thickness of 8 to

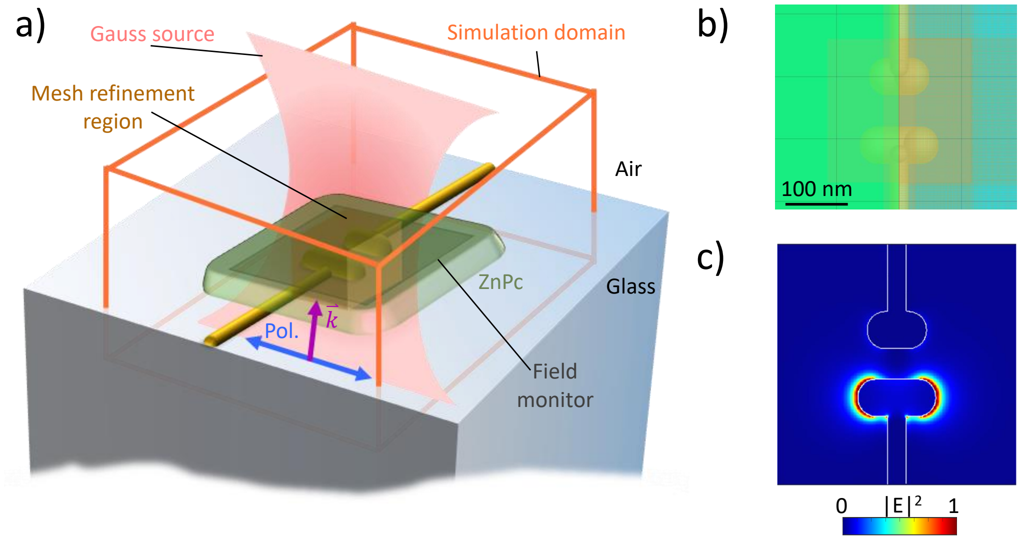

Figure 4.2 – **Setup of an FDTD Simulation a)** Artistic sketch of the setup with the most important elements labeled. The physical structure under study, taken from Chap. 6, is an electrically connected gold nanorod dimer (distinct rod lengths) embedded in a zinc phthalocyanine (ZnPc) layer on a glass substrate. The polarization and propagation direction of the Gaussian source is also labeled. **b)** Top view of the rod dimer with mesh drawn in orange. Mesh refinement regions incorporate rods and connector wires. Here, antisymmetric boundary conditions are enforced as indicated by the green area. **c)** Electric near-field intensity at $\lambda = 920\,\mathrm{nm}$ retrieved from the 2D (frequency-domain) field monitor depicted in a). Near-fields around the longer nanorod are resonantly enhanced. The scale bar from b) applies here as well.

64 Yee cells. As a rule of thumb, the distance between PML and scattering objects is kept at least at one multiple of the longest wavelength of the source, preventing evanescent field components from being artificially absorbed. A substrate, in turn, can be extended through the PML to simulate e. g. a glass halfspace. If a nanowire carrying SPPs penetrates PML in normal direction, it does not experience any back-reflected SPPs. This is particularly useful when modeling semi-infinite waveguides or electrical connector leads (cf. Fig. 4.2 a).

As discussed in Sec 4.1, Yee cells have to be created by applying a 3D Cartesian mesh throughout the simulation volume. While Fig. 4.1 b shows a cubic cell, it is convenient to divide space in a nonuniform manner. One the one hand small mesh sizes are necessary near metallic objects. Little features which might influence plasmonic resonances as well as curved surfaces are then properly resolved. Small mesh steps reduce the formation of sharp corners and edges. These stair-casing elements would give rise to spurious charge accumulations and field hotspots mediated by the lightning rod effect. Likewise, electromagnetic fields require a high spatial resolution. Around metallic objects, in particular, strong field gradients emerge (cf. Sec. 3.2, Sec. 3.3) and only a fine meshgrid is able to accurately resolve rapidly varying fields. On the other hand, for vacuum or glass substrate regions it is sufficient to choose bigger mesh sizes

($\lambda/40 \sim \lambda/20$) which are still capable of correctly modeling wave propagation on the grid. Therefore mesh refinement regions are deliberately placed around plasmonic structures and gaps between such structures, which allows fine discretization of the corresponding subvolumes (cf. Fig. 4.2 b). Refined cell dimensions from $0.5 \times 0.5 \times 0.5$ nm^3 to $1 \times 1 \times 1$ nm^3 are used for isolated antenna structures and gaps. Around unperturbed sections of nanowires which support SPPs the cell size is enlarged in the direction parallel to the wire axis to 4 nm.

The FDTD software offers a variety of built-in materials, characterized by tabulated complex dielectric constants, for use in simulations. Also, several analytical models are available to create custom materials with non-dispersive dielectric constants or frequency-dependent dielectric functions. Here we implement the sampled material data from Olmon *et al.* [68] and Yang *et al.* [74] for gold and silver, respectively. However, since FDTD is a time-domain solver, the material response evolving over time needs to be treated explicitly. Therefore we convert the constitutive relation Eq. (2.13a) to the time domain,

$$\vec{D}(\vec{r},t) = \varepsilon_0 \varepsilon(\vec{r},t) * \vec{E}(\vec{r},t) = \varepsilon_0 \int_0^t \varepsilon(\vec{r},t-t')\vec{E}(\vec{r},t')\mathrm{d}t', \tag{4.7}$$

where the multiplication becomes a convolution over the past time. The dielectric function is converted via Fourier transform,

$$\varepsilon(\vec{r},t) = \int_{-\infty}^{+\infty} \varepsilon(\vec{r},\omega)\, e^{-\mathrm{i}\omega t}\mathrm{d}\omega. \tag{4.8}$$

Causality places constraints on $\varepsilon(\vec{r},t)$, e. g., the criterion that the displacement field at presence may only depend on electric field values in the past but not in the future must be met. Consequently, in light of the Kramers-Kronig relations, $\Re(\varepsilon)$ and $\Im(\varepsilon)$ are not independent from each other. The built-in multi-coefficient material (MCM) fitting procedure obeys these constraints when calculating a fit to sampled material data [73]. As presented in Sec. 3.1, the fit results are remarkably good for both noble metals over the entire wavelength range of interest. In this work we assume glass to be a nondispersive dielectric with refractive index $n = 1.52$ ($\varepsilon = 2.3104$).

In order to inject electromagnetic energy into the simulation domain, several sources are available. Plane waves are the most intuitive way to excite a structure from the far-field. An advanced version, the total-field scattered-field (TFSF) source, separates scattered fields from incident field components in far-field regions of the simulation domain to only record the scattered fraction. Gaussian beams offer another possibility of far-field excitation. By superimposing a set of plane waves, a vectorial beam with Gaussian profile is generated, as if a focused beam originating from a microscope objective with specified numerical aperture was illuminating the structure of interest (cf. Fig. 4.2 a). Polarization and propagation direction are defined by the user. Electromagnetic energy can also be injected locally by a point dipole source whose orientation is adjustable. In contrast to a global illumination, a point dipole allows a highly asymmetric, localized excitation of a structure. This is beneficial e. g. for selectively accessing subradiant modes which radiate only weakly into the far-field due to symmetry reasons. Waveguides can be driven locally by a third type of sources, the mode source. First, the guided eigenmodes of interest need to be determined by applying a 2D FDFD solver (cf. Sec. 4.3) to a cross-section of the waveguide. The resulting near-field distribution is then declared as excitation field and propagates in the chosen direction along the waveguide starting at the aforementioned cross-section. Mode sources are used, for instance, to feed plasmonic nanocircuits. If physical structures and source fields fulfill certain symmetry properties, symmetric or antisymmetric boundary conditions can be invoked. Fig. 4.2 b illustrates such a condition with the green colored area. These conditions enable the algorithm to simulate only a fraction of the entire domain which reduces the computational burden (simulation time, memory) significantly. All source fields are injected as a short pulse $s(t)$ with durations of a few fs, thereby carrying a broad spectrum of frequencies in the visible and NIR. This is indeed an important advantage of time-domain simulations: A single run yields the system's response to a whole range of frequencies.

Each time iteration requires the computation of the $\vec{E}$ (or $\vec{H}$) field in Yee cells across the whole simulation volume (cf. Sec. 4.1). Thus, huge amounts of data accumulate and it is impractical to store them entirely. Depending on the problem at hand, one may only be interested in near-fields at specific locations. The recording of field quantities is subject to monitors which occupy user-defined sub-regions (points, lines, areas or cubes) of the simulation domain (cf. Fig. 4.2 a). Time-domain monitors directly record electromagnetic fields as a function of time. Such results can be used to create movies of the temporal evolution of fields. Frequency-domain monitors act with a Fourier transform on the time-domain signals and store field information as a function of frequency (cf. Fig. 4.2 c),

$$\vec{E}(\vec{r},\omega) = \frac{1}{2\pi}\int\limits_{0}^{t_f} \vec{E}(\vec{r},t)e^{\mathrm{i}\omega t}\mathrm{d}t. \tag{4.9}$$

Here, in contrast to Eq. (2.3), the integration runs from $t = 0$ up to a final time $t = t_f$ which needs to be chosen long enough (hundreds of fs) until the electromagnetic energy within the simulation volume has decayed below a certain threshold value. We apply fractions of the injected energy between 10^{-6} and 10^{-5} as thresholds in most simulations. Special care in interpreting field distributions must be taken when dipole sources are used. Since dipolar fields bear a singularity at the oscillator's position, the recorded fields in the surrounding assume very large magnitudes and would overshadow physically meaningful fields of e. g. nearby metallic structures. It is thus necessary to eliminate the source fields to obtain accurate plasmonic field distributions. The FDTD software provides an apodization technique, i. e. a smooth time-domain window function which multiplied with $(\vec{E},\vec{H})(\vec{r},t)$ suppresses excitation fields to an acceptable extent. As such, $\vec{E}(\vec{r},\omega)$ from Eq. (4.9) also depends on the input pulse

$s(t)$. By applying the so-called continuous wave (CW) norm,

$$\vec{E}_{\text{imp}}(\vec{r},\omega) = 2\pi\,\frac{\vec{E}(\vec{r},\omega)}{\int\limits_0^{t_f} s(t)e^{\mathrm{i}\omega t}\mathrm{d}t}, \tag{4.10}$$

the dependency is lifted and for each frequency one obtains the system's response as if the input was a CW source (impulse response).

4.3 Finite-difference frequency-domain simulations

Plasmonic waveguides are a central tool in optical nanocircuitry. Supporting propagating SPPs, they serve as link e. g. between plasmonic incoupling and outcoupling entities [139] or as direct near-field source for driving optical antennas (cf. Chap. 7). Only a few simple waveguide designs can be addressed analytically (cf. Sec. 3.2.1). Many realistic shapes require numerical approaches to be modeled accurately. The finite-difference frequency-domain solver, available within Lumerical's portfolio (MODE Solutions, ANSYS Lumerical Software ULC, Vancouver, CA), is used throughout this thesis to compute eigenmodes of plasmonic waveguides. Just as in the FDTD algorithm, Sec. 4.1, 2D Yee cells discretize the cross section of the waveguide under study. To avoid stair-casing effects due to curved interfaces the algorithm incorporates a refractive index averaging technique for Yee cells across material boundaries [140]. It is assumed that the solution propagates in the dimension perpendicular to the cross section (x-direction), i. e. the wave equation (2.20) is set up for the transverse fields [140],

$$(\vec{\nabla}_t^2 + \frac{\omega^2}{c^2}\varepsilon)\vec{E}_t + \vec{\nabla}_t[\vec{E}_t \cdot \vec{\nabla}_t \ln \varepsilon] = k^2\vec{E}_t, \tag{4.11}$$

with the generally complex propagation constant k, and $\vec{\nabla}_t$ acting in y- and z-direction. Again, using central-difference approximations for the spatial derivatives and some algebra, one obtains an eigenvalue equation for the transverse field components,

$$\overleftrightarrow{P}\begin{bmatrix} E_y \\ E_z \end{bmatrix} = k^2 \begin{bmatrix} E_y \\ E_z \end{bmatrix}, \tag{4.12}$$

with eigenvalues k^2. The entries of the 2×2-matrix $\overleftrightarrow{P}$ depend on discretization, material, and wavelength. Similar steps can be carried out for the magnetic fields. Diagonalization yields the transverse fields of the eigenmode, which in turn allow the calculation of the longitudinal components. Repeating the procedure for each wavelength of interest, the full modal information (dispersion relation and field distribution) is obtained.

FDFD simulation setups have some aspects in common with the FDTD simulations discussed in Sec. 4.2. The transverse domain size must be sufficiently large to resolve the entire evanescent modal fields. For instance, a 30 nm diameter nanowire is embedded in a simulation window of 1 µm × 1 µm, ensuring that no fields are truncated by

PML boundaries. Also the aforementioned mesh refinement settings around metallic structures are adopted in FDFD simulations which guarantees a proper resolution of physical structures, interfaces, and field gradients.

4.4 Post-processing steps and data evaluation

While frequency-domain results from FDTD simulations are directly returned from frequency-domain field monitors via an inherent Fourier transform, some quantities of interest in this work have to be determined by explicit post-processing computation of simulation data. We summarize the most important procedures in this section.

4.4.1 Near- to far-field projections

Owing to the limited size of the FDTD simulation domain, only near field profiles around nano-objects are directly accessible from field monitors. The far-field radiation behavior of an optical antenna, however, is a fundamental property as it determines the antenna's directionality performance. Under certain circumstances it is possible to retrieve far-field radiation patterns from a projection of 2D near-field monitor data. The latter are decomposed into a series of plane waves propagating at different angles [13],

$$\vec{E}(x,y,z) = \iint\limits_{-\infty}^{+\infty} \vec{E}(k_x,k_y;0)e^{\mathrm{i}(k_x x+k_y y\pm k_z z)}\mathrm{d}k_x\mathrm{d}k_y. \tag{4.13}$$

The angular representation $\vec{E}(k_x,k_y;0)$ is multiplied with a propagator, mapping the fields onto a hemisphere of 1 m radius around the nanostructure, through the medium present at the location of the near-field monitor. As a prerequisite, the monitor must be embedded in a single homogeneous material and record both $\vec{E}$ and $\vec{H}$ fields. A closed box of monitors in a homogeneous surrounding is another option for far-field projection.

In most cases we are interested in radiation patterns obtained through a glass substrate because this is also accessible in experiments through back-focal plane imaging. We therefore place a 2D field monitor inside the glass halfspace parallel to the interface and apply far-field projection as a post-processing step. Fig. 4.3 depicts a double rod antenna lying on a glass substrate whose far-field is studied in the lower hemispherical region. After expanding the fields on the hemisphere the emission pattern is further projected onto a planar surface which equals a top view onto the hemisphere. It should be mentioned that in this technique higher elevation angles θ are plotted more densely. Since the antenna dimer supports a dipolar resonance the radiation pattern here shows the typical double lobe distribution of a dipole source oriented parallel to the underlying glass halfspace. Intensity maxima appear in the direction perpendicular to the antenna axis around the critical angle of the air-glass interface,

$$\theta_c = \arcsin\left(\frac{n_{\mathrm{air}}}{n_{\mathrm{glass}}}\right) = \arcsin\left(\frac{1}{1.52}\right) \approx 41^\circ. \tag{4.14}$$

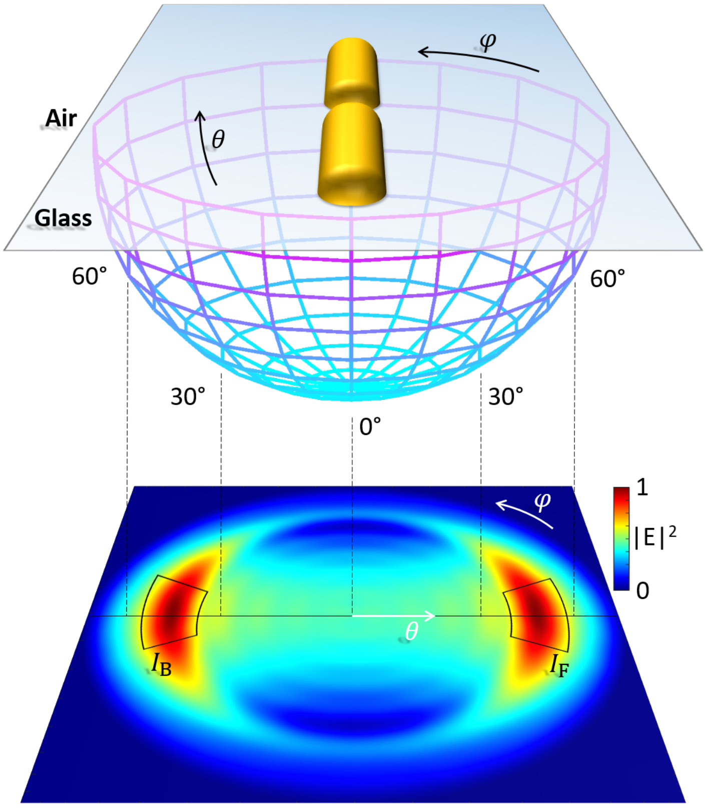

Figure 4.3 – Far-field radiation pattern of a dipole antenna. Near-fields of a dipole antenna consisting of a plasmonic rod dimer are recorded in a plane inside the glass substrate, decomposed into plane waves at various angles and propagated onto a hemisphere (azimuth angle φ and elevation angle θ) in the far-field. Some elevation angles are indicated. The intensity distribution on the hemisphere is projected onto a planar surface, yielding a 2D representation of the radiation pattern. Typical dipolar radiation characteristics are obtained for the dipole antenna. The far-field intensities in specific solid angle regions in forward (I_F) and backward direction (I_B) can be integrated to calculate a forward-to-backward ratio.

Indeed, only a small fraction is emitted into the air halfspace. One can integrate the far-field intensity of a radiation pattern throughout specific solid angle intervals and subsequently calculate forward-to-backward (FB) ratios of the form $\mathrm{FB} = I_\mathrm{F}/I_\mathrm{B}$ to quantify directionality. The dipolar antenna mode has $\mathrm{FB} = 0\,\mathrm{dB}$.

The quality of emission patterns critically depends on the lateral size of the near-field monitor since the projection algorithm assumes zero field strength beyond its borders. Too small monitor dimensions introduce nonphysical artifacts into far-field patterns, such as smeared out emission lobes or fringes which are also slightly visible in Fig. 4.3. Depending on the size of the structure, at least $10\,\mu\mathrm{m} \times 10\,\mu\mathrm{m}$ monitor span (and simulation domain span) is recommended for acceptable accuracy, in conjunction with heavier computational burden.

4.4.2 Eigenmode expansion

After determining eigenmodes on a nanowire waveguide cross section with the method discussed in Sec. 4.3, it is interesting to study how the fields behave upon encountering an open end or a discontinuity along the nanowire. Within such perturbations the modes are not eigenmodes of the original system. This can also lead to conversion among eigenmodes [141, 142]. Eigenmode expansion allows quantifying how exactly the modes are converted and where their energy is flowing. If a complete, orthogonal set of eigenmodes $\psi_m = (\vec{E}_m, \vec{H}_m)$ is known it can be used as basis to express any input field profile by a superposition [143]:

$$\vec{E}_{\mathrm{in}} = \sum_m \left(a_m \vec{E}_m^f + b_m \vec{E}_m^b \right), \tag{4.15a}$$

$$\vec{H}_{\mathrm{in}} = \sum_m \left(a_m \vec{H}_m^f + b_m \vec{H}_m^b \right). \tag{4.15b}$$

Here a_m and b_m are the complex expansion coefficients for mode m, bearing amplitude and phase information which add to the total field. The superscripts f, b refer to forward and backward propagating waves. These are also related by symmetry [144]:

$$\vec{E}_m^b = \vec{E}_{t,m}^f - E_{x,m}^f \vec{e}_x, \tag{4.16a}$$

$$\vec{H}_m^b = -\vec{H}_{t,m}^f + H_{x,m}^f \vec{e}_x. \tag{4.16b}$$

Similar to Sec. 4.3 the total fields have been decomposed in transverse (subscript t) and longitudinal components with x being the propagation direction. Hence the input fields in Eqs. (4.15) can be formulated solely in terms of forward-propagating modes. We define a power orthogonality relation as

$$\langle \psi_m \,|\, \psi_n \rangle \equiv \frac{1}{2} \int (\vec{E}_m \times \vec{H}_n^*) \cdot \mathrm{d}\vec{S} = N_m \delta_{mn}, \tag{4.17}$$

where $\vec{S}$ and δ_{mn} are the cross section normal vector and the Kronecker symbol. N_m serves as a normalization factor describing the power carried by mode m. The expansion coefficients are then obtained by overlap integrals of the input field with each eigenmode:

$$\frac{1}{2} \int (\vec{E}_{\mathrm{in}} \times \vec{H}_m^*) \cdot \mathrm{d}\vec{S} = (a_m + b_m) N_m, \tag{4.18a}$$

$$\frac{1}{2} \int (\vec{E}_m^* \times \vec{H}_{\mathrm{in}}) \cdot \mathrm{d}\vec{S} = (a_m - b_m) N_m^*. \tag{4.18b}$$

Solving Eqs. (4.18) for a_m, b_m one finds

$$a_m = \frac{1}{4} \left(\frac{\int (\vec{E}_{\mathrm{in}} \times \vec{H}_m^*) \cdot \mathrm{d}\vec{S}}{N_m} + \frac{\int (\vec{E}_m^* \times \vec{H}_{\mathrm{in}}) \cdot \mathrm{d}\vec{S}}{N_m^*} \right), \tag{4.19a}$$

$$b_m = \frac{1}{4} \left(\frac{\int (\vec{E}_{\mathrm{in}} \times \vec{H}_m^*) \cdot \mathrm{d}\vec{S}}{N_m} - \frac{\int (\vec{E}_m^* \times \vec{H}_{\mathrm{in}}) \cdot \mathrm{d}\vec{S}}{N_m^*} \right). \tag{4.19b}$$

At waveguide terminations or obstacles the expansion coefficients can be used to characterize the reflection and transmission behavior of eigenmodes, which will be a central topic in Chap. 7.

5

Electrically-driven Yagi-Uda antennas for light

Yagi-Uda antennas, named from their Japanese inventors Hidetsugu Yagi and Shintaro Uda [145, 146], have a long-standing tradition as directional transmitters and, owing to reciprocity, receivers in radio and television broadcasting. As such, they set a milestone for long-distance wireless communication, first deployed in military radar and later commercialized. An actively driven dipolar feed antenna induces oscillating currents in parasitic reflector and director elements. While the reflector is designed to be longer as the feed the directors possess shorter lengths (cf. Fig. 5.1) which leads to resonance frequency detunings to the red and blue, respectively, imposing phase lags on re-radiated electromagnetic waves. Moreover, the parasitic elements are assembled at specific locations w. r. t. the feed, adding to the phase lags. Interference between all re-radiated waves generates a narrow phase-coherent beam in the forward direction, i. e. along the directors, whereas in backward direction destructive interference suppresses radiation.

Miniaturizing the Yagi-Uda concept from the radio-frequency (RF) to the optical regime promises two key benefits: the bandwidth dramatically grows due to substantially higher frequencies and at the same time the footprint shrinks down to the nanometer scale. The resulting devices represent an efficient link between electron-based integrated computer chips and photon-based fiber networks and in particular enable on-chip wireless optical data communication because antennas outperform subwavelength waveguides for longer distances [147, 148], allow for multiple beam crossings, have an adaptable footprint and are not restricted by Joule heating [149, 150]. Realizing optical Yagi-Uda antennas encompasses two key challenges: precise fabrication of an arrangement of nanostructures and the selective driving of only one of these elements. Even though quite some effort has already been devoted to optical Yagi-Uda antennas [151] – best possible design parameters have been found for both vertical [152] as well as in-plane emitting antennas [153–155] and different kinds of antennas have been realized [156–161] – the main drawback of the hitherto approaches is that the light is not generated locally but bulky lab-scale setups are needed as excitation sources. Generating light locally at the nanoscale is possible by different means, for example via scanning tunneling microscopes (STMs) [162, 163], carbon

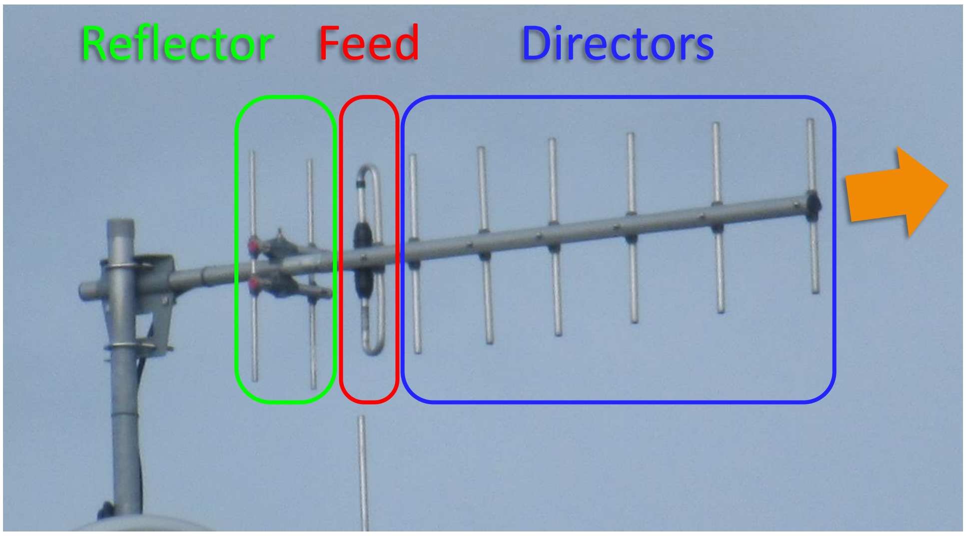

Figure 5.1 – Yagi-Uda antenna for television broadcasting. Around the feed antenna (folded dipole, red frame) a double reflector (green frame) and an array of directors (blue frame) are arranged with spacings around 0.25λ. The orange arrow indicates the direction of main transmission/reception.

nanotubes [164–167], quantum dots [168] and optical antennas [30, 33, 35]. However, obtaining directed electrically driven emission is only possible by utilizing scanning tunneling microscopes (STMs) [169, 170] which again involves large-scale setups, or by twisting the arms of electrically driven dipole antennas in order to break the point symmetry [32]. The latter show a limited geometrical definition and directionality only, are by design not scalable to significantly higher values and, hence, not suitable for, e. g., cross-talk free on-chip data communication. Therefore, key breakthroughs in antenna design, quality and fabrication are still needed to achieve on the nanoscale the same performance, versatility and usability as for classical radio-wave antennas.

In this chapter we demonstrate the feasibility of a complex electro-optical nanosystem that consists of multiple antenna elements with precisely adjusted positions and resonances as well as a sophisticated electrical subsystem for local excitation of the central feed antenna, giving rise to highly directed light emission via inelastic tunneling. As an example, we realize electrically driven in-plane Yagi-Uda transmitters for light that require single-crystalline connector wires [29, 65], advanced focused-ion beam milling (FIB) as well as novel fabrication methods such as feedback-controlled single-particle dielectrophoresis (DEP). We experimentally show that the resulting optical antennas consisting of one reflector and three directors have unprecedented forward-to-backward (FB) ratios of up to 9.1 dB and are scalable up to 15 elements where even higher FB ratios have been simulated. Numerical simulations further suggest that switching to hybrid systems consisting of antennas embedded in high-index films can even outperform the characteristics of conventional Yagi-Uda antennas in the RF regime. This work opens the road to high bandwidth on-chip data communication that is not restricted by Joule heating but also for light-emitting devices.

5.1 General antenna design and fabrication

The electrically connected Yagi-Uda antenna systems consist of gold structures placed directly on a glass substrate. We choose the array to consist of one reflector, one feed, and three directors, in order to keep the complexity within bounds. A scanning electron microscopy (SEM) image is given in Fig. 5.2 a. Following the Yagi-Uda principle, it is important to position the elements accurately to each other. The correct dimensions of the constituents also play a crucial role in order for the feed resonance to lie within the "spectral window" defined by the peaks of reflector and director spectra, which are visualized in the inset of Fig. 5.2 a. This requires a precise fabrication method. Thus, the antenna constituents are obtained by FIB milling (Helios Nanolab 600) of chemically grown single-crystalline gold microplatelets [65–67]. The task of the feed element, shown in close-up view in Fig. 5.2 b, is to drive the parasitic elements, so it is electrically connected via FDTD-optimized kinked single-crystalline wires (cf. Sec. 5.2.1) to evaporated electrode structures that are accessed via micromanipulators from a sourcemeter (Keithley 2636B, Tektronix Inc., Beaverton, USA). This arrangement establishes a low-resistance electrical connection to the tunnel gap region without disturbing the optical fields [29]. Provided that all elements are aligned and resonating at the correct wavelength, interference effects lead to directional emission, as supported by an analytically calculated radiation pattern in Fig. 5.2 c. The forward-to-backward (FB) ratio, here the figure of merit, compares the intensities obtained in forward and backward direction as given by the formula in the plot. Specific FB values are stated further below.

For generating light in the center of the feed, we employ inelastic electron tunneling (IET), which was first discovered in planar MIM tunnel junctions [172] in 1976 and later on studied in STM experiments [173]. When electrons traverse a nanoscale barrier, inelastic processes can occur in which the electrons lose energy by generating light. This mechanism is illustrated in Fig. 5.2 d. The efficiency of IET can be strongly enhanced by a high local density of optical states (LDOS; cf. Sec. 3.4) [30, 33, 35]. IET offers distinct advantages such as the absence of any active materials resulting in a large bandwidth, accompanied by femtosecond switching timescales [174]. In order to create a nanometer sized tunnel junction, we introduce dielectrophoresis (DEP) [175, 176] into the fabrication process and improve it for controlled single-particle deposition by implementing a feedback mechanism.

To perform DEP, a water droplet containing gold nanospheres is placed on top of the antenna structures and the glass substrate facilitates optical access from below via an immersion oil microscope objective (Nikon Plan-Apochromat, 100×, $NA = 1.45$) as schematically sketched in Fig. 5.3 a. One of the two electrodes is grounded while an alternating electric field is applied to the other electrode in order to polarize the particles in solution. Depending on the voltage and frequency, nanospheres are then attracted to regions of the highest field gradient, i. e. the feed gap. To ensure that exactly one particle is placed into the antenna gap, we continuously monitor the white-light (WL) scattering spectrum of the antenna at 10 Hz repetition rate. When a particle enters the feed gap, the spectrum strongly red-shifts and the shift becomes stronger if many parti-

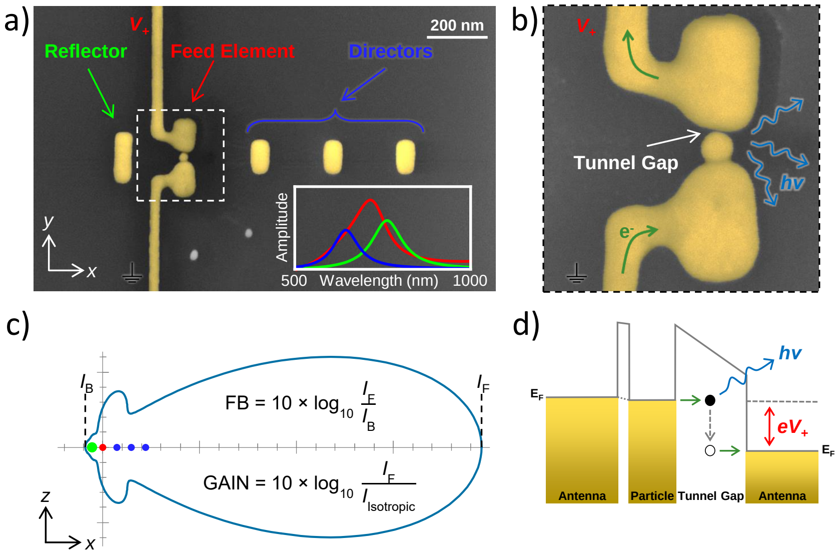

Figure 5.2 – Concepts of an optical Yagi-Uda antenna and inelastic electron tunneling. **a)** SEM micrograph of a Yagi-Uda antenna containing reflector, feed element with kinked connectors and three directors on a glass substrate. The inset schematically visualizes spectra for the functional elements. According to the Yagi-Uda working principle, the feed resonance lies within the "spectral window" imposed by the passive elements. **b)** Zoom into the feed element highlighting the asymmetrically positioned spherical particle creating a tunnel gap toward the top antenna arm. **c)** Emission characteristics of a Yagi-Uda antenna in the *xz*-plane for a homogeneous surrounding, calculated with a dipole interaction model (cf. Sec. 5.2.2). The reflector and director elements lead to a highly unidirectional emission by interference, in analogy to their RF counterparts. The intensities in forward and backward direction are used to define a forward-to-backward (FB) ratio and the antenna gain, see inset. **d)** Schematics of the inelastic electron tunneling (IET) process. Adapted from [171].

cles are attracted (see Figs. 5.3 b-e). We thus optimized the basic parameters (voltage, frequency, concentration) and achieved a success rate of single-particle deposition of 49.8 %; for more information about DEP the reader is referred to [171].

5.2 Design optimization

Our Yagi-Uda antenna consists of a single reflector, a feed element and directors. To achieve a high FB ratio of the emitted light the geometric parameters of the antenna structures need to be optimized. First we describe an electrical connection scheme which conserves the resonant properties of the feed element and simultaneously contributes to a positive FB ratio, making use of FDTD simulations. Under the constraints of a favorable connector geometry we then optimize the dimensions of passive elements, first using an analytical model for a quick overview analysis and afterwards via numerical simulations (boundary element method, BEM) which are able to handle more realistic structures.

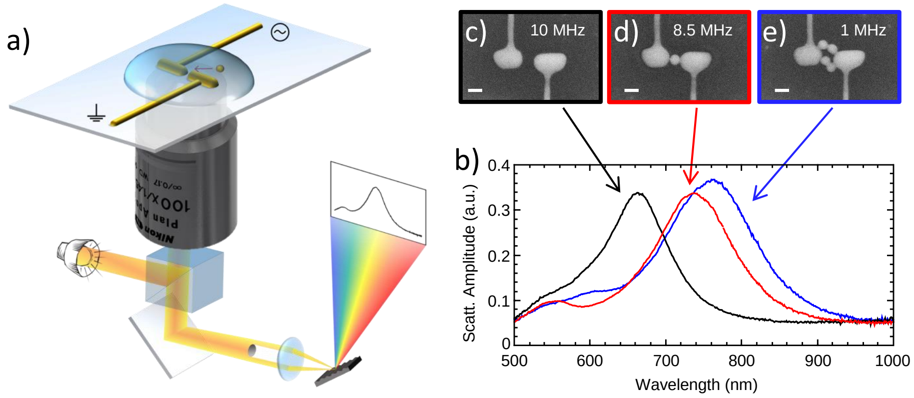

Figure 5.3 – Feedback-driven dielectrophoresis at optical antennas. **a)** Schematics of the DEP setup: while WL dark-field scattering spectra are continuously acquired, a high-frequency AC voltage is applied. As soon as a particle is deposited in the gap the spectrum visibly red-shifts as plotted in **b)** from the black to the red curve and the voltage is subsequently switched off. Larger particle numbers result in even stronger red-shifts (blue curve). **c)-e)** Associated SEM images for various DEP frequencies showing an optimum of single-particle attraction at 8.5 MHz. The study here is carried out with conventional dipole antennas but works equally for feed elements of Yagi-Uda antennas. Scale bars, 50 nm. Adapted from [171].

Previous publications about directional optical antennas have reported FB ratios, however, this quantity was obtained in different ways. The first is the "pixel" method used by Curto *et al.* [157] where the most intense pixel in forward direction is selected and compared to the diametrically opposite pixel of the angular emission pattern. For both pixels the background (CCD offset) is subtracted and then the forward pixel value is divided by the backward one to obtain the ratio. This method provides straightforward results and is well established in literature, however, is also very prone to errors in experiments as noise in backward direction can lead to high FB-ratio fluctuations. It is reduced for high signal-to-noise ratios and for our experimental data we estimate the error to be ±1.4 dB. In numerical simulations this value remains stable and reliable. The second way is the "areal" method introduced by Gurunarayanan *et al.* [32]. By integrating the emission pattern over a solid angle section in forward and backward direction, as exemplarily depicted in Fig. 4.3, the fluctuations are greatly reduced. However, since the intensity drops when moving away from the forward maximum the value is not fixed and decreases with increasing $(\Delta\theta, \Delta\varphi)$. Hence, it is inherently smaller than the one of the "pixel" method and based on the uncertainty of the emission pattern size in experiments we estimate the error to be ±0.2 dB.

5.2.1 Electrical connectors

To drive Yagi-Uda antennas electrically, metallic contact wires are necessary to connect the feed element to an external DC voltage source. Due to the significant size of wires in the nanoworld, the connector attachment position as well as their routing must be optimized in order to not disturb the operation of the feed and the passive elements. Additionally, it must be possible to fabricate the structure using the FIB milling technique. FDTD simulations have been performed to find the optimal attachment position and routing. Dipole antennas are modeled with refined mesh and a Gaussian source, polarized parallel to the antenna long axis, is chosen to excite the structure through the glass substrate at normal incidence. As seen in Fig. 5.4 the dipole antennas are then contacted at different positions: at the end of each arm pointing straight away from the antenna and near the middle of each arm similar to ref. [29] but mounted on the same side and featuring a kink in order to accommodate parasitic elements in the surrounding.

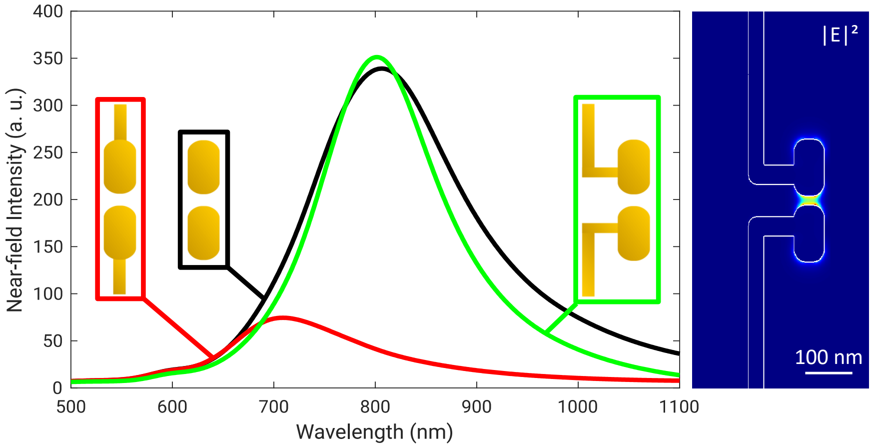

Figure 5.4 – Influence of the connectors on the near-field. Left: Simulated near-field intensities inside the antenna gap for different connector configurations. If the leads are attached from the top and bottom (red) the near-field intensity is strongly decreased while the one-sided configuration (green) conserves resonance position and amplitude of the antenna as compared to the case without connectors (black). Right: Near-field intensity map for the chosen one-sided configuration. Taken from [171].

Analogous to ref. [29], the near-field intensity spectra in Fig. 5.4 reveal that wires attached at positions of high field intensity, i. e. the ends of the antenna arms (red), strongly decrease the near-field intensity inside the antenna gap as compared to an antenna without any leads (black). However, by attaching the wires from the side at positions of low field intensities (green), the performance of the antenna is nearly unaltered. The associated near-field intensity map of this configuration (right panel of Fig. 5.4) shows high confinement of electrical fields in the antenna gap and no significant near-fields along the connectors, i. e. the energy leakage is minimal. For these reasons we are able to ignore the connector wires when optimizing the dimensions of parasitic elements using BEM simulations (see Sec. 5.2.2.

It is worth mentioning that the kinked connectors also positively contribute to a directed emission. Fig. 5.5 displays SEM images and experimental/simulated emission patterns of a conventionally connected dipole antenna (cf. also Fig. 4.3) as well as a dipole antenna connected from the left-hand side. Measured and simulated radiation

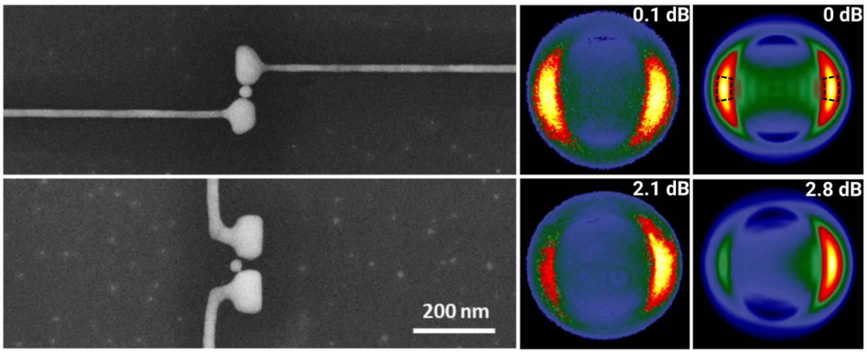

Figure 5.5 – Influence of the connectors on the far-field. Left: SEM micrographs of the corresponding antenna structures. Measured (middle) and simulated (right) electroluminescence (EL) radiation patterns showing dipolar emission for the conventional structure (cf. also Fig. 4.3) and directed emission when one-sided kinked leads are employed. FB ratios (areal method) are given for each pattern. The solid angle sections used for integration in each case ($\Delta\theta = 15°, \Delta\varphi = 20°$) are drawn in the upper right radiation pattern (black dashed lines). Adapted from [171].

characteristics are in very good agreement. The regular dipole antenna shows basically no directionality which is expected due to symmetry consideration. However, for the antenna with kinked wiring, FB ratios (areal method, ($\Delta\theta = 15°, \Delta\varphi = 20°$)) exceeding 2 dB can be observed. Hence, we obtain already a remarkable directionality caused by the parts of the connector that run parallel to the dimer. They act as reflecting elements in the chosen configuration and the parasitic reflector will later be placed on the same side of this system that we utilize as feed element. The directed emission to the right can in principle be further optimized by tuning the distance between antenna and the kink in the connecting wires. However, in our Yagi-Uda antennas we are on the one hand restricted by the fabrication resolution and on the other hand aim at placing the reflector in the proximate surrounding. Therefore we set the connector spacing to 100 nm. Nevertheless, this effect aids in improving the performance of Yagi-Uda antennas in the nanoworld, especially for low director numbers.

5.2.2 Parasitic elements

As stated above, proper functionality of a Yagi-Uda antenna requires a reflector whose resonance is red-shifted w r. t. the feed resonance and directors with blue detuned resonances. It would be impractical to produce hundreds of Yagi-Uda nanoantennas including tunnel gaps with the protocol described in Sec. 5.1 and vary the plethora of free parameters step by step. We therefore conduct calculations and simulations to optimize the dimensions and positions of the parasitic elements with the FB ratio as figure of merit. Before that we briefly introduce the analytical dipole interaction model (DIM) and the numerical boundary element method (BEM) in this section. Thereafter, with the DIM a quick and coarse overview over an appropriate Yagi-Uda geometry is obtained first. Based on this starting point, more accurate BEM simulations yield reliable parameter values which are readily transferred to the fabrication protocol.

Dipole interaction model

To quickly estimate resonance frequencies and spacings of the passive antenna elements a dipole interaction model is employed [153]. We consider the individual particles to be much smaller than the wavelength such that the field can be assumed to be homogeneous across each particle. In this quasi-static approximation all antenna elements are treated as coupled dipoles as pictured in Fig. 5.6.

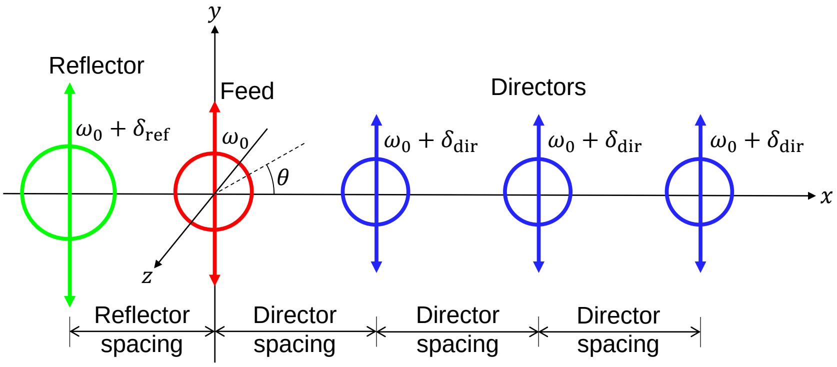

Figure 5.6 – **Analytic dipole interaction model.** All antenna elements are treated as dipoles in the quasi-static approximation and interact with each other. The driving frequency ω_0 of the feed is fixed while reflector and directors are detuned by δ_{ref} and δ_{dir}, respectively. The directors are equally spaced along the array. Adapted from [171].

The local electric field at a dipole E_{loc} is given by the emitted fields of the feed element (E_{feed}) and of the other dipoles E_j:

$$E_{\mathrm{loc},i} = E_{\mathrm{feed}} + \sum_{j \neq i} E_j. \tag{5.1}$$

Since on the dipole chain axis (x-axis in Fig. 5.6) the only nonzero field component is E_y we here omit vector notation. The quasi-static polarizability $\xi(\omega)$ of metallic nanoparticles is modeled in terms of the radiation reaction field [153], as a function of the effective particle volume V_{eff}, dielectric function $\varepsilon_{\mathrm{NP}}(\omega)$, and the depolarization factor N which depends on the particle shape and aspect ratio [60, 156],

$$\xi(\omega) = \frac{V_{\mathrm{eff}}}{\dfrac{1}{\frac{\varepsilon_{\mathrm{NP}}(\omega)}{\varepsilon_{\mathrm{surr}}} - 1} + N - \mathrm{i}(V_{\mathrm{eff}}\omega^3/6\pi c^3)}, \tag{5.2}$$

with $\varepsilon_{\mathrm{surr}}$ the dielectric constant of the surrounding and ω the light frequency. Analytical, albeit transcendental, relations exist between aspect ratio and depolarization factor of ellipsoids [60, 99]. Eq. (5.2) constitutes a generalization of Eq. (3.14) extended by an imaginary radiation damping term in the denominator. The total electric field due to an induced dipole can then be written as

$$E_j = \frac{k^3}{\mathrm{i}} \xi_j E_{\mathrm{loc},j} \frac{e^{\mathrm{i}kr_j}}{(kr_j)^3} \left[\mathrm{i}(kr_j)^2 - kr_j - \mathrm{i}\right] = A_j \frac{e^{\mathrm{i}kr_j}}{(kr_j)^3} \left[\mathrm{i}(kr_j)^2 - kr_j - \mathrm{i}\right], \tag{5.3}$$

where we introduce the complex dipole amplitude $A_j = -\mathrm{i}k^3\xi_j E_{\mathrm{loc},j}$. $k = \omega/c$ is the wave number and r_j denotes the distance between j-th dipole position and observer on the x-axis. We express the amplitude of the j-th dipole by the shorthand notation [153]

$$A_j = \frac{E_{\mathrm{loc},j}}{1+\gamma_j+\mathrm{i}\delta_j}. \tag{5.4}$$

Here, γ_j and δ_j describe absorption losses and effective resonance detuning from the feed as ratios of the corresponding fields to the radiation damping field of the dipole. From Eq. (5.2) their expressions read:

$$\gamma = \frac{6\pi c^3}{V_{\mathrm{eff}}\omega^3}\frac{\Im\left(\dfrac{\varepsilon_{\mathrm{NP}}}{\varepsilon_{\mathrm{surr}}}\right)}{\left|\dfrac{\varepsilon_{\mathrm{NP}}}{\varepsilon_{\mathrm{surr}}}-1\right|^2}, \tag{5.5a}$$

$$\delta = \frac{6\pi c^3}{V_{\mathrm{eff}}\omega^3}\left[N+\frac{\Re\left(\dfrac{\varepsilon_{\mathrm{NP}}}{\varepsilon_{\mathrm{surr}}}-1\right)}{\left|\dfrac{\varepsilon_{\mathrm{NP}}}{\varepsilon_{\mathrm{surr}}}-1\right|^2}\right]. \tag{5.5b}$$

As indicated in Eq. (5.5b) the detuning can be adjusted via the depolarization factor N, i. e. the geometry of the particle. Capacitive (blue) detuning of a dipole resonance gives rise to $\delta > 0$, inductive (red) detuning results in $\delta < 0$. Writing out Eq. (5.1) we obtain an equation system for the dipole amplitudes whose solution is found in a self-consistent way for all antenna elements. This leads to the far-field emission pattern in the plane perpendicular to the dipole axes [153] (xz-plane in Fig. 5.6):

$$I(\theta)\Big/I_{\mathrm{feed}} = \left|1+\sum_i \frac{A_i}{A_{\mathrm{feed}}}e^{\mathrm{i}kr_i\cos(\theta)}\right|^2. \tag{5.6}$$

The radiated intensity is normalized to the emission intensity of the feed I_{feed} with the oscillation amplitude A_{feed}. θ is the angle between antenna axis and the considered direction in the xz-plane and r_i is the distance between feed and i-th dipole (labeled as reflector/director spacings in Fig. 5.6). An example emission pattern for the values $\gamma_{\mathrm{ref}} = \gamma_{\mathrm{dir}} = 0.4$, $\delta_{\mathrm{ref}} = -0.4$, $\delta_{\mathrm{dir}} = 2$, reflector spacing $0.22\lambda_0$, and director spacing $0.32\lambda_0$, which are typical for gold nanorods in terms of absorption losses [153], is depicted in Fig. 5.2 c and FB = 13.4 dB is obtained. For a driving wavelength of $\lambda_0 = 800$ nm and $\varepsilon_{\mathrm{surr}} = 1.52$ those detuning values correspond to a dipolar reflector resonance at 815 nm and director resonance at 740 nm in the case of gold nanoparticles. For spheroidal particles the FB-ratio $I(0)/I(\pi)$ can now be optimized by adjusting the effective detuning (by varying the aspect ratio) of the parasitic antenna elements and their inter-particle distances.

Although this method provides a quick and simple assessment that helps understanding the physics of Yagi-Uda antennas, it is limited by the quasi-static approximation, which is only valid for small particles and not too narrow inter-particle spacings, and the homogeneous dielectric surrounding. Hence, additional full numerical models are necessary to better match the experimental conditions.

Boundary Element Method

As mentioned in Chap. 4 the boundary element method (BEM) is a frequency-domain algorithm to solve partial differential equations. By reducing the problem to the surface boundary of materials, computational power and time can be saved compared to volume methods. Here we employ the open-source MNPBEM toolbox which was developed to solve Maxwell's equations (2.1) for metal nanoparticles in dielectric environments [127, 177–179].

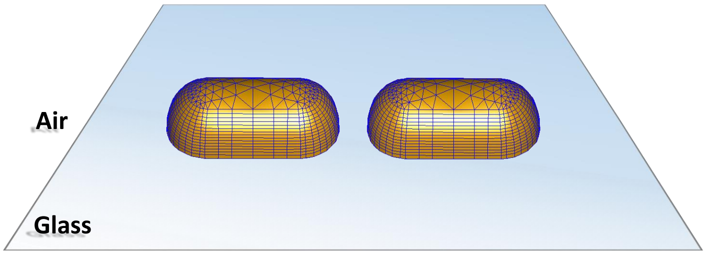

Figure 5.7 – BEM geometry of a two-arm nanoantenna. The antenna surface towards air and glass (not visible) is discretized into triangles and quadrilaterals. Surface charges and currents are chosen such that the boundary conditions of Maxwell's equations are satisfied. Adapted from [171].

Antenna elements are modeled using rounded polygons that are extruded via custom-made edge profiles (cf. Fig. 5.7). The dielectric function of gold according to Olmon *et al.* [68] can be directly plugged in without fitting procedure. We define the lower halfspace to consist of glass to include a substrate. Retardation effects beyond the quasi-static approximation are deliberately included into the calculation. The BEM model is used for optimizing the dimensions of Yagi-Uda antennas, but also to study the influence of a gold sphere in antenna gaps to predict and verify spectral shifts observed in DEP experiments [180]. In the latter case the gold nanoparticle is placed into the gap of the two-arm antenna and scattering spectra are simulated upon plane wave illumination. As BEM produces unstable numerical results if too elongated/complex shapes such as the kinked connectors of the feed element are involved we later return to the FDTD algorithm to simulate the final electrically connected Yagi-Uda antenna.

Optimal geometry

In this section we perform optimization sweeps to obtain well-suited dimensions for the parasitic elements exploiting the DIM and also the BEM algorithm in the final step. Since the feed resonance shifts upon placing a particle into the gap by means of DEP, the "spectral window" between reflector and director resonances, see inset of Fig. 5.2 a, has to be sufficiently broad to reproducibly fabricate stable forward emitting antennas.

Translated into the language of the DIM we face a constraint of sufficiently large detuning values for the passive elements. Indeed we would reach a "global" optimum for moderate detunings, however, the directionality is then more sensitive to structural imperfections and experimental realization of these designs is still a challenge on the nanoscale. On the other hand, previous studies demonstrate that too strong director detunings to the blue side still yield good FB-ratios while too weak blue-shifts do not [153]. Hence, the constraint of larger detunings is quite acceptable within the optimization procedure. Using feed driving wavelengths between 800 nm and 880 nm (cf. Fig. 5.11 e-f) in measurements we find that stable forward emitting Yagi-Uda arrays are possible with a reflector resonance at 890 nm and director resonance at 680 nm and fix these parameters, corresponding for instance at $\lambda_0 = 850\,\text{nm}$ to detunings $\delta_{\text{ref}} = -0.86$ and $\delta_{\text{dir}} = 9.50$.

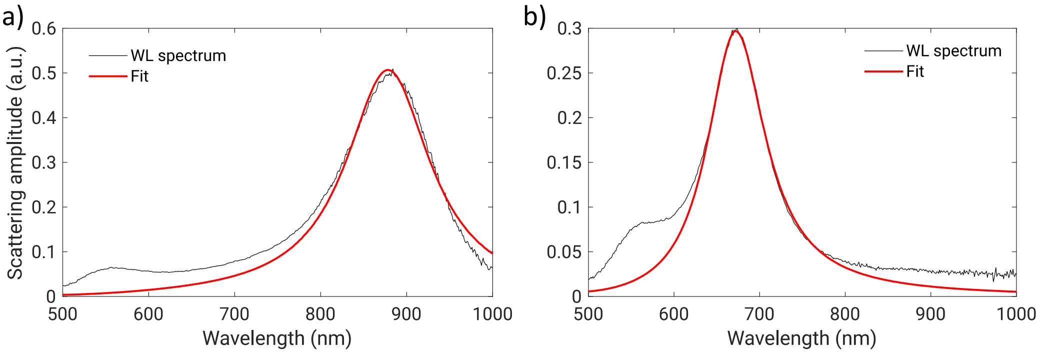

Figure 5.8 – Fit of quasi-static polarizability to WL scattering spectra. a) Reflector spectrum acquired under WL illumination (black) and corresponding fit (red). **b)** Director spectrum measured under WL illumination (black) and corresponding fit (red). The fitting outcomes are used to calculate loss parameters. More details are given in the text.

In order to calculate the absorption parameters $\gamma_{\text{ref}}, \gamma_{\text{dir}}$ required for the DIM, experimental WL scattering spectra of isolated parasitic elements (cf. Fig. 5.11 e) are fitted using Eqs. (3.13b) and (5.2). To mimic the effect of a glass substrate as well as possible within the DIM, an effective homogeneous background medium with $\varepsilon_{\text{surr}} = 1.52$ is assumed. Fig. 5.8 displays the original spectra together with the fit. Because of off-resonant background light the curves show good agreement primarily in the peak region. The side peak around 560 nm stems from the short axis mode of the nanorods, which is partially collected with the $NA = 1.45$ microscope objective. Inserting the resulting effective volumes V_{eff} into Eq. (5.5a) yields $\gamma_{\text{ref}} = 0.370$ and $\gamma_{\text{dir}} = 0.531$ which is in good agreement with results reported in ref. [156] for similar gold nanorods.

Now we are able to run a parameter sweep regarding the reflector with the analytic model. Varying the distance between feed and reflector in a two-particle system, we plot the FB-ratio in Fig. 5.9 and find a pronounced maximum around $x_{\text{ref}} = 160\,\text{nm}$. However, since the kinked connectors (cf. Sec. 5.2.1) run between feed and passive reflector a sufficiently large reflector spacing is required to avoid near-field coupling between the latter and the electric leads. Under this constraint we place the reflector at $x_{\text{ref}} = 200\,\text{nm}$. We also visualize the radiation pattern of the two-particle system

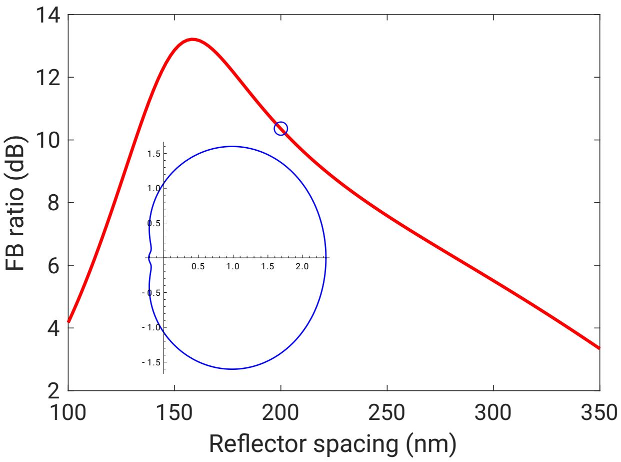

Figure 5.9 – Optimization of reflector spacing. FB-ratio (red) as a function of reflector spacing for a feed-reflector entity ($\lambda_0 = 850\,\text{nm}, \lambda_{\text{ref}} = 890\,\text{nm}$) within the DIM. The blue inset shows the radiation pattern in the plane perpendicular to the dipole axes, calculated at $x_{\text{ref}} = 200\,\text{nm}$ (blue circle).

at this configuration in the inset of Fig. 5.9. As is clearly seen, despite a decent FB-ratio the opening angle of the forward beam is quite large. Indeed, narrower beam angles are achieved by adding directors as demonstrated in Fig. 5.2 c. Another factor contributing to a beam narrowing is introducing a refractive index contrast via e. g. a glass substrate. Then the main emission concentrates close to the critical angle of total internal reflection, even for a mere connected feed element (cf. Fig. 5.5).

We proceed with adding three directors to the system and optimizing their spacing by also varying the driving wavelength of the feed. A subsequent map of the FB-ratio obtained from the DIM is depicted in Fig. 5.10 a. The FB-ratio reaches a maximum for a wavelength of $\sim 860\,\text{nm}$ and spacings of $x_{\text{dir}} = 330\,\text{nm}, 200\,\text{nm}$ and below $100\,\text{nm}$. The latter distance, however, is less reliable as the dipole approximation breaks down if the nanoparticles come too close to each other.

For similar but more realistic FB maps with the BEM model, a connector-less Yagi-Uda antenna is assumed with the same reflector/director resonance wavelengths and reflector spacing as mentioned above. A dipole source oriented parallel to the long axis of the feed is placed centrally inside the gap 15 nm above the substrate. The driving wavelength of the source dipole is swept while the geometry of the feed element itself is kept constant. The results are plotted in Fig. 5.10 b where one can see that the optimum driving wavelength blue-shifts slightly to $\sim 850\,\text{nm}$ and, more importantly, the director spacings to values of $\sim 240\,\text{nm}$ and $\sim 130\,\text{nm}$. Furthermore, the FB-ratio decreases noticeably – an overall effect we observe with asymmetric dielectric environments such as the air-glass interface. Nonetheless, director spacings around 240 nm, easier to implement into the fabrication protocol than 130 nm, and driving wavelengths around 850 nm constitute good values for experimental realization.

Table 5.1 lists an overview of all the obtained parameters from the calculations and experiments. Little differences in the reflector/director spacings are attributed to

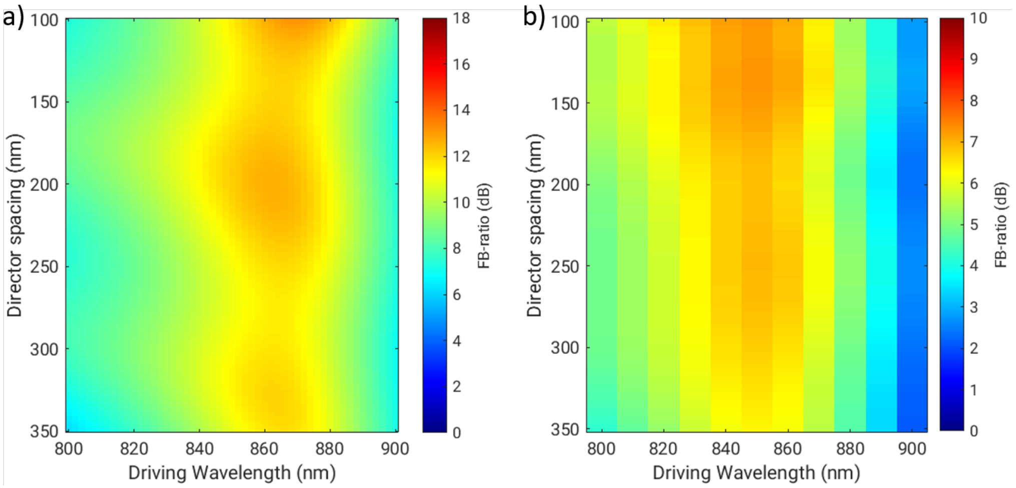

Figure 5.10 – Optimization of director spacing. a) Optimization map visualizing the FB-ratio for a Yagi-Uda antenna with one reflector, feed element, and three directors within the DIM where director spacing and feed driving wavelength are swept. **b)** Same optimization procedure carried out with the BEM algorithm. Taken from [171].

Parameter		**DIM**	**BEM**	**FDTD**	**Experiment**
Connector	*Width*	–	–	30	30
	Spacing	–	–	100	100
Reflector	*Length*	–	180	166	166
	Height	–	40	40	40
	Width	–	60	60	60
	Spacing	200	200	200	200
Feed	*Length*	–	145	145	115
	Height	–	40	40	40
	Width	–	80	80	80
	Gap	–	30	30	25-30
Director	*Length*	–	111	108	108
	Height	–	40	40	40
	Width	–	60	60	60
	Spacing	200/330	240	240	240
Particle	*Diameter*	–	–	–	30

Table 5.1 – Synopsis of optimum geometric parameters and dimensions of fabricated antennas. All values are in units of nm. Adapted from [171].

slightly dissimilar particle shapes in BEM and FDTD models due to custom-made edge profiles. Here the important quantity is the resonance wavelength of 890 nm/680 nm, respectively, out of which the length follows. Length differences of the feed element between experiment and simulations stem from the fact that the final driving wavelength is determined experimentally by the two-arm antenna including the spherical particle in the gap that causes a significant red-shift (cf. Fig. 5.3 b). This resonance shift is compensated in simulations, where the 30 nm interstice is left empty for the sake of much lower computational burden, via increasing the arm length of the feed constituents.

5.3 Optical and optoelectronic characterization

In order to fabricate optimized Yagi-Uda antennas we first study the individual elements separately. In Figs. 5.11 a-e, SEM images and associated scattering spectra of the final elements as well as a fully assembled antenna are shown. As intended, the resonance position of the reflector and directors occur at 890 nm and 680 nm, respectively, while the feed element and the whole Yagi-Uda antenna are resonant around 810 nm. It is worth mentioning that the resonance of the empty feed lies around 660 nm and red-shifts upon deposition of the spherical particle inside the gap towards 810 nm which is demonstrated by subtracting the contribution of passive elements from the scattering spectrum of the entire Yagi-Uda antenna. The outcome is visualized as red dotted line in Fig. 5.11 e.

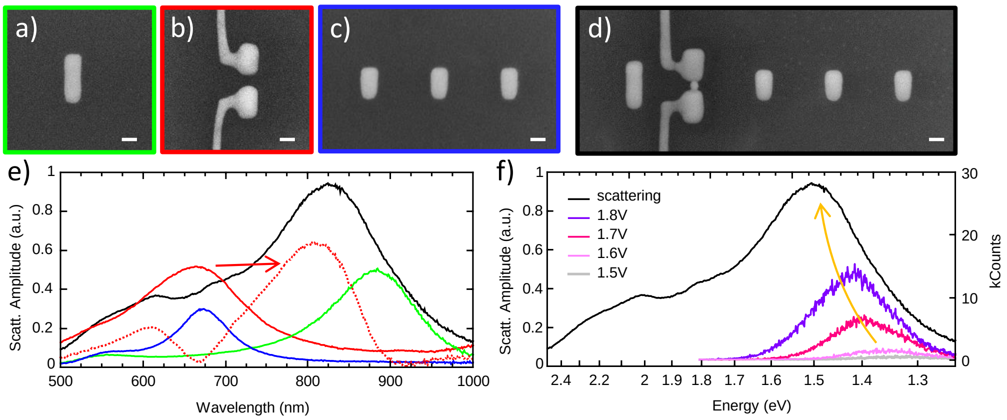

Figure 5.11 – Characterization of the Yagi-Uda antennas. a)-d) SEM images and **e)** associated spectra of a reflector (green), an unloaded feed element (red), the directors (blue) as well as a completely assembled Yagi-Uda antenna (black). The dotted line in e) is the delta of complete antenna minus parasitic elements and corresponds to the feed element now loaded and red-shifted due to the particle inside the gap. **f)** Scattering spectrum vs energy of the Yagi-Uda antenna (same as in e) and resulting EL spectra for various DC voltages. With growing voltages, the EL peak blue-shifts and becomes stronger as indicated by the yellow arrow (cf. ref. [30]). Note the voltage drop-off is close to zero. Scale bars, 50 nm. Taken from [171].

Electroluminescence (EL) is measured by applying a DC voltage V_b of up to 1.8 V and collecting the emitted light via a high-NA objective. The corresponding results in Fig. 5.11 f exhibit an emission peak which blue-shifts and increases in amplitude with increasing voltage. Previous experiments showed that the high LDOS in the antenna gap is responsible for an enhanced inelastic tunneling rate – i. e. the emission peak – and that the blue-shift as well as the amplitude increase can be explained by a quantum-shot noise model [30, 181]. Due to the discrete nature of single electrons and their charges the tunneling current bears fluctuations whose power spectrum depends on the junction resistance and frequency and is nonzero up to the cutoff frequency $\omega_{\mathrm{max}} = eV_b/\hbar$. Multiplication of the power spectrum of current fluctuations and the antenna's scattering resonance yields very good agreement with the observed EL peak [30]. In order to prevent destruction of the antenna, we limit the applied voltage to 1.8 V, which results in an emission maximum around 870 nm that is close to ideal for driving the Yagi-Uda antenna. Furthermore, the voltage drop-off between applied voltage and maximum emitted photon energy in eV is close to zero indicating only a single tunneling barrier. External quantum efficiencies, *viz.* number of detected photons per tunneling electron, on the orders of 10^{-5}-10^{-4} are obtained for the present structures, in compliance with previously published values of electrically driven dipole antennas [30].

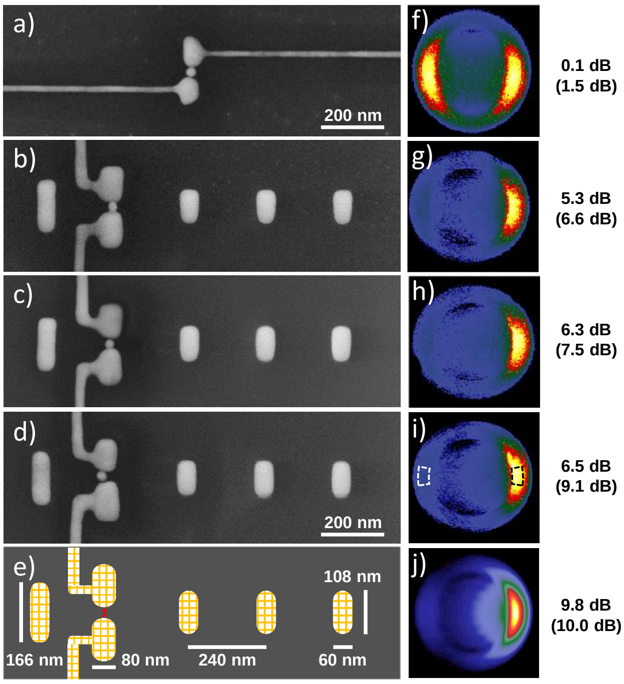

Figure 5.12 – **Far-field comparison of dipole and Yagi-Uda antennas. a)-e)** SEM micrographs of one dipole as well as three Yagi-Uda antennas and a sketch of the FDTD model. **f)-j)** Corresponding radiation patterns. While the dipole antenna has a balanced emission, the Yagi-Uda antennas show a high directionality to the right (forward direction) and nearly no emission to the left (backward direction). The adjacent numbers give the resulting FB-ratios determined by the areal (pixel) method. The solid angle segments ($\Delta\theta = 15°, \Delta\varphi = 20°$) used for integration are indicated in i). Adapted from [171].

In order to experimentally estimate the FB-ratio, we record the emission pattern of the EL by back-focal plane imaging for various antennas and evaluate them with the common “pixel” method and the more accurate “areal” method (cf. Sec. 5.2). First, as a reference, we investigate a dipole antenna (Figs. 5.12 a, f; same as in Fig. 5.5 top row) and observe a FB-ratio of (1.5 ± 1.4) dB and (0.1 ± 0.2) dB with pixel and areal method, respectively, which is close to the theoretically expected 0 dB. Fig. 5.12 also depicts the results for three experimental Yagi-Uda antennas. The first Yagi-Uda antenna is the one discussed in Fig. 5.11 and shows a directionality of 6.6 dB or 5.3 dB, respectively. This is a larger value than the maximum of 6 dB (pixel method) measured by Curto *et al.* for optically driven Yagi-Uda antennas [157] as well as the maximal 5 dB (areal method) obtained by Gurunarayanan *et al.* with their twisted dipolar antenna approach [32]. We fabricate several antennas with similar or better performance and the two remaining antennas in Fig. 5.12 show FB-ratios of up to $9.1/6.5$ dB. These results exceed the values of hitherto published optical antennas and, hence, highlight the potential of electrically driven Yagi-Uda antennas for light. Variations between the individual antennas can be traced back to slight deviations in antenna geometry and particle placement. Furthermore, the results are qualitatively and quantitatively very close to the numerical results from FDTD simulations shown in Fig. 5.12 e, j, indicating a limit of this design around 10 dB. Moreover, compared to the radiation pattern of the feed (cf. Fig. 5.5), the Yagi-Uda antennas in Fig. 5.12 exhibit a narrowed forward beam angle as a result of the interference among the parasitic elements.

5.4 Limits of Yagi-Uda antennas in the optical regime

Analogous to the RF regime, higher directivities can be reached by simply adding more directors to a Yagi-Uda array [182, 183]. However, care needs to be taken when nanostructures are addressed, as explained in the following. In terms of fabrication, single-particle deposition is still possible with Yagi-Uda antennas featuring e. g. 13 directors and thereafter, light emission is observed upon bias application. Surprisingly, the FB-ratios are lower than the lowest ones found for three-director arrays. Overall, we find the tendency that with increasing number of directors the FB-ratio decreases.

The reason for this counterintuitive behavior is the asymmetric air-glass dielectric surrounding and the subsequent refraction of light into the higher-index substrate. A more detailed picture is conveyed by Fig. 5.13, where FDTD-simulated near-field intensity maps for 15-director Yagi-Uda antennas on an air-glass interface as well as in an index-matched oil-glass environment ($n = 1.52$) are presented. The antennas are excited via a dipole source situated inside the feed gap. For the air-glass interface in Fig. 5.13 a the directors further away from the feed show little intensity because most of the light is refracted into the glass. Hence, directors further away do not contribute to the antenna performance, i. e. they do not increase the antenna directionality. In addition, the extra path length the light needs to travel from the source via the more distant directors to the detector sitting below the substrate results in a phase lag and, therefore, a slight destructive interference at the detector, i. e. reduced signal. With every additional director, this destructive interference increases. Another general effect in experiments which might come into play with increasing antenna length is a limited coherence along the array. As the directors are not well coupled among each other due to the weak near-fields in the case of the air-glass interface, the re-radiated waves are less correlated.

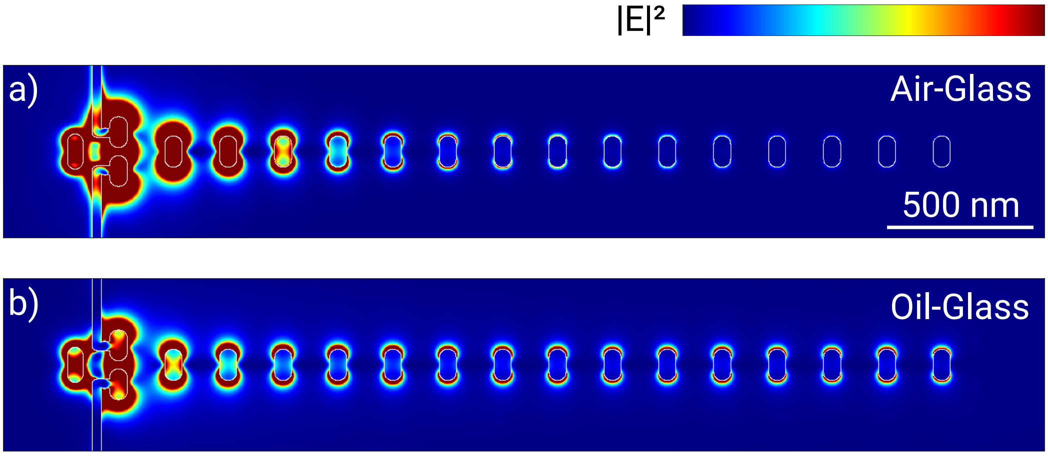

Figure 5.13 – FDTD simulated near-field intensity distribution of a 15-director Yagi-Uda antenna. **a)** Antenna placed on an air-glass interface. **b)** Antenna embedded in a homogeneous refractive environment. Taken from [171].

Invoking a dielectric environment with constant refractive index (cf. Fig. 5.13 b) changes the situation substantially: In contrast to the experimental setting with air-glass interface, no light is refracted out of the antenna plane such that all directors exhibit significant field intensity and, thus, can contribute to a more directed emission. This is analogous to the RF regime where Yagi-Uda antennas are situated in free space if the mechanical support is neglected. In practice, a droplet of immersion oil on top of the nanostructures would easily create such a configuration but it also prevents a straightforward acquisition of the radiation pattern with the main lobe being pushed beyond the acceptance angle of even high-*NA* microscope objectives. Such experiments demand advanced detection schemes and are therefore beyond the scope of the current project.

Fig. 5.14 a combines an SEM micrograph of a fabricated Yagi-Uda antenna with 13 directors and the acquired xz-plane angular radiation profile where the emission maxima occur near the critical angle of total internal reflection, analogous to the previous back-focal plane images, yielding FB $= 2.1/3.1$ dB with the “areal”/“pixel” method, respectively. The emission behavior in a symmetric surrounding can be simulated and compared to conventional RF Yagi-Uda antennas to judge their performance. We therefore simulate an antenna embedded in a homogeneous $n = 1.52$ surrounding, as if the antenna on glass were exposed to a droplet of immersion oil, adjust the geometry to match the new dielectric environment and plot the resulting xz emission pattern in Fig. 5.14 b. As expected, contrary to the experimental setting with air-glass interface the shape of the pattern is now symmetric and features a much higher FB-ratio of up to 13.2 dB at 870 nm. This corresponds to an antenna forward gain of 11.7 dBi, a quantity which we use now for comparison with macroscopic antennas. The gain is defined by

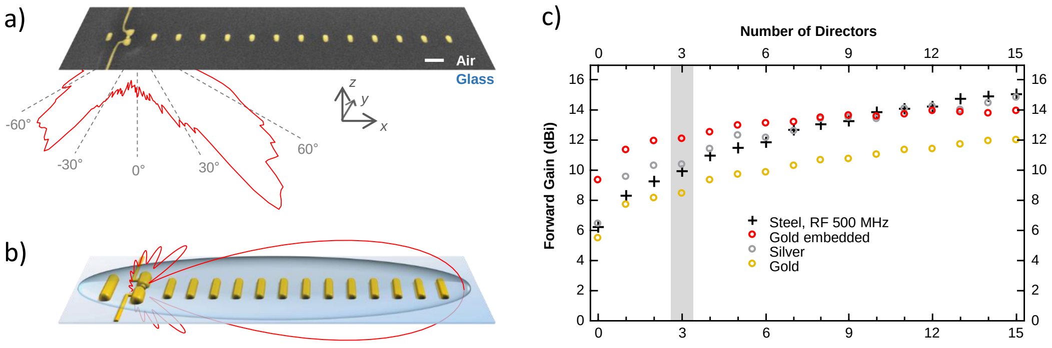

Figure 5.14 – Limits of an optical Yagi-Uda antenna. **a)** SEM image of the experimental Yagi-Uda array with 13 directors and superimposed measured *xz* radiation characteristics. The bending towards the bottom is caused by the air-glass interface, as in the measurements of 3-director Yagi-Uda antennas on glass. Scale bar, 200 nm. **b)** Perspective sketch of the optical antenna with 13 directors in an assumed homogeneous surrounding ($n = 1.52$), visualized by an immersion oil droplet, and the simulated *xz* emission characteristics superimposed, yielding a forward gain of 11.7 dBi. **c)** Simulated forward gain of a conventional stainless-steel Yagi-Uda antenna in the RF regime (500 MHz) for a varying number of directors (black crosses). Its counterparts in the optical regime (870 nm) for gold and silver antennas (golden and silver circles) in the homogeneous environment as well as a hybrid system consisting of a gold antenna embedded in a 300 nm Al_2O_3 layer surrounded by a homogeneous $n = 1.52$ medium (red circles). The case of three directors is highlighted (gray area). Adapted from [171].

$I_F/I_{isotropic}$ where I_F is the antenna's forward intensity and $I_{isotropic}$ the intensity of a hypothetical isotropic emitter[1].

In Fig. 5.14 c, this forward gain is plotted as a function of the number of directors for an optical antenna (emission wavelength 870 nm) and also for a conventional RF Yagi-Uda (500 MHz, stainless steel). In order to simulate gains of RF antennas we use the publicly available NEC-2 code that is based on the method of moments to solve the integral electromagnetic equations [184, 185]. The RF model consists of a $\lambda/2$ feed element (length 0.3 m) driven by a voltage source, one reflector (length 0.302 m, spacing 0.1 m) and the directors (length 0.209 m, spacing 0.189 m). All cylindrically shaped antenna elements have a diameter of 8 mm and are discretized into 19 segments. The finite conductivity of stainless steel is taken into account.

Forward gain values from FDTD simulations are evaluated by first calculating the logarithm of the ratio of the intensity emitted in forward direction by a Yagi-Uda antenna and the forward intensity emitted by the bare feed-element without connector wires. This ratio in dBd (decibels-dipole) represents the forward gain over a dipolar emitter because the isolated feed element already shows a dipolar far-field emission. To obtain the gain over an isotropic emitter in dBi (decibels-isotropic) the inherent di-

---

[1] The antenna forward gain is the figure of merit in RF antenna technology; however, it is not easily accessible in nano-optical experiments in contrast to the FB-ratio because a reference antenna with exactly the same performance would be required.

rectivity of a short dipolar antenna of $10 \cdot \log_{10}(1.5) \approx 1.76\,\mathrm{dBi}$ [3] has to be added to the dBd values from the FDTD simulations.

For both optical and RF antennas in Fig. 5.14 c, the forward gain starts at relatively moderate values for a small number of directors, initially increases strongly with increasing number of directors, subsequently flattens out and reaches a plateau around 12.0 dBi and 15.1 dBi, respectively. This means that the directionality characteristic of this optical Yagi-Uda antenna is similar to the radio antenna. By substituting gold with the less lossy silver, the RF values can even be reached. This proves that optical Yagi-Uda antennas perform analogous to their RF counterparts and, therefore, concepts of RF antenna theory should be easily transferable to optical Yagi-Uda designs to further improve or adapt their performance.

We also note that optical Yagi-Uda antennas are even outperforming RF antennas for small numbers of directors. The reason is that in the RF case, the connecting wires are considered to be infinitesimally small and, hence, negligible. In the optical case, the connectors inevitably have a finite size and therefore act as additional passive elements (cf. Sec. 5.2.1). Therefore, we include them in the gain simulations, which becomes especially apparent for small numbers of directors.

Additionally, for optical fields, it is possible to mold the flow of light by designing a dielectric index landscape. For radio waves, this ability is very restricted due to the lack of suitable materials. Here, we consider embedding the Yagi-Uda antenna in a thin film with high refractive index in order to confine the emitted light to a 2D waveguide mode. By embedding antennas into a 300 nm thick Al_2O_3 layer ($n = 1.67$ [186]), surrounded by a $n = 1.52$ medium, and adapting again the geometry, we are able to increase the forward gain drastically by up to 3.6 dBi. This means that for nearly any number of directors, a waveguide-coupled optical Yagi-Uda antenna outperforms the RF stainless steel and pure optical silver antennas – see red circles in Fig. 5.14 c. The increase in performance is most apparent for low numbers of directors (e. g. to 12.1 dBi for three directors) and also particularly interesting because it opens the road toward highly directive optical antennas with very small footprint.

Finally, alongside the gain increase another intriguing figure is the beam angle of the forward emission lobe. With growing director number the main emission lobe is expected to narrow in forward direction, which is confirmed in Fig. 5.15. Here the in-plane FWHM angle is plotted for the same four antenna systems as in Fig. 5.14 c. Qualitatively, all Yagi-Uda arrays share the same behavior, namely that the beam angle is reduced when adding more directors. Silver antennas with sufficient directors show values very similar to the RF antenna made of stainless steel. We observe a rather linear decrease for the gold antenna embedded in the Al_2O_3 film while the other curves are nonlinear. It is worth mentioning that the radiation pattern of the former differs fundamentally from the other patterns. The high-index film determines the out-of-plane beam angle (perpendicular to the angle defined in the inset of Fig. 5.15), which assumes a constant value of $\sim 14^\circ$ regardless of director number. In contrast, the out-of-plane angle of the Yagi-Uda arrays in homogeneous surrounding again depends on how many directors are used. From this study we conclude that it is possible to reduce cross-talk with neighboring antennas, which would disturb optical data communica-

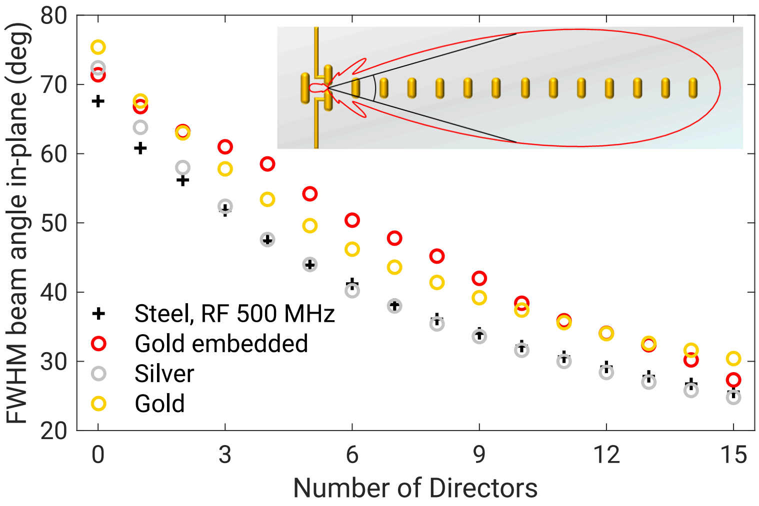

Figure 5.15 – In-plane beam angle of Yagi-Uda antennas. The FWHM angle is given for the antenna systems shown in Fig. 5.14 c as a function of director number. The inset illustrates the definition of the FWHM angle and depicts the exemplary case for a 13-director gold antenna, whose beam angle is 32.6°.

tion, via adding directors. By virtue of the narrowing of the main emission lobe it is possible to arrange Yagi-Uda antennas on a common chip with higher lateral packing density.

5.5 Concluding and prospective remarks

In summary, we have shown that inelastic electron tunneling across a nanometer sized interstice between gold particles can be applied as local driving mechanism to complex plasmonic antenna designs that possess light-shaping functionalities beyond the pure dipole antenna. We conceived an optical Yagi-Uda antenna consisting of a feed element with nanowires attached to apply a bias. The tunnel gap was created by placing a spherical nanoparticle in the prefabricated feed gap via DEP. Furthermore, the active element was surrounded by various parasitic elements on a common glass substrate. Numerical simulations were deployed to optimize the structure, assisted by an analytical coupled dipole model, and to develop an electrical subsystem, in order to eventually reach high FB-ratios. As a result, measurements and simulations yielded unprecedented directionalities of the emitted light. Further numerical studies suggest that gain and beam angle of optical Yagi-Uda antennas can be improved by enlarging the director array, in accordance with their RF counterparts. Ohmic losses inside the (plasmonic) material turn out to be the main limiting factor of the presented approach. At optical frequencies it is also possible to guide the emitted photons by a suited combination of high-index dielectric films, e. g. Al_2O_3 encapsulating the antenna and polymethyl methacrylate (PMMA) on top. This strategy not only boosts the forward gain but also restricts the light emission to the substrate plane, as required for on-chip data exchange between different entities.

Highly directive low-footprint optical Yagi-Uda antennas are therefore specifically promising for on-chip data communication applications where they can act both as sender and receiver of data with an ultrahigh bandwidth. The modulation speed is not limited to exciton lifetimes characteristic for LEDs but rather to the *RC* time constant of electric leads and tunnel junction [31], regarded as plate capacitor, yielding a cut-off frequency in the terahertz regime [30]. Furthermore, the resulting communication schemes would also allow transistors from one computer chip to be directly linked via optical networks to transistors on other chips, which reduces latencies and allows novel computational concepts. Hence, optical Yagi-Uda antennas may play a role in future computational devices. However, a major obstacle still to overcome is the inherently low efficiency of the IET process of about 10^{-6} [30, 33, 187], although values up to 2 % have been observed in geometrically sharp junctions between silver antenna arms with facets of well defined single-crystal lattices [35]. Very recently, resonant IET has been experimentally demonstrated by harnessing resonant electronic states in a “higher order” tunnel junction, a metallic quantum well heterostructure embedded between two electrodes. Quantum efficiencies reaching 30 % are reported [188]. One has to keep in mind that the bandwidth of the current power spectrum is naturally narrowed in resonant IET compared to IET and that the devices under study have a large planar extension with a silver nanorod placed on top of the tunnel area. Therefore, the concept of metallic quantum wells is not straightforwardly transferable to the overall nanoscopic gap dimensions in Yagi-Uda antennas. Nonetheless, resonant IET marks one step further towards technological viability.

Besides a Yagi-Uda transmitter a receiving unit is necessary to demonstrate truly optical communication on a chip. Hot electron assisted rectification of NIR radiation with gold nanoantennas was pioneered in 2011 [107]. At optical frequencies, multiwalled carbon nanotubes were proposed to engineer rectifying MIM tunnel diodes with antenna effects [189]. Even a wireless optical interconnect between directional antenna and a biased tunnel junction based rectenna was recently built [27]. This rectenna design did not support a plasmon resonance which makes the transduction yield low. By virtue of reciprocity, a Yagi-Uda design qualifies for a directional, resonant rectenna structure. Yet, the investigation of nanoscale resonant rectennas is still in its infancy [190].

Another intriguing aspect is the plasmonic coherence in electrically driven nanodevices in view of the fact that tunneling is a quantum mechanical, statistical process. The experimental realization of highly directive 3-director Yagi-Uda antennas and the agreement with fully coherent FDTD simulations has evidenced coherent electrically excited plasmons that propagate among several parastic elements separated in such a way that no near-field interaction takes place. On the other hand, the more directors are added the more it might become important to consider dephasing phenomena. Presumably, the dielectric index landscape also has an impact on the coherence behavior because it controls the coupling between the elements as shown in Fig. 5.13. If the coherence is lost by random phase jumps, the working principle of the parasitic elements breaks down, giving rise to less directional far-field radiation. Therefore, it would be interesting to reveal the coherence behavior of larger director arrays, e. g. by placing scattering particles around an in-plane emitting Yagi-Uda antenna with a specific director number and probe the scattering particles to reconstruct the radiation characteristics. This could be performed with the scanning near-field optical microscopy (SNOM) technique [4, 5]. Comparison with FDTD simulations would yield a hint whether the coherence is maintained. An alternative but equally challenging route would possibly be a phase-resolved near-field investigation of the electrically-driven Yagi-Uda antenna with cathodoluminescence [191, 192].

Finally, the modeling and simulation framework presented in this chapter can also be utilized to study and optimize the directionality of other complex nanoantenna systems consisting of multiple particles. An analytical quasi-static model for estimating the most important parameters benefits from the low computational load and fast calculation times. This yields a reasonable set of initial values for more sophisticated numerical simulations that take into account several experimental aspects such as substrate, refined particle shapes, material properties, manufacturing constraints, excitation conditions, as well as the fully vectorial structure of Maxwell's equations (2.1). When these additional conditions, satisfying the ever-increasing demand for higher accuracy in nanostructures, are included in the optimization procedure, highly performing antenna systems can be conceived, but also their limitations can be elucidated. The presented manufacturing toolbox provides a powerful platform to reliably produce those refined particle geometries and integrate them with nanometer gap junctions, paving the way towards implementing more elaborate electrically driven antenna configurations such as log-periodic antennas [193] or antennas with a parabolic reflector as well as novel devices, e. g. electrically driven plasmonic waveguides [139].

6

Color-switchable subwavelength organic light emitting antennas

Artificial light sources have always been an essential tool in the history of mankind as they decouple human activity from the natural rhythm of solar irradiation. Hundreds of millennia ago, flames of burning wood helped illuminate the immediate environment of our ancestors after sunset. Light generation via combustion became a more controlled process in oil lamps, having remained an indispensable equipment for thousands of years. An important benchmark was the invention of electrical light sources, pioneered by the light bulb in the 19^{th} century and followed by gas discharge lamps [194]. Due to the laws of black-body radiation and the electronic configuration of the gases, considerable part of the emitted photons from the aforementioned sources, however, lies energetically above or below the visible spectral window, which keeps the light generation efficiency inherently low. The latter can be improved by a more narrowband emission centered in the visible regime. The material class of semiconductors offers such emission properties from recombining charge carriers, which led to the invention of light-emitting diodes (LEDs), assisted by the emergence of transistors in the mid 20^{th} century [194]. Owing to the bandstructure of a specific semiconducting material, the wavelength can be selected.

Semiconducting properties were also discovered in organic compounds, accompanied by the observation of electroluminescence (EL) from molecular crystals [195, 196] in the 1960s. A decade later conjugated polymers with systematic doping were studied and a new class of organic semiconducting materials began to develop [197–199]. However, these early devices suffered from very high applied biases and unstable carrier injection from metal contacts [45], which hindered a broad deployment. In the late 1980s, Tang *et al.* reported on the first high-performance organic light-emitting diodes (OLEDs) based on vapor deposited thin films [200, 201], soon followed by Burroughes *et al.* who presented electroluminescent structures that involved conjugated polymers [202]. Nowadays, the high-tech based society's ever-growing demand for multifunctional, efficient, and color rendering light sources led to tremendous research efforts addressing organic semiconductors. They promise large area integrated light sources on flexible substrates using low cost printing of commonly available composites [45], which may revolutionize once more the market of future illumination solutions. Meanwhile, OLEDs have been utilized in commercial display applications [46, 203].

OLEDs typically consist of stacked multilayers including transparent conductive oxide (TCO) and metallic opaque electrodes, charge injection, and transport layers as well as exciton recombination layers. Radiative recombination of excitons can thus be spatially separated from the metallic electrodes to avoid exciton quenching which leads to heat or to surface modes at the metal interface (see Fig. 6.1 a). On the other hand, the thickness of functional layers must be kept small due to the low mobilities for electrons and holes in most organic semiconductors in order to facilitate fast switching and to avoid losses. Furthermore, the stacked device architecture offers only limited possibilities to engineer the emission characteristics of OLEDs. Plasmonic effects have been studied in the context of organic LEDs, inorganic LEDs, and quantum dot LEDs to increase their brightness via increased local density of states [42, 204–207] and partial scattering of guided modes into the far-field [43, 44, 208, 209]. Even though antenna effects are mentioned in some of these publications [205], the dominant effect is always coupling to guided, i. e., nonradiative modes.

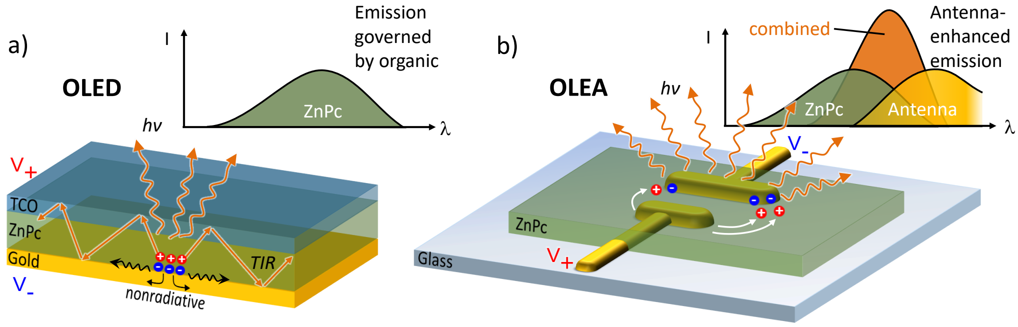

Figure 6.1 – Comparison between a traditional stacked OLED device and the lateral OLEA design. a) Typical OLEDs use a stacked design which suffers from internal losses due to total internal reflection (TIR). Blocking layers (not shown) are needed to avoid recombination of charge carriers at the electrode interfaces which would lead to nonradiative losses such as surface modes and quenching. The emission spectrum is solely governed by the active organic material (ZnPc). **b)** The OLEA design uses lateral electrodes that act as optical nanoantennas. This results in an ultracompact lateral device design. Charge recombination at interfaces is desired since it leads to efficient coupling to radiative antenna modes. The properties of these antenna modes largely influence the characteristics of the emitted light, such as polarization, spectrum, and directionality. The freedom of choice of the antenna design as well as the overall simplicity of the approach can lead to novel degrees of freedom in the performance of such devices, such as the wavelength and directional switching presented in this chapter. Reprinted with permission from [37]. © 2022 American Chemical Society.

In this chapter, we introduce a new device concept for OLEDs. As sketched in Fig. 6.1 b, we propose a laterally structured design in which the electrodes at the same time deliver charge carriers to the OLED's active region and serve as highly efficient nanoantennas. Such organic light-emitting devices based on plasmonic nanoantennas, short organic light-emitting antennas (OLEAs), bear several advantages: (i) The absence of guided modes and the radiative character of the antenna resonance ensure highly efficient outcoupling of power to the far-field. (ii) The overall device footprint, i. e., the pixel size, reaches into the subwavelength regime avoiding parasitic effects of large scale emission volumes in OLEDs. (iii) By means of antenna engineering, the emission wavelength and the radiation pattern of the OLEA can be controlled, and (iv) the antenna's enhanced density of states strongly reduces excited state lifetimes of the organic molecules [210], thereby removing a bottleneck for the generation of photons as well as for the outcoupling of photons into far-field radiation. Finally, (v) the OLEA design is compatible with large scale integration.

Prior to discussing OLEA devices, a brief overview over the physics of organic semiconductors is given and the organic compound used here, zinc phthalocyanine (ZnPc), is precharacterized. Afterwards, the structure design is outlined and electro-optic measurements on OLEA devices are shown, using local electrical excitation via the antenna electrode subsystem similar to Chap. 5. Instead of generating light via inelastic electron tunneling across a nanometer gap we make use of the radiative recombination of excitons inherent to the active organic material. FDTD simulations are carried out to study the far-field radiation characteristics of the OLEA device, as well as spectral and near-field properties of the antenna electrodes embedded in ZnPc. Here, special care must be taken with the simplified optical response of the organic as explained below. Subsequently, based on the astonishing observations in electro-optical measurements, we establish a qualitative model of the charge carrier recombination behavior in OLEA structures and demonstrate controlled color switching upon inverting the bias polarity, accompanied by a change in directionality of the emission. Finally, we investigate experimentally and numerically how the angular radiation pattern can be further influenced by an additional passive element.

6.1 Introduction to organic semiconductors

While inorganic semiconductors are characterized by continuous energy bands of electronic states, their organic counterparts feature a distinct electronic configuration. As carbon atoms in molecular bonds undergo hybridization involving 2s and 2p orbitals they form σ-bonds and π-bonds with adjacent C and H atoms, depending on the degree of H-saturation. While the σ-bonds formed by the sp^2 hybrid orbitals are relatively strong and thus lowered in energy, the π-bonds emerge from unhybridized p$_\mathrm{z}$ orbitals and have weaker binding energy [45]. As the simplest example, Fig. 6.2 a depicts the formation of the π-bond in an ethene molecule via mixing of the basic atomic p$_\mathrm{z}$ orbitals. In the energetic ground state, the highest occupied molecular orbital (HOMO) is the bonding π-orbital, as illustrated in Fig. 6.2 b. Due to the aforementioned low binding energy, the lowest unoccupied molecular orbital (LUMO) is π^*, which is populated by one electron in the first excited state of ethene. The π-π^* energy gap usually lies in the visible spectral range, which renders these transitions desirable in light-emitting devices.

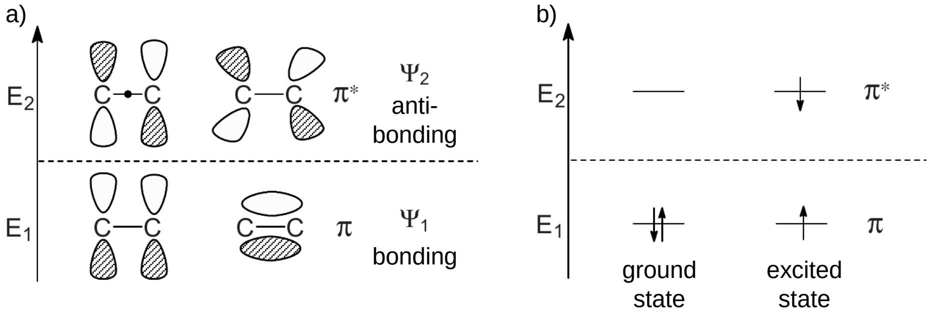

Figure 6.2 – Molecular orbitals and energy diagram of ethene molecule. a) Left: Basic p_z atomic orbitals which do not participate in the sp^2 hybridization. The • symbol denotes a nodal plane. Right: Delocalized bonding π and antibonding π^* molecular orbitals. The C–C σ-bond is illustrated by a line. **b)** Energy diagram of ethene in its ground state (empty π^*-orbital) and first excited state (one electron in π^*-orbital). Reprinted and adapted with permission from [211]. © 2008 Springer Nature.

Organic semiconducting materials typically feature a conjugated π-electron system consisting of staggered single (σ) and double ($\sigma + \pi$) bonds. This gives rise to delocalized π-electrons over the length of the conjugated system with a pronounced intramolecular mobility. The HOMO-LUMO gap also depends on the size of the conjugated π-system, offering a broad tunability of optoelectronic properties within the organic material class [45]. Moreover, halogenation can be used to shift the energy level offset w. r. t. the vacuum level while retaining the energy gap itself [212, 213]. Such chemical modifications allow specific designs and enable vast possibilities in engineering organic semiconductors, e. g. electron donor and acceptor compounds.

Contrary to covalent bonds in inorganic solids, the intermolecular coupling in an organic crystal consists of significantly weaker van-der-Waals bonds which brings along several implications on the optoelectronic properties. Excited states remain more localized and appear as coupled electron-hole pairs, called excitons. They can be spread across one (Frenkel exciton) or several adjacent molecules. For instance, charge transfer (CT) excitons are formed by charge carriers sitting on neighboring molecular sites. In organic materials, the Coulomb interaction between hole and electron can assume relatively high values up to 1 eV, and optical gap and free-carrier gap differ by this value [45]. One has to distinguish between spin singlet states S_i and triplet states T_i as indicated in Fig. 6.3. This Jablonski diagram summarizes the most important electronic transitions in an organic semiconductor, including the vibrational sublevels. Typically, the ground state is given by a filled S_0 state and photon absorption promotes an electron to the HOMO with the resulting exciton occupying a singlet state. Between the vibrational modes that also can include different electronic levels, radiationless internal conversion takes place on very short time scales ($\tau_{\mathrm{IC}} \sim 10^{-13}\,\mathrm{s}$) so that fluorescence ($\tau_{\mathrm{Fl}} \sim 10^{-9}\,\mathrm{s}$) usually occurs from the lowest sublevel [211], and in particular, from the lowest excited state of the corresponding spin multiplicity (Kasha's rule [214]). Due to selection rules of electron transitions in atoms, processes such as intersystem crossing, triplet deexcitation (phosphorescence) and photon absorption into triplet states would be dipole-forbidden because of the involved spin flip. However, as organic compounds are molecular and sometimes even include a metal atom with high atomic number, spin-orbit coupling weakens the selection rule and enables these processes, albeit on longer time scales [211, 215]. On the other hand, the weak nature of the phosphorescence mechanism imposes a fundamental limit to the external quantum yield of OLED devices [45] because the spin multiplicity of S_1 and T_1 dictates that only 25 % of injected charge carriers enter the S_1 state and decay fast via fluorescence. The spin triplet states are accompanied by an antisymmetric spatial wavefunction of the electrons and lie therefore energetically lower than the corresponding singlet states.

According to the Franck-Condon principle, absorption and fluorescence processes from the lowest vibronic sublevel of an initial electronic state to higher vibronic sublevels of the final electronic state may have higher probability, *viz.* intensity, because of a stronger overlap of the involved vibrational wavefunctions. Since the electron transitions happen very fast the nuclear positions are assumed constant during the transition (Born-Oppenheimer approximation). Upon electronic (de)excitation, however, the equilibrium nuclear distance in molecular compounds might change which determines the overlap of vibrational wavefunctions [215]. The fact that the outgoing photons possess a longer wavelength (lower energy) than the absorbed ones is known as Stokes shift and depends on the population of the vibrational states as well as geometrical relaxation effects [215].

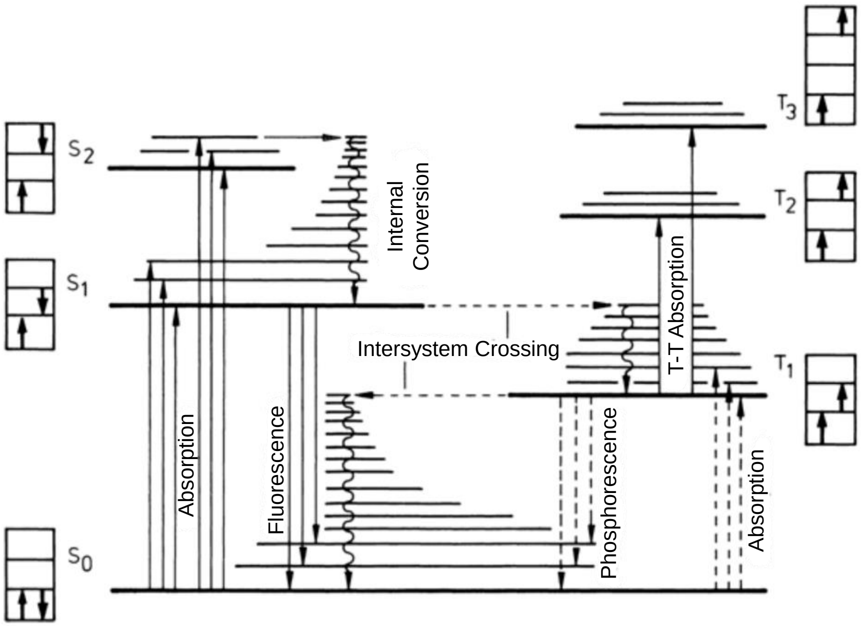

Figure 6.3 – Jablonski diagram of a typical organic molecule. The singlet states S_i, including the molecule's ground state, exhibit an antisymmetric spin wavefunction whereas the triplet states T_i have a symmetric one. Vibronic sublevels are depicted with thin lines. Allowed, fast transitions involving a photon are drawn with solid arrows. Weak radiative processes are shown with dashed vertical arrows. Transitions such as intersystem crossing (horizontal arrows) and internal conversion (wavy arrows) are radiationless. Reprinted and adapted with permission from [215]. © 2006 Springer Nature.

Besides optical properties, the charge carrier transport is also affected by the weak van-der-Waals binding in organic molecular crystals. When a surplus or defect electron resides on a molecular entity it forms an ionic state within the crystal lattice. The ionic state is energetically stabilized within the condensate as compared to an isolated molecule, i. e. the HOMO (LUMO) is raised (lowered) by polarization energies which stem from screening effects of surrounding molecules. Moreover, typical organic thin films exhibit spatial disorder with varying polarization energies so that the HOMO and LUMO are spectrally broadened, following a Gaussian distribution [45]. Hence, the transport behavior in organics lies between the limiting cases of coherent band transport and incoherent hopping transport. The former is predominantly observed in highly purified single-crystalline samples, featuring decent mobilities which, however, are still well below the values of crystalline Si or Ge. In poly-crystalline organic thin film samples, such as used in this work, hopping processes prevail, giving rise to orders of magnitude lower mobility values for charge carriers. Here the mobilities also depend on the applied electric field which may partially mitigate the spatial disorder effect by overcoming local energy barriers.

Compared to inorganic semiconductors, organics possess a low intrinsic carrier density. Thus in applications like OLED devices it is important to provide charge carriers via external metal contacts. In general, a Schottky barrier has to be overcome by the charge carrier upon injection, or the contact is Ohmic, depending on the metal work function and the HOMO/LUMO energies. If a Schottky barrier is present (see also Fig. 6.13), two injection mechanisms at metal-organic interfaces play an important role. One contribution stems from the thermally induced surpassing of the barrier and is called thermionic emission. This phenomenon is modeled by the Richardson-Schottky equation and dominates at high temperatures [216]. The other contribution, known as Fowler-Nordheim (FN) tunneling, can be understood as field assisted quantum mechanical electron tunneling across the barrier [216, 217]. This temperature independent process dominates at intense electric fields and changes drastically with barrier height and width. Both effects can be influenced by a space charge within the organic close to the contacts which weakens the local electric field [218, 219]. In the FN representation of current-voltage curves, the two contributions can be identified by their different signs of slope, as is shown below in Sec. 6.5.

6.2 Characterization of ZnPc thin films

6.2.1 Molecular and electronic structure

Zinc phthalocyanine (ZnPc) is a member of the metal phthalocyanine family which is widely used in organic photovoltaics [220] and constitutes an ideal model system for the present study because of the solid background knowledge about its growth and photophysical properties, its support of ambipolar transport as well as the possibility to inject charges by symmetric gold contacts, and finally, because it emits in a near-infrared spectral range that matches the plasmonic excitations of the gold nanoantennas introduced later. Fig. 6.4 a depicts the chemical structure of ZnPc with the central Zn atom surrounded by the phthalocyanine ligand system [213]. The orbitals relevant for the photophysical properties are listed in Fig. 6.4 b, together with the electronic configurations of ground state and first excited state (Q-band, $\pi - \pi^*$). ZnPc features a fully occupied 3d orbital which discriminates it from other MPcs such as CuPc, NiPc, and FePc [220]. Hence, the formation of ligand-metal exchange coupled states and subsequent fluorescence quenching is excluded, resulting in a higher intrinsic quantum yield than other MPcs. Owing to the D_{4h} symmetry at ground state, ZnPc has degenerate HOMO and LUMO levels [221]. Two separate absorption peaks are visible in the Q-band spectrum and there is an ongoing dispute within the community about which effect to ascribe to this observation. Upon excitation, a symmetry break in the molecule may occur which lifts the degeneracy and causes a splitting of the Q-band absorption (Jahn-Teller splitting) [222]. Recent theoretical studies attribute the finding to a mixture of coexisting bright Frenkel exciton and CT exciton. They also predict the intensity ratio between the mixed states, i. e. their oscillator strengths [223, 224]. It is worth mentioning that crystalline ZnPc exhibits polymorphism. The metastable α-phase features a triclinic unit cell with the molecules stacked in a uniform brickstone orientation. Thin films are observed to preferably grow in the α-phase at room temperature. The thermodynamically stable β-phase is characterized by a monoclinic unit cell with molecules oriented in a herringbone pattern [220, 224]. A transition from the α to the β form can be induced by high temperature annealing [225–227] or solvent exposure [228], accompanied by changes in the photoluminescence (PL) spectrum.

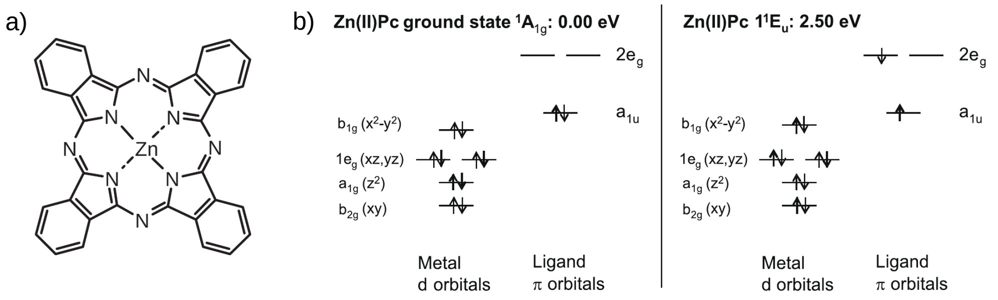

Figure 6.4 – **ZnPc molecule. a)** Chemical structure of ZnPc. Reprinted with permission from [213]. © 2011 John Wiley & Sons. **b)** Electronic configuration of ZnPc in its ground state and first excited state, showing 3d orbitals of Zn and the ligand π-orbitals. Reprinted with permission from [220]. © 2010 Elsevier.

6.2.2 Dielectric function

Regarding OLEA devices, the presence of a ZnPc film with a certain dielectic constant surrounding the plasmonic structure is expected to drastically alter the antenna resonance. Such resonance shifts must be accounted for when designing the antenna electrodes via simulations. It is therefore of interest to model the complex dielectric function of the active organic material and implement the outcome into the FDTD algorithm (cf. Chap. 4). The low symmetry of the triclinic crystal structure manifests itself as an anisotropic optical response. Additionally, the crystallographic axes do not coincide with the optical axes. As a result, we would obtain individual dielectric tensors for real and imaginary part with frequency dependent orientation of the principal axes [229] and the Kramers-Kronig relations, which are based on the holomorphism of the dielectric function and causality, do not hold anymore. This would prevent a successful fit with Lumerical's MCM fitting procedure (cf. Sec. 4.2). To overcome this hurdle we adopt a simplified analytical model to describe the complex dielectric function of ZnPc:

$$\varepsilon(\omega) = \varepsilon_\infty + \sum_{k=1}^{2} f_k \frac{\omega_k^2}{\omega_k^2 - \omega^2 - \mathrm{i}\gamma_k \omega}. \tag{6.1}$$

Here, f_k, ω_k, and γ_k denote the oscillator strength, transition frequency, and damping of the k-th transition, respectively, in accordance with the quantities defined in Eq. (3.4). Summing over two Lorentz oscillators accounts for the split Q-band. As a starting point for the determination of the model parameters we use the dielectric function reported by Wojdyła *et. al.* [230] and, in particular, we fit Eq. (6.1) to its imaginary part. The real part then follows according to the Kramers-Kronig relations and the resulting dielectric function is isotropic. We find $\varepsilon_\infty = 2.7$, $f_1 = 0.09$, $\hbar\omega_1 = 1.69\,\mathrm{eV}$, $\hbar\gamma_1 = 0.22\,\mathrm{eV}$, $f_2 = 0.14$, $\hbar\omega_2 = 1.99\,\mathrm{eV}$ and $\hbar\gamma_2 = 0.32\,\mathrm{eV}$ as fitting parameters.

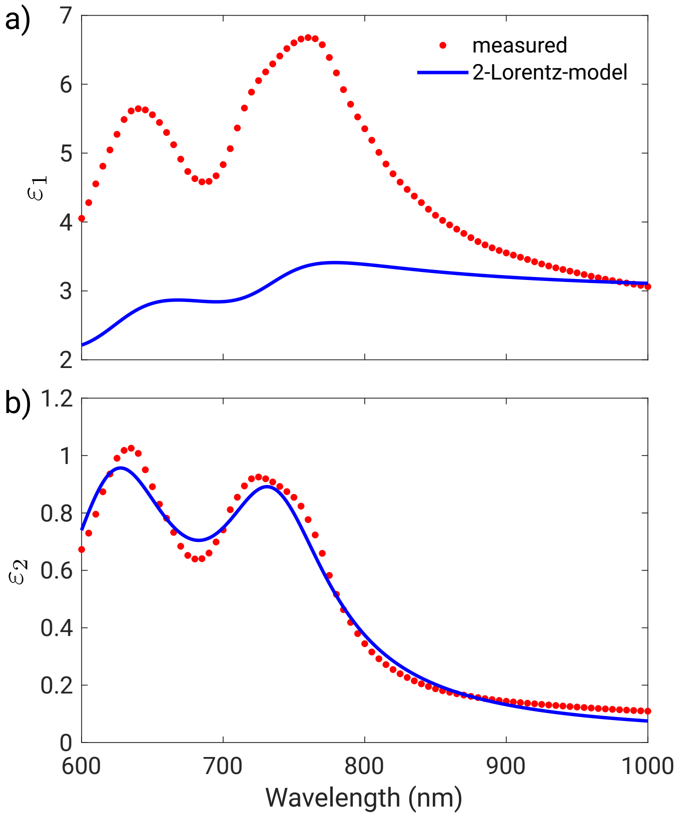

Figure 6.5 – Dielectric function of α-ZnPc. a) Real part ε_1 of the measured data [230] as red dots and Kramers-Kronig consistent fit of Eq. (6.1) as blue solid line. Fit parameters are given in the text. **b)** Imaginary part ε_2 of measured dielectric function with corresponding fit.

Fig. 6.5 displays the reported data together with the simplified model. One observes that the imaginary part ε_2 (panel b) is reproduced rather accurately throughout the spectral range of interest, whereas the real part (panel a) shows a clear deviation between fit result and measured data around the Q-band transitions. The situation improves when approaching the NIR regime where the dielectric function flattens out. It is worth mentioning that the exact value of $\varepsilon(\omega)$ also depends on the preparation method and growth conditions. In our fabrication, commercially obtained ZnPc is purified twice by gradient sublimation and evaporated on a Si wafer for reference measurements as well as on the pre-structured antenna substrates in a high-vacuum multi-chamber system operating at a base pressure of 10^{-8} mbar. The deposition proceeds at an evaporation rate of 10-15 Å per minute controlled by quartz crystal balance until a film thickness of 30 nm, in most experiments, is reached. To avoid parasitic leakage currents, a shadow mask is used to deposit the organic material only on the relevant areas of the sample. Wojdyła *et al.* also prepare thin films via vapor deposition of α-phase ZnPc, however, with increased thickness (220 nm) [230]. While their values are a good approximation we note that generalized ellipsometry [229] of ZnPc would be needed to obtain the full tensorial dielectric function which has not been reported yet in literature. FDTD simulations of plasmonic nanoantennas embedded in a ZnPc film using the isotropic 2-Lorentz-model are shown and discussed in Sec. 6.3, in view of the deviations in the real part of $\varepsilon(\omega)$.

6.2.3 Morphology

A high quality of the Au/ZnPc interface is crucial to avoid parasitic currents and short circuits in OLEA devices. Fig. 6.6 a displays an optical micrograph of a test sample showing an unstructured single-crystalline hexagonal gold platelet on top of a gold electrode structure to provide electrical contact. Towards the right side, a 30 nm thick α-ZnPc film (greenish appearance) is evaporated through a rectangular shadow mask such that it partially overlaps with the gold platelet as well as with the glass substrate. This allows us to study the growth behavior of ZnPc on both materials. Atomic force microscopy (AFM; AIST-NT CombiScope-1000 SPM) is employed to measure the film thickness and surface morphology. Fig. 6.6 c displays topographic scans on glass and on top of the gold flake, parallel to the gold platelet's edge, covering the transition region of areas with and without ZnPc (see AFM topography image, Fig. 6.6 b). Both line profiles confirm the nominal ZnPc film thickness of 30 nm. The AFM image (Fig. 6.6 b) of the interface region (white square in Fig. 6.6 a) shows the well-defined edge of the gold flake and the onset of the ZnPc film as a slight increase in the height values towards the right. The red and the green line indicate the respective linecut positions.

In addition to these topographic overview images, we also investigate the surface morphology of the ZnPc thin films in more detail. Fig. 6.6 d shows the clean surface of the gold platelet which is very flat with a root-mean-square (RMS) roughness as small as 317 pm. The AFM topography of a ZnPc film (Fig. 6.6 e) of the same plot range reveals a granular morphology, evidencing the α-phase of ZnPc [227], with domains

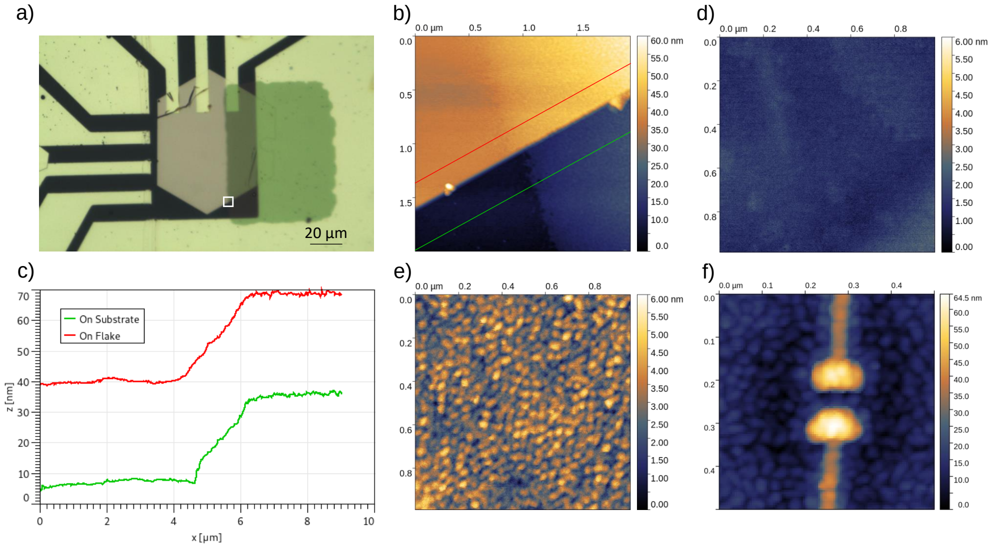

Figure 6.6 – ZnPc thin film characterization. a) Optical image of a single-crystalline gold platelet on a gold electrode structure. On top, a 30 nm α-ZnPc film (green) is deposited. **b)** Atomic force microscopy (AFM) image of the region indicated by the white square in a), where glass substrate, gold platelet and organic film interface each other. **c)** Height profiles at the glass-gold-ZnPc interface region, along the lines depicted in b) (the line scans exceed the plot range of the AFM image). On both glass substrate (green) and gold flake (red), the nominal ZnPc thickness of 30 nm is confirmed. **d)** AFM image of the pristine surface of a gold platelet (RMS roughness 317 pm). **e** AFM image of region with 30 nm ZnPc film on the same gold platelet (RMS roughness 765 pm). **f)** AFM image of an OLEA antenna system covered with ZnPc. Across the gap, on average, only one ZnPc domain is found. Reprinted with permission from [37]. © 2022 American Chemical Society.

of $\sim$ 50 nm in diameter, yet still with a low RMS roughness of 765 pm, which ensures a high interface quality. As the gap width of OLEA antenna structures approximately equals the domain size, we find the gaps to be filled with only few or even a single ZnPc domain (see Fig. 6.6 f).

6.2.4 Photoluminescence

The optical response of the organic material is a key property for the operation of light-emitting devices. Here we present photoluminescence (PL) measurements on α-phase ZnPc films in Fig. 6.7. A 30 nm film grown on a Si wafer with thermal oxide layer is used for a neat characterization of the PL in the wavelength range of interest above 700 nm (black). We also acquire a spectrum on a completed OLEA structure where the film is supported by a glass substrate. In the latter case a different experimental setup with lower quantum efficiency in the detection of high wavelengths is used. The right shoulder of the spectrum (red) is superimposed by slight etaloning oscillations. Apart from that, both spectra agree very well, featuring a broad maximum around 910 nm, which is a clear signature of the excimer state of the ZnPc α-phase [227].

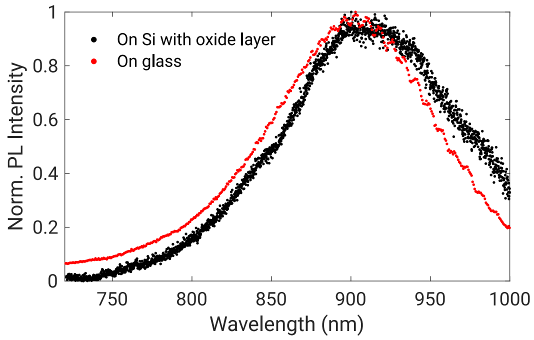

Figure 6.7 – **Photoluminescence of α-ZnPc.** Spectra are taken at room temperature on 30 nm thick ZnPc films on glass (red) and on a Si wafer with thermal oxide layer (black). Reprinted with permission from [37]. © 2022 American Chemical Society.

6.2.5 Electroluminescence of ZnPc with nonresonant gold electrodes: stacked plasmonic OLEDs

The simplest possible plasmonic OLED is a symmetric stack with two electrodes surrounding one active organic film (cf. Fig. 6.8 a). To obtain electroluminescence spectra of the Au/ZnPc/Au-system we fabricate Au/ZnPc/Au stacks with organic layer thickness of 10 nm. The single-crystalline gold microstripes are assembled as shown in Fig. 6.8 b to yield an array of OLED pads which are formed at the positions where two electrode stripes overlap (Fig. 6.8 a). This opens the possibility to apply a voltage to each pad separately.

Applying a voltage of 2.3 V to an exemplary stacked OLED (white rectangle in Fig. 6.8 b) results in electroluminescence (EL) which is distributed over the pad surface and the edges of the gold contacts (cf. Fig. 6.8 c). Clean and flat interfaces (see Sec. 6.2.3) prevent short circuits even for ultrathin devices featuring only 10 nm ZnPc layer thickness. The EL spectrum of the brightest area in Fig. 6.8 c, marked by a red arrow, shows a maximum around 930 nm, as presented in Fig. 6.8 d, hinting at the excimer state of α-ZnPc (see Sec. 6.2.4) as a source. Hence, in the absence of a plasmonic resonance, the emitted electroluminescence spectrum is solely determined by the properties of the organic material.

6.3 OLEA structure design

The device concept is depicted in Fig. 6.9 a. We make use of the well-established concept of single-crystal electrically connected antennas [29, 30, 171] which we fabricate by focused ion beam milling from single-crystal gold platelets [65–67] on glass. Two parallel gold bars of different lengths serve as nanoantennas for light. Their resonances around 800 and 920 nm are chosen such that both of them overlap with the photoluminescence spectrum of the organic semiconductor ZnPc (cf. Sec. 6.2.4) but remain

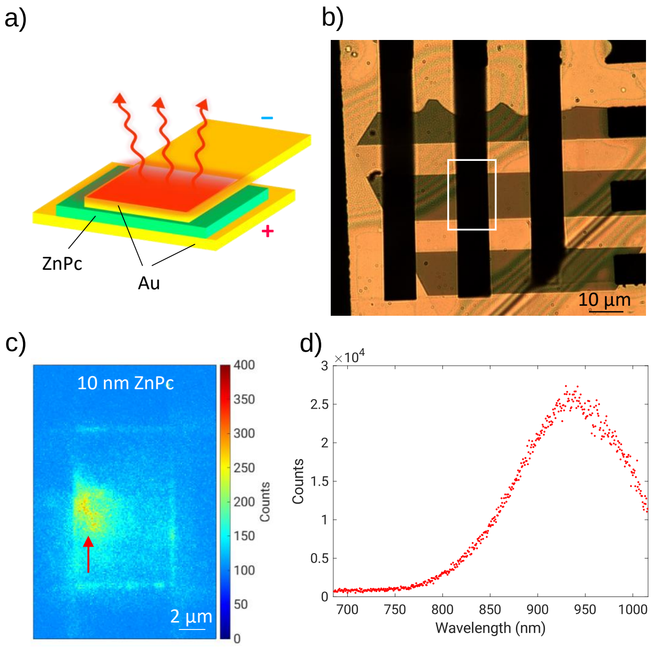

Figure 6.8 – **Stacked plasmonic OLEDs with planar electrodes.** **a)** Schematic sketch of OLED stack with overlapping gold stripes. **b)** Optical microscope image of stacked Au/ZnPc/Au structure with Au bottom and top contacts in dark green and a 10 nm ZnPc film in between. **c)** Electroluminescence in the region indicated by the white rectangle in b) imaged by an EMCCD camera. A bias of 2.3 V is applied between the Au electrodes. **d)** Electroluminescence spectrum recorded at the bright spot marked by the red arrow in c). Reprinted and adapted with permission from [37]. © 2022 American Chemical Society.

sufficiently well separated to provide a distinct spectral signature for each antenna (cf. Fig. 6.9 c). Width and height of the gold bars are fixed to ~ 50 nm.

In order to obtain optimized antenna geometries for the desired resonance wavelengths, we perform FDTD simulations of gold nanorods embedded in an organic film. Using the simplified 2-Lorentz-model for the dielectric function of ZnPc as described in Sec. 6.2.2, the plasmon resonances experience a red-shift compared to the bare antennas on glass substrate. We find a systematic difference between the experimentally obtained red-shift in white-light (WL) scattering measurements and simulated spectra. In simulations spectra of embedded antennas are shifted about 80 nm further towards the red than experimental spectra. The main factor leading to the mismatch is the exact value of $\Re(\varepsilon(\omega))$, which is unknown for our specific film growth and substrate conditions. As an alternative route, to compensate the systematic deviation caused by the simplified dielectric function, we optimize antenna dimensions for resonances red-shifted by additional 80 nm in simulated spectra and find that rod lengths around 110 and 150 nm (cf. SEM micrograph in Fig. 6.9 b) should produce plasmon resonances at 800 and 920 nm in experiments, respectively.

Conversely, to demonstrate the device functionality at the experimentally obtained resonances, it is possible to blue-shift simulated resonances, e. g. by reducing the antenna lengths while keeping the cross-section constant. Thus to achieve simulated

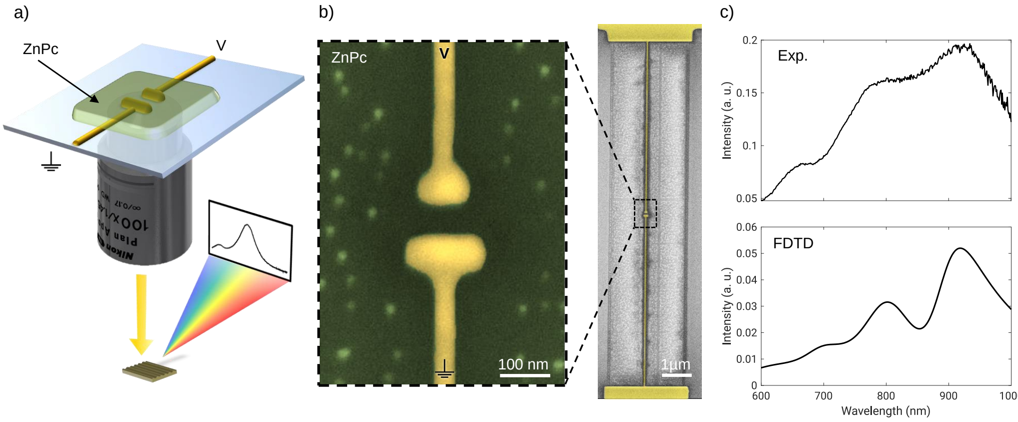

Figure 6.9 – Device layout and scattering spectra. a) Sketch of the setup. **b)** Left: Zoomed SEM micrograph of the electrically connected gold antenna dimer. Right: Overview SEM image showing antennas, connector wires, and electrical contact pads. After evaporation of a ZnPc thin film (30 nm), a DC voltage is applied between the two antennas, as sketched in the left panel. **c)** Upper panel: Acquired WL scattering spectrum of OLEA device (WL setup components see Fig. 5.3 a). The lengths of the plasmonic nanoantennas are approx. 110 and 150 nm. Lower panel: Simulated scattering spectrum of OLEA structure with antenna lengths of 96 and 126 nm, respectively. The lengths have been shortened to compensate the systematic red-shift observed in FDTD simulations. Applying this systematic correction, the resonance positions agree very well. A slight Q-band peak of ZnPc around 680 nm is observed in both experiment and simulation. Reprinted and adapted with permission from [37]. © 2022 American Chemical Society.

resonances around 800 and 920 nm, we used rod lengths of 96 and 126 nm, as compared to fabricated antenna lengths of 110 and 150 nm, respectively. Fig. 6.9 c compares an experimental scattering spectrum of the antenna dimer with these dimensions to a simulated dimer with optimized, shortened lengths. Both spectra show comparable resonance wavelengths. The fact that experimental linewidths are broader than the simulated ones can be attributed to an uncertainty in $\Im(\varepsilon(\omega))$ of ZnPc film and to systematic deviations between the idealized antenna geometry used in simulations and the real antenna geometry obtained in experiments, in particular considering the varying curvature radii of the nanorod ends. It is worth mentioning that the Q-band feature [231, 232] around 680 nm is reproduced in FDTD simulations with ZnPc film, albeit slightly red-shifted. Thus, while the systematic red-shift of simulated antenna spectra has to be accounted for, the FDTD simulations can still be used to design antenna systems embedded in ZnPc quite precisely.

We have varied the distance between the two antennas to make sure that at the chosen distance of 50-60 nm both resonances do not hybridize, i. e., they exhibit negligible resonance shifts. Yet, they still exhibit sufficient coupling to produce directionality effects. ZnPc has been deposited on top of the gold structures as described in Sec. 6.2.2, showing a homogeneous greenish color in optical micrographs (see Sec. 6.2.3). The presence of the metastable crystalline α-phase of ZnPc can be inferred by its distinct excimer dominated PL spectrum (cf. Sec. 6.2.4) as well as its characteristic circular grain morphology (cf. Sec. 6.2.3) [227]. Each horizontal antenna bar is contacted by a thin wire to provide an electrical connection. The thin wires in turn are attached to larger gold pads (cf. Fig. 6.9 b, right panel) that are contacted via micromanipulator needles. The connector wire is attached to the center of the antenna rod to avoid any disturbance of the plasmon modes [29].

6.4 Antenna-selective electroluminescence

When applying a DC voltage between the rods, we observe emission of light as a diffraction-limited spot (cf. Eq. (2.26)) localized at the position of the nanorod pair as demonstrated in Fig. 6.10 a, compatible with an electrically driven subwavelength point source. This holds true regardless of the applied polarity. Astonishingly, we find that instead of a broadband emission representing the sum of the resonances of both antenna rods, the spectrum depends strongly on the polarity of the applied voltage (cf. Fig. 6.10 b). Following the bias definition in Fig. 6.9 a, for negative (positive) voltages, the emission spectrum peaks at 830 nm (910 nm). All spectra have been corrected by the detection efficiency of the experimental setup, whose transfer function includes contributions of all individual components (microscope objective, mirrors, confocal lens, spectrometer mirrors, grating, EMCCD camera) [30].

In the following we study the emission polarization of the device. We fabricate stacked test devices with single-rod antenna as bottom electrode and a planar gold top contact as grounded counter electrode. The ZnPc film in between has again 30 nm thickness. Then the recombination zone is expected to reside between the plasmonic antenna and the non-resonant planar top contact. Applying both $+2$ V and -2 V results in localized light emission from a subdiffraction volume of the antenna region as evidenced by the emission spot images with underlying SEM micrographs in Figs. 6.11 a, c. The second antenna, displaced 1.5 μm towards the upper region in the images, does not affect these experiments. As the measurement in Fig. 6.11 a has been performed after those in Figs. 6.11 b-d, degradation of the device commences which explains the reduced counts in panel a. Hence, absolute intensities cannot be compared. Figs. 6.11 b, d depict polarization resolved WL scattering spectra and EL spectra, acquired with a Wollaston prism, for the two voltage polarities. The longitudinal plasmon resonance with its peak around 790 nm scatters mainly x-polarized photons (light green solid lines) which also determines the emission behavior obtained in EL measurements. At negative bias the degree of x-polarization is very pronounced (dark green dots vs red dots in Fig. 6.11 b). For the positive bias case the polarization selectivity is less pronounced, yet still clearly observable (dark green dots vs red dots in Fig. 6.11 d). In both cases the peak of the EL spectrum carries an influence of the α-ZnPc excimer signature but largely follows the antenna's plasmon resonance, confirming the important role of resonant gold electrodes in OLEA devices. A detailed explanation for this observation is conveyed in the following section.

As hot-electron-induced gold luminescence [233, 234] has been shown to possess fairly low external quantum yields of $\sim 10^{-11}$, this process together with an average antenna enhancement factor around 10 [30] and typical currents of 50 nA (current den-

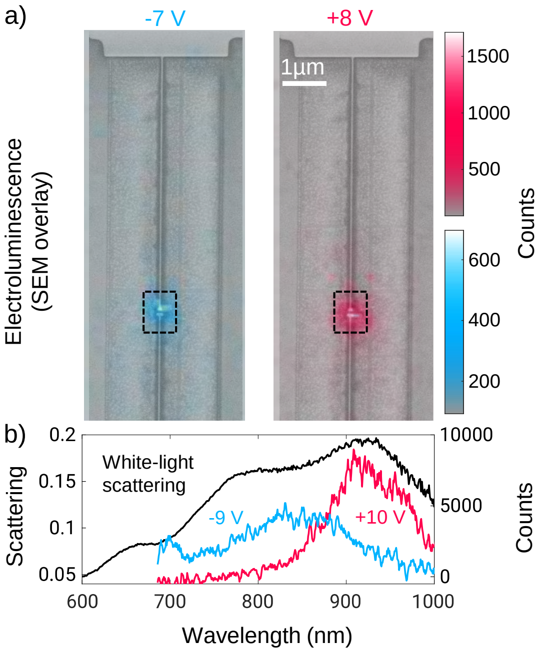

Figure 6.10 – Electroluminescence of OLEA device. a) SEM micrographs with an overlay of emission spots imaged by an EMCCD camera. For both polarities, light is generated from a subdiffraction volume where the antennas are located. **b)** The EL spectra (red line for positive voltage, blue for negative voltage) of the device are related to the peaks observed in WL scattering of the antenna structure (black line, same as in Fig. 6.9 c). Depending on the voltage polarity, the emitted light is governed by the plasmon resonance of either antenna. Reprinted and adapted with permission from [37]. © 2022 American Chemical Society.

sity $\sim 100\,\mathrm{A/cm^2}$) would result in much fewer counts than observed in Fig 6.10 b. Therefore, gold luminescence can be ruled out as the dominating emission process.

6.5 Model for color selectivity

Single-band excimer emission inherent to α-ZnPc cannot lead to the observed phenomena, either. We suggest that the polarity-dependent spectral shift is caused by the fact that ZnPc in connection with gold electrodes behaves as a preferential hole conductor [235]. This behavior can result from either a higher charge carrier mobility for holes than for electrons or by different charge carrier injection barriers for both charge carrier types. For the first case, no comprehensive or reliable data sets, in particular on the electron mobility, are available in the literature.

In Figs. 6.12 a, b (red dots) we plot the current density of OLEA devices as a function of applied external voltage. In general, the obtained current densities exceed those in stacked macroscopic OLEDs with ZnPc as active material by several orders of magnitude. For a rough estimation of the mobility, we model j-V-curves of OLEA devices by assuming trap-free space charge limited currents (SCLC), a Poole-Frenkel-type

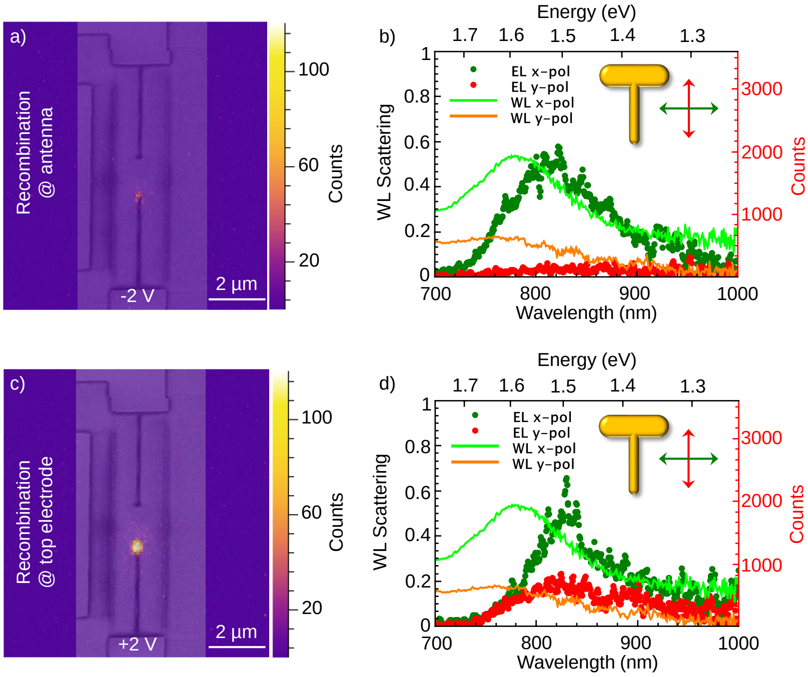

Figure 6.11 – EL from stacked device with planar top electrode and emission polarization. a) SEM micrograph of single-rod bottom electrode, prior to organic evaporation and top contact transfer, with overlay of emission spot image. The applied bias is -2 V. **b)** WL scattering spectra of rod antenna acquired for polarization along the long axis (x-pol, green solid line) and short axis (y-pol, orange solid line), accompanied by EL spectra for the given polarizations (dark green and red dots, respectively). The inset illustrates the antenna orientation together with polarization directions. **c), d)** Same as a) and b) but with $+2$ V applied. Reprinted with permission from [37]. © 2022 American Chemical Society.

field-dependent mobility, and zero built-in voltage (due to identical electrode work functions) [236]. The current density can then be expressed as

$$j_{\mathrm{SCLC}} = \frac{9}{8} \cdot \mu \cdot \varepsilon_0 \varepsilon_r \cdot \frac{V^2}{d^3} \cdot e^{\gamma \sqrt{V/d}} \tag{6.2}$$

with μ the zero-field mobility, ε_0 the vacuum permittivity, $\varepsilon_r = 3.25$ the dielectric constant of ZnPc (at ~ 900 nm wavelength, cf. Fig. 6.5 a), $d = 50$ nm the gap width between the antenna electrodes, and V the applied voltage. γ is a field activation parameter, which we use as second fit parameter besides μ.

Fitting the j-V-curves (blue solid lines in Figs. 6.12 a, b) results in zero-field mobilities on the order of 10^{-6} to 10^{-5} cm^2/Vs, in agreement with a previous study where CuPc, a metal phthalocyanine compound showing identical crystal structure, polymorphs as well as absorption characteristics, has been used as active layer [236]. We therefore assume similar charge carrier mobilities for ZnPc as for CuPc. For the latter material, the mobility for electrons has proven similar or even higher than that for holes [236]. Again it should be emphasized that this is a coarse estimation. In another OLEA structure a zero-field mobility of almost 10^{-4} cm^2/Vs was found, which repro-

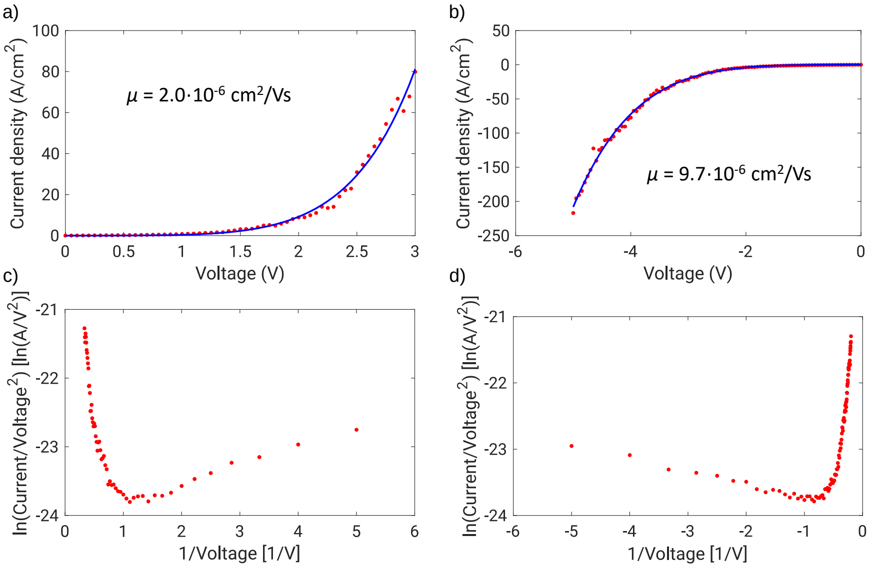

Figure 6.12 – Current-voltage characteristics. a) Current density as a function of voltage for positive applied bias. Measured data are depicted by red dots. A fit according to Eq. (6.2) is included as blue solid line and the obtained zero-field mobility μ is given. **b)** Current density vs voltage for negative applied bias. **c), d)** FN representation of the measured data in a) and b), respectively. Reprinted and adapted with permission from [37]. © 2022 American Chemical Society.

ducibly demonstrates low mobility values, characteristic for incoherent hopping transport [45]. Figs. 6.12 c, d display FN representations of the acquired j-V-curves. For both bias polarities two branches of opposing slope are observed. The steep branches mark the regime of FN tunneling. Since we mostly observe reasonable light emission at these elevated voltages we conclude that the charge carrier injection into the ZnPc film is mainly established by field emission. The two branches meet at transition voltages of about 1 V. Below the transition voltage, the charge carriers undergo thermionic emission from the electrodes.

Concerning the observed emission color selectivity, we therefore exclude mobility and propose charge carrier selective injection barriers to be the main reason. This scenario is supported by the respective energy levels of the gold metal work function and the ZnPc HOMO and LUMO energies in Fig. 6.13, that shows the energetics at the junction under zero bias. As the nanoantennas are structured from single-crystal Au platelets exhibiting a (111) surface, the work function of the low-index (111) facet is expected to be the prominent one. For this facet, a work function of 5.33 eV is reported in the literature [237] which together with an interface dipole of 0.76 eV observed by Gao and Kahn at the Au(111)/ZnPc boundary [238] yields a hole injection barrier of about 0.71 eV and an electron injection barrier of about 1.23 eV. For the ZnPc layer, an ionization energy of 5.28 eV and an electronic band gap of about 1.94 eV are assumed [238].

Under nonzero bias, this means that after passing their injection barrier at the anode, holes can propagate across the entire ZnPc layer without radiative charge carrier

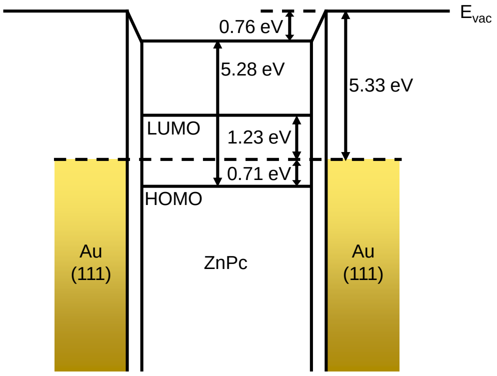

Figure 6.13 – Energy diagram of a Au/ZnPc/Au junction under zero bias. Various energy levels are labeled and taken from the literature as described in the text. Inspired from [37]. © 2022 American Chemical Society.

recombination processes until they reach the proximity of the opposite electrode as visualized in Fig. 6.14 a. At the cathode, electrons are injected at a much lower efficiency across the higher Schottky barrier either by field-induced FN tunneling, supported by the additional local field component generated by the piled-up holes, or thermionic emission. As a general observation, the value of the applied voltage exceeds the energy of emitted photons. We attribute this drop-off to the Schottky barriers and interface dipoles, in conjunction with a formation of local space charges near the contact interfaces owing to the low carrier mobilities. We do not observe systematic spectral shifts with varying the bias between $|2\,\mathrm{V}|$ and $|10\,\mathrm{V}|$. Since the electrode material is identical for both electrodes, the only effect induced by a reversed voltage is the shift of the exciton recombination zone toward the opposing antenna and thus the coupling to the respective plasmonic resonance. Fig. 6.14 b depicts the schematic band diagrams for the nonzero bias scenarios. Excitons are only formed close to the cathode after injection. Due to the proximity of the plasmonic antenna, the excitonic decay is enhanced within the bandwidth of the corresponding resonance leading to the excitation of antenna plasmons that efficiently decay into photons.

In order to analyze a possible quenching behavior of radiative recombinations near the antenna surface, FDTD simulations with dipole sources ($\mathrm{IQE} = 1$) in varying distances to the antenna are performed, as sketched in Fig. 6.15 a. Asymmetric placement of the source w. r. t. the geometry is necessary to excite the fundamental modes (see also Sec. 6.7.2). Closed transmission boxes around dipole source and antenna rods record the total radiated power P_{rad} and absorbed power P_{abs} according to Eq. (2.9). Fig. 6.15 b shows the resulting quantum efficiency $P_{\mathrm{rad}}/(P_{\mathrm{rad}}+P_{\mathrm{abs}})$ (see also Eq. (3.22)) for dipole moments oriented along the x- and y-direction.

At very small separations from the gold antenna surface the quantum efficiency reduces to $\sim 75\,\%$ as an effect of increased nonradiative coupling (“quenching”), indicating that the radiative decay channel still dominates over nonradiative dissipation for both dipole orientations. At separations of 6 nm the quantum efficiency approaches 100 %. This suggests that even molecular layers closely located to the antenna rods contribute to the observed EL. The corresponding emission spectrum should therefore

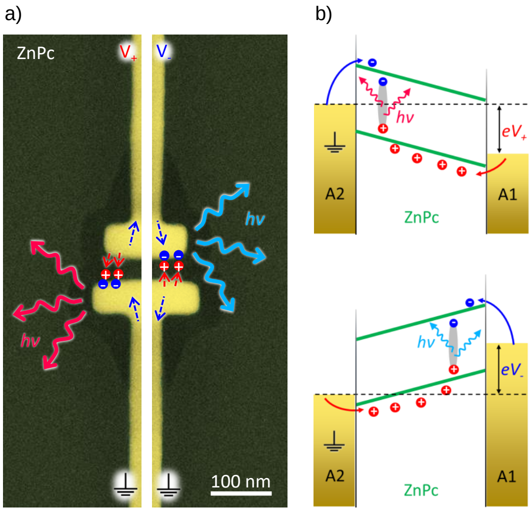

Figure 6.14 – Model of polarity-dependent recombination zones. a) Illustration of site-selective charge carrier recombination and corresponding antenna-enhanced light emission for positive (left panel) and negative (right panel) applied voltage to the upper antenna. Here, as ZnPc behaves as a preferential hole conductor, the recombination occurs at the cathode, i. e., the negatively charged antenna, which dictates the EL spectrum. **b)** Schematic simplified energy diagram of the Au/ZnPc/Au junction under applied bias V illustrating the hole conduction. A1 and A2 represent the upper and lower antenna, respectively. Reprinted and adapted with permission from [37]. © 2022 American Chemical Society.

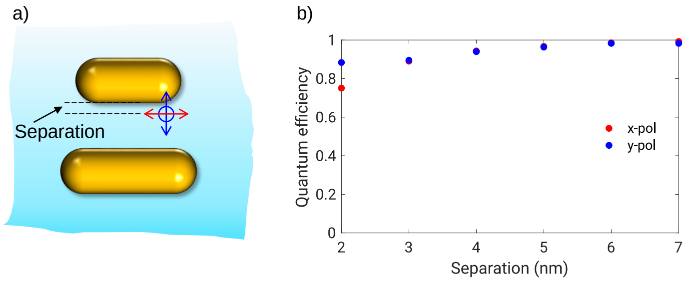

Figure 6.15 – Quantum efficiency of a source dipole near the antenna. a) Sketch of the simulated geometry. The x- (red) and y-polarized (blue) source dipoles are placed near the end of the shorter nanorod with varying separation distance. **b)** Quantum efficiency vs separation for the two dipole orientations. Reprinted and adapted with permission from [37]. © 2022 American Chemical Society.

be the product of the scattering resonance of the cathode antenna and the neat ZnPc emission spectrum.

To support this hypothesis and deepen the understanding of exciton-plasmon coupling, we analyze the experimentally obtained WL scattering spectrum of the antenna pair covered with ZnPc by fitting two independent Gaussians–the resonances of the two antennas. This reveals antenna resonances at around 800 and 920 nm as sketched in Fig. 6.16 b and as predicted by FDTD simulations with systematic corrections (cf.

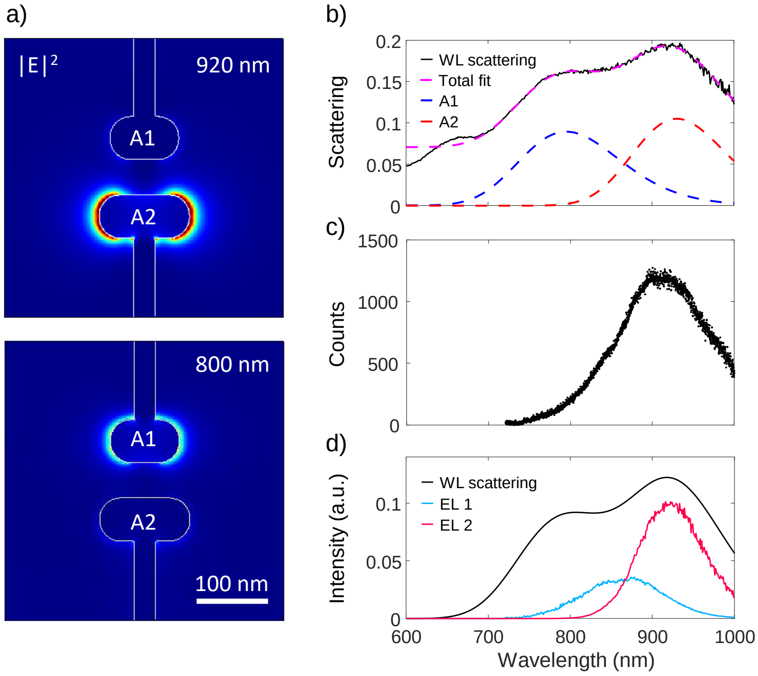

Figure 6.16 – **Model of polarity-dependent emission color.** **a)** Simulated near-field intensity distributions for the antenna resonances around 920 and 800 nm. Spatially selective field hotspots on the top antenna (A1) and the bottom antenna (A2) depending on the wavelength are observed. **b)** WL scattering spectrum of the device (black; same as in Fig. 6.9 c). A fit function (magenta dashed curve) composed of two Gauss oscillators (red and blue dashed curves) is used to fit the scattering spectrum from 689 to 1000 nm. **c)** PL spectrum of a 30 nm α-ZnPc film evaporated on a Si wafer with a thermal oxide layer measured at room temperature (same as in Fig. 6.7). **d)** The multiplication of the ZnPc PL spectrum in c) with the Gaussian peaks in b) gives rise to the EL 1 and EL 2 spectra, representing the expected electroluminescence. They agree well with the measured spectra shown in Fig. 6.10 b, indicating the coupling of excitonic recombinations to the fundamental plasmon resonance of the antennas. Reprinted and adapted with permission from [37]. © 2022 American Chemical Society.

Sec. 6.3). The leftmost peak of the white-light scattering spectrum at 680 nm is related to the ZnPc Q-band and, due to its mismatch with the nanoantenna resonances, is excluded from the fitting procedure [231, 232]. The corresponding near-field intensity distributions of the two antenna resonances are displayed in Fig. 6.16 a and illustrate that for 800 nm (920 nm) the mode is clearly localized on the upper (lower) antenna, only. In Secs. 6.2.4 and 6.2.5 it was demonstrated that PL and EL of neat α-phase ZnPc show a very similar spectral fingerprint. Because of the higher data quality we use the PL data (cf. Fig. 6.16 c) for the current model. This spectrum is then multiplied with the two Gaussian distributions representing the resonances of the antennas. The resulting EL model spectra are presented in Fig. 6.16 d and match the experimentally obtained spectra in Fig. 6.10 b very well, supporting the idea of controlling the position of the charge carrier recombination zone within the device.

6.6 Color switching and external quantum efficiency

Now it is possible to deliberately control the emission color via the sign of the applied bias. Indeed, we observe that switching the polarity leads to a reproducible switching of the emission spectrum, as seen in Fig. 6.17 a, perfectly in line with the color selectivity model. It must be mentioned that the current density and emission intensity are subject to some fluctuations over time during the acquisition of a single spectrum. All in all, we observe currents ranging from about 5 nA to about 140 nA. Typical fluctuations within a single spectrum are on the order of 10-20 nA. There are also systematic variations in the current density and we visualize the current vs time exemplarily for the 4^{th} to the 12^{th} switching cycle in Fig. 6.17 b. Some of the remaining j-t-curves were cutoff by the current limit imposed by the sourcemeter, so they are less meaningful and not shown here. Directly after switching to negative bias we observe a low current density which first grows moderately over time and then more abruptly after 10-20 s, whereas the j-t-curves at positive bias show a less deterministic and more noisy behavior. The underlying physical process of the current evolution at negative bias could be an activation of the charge carrier transport process within the organic after polarity reversal, in conjunction with a depletion of filled trap states. Yet, the spectral position of the emitted light turns out to be more reliable, especially in the first 12 switching cycles. It is worth emphasizing that the devices studied here have prototype character and lack an encapsulation as well as other engineering steps to promote stability. Some improvements are added to the fabrication and setup, such as He-ion beam milling of the antenna electrodes and a continuous nitrogen stream during electro-optical measurements to avoid oxidation of the sample. The spectra in Fig. 6.17 a are integrated over 60 s (spectra 13 and 14 over 10 s) and normalized to highlight the switching behavior.

Notably, the switching effect diminishes with an increasing number of cycles, here found after 12 measurements. A possible explanation is provided by degradation of the Au/ZnPc contact interfaces upon heat generation due to high current densities of about 10-100 $\mathrm{A/cm^2}$ in the OLEA devices under operation. These current densities are more than 3 orders of magnitude higher compared to the corresponding large-area OLEDs based on ZnPc [227]. The pronounced contact resistances then likely lead to a significant temperature rise in these regions (as high as 250 °C [227]) and, as a result, to thermally induced changes in the morphology of the organic ZnPc layer as well as of the nanoantenna contact interface, supported by the occurrence of β-ZnPc emission at 780 nm in spectra 14 and 15 of Fig. 6.17 a, i. e., prior to irreversible failure of the device. Before and after the switching measurements, the WL scattering spectra of the device resemble each other very well (cf. Fig. 6.17 a black curves), indicating that the antenna electrodes are still intact.

For each switching cycle we evaluate the maximum external quantum efficiency as described in [30]. The detection efficiency-corrected EL spectrum with highest intensity is integrated to yield the number of photons/s. The simultaneously recorded external current is used to reconstruct the number of input electrons/s. The obtained ratios are provided in Fig. 6.17 c. Red and blue dots indicate the sign of the applied voltage as positive and negative, respectively. Most cycles show EQEs on the order of 10^{-6}.

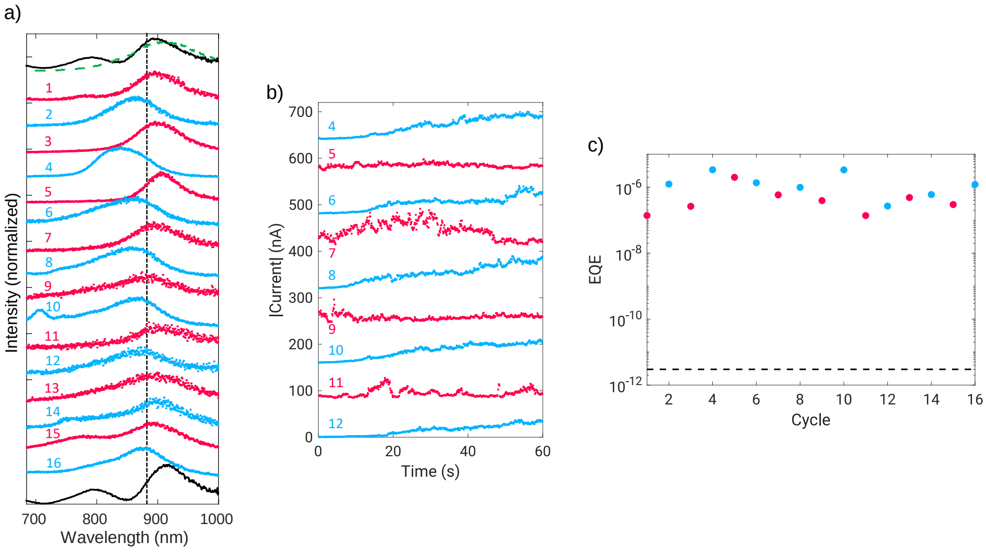

Figure 6.17 – Switching between colors, temporal evolution of electrical current, and external quantum efficiency of OLEA device. **a)** Multiple switching of the emission (red for positive and blue for negative applied voltages) with chronological order from top to bottom, scattering spectra before (black, top) and after (black, bottom) EL as well as the PL spectrum of the ZnPc layer (green top, same as in Fig. 6.16 c). **b)** Absolute value of current vs time for cycles 4-12. An incremental offset is added to enhance visibility. **c)** External quantum efficiency (EQE) for each cycle with red dots corresponding to positive and blue dots corresponding to negative applied voltage, respectively. The horizontal dashed line indicates the expected EQE for stacked macroscopic OLEDs with ZnPc as active material. Panel a) and c) reprinted and adapted with permission from [37]. © 2022 American Chemical Society.

As the excimeric nature of the excited state in an α-ZnPc aggregate renders it prone to nonradiative decay due to a change in the intermolecular geometry, the fluorescence yield is low compared to other organic compounds [239, 240]. Thus, commonly stacked OLEDs based on α-ZnPc thin films are expected to show very low quantum yields on the order of 10^{-12} as estimated from previously published data [227]. Complying with the simulations in Sec. 3.4, the EQEs observed in our devices corroborate the important role of the increased local density of photonic states and the resulting emission enhancement caused by the resonant plasmonic nanoantennas and eventually the potential of the demonstrated OLEA concept.

6.7 Far-field characteristics of OLEA devices

A further important effect of the relocation of the recombination zone by polarity switching are changes in the angular emission pattern. While the antenna electrode resonances do not hybridize, their distance is short enough for the antenna electrode directly driven by exciton recombination to also drive the opposing passive antenna electrode. According to the analysis performed in Chap. 5 the coherent superposition of both antenna emissions will typically lead to a directed radiation pattern similar to that of a Yagi-Uda antenna [171], with the additional feature that active and passive elements can be interchanged by changing the polarity. Although the underlying antenna system of the OLEA devices is not optimized to maximize these effects, changes in the light directionality can be expected as the applied polarity is switched. In this section it is also investigated how an additional passive element, a gold top reflector, modifies the far-field angular characteristics.

6.7.1 Measured radiation patterns

In experiments, the angular radiation pattern can be obtained by back-focal plane imaging of the emitted electroluminescence [30]. Fig. 6.18 a provides an exemplary top view of an array of OLEA devices prior to ZnPc deposition, here with single antennas spaced 2 µm, with their lateral arrangement. The antenna electrodes appear as small red dots in the optical reflection image. A schematic sketch of this conventional geometry is given in Fig. 6.18 b. When measuring the emission patterns of 50 nm spaced double-antenna devices (same sample as in Figs. 6.9, 6.10), effects of parasitic light sources from the setup's environment are observed as plotted in Figs. 6.18 c, d. Therefore, we apply the following background correction to the raw data.

After acquiring the angular emission patterns for both polarities we set the applied voltage to zero and measure the radiation pattern again, with the same exposure time of the EMCCD camera. The obtained parasitic contribution is depicted in Fig. 6.18 e. All the background light is found below the critical angle of the air-glass interface of the sample, which is indicated by the inner white dashed circle in the emission patterns. The OLEA emission, instead, is restricted to high angles up to the limit set by the numerical aperture of the microscope objective ($NA = 1.45$, i. e. $\theta_{\max} = 72.5°$, outer white dashed circle, cf. also Fig. 4.3). This allows subtracting the background light without perturbing the OLEA emission characteristics and the following discussion.

The corrected radiation patterns are plotted in Figs. 6.18 f, g. Light emission mostly beyond the critical angle of total internal reflection is observed, as expected for laterally arranged active and passive antenna elements (cf. also Fig. 5.12) [30, 171]. A pronounced directionality change is perceived upon changing the polarity compatible with the model of switching the roles of active and passive elements in the device. The reflector-feed system established when applying a negative bias (cf. also Fig. 6.14 a) outperforms the feed-director system formed by a positive bias (cf. *ibid.*) in terms of directional emission. The latter appears to be a less optimized Yagi-Uda archetype regarding antenna dimensions and interparticle spacing. This could be mitigated by geometric variations of the antenna system which would, however, also change other key figures, e. g., the spectral overlap between α-ZnPc excimer and antenna resonances, or simply by adding further isolated passive elements.

The second OLEA design considered here includes a monocrystalline gold stripe used as reflector. Via a mechanical dry transfer process the stripe is pressed from a polydimethylsiloxane (PDMS) film onto the OLEA structure and the PDMS is removed. An exemplary top-view image of the resulting stack is given in Fig. 6.18 h.

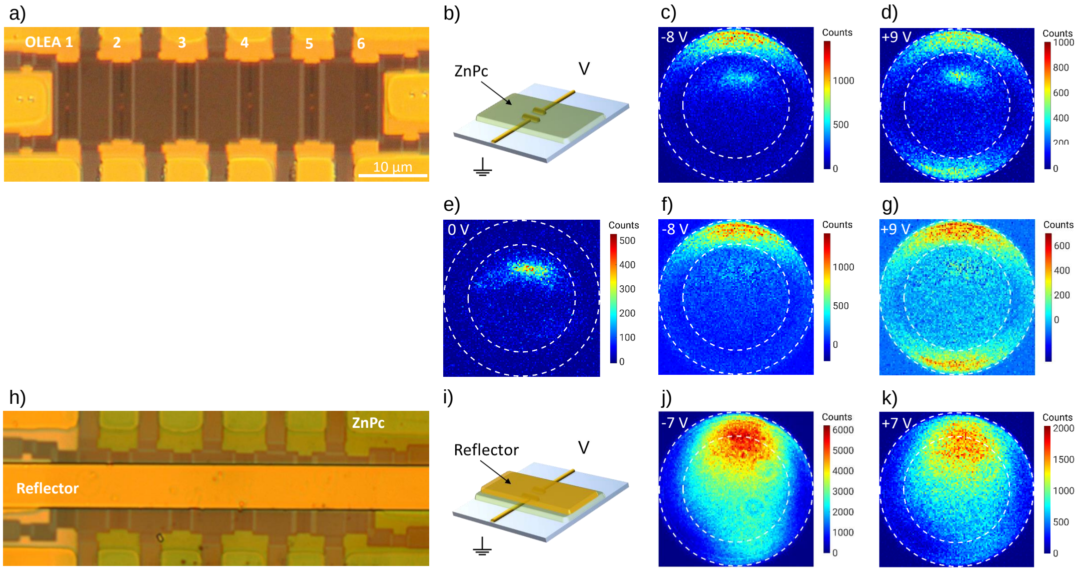

Figure 6.18 – Radiation patterns of the device and reflector. **a)** Six exemplary 2-µm-distance single-antenna OLEA structures that are visible as pairs of small sred dots (reflection image, 100×). **b)** Sketch of a conventional OLEA with 30 nm ZnPc and raw experimental radiation pattern for **c)** negative and **d)** positive applied voltages (exposure time 60 s). The radiation patterns show a clear dependency on the bias. Some parasitic background light at elevation angles below the critical angle of the air-glass interface (inner white dashed circle) is also visible. The outer white dashed circle denotes the maximum collection angle of the microscope objective ($NA = 1.45$). **e)** Parasitic light recorded separately under zero bias and otherwise equal conditions. **f), g)** Subtraction yields the background-corrected radiations patterns. **h)** Stacked geometry realized by placing a thin monocrystalline gold stripe (“reflector”) on top of the OLEA structures. **i)** Schematic side view of the configuration and experimental radiation pattern for **j)** negative and **k)** positive applied voltages (exposure time 5 s). The two patterns are more similar in this case, showing emission close to and below the critical angle of the air-glass interface, and are an order of magnitude higher in intensity. Reprinted and adapted with permission from [37]. © 2022 American Chemical Society.

The ZnPc film is again recognized by its green color. The entire stack is schematically shown in a side view in Fig. 6.18 i. With such a top reflector it is possible to redirect the emission toward the substrate direction (cf. Figs. 6.18 j, k). The gold layer effectively adds additional out-of-plane passive elements due to image dipole effects. Now a significant portion of the emitted photons leave the device below the critical angle. Yet, the directionality change with switching the polarity becomes hardly visible for this configuration. Only a single forward lobe with broad beam angle is obtained in both polarity settings. No parasitic light is present in these radiation patterns such that a correction is not needed here.

6.7.2 Simulated radiation patterns

FDTD simulations are carried out to evaluate the angular distribution of the emitted light in the two geometries introduced in Figs. 6.18 b, i. An electric dipole source placed in regions of electric field hotspots mimics radiatively recombining excitons close to the plasmonic nanoantennas. The source polarization is parallel to the direction of charge carrier transport, i. e. perpendicular to the antenna axis. A field monitor inside the glass substrate parallel to the substrate allows computing the emission angles into the glass halfspace according to Sec. 4.4.1. For these simulations we neglect the connector wires because they do not influence the plasmonic modes on the antenna rods.

In Fig. 6.16 a it can be seen that electric field hotspots are distributed at the ends of the nanoantennas rather than in the central region. Thus, to excite the OLEA structure, it is necessary to place the dipole source in an asymmetric position w. r. t. the physical geometry, as sketched in Figs. 6.19 a-d on the left side. Such a simulation setup gives rise to asymmetric emission patterns, i. e. the main lobes are rotated azimuthally. In all measurements, however, quite symmetric far-field emissions are recorded, indicating that radiative recombinations take place at both antenna ends equally. In order to reproduce the experimental case, we mirror the simulated emission pattern along the vertical axis, as if a second simulation with dipole source on the opposing antenna end had been run, and average over the two patterns.

The results without top reflector are displayed on the right side of Figs. 6.19 a, b. Symmetric far-field distributions with a forward directionality into high aperture angles are obtained for exciting both the shorter and the longer antenna selectively. In case a, the longer antenna is the passive element, acting as a reflector, if the Yagi-Uda language from Chap. 5 is applied. The unidirectional emission for negative bias (Fig. 6.18 f) is in excellent agreement with the FDTD simulation. In case b, the shorter antenna is passive and forward-directs the light. In this case the directionality is less pronounced. Hence, the less directive case for positive bias (Fig. 6.18 g) is also qualitatively reproduced by simulation despite small quantitative differences in the directionality. Possible effects causing the deviations may stem from the intrinsic anisotropy of the evaporated ZnPc film which is not accounted for in the FDTD model. Nonetheless, this further corroborates our model of a relocation of the recombination zone.

Next, FDTD simulations of OLEA devices covered with a top reflector are discussed. The additional metallic layer produces image dipoles above the antenna structures, leading to a substantial change in the emission direction. Now the photons are sent mainly along low aperture angles, i. e. more into the substrate direction than in the absence of the top reflector. Contrary to the gold film encountered in experiments the top reflector is approximated by a perfect metal boundary condition in the simulations in order to keep the problem manageable in terms of memory and computation time. Owing to the perfectly conducting boundary the electromagnetic fields do not penetrate the material, i. e., the image dipoles do not experience a phase shift as opposed to those in a gold film and no surface plasmon polariton (SPP) modes form at the boundary, which alters the total radiation characteristics. Therefore, in Figs. 6.19 c, d the emission maximum is located at a lower elevation angle than in experimental radiation

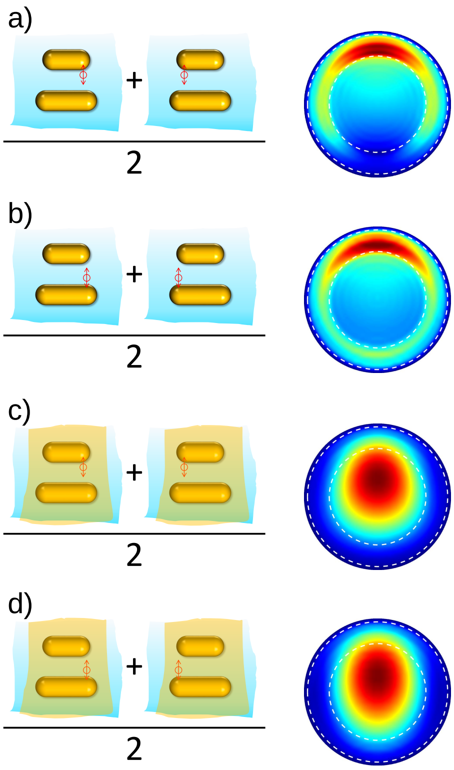

Figure 6.19 – Simulated radiation patterns of OLEA devices. a) Left: Simulated geometry of standard OLEA with nanorods embedded in ZnPc (not shown) on glass substrate including the dipole source at a field hotspot close to the upper antenna. To obtain a symmetric emission pattern for asymmetric simulation setups, the simulated data is mirrored by the vertical axis and averaged to mimic the superposition of both hotspot contributions. Connector wires are neglected. Right: Resulting radiation pattern. The two white dashed circles have the same meaning as in Fig. 6.18. **b)** Left: Same as in a), but with the source residing at field hotspots near the lower antenna. **c)** Same as in a), but including the gold top reflector (implemented as metal boundary condition). **d)** Same as in b), but including the gold top reflector. Reprinted and adapted with permission from [37]. © 2022 American Chemical Society.

patterns (Figs. 6.18 j, k). Compared to the neat planar OLEA device discussed above, here the polarity has less impact on the directivity of the light emission and manifests a similar emission direction for exciting both shorter and longer antenna, in agreement with measurements.

Finally, it can be seen that the asymmetry caused by the dipole position is less pronounced in the case of covered OLEA structures. Therefore, non-symmetrized radiation patterns are presented in Figs. 6.20 a, b for exciting the upper and lower antenna, respectively. Interestingly, a very similar azimuthal offset is found in experiments (Figs. 6.18 j, k). The underlying asymmetry may be caused by different recombination rates at left and right ends of the nanoantennas and this disequilibrium is transferred to the radiation characteristics of the OLEA device.

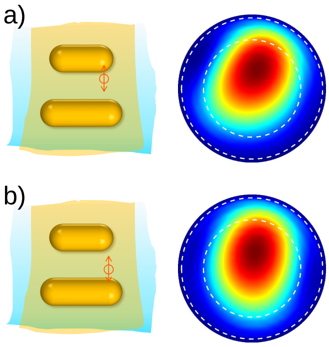

Figure 6.20 – Simulated radiation patterns of covered OLEA devices with asymmetric dipole source. **a)** Left: Simulated geometry including the dipole source at a field hotspot close to the upper antenna. Right: Resulting radiation pattern. **b)** Same as in a), but with the source residing at a field hotspot near the lower antenna. Reprinted with permission from [37]. © 2022 American Chemical Society.

6.8 Concluding and prospective remarks

In summary, a new concept of nanoscale OLEDs was introduced. Their main component are resonant plasmonic electrodes that act as antennas and control the device emission properties. The resulting OLEA devices are assembled in a lateral geometry on a highly transparent substrate as opposed to conventional stacked multilayer OLEDs. Because of their subdiffraction size, the structures presented here act as optical point sources. By switching the sign of the applied voltage, the recombination zone can be shifted toward a specific antenna due to a difference in charge carrier injection efficiency into the ZnPc film. This allows to spectrally shape and switch the emitted light according to the resonance of the respective antenna in the vicinity of the recombination zone. Moreover, the close proximity of several nanoantennas gives rise to directional light emission whose angular distribution can therefore also be switched. Coupling of the exciton recombination to the antenna electrodes in the devices is therefore evident because of the observed spectral shaping, the increased external quantum efficiency, and the observed directional emission of the OLEA devices.

The electrically connected plasmonic antenna system presented here can also be used to study the coherence between spatially separate excitonic recombinations. Considering the near-field distributions displayed in Fig. 6.16 a, each antenna electrode with its longitudinal resonance features two distinct regions of enhanced near-fields, namely at the rod ends, separated by a zero-field region around the rod center. In order to overcome the asymmetry when placing a dipole source in a field hotspot for far-field simulations, intensities must be added up without phase information as illustrated in Fig. 6.19. This procedure yielded azimuthally symmetric radiation patterns complying with the experimental findings. Thus one can conclude that the excitons in OLEA devices recombine and couple incoherently at both antenna ends. On the other hand, FDTD simulations offer the possibility to include two dipole sources with fixed phase relation at the opposing ends of one nanorod. This scenario corresponds to a coherent radiative recombination of excitons. Preliminary simulations suggest, that the resulting angular emission pattern critically depends on the phase shift between the source dipoles: The main lobe moves in the azimuthal direction as an effect of the phase-dependent interference behavior. Also the wavelength plays a role here. This means that the information of a fixed phase relation between recombination events can be encoded in the angular radiation pattern. Hence, the antenna system employed in OLEA devices may serve as an interesting platform for coherence studies.

As another prospect, the stability of charge carrier paths and subsequent light emission could be increased by reducing the gap between the antenna electrodes. This is not a straightforward task because significant near-field coupling between the plasmon resonances would occur when the rods are approached towards each other. Then the near-field of a hybridized mode is not restricted to a single particle anymore, hampering the switching ability. One idea to advance the design is the implementation of extrusions at one end of each nanorod and placing the rods asymmetrically as sketched in the inset of Fig. 6.21 a. Then the shortest path for the charge carriers is oriented along the diagonal gap and the recombination of excitons is expected close to either extrusion, depending on the sign of the applied bias. We plot the simulated scattering spectrum of an antenna dimer with a diagonal gap of 20 nm and extrusion depth 15 nm in Fig. 6.21 a. The system is embedded in a ZnPc layer. In general, the extrusion causes a red-shift of the particle resonance compared to the bare rod geometry. Two distinct scattering peaks are observed in the spectrum. It appears that a Fano-like interaction takes place and forms the dip at 1000 nm wavelength. Fig. 6.21 b visualizes near-field intensity distributions at the two resonance wavelengths, demonstrating near-field maxima predominantly localized on either antenna, which suggests the possibility to switch the light emission wavelength in such a design. One must keep in mind, however, that the ultra-precise fabrication of such extrusions requires a helium-ion microscope and a sophisticated milling recipe.

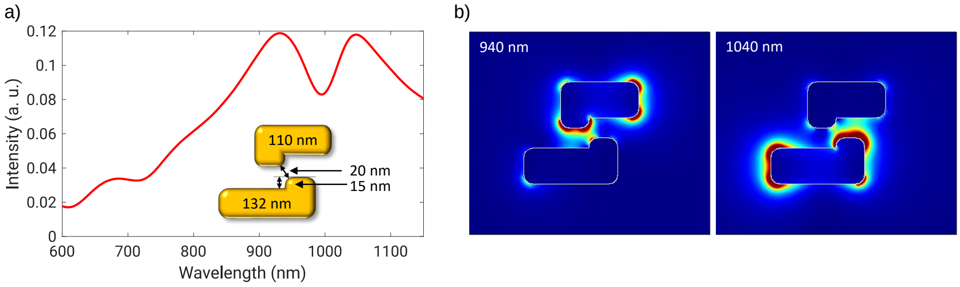

Figure 6.21 – Simulation of an antenna dimer with extrusions. a) Scattering spectrum of the dimer. The arrangement of the particles is sketched in the inset and the rods are labeled with the lengths. Width and height are fixed to 50 nm. The dimensions of gap and extrusions are also indicated. **b)** Near-field intensity distributions at the peak wavelengths 940 and 1040 nm. An embedding ZnPc layer is taken into account.

In the future, organic materials covering the blue and green visible wavelength regime, encompassing phosphorescent emitters [241, 242] and thermally activated delayed fluorescence (TADF) molecules [243–245] are appealing candidates with high internal quantum yields to be employed in OLEA devices. The former rely on a transition metal complex, often Pt or Ir [246], to enhance intersystem crossing and light emission from triplet states via strong spin-orbit coupling. The latter incorporate a small energetic difference between singlet and triplet levels. This is accomplished by spatially separating donor and acceptor units onto different molecular moieties with sterically twisted planes, giving the S_1 state a CT character [244]. Hence, the thermal energy of the surrounding can be exploited for reverse intersystem crossing at room temperature. These molecular species can be combined with silver nanoantennas to obtain resonances at shorter wavelengths with increased efficiency.

Again, the numerical simulation framework enables accurate modeling of the optical behavior of such devices if experimental details like particle shape and material properties are known. In particular, the optical properties of organic compounds play a delicate role and need to be implemented carefully. Generalized ellipsometry provides a means to evaluate the complex dielectric function of crystal samples with low symmetry [229]. Alternatively, as carried out in this chapter, a suitable simplification of the rich optical response may be attained within a certain spectral range, whose ramifications on the simulation results, however, must be explored and compared to experimental data.

Stability and external quantum efficiency of OLEA devices will benefit from suited engineering as was demonstrated for common state-of-the-art OLED pixels [46]. In particular, device encapsulation will suppress exposure to oxygen and humidity of the organic and thus, prolong the active material's lifetime to technologically relevant time spans. Likewise, suitable doping or preparation of self-assembled monolayers at the interface will lead to reduced Schottky barriers between the metal workfunction and the transport levels of the organic compound [238, 247], opening the possibility to lower the current densities in the antenna gap, in conjunction with decreased local heat generation. Thereby, this proof-of-concept work opens new perspectives for the design of ultracompact reconfigurable organic light emitting devices, e. g., for advanced display applications with highest pixel densities.

7

Local driving of plasmonic nanoantenna systems using generalized coherent perfect absorption (gCPA)

Plasmonic nanoantennas, after their local excitation by radiative recombination of excitons, have been employed as light outcouplers in the context of OLEA structures in the last chapter. As an alternative route, plasmonic waveguides can couple light out of quantum well LEDs [205]. Their cross section mimics the shape of an antenna and thus mediates the electroluminescence of the device in terms of polarization and emission direction. Via engineering of the cross section Huang *et al.* addressed several antenna modes [205]. Using a pure waveguide architecture, however, hampers efficient far-field coupling due to the high reflectivity at its termination and concomitant propagation losses further damp the plasmon mode.

In order to facilitate a broad deployment of lossy SPPs in nanocircuitry it is desirable to couple them efficiently to other forms of energy such as heat (e. g. for heat induced recording, local thermal therapy, nano-chemistry and other applications [53, 248]) or radiation. A key step would be the controlled feeding of an SPP into a plasmonic nanoresonator, constituting a purely near-field mediated local driving mechanism of a nanoantenna. Inspired from classical transmission line theory, a necessary condition for efficient feeding is perfect impedance matching between feed line and the actual antenna that acts as a load within the circuit [48]. With a perfectly matched load all energy is transmitted there, whereas the reflection back into the transmission line is turned to zero. Impedance concepts have been examined for optical antennas and quantum emitters alike, and a Green tensor approach has been formulated [6, 50, 249, 250]. Nevertheless, decent impedance matching in the realm of plasmonic nanocircuitry is an ongoing challenge because of the mismatch between the wavelength of guided plasmons and free-space waves [114]. It has been studied mainly by means of extensive numerical simulation efforts [51]. Gratifyingly, the concept of coherent perfect absorbers offers a way to rethink impedance matching in a more formal and more analytic framework. A generalization of coherent perfect absorption (CPA), here denoted as gCPA, allows an elegant semi-analytical approach towards perfect impedance matching of nanoantennas that exhibit both radiative and nonradiative dissipation channels and thereby towards optimized antenna driving. Eventually, gCPA enables strong far-field radiation or local heat generation, depending on the chosen nanorod resonance, under perfect impedance matching from the initial condition of guiding a surface plasmon on a nanowire.

Perfect absorption of selected frequencies of coherent light is a special condition that can occur in systems that scatter light and possess lossy resonances. Such CPA is based on complete destructive interference of all outgoing modes and corresponds to the time-reversed process of lasing at threshold [52, 251–255]. At the CPA condition incoming modes are completely absorbed by the system and completely converted to other forms of energy, usually heat. Naturally, CPA occurs at Fabry-Pérot resonances of the lossy resonator. This is because the multiple reflections which accompany such resonances can lead to perfect destructive interference between the first reflected wave and all subsequent outgoing waves. This requires matching both total phase and amplitude. Technically, a CPA condition corresponds to a zero eigenvalue of the scattering matrix (S-matrix) associated with phase singularities located on the emitted mode's dispersion characteristic in the complex wave vector plane, as shown below.

Being lossy is a rather natural property of plasmonic systems, which are therefore well suited to exhibit CPA. Indeed, CPA has previously been proposed or observed in systems combining localized plasmonic resonators with photonic modes in dielectrics or free space [256–264]. Compared to dielectric Fabry-Pérot-type resonators originally used for CPA, plasmonic resonators, i. e., optical antennas, exhibit much more flexibility because they offer resonances whose properties can be tailored to exhibit e. g. superradiant or subradiant characteristics (cf. Sec. 3.3.2). In any case, radiative losses cannot be ignored and even for subradiant modes they contribute significantly to the overall losses of such an antenna w. r. t. the driving guided modes. Yet, in the original concept of CPA, radiation losses are usually neglected.

In this chapter we show that the concept of CPA, which requires at least one eigenvalue of the complete scattering matrix to vanish, can be generalized to situations where this applies only to a submatrix. As a simple, yet insightful example, we consider a semi-infinite single-mode gold plasmonic nanowire which is coupled to a single gold nanorod antenna via a gap. Here, at least one zero eigenvalue of the scattering matrix is required only for the guided wire mode, while the infinite number of radiative modes of the nanorod is treated as losses. By doing so, we sacrifice the instructive, but practically not very relevant correspondence of CPA to the time-reversed version of lasing at threshold. On the other hand, gCPA can now be applied to any resonant absorber with both radiative and nonradiative loss channels, possibly including the absorption of light by quantum emitters.

Recently, Sweeney and Stone reported a generalized theory of reflectionless scattering modes (RSM) [254, 255], which allows for reaching zero reflection of the selected input modes by evaluating the eigenvalue of the corresponding subset of the scattering matrix. The reradiation from the system can be considered as one of the complementary output channels. While the RSM theory may also be applied to address resonators with radiative loss, the gCPA presented in this chapter is developed independently to address the coupling of a guided subwavelength surface plasmon mode to an optical nanoantenna via transfer matrices. To further corroborate the outcome of the transfer matrix approach we complement it by showing that a power series ansatz, related to the roundtrips in the Fabry-Pérot cavity, yields a mathematically equivalent expression for the total reflectivity of the wire-rod system. After a detailed analysis of the gCPA mechanism, we demonstrate the possibility of background-free sensing using a disturbed gCPA condition and coherent control of the radiation from a nanorod.

Later in the chapter, we invoke more complex antenna designs such as a rod dimer and nanorod chains to be driven locally under gCPA. The chains exhibit a rich variety of extremal reflectivity features found in the complex wave vector plane that can be attributed to collective modes supported by the chain. Choosing alternating gap sizes between adjacent nanorods, the chains represent a classical optical analog of the well known tight-binding Su-Schrieffer-Heeger (SSH) model of the electronic states in a *trans*-polyacetylene chain [265], where topologically nontrivial edge states are predicted to exist at the open boundaries for a particular choice of nearest neighbor hopping strengths. Similar to the tight-binding system, specific plasmonic SSH chains are shown to support localized edge states by analyzing the reflectivity with the gCPA methodology and by simulating optical near-field maps. All in all, our findings establish gCPA as a tool in plasmonic nanocircuitry and nanoantenna design and technology. They additionally pave the road towards conceiving nanoscale analogs of topological matter operating at optical frequencies.

7.1 Concept of generalized coherent perfect absorption

As stated above, far-field radiation has not been considered in dielectric waveguide structures combined with lossy resonators. Under such assumptions, a scattering matrix $\overleftrightarrow{S}$ consisting of the coupling coefficients between the incoming and outgoing guided modes E_{guided} fully captures the modal conversion and energy exchange within and between the resonator and waveguides. However, the situation is different when it comes to plasmonic nanoantennas, where the oscillating surface plasmon leads to radiative decay in addition to the nonradiative loss into heat. In this case, the concept of gCPA would allow us to concentrate on the perfect absorption of the input mode of interest without fulfilling the requirements of CPA for the complete system. As an example, we illustrate the concept of gCPA at the case of a plasmonic nanoantenna driven by two semi-infinite single-mode plasmonic nanowires in Fig. 7.1. The resonator exhibits both Ohmic damping and far-field radiation. The latter can be expressed as a superposition of suitable free-space modes E_{rad}, e. g., plane waves propagating in different directions.

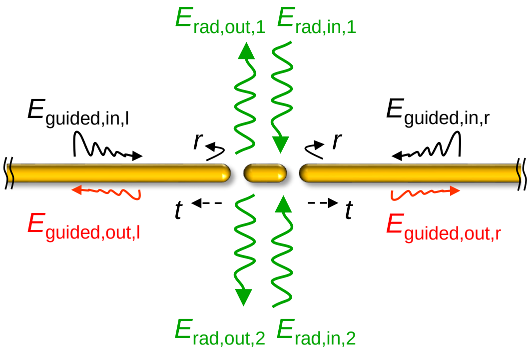

Figure 7.1 – Input and output channels of a symmetric wire-rod-wire system. In general, guided surface plasmons E_guided (red, black) as well as radiative modes E_rad (green) have to be used as incoming and outgoing modes. Within the generalized CPA formalism in this thesis, only the subset of guided surface plasmons is considered as incoming modes. Adapted from [266].

The total scattering matrix $\overleftrightarrow{S}_\text{global}$ of the wire-rod-wire system is defined by

$$\begin{pmatrix} E_\text{guided,out,l} \\ E_\text{guided,out,r} \\ E_\text{rad,out,1} \\ E_\text{rad,out,2} \\ \vdots \end{pmatrix} = \overleftrightarrow{S}_\text{global} \begin{pmatrix} E_\text{guided,in,l} \\ E_\text{guided,in,r} \\ E_\text{rad,in,1} \\ E_\text{rad,in,2} \\ \vdots \end{pmatrix}, \tag{7.1}$$

connecting *all* incoming with *all* outgoing modes. The four coefficients describing the coupling between the guided modes E_guided occupy the upper left corner of the scattering matrix as a two-by-two matrix,

$$\overleftrightarrow{S}_\text{global} = \begin{pmatrix} \begin{bmatrix} r & t \\ t & r \end{bmatrix} & \begin{matrix} c_{l1} & c_{l2} & \cdots \\ c_{r1} & c_{r2} & \cdots \end{matrix} \\ \begin{matrix} c_{1l} & c_{2l} \\ c_{1r} & c_{2r} \\ \vdots & \vdots \end{matrix} & \begin{matrix} d_{11} & d_{12} & \cdots \\ d_{21} & d_{22} & \cdots \\ \vdots & \vdots & \ddots \end{matrix} \end{pmatrix}. \tag{7.2}$$

Here, r and t are the reflection and transmission coefficients of guided surface plasmons at the gap-rod-gap unit, the c_{ij} are coefficients describing the modal coupling between surface plasmons and radiative modes, and the d_{ij} establish the coupling among radiative modes. In this generalized framework, the "complete" CPA would require to find a condition for which an eigenvalue of the *entire* scattering matrix $\overleftrightarrow{S}_\text{global}$ becomes zero. This means *all* outgoing channels, guided modes and radiation, would turn to zero simultaneously. Achieving such complete CPA can be experimentally challenging or even impossible for resonators with radiative loss, such as nanoantennas.

In this thesis, the input and output modes of interest are the left-propagating and right-propagating fundamental guided modes E_guided on a plasmonic nanowire. All other modes are treated as loss channels, including the radiation of the nanoantenna.

The input field vector that is multiplied with the scattering matrix therefore only contains finite values for the top two components in Eq. (7.1). All the other components are set to zero. Now, gCPA requires only finding and zeroing the eigenvalue of the subset of the resulting upper left two-by-two matrix, as marked by the square brackets in Eq. (7.2), which describes the coupling between the guided modes only. Since the major part of the scattering matrix which connects the radiative modes is not considered in the required diagonalization the coupling to radiative modes will in general not be zero, meaning that complete CPA of the whole system is in general not achieved. As we will show in the following, by choosing the nanoantenna to be subradiant or superradiant, the amount of radiation losses can be controlled to a large degree. Generalized CPA, i. e., a vanishing eigenvalue of a submatrix, occurs if the energy from a few incoming guided wire plasmons is entirely converted to other forms of energy, no matter radiative or nonradiative, featuring the zero reflection of the input modes. This provides a practical route to find the condition for perfect impedance matching between plasmonic waveguides and plasmonic nanoantennas in nanocircuitry.

7.2 Electric fields in a wire-rod system

An even simpler nanocircuit with the ability to exhibit gCPA than the one depicted in Fig. 7.1 is a wire-rod system where the rod antenna is fed only from one side with guided plasmons E_{guided}. The wire-rod system is used as a showcase in the first part of the current chapter. Despite its conceptual simplicity, such a circuit incorporates rich physics which will be unveiled by a gCPA analysis in the complex wave vector plane. Prior to analyzing the wire-rod system with mathematical methods we describe the phenomenological behavior of the EM fields in this archetypical nanocircuit.

We consider a semi-infinite gold nanowire with a circular cross section (30 nm diameter) in the vacuum in the near infrared regime (310-440 THz, corresponding to vacuum wavelength 681-967 nm). The wire is terminated by a hemispherical end cap. A gold nanorod with the same diameter and end caps is coupled to the nanowire via a variable gap in the range of a few nm, as sketched in Fig. 7.2 a. Throughout this chapter, the minimum gap width studied is 3 nm. Since these gaps are sufficiently large we neglect quantum effects [267, 268]. Owing to the relatively small wire diameter compared to the vacuum wavelength, the nanowire supports only the fundamental plasmonic TM_0 eigenmode [269, 270], which resembles the highly confined hybrid symmetric SPP in a thin metal film discussed in Sec. 3.2.2. Its transverse mode profile is displayed in the inset of Fig 7.2 a, and in the xz-plane E_z constitutes the dominant field component.

The complex wave number according to Eq. (3.8) is found using the finite-difference frequency-domain (FDFD) method (cf. Sec. 4.3) [140] and further studied in Sec. 7.3.3. As mentioned in Sec. 3.1, the dielectric function of gold is modeled using single-crystal data [68]. The obtained eigenmode is used as a source in three-dimensional FDTD simulations (cf. Sec. 4.2). Taking plasmon reflection at the wire termination into account,

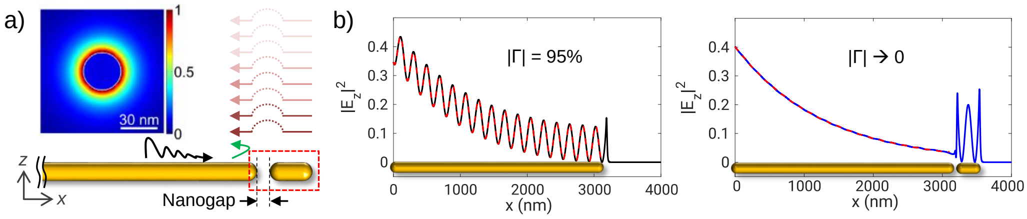

Figure 7.2 – Electric field distribution in wire and wire-rod systems. a) Reflection of the right propagating guided plasmonic mode (black arrow) at the termination of a gold nanowire. The total reflection at the wire termination (red dashed rectangle) is determined by the interference between the directly reflected mode at the gap (green arrow) and a series of coherent transmissions from the mode oscillating on the nanorod (dark red arrows). See Sec. 7.3.1 for details. Inset: modal profile of the guided wire mode. **b)** Simulated standing wave patterns $|E_z|^2$ of the guided wire mode at $\nu = 362\,\mathrm{THz}$ (828 nm) for a termination open to vacuum (left panel, black) and facing a 346 nm nanorod (right panel, blue) via a 5 nm gap. The red dashed lines show the fits of Eq. (7.3) to these standing wave patterns using the complex reflectivity Γ as the only fit parameter. Adapted from [266].

the electric near-field intensity distribution along the semi-infinite wire is [51, 271]

$$|E_z(x)|^2 = |E_{z,0}[e^{ikx} + e^{ik(x_0-x)}\Gamma e^{ikx_0}]|^2, \tag{7.3}$$

where $E_{z,0}$ is the initial amplitude of the mode, x is the spatial coordinate in the propagation direction, x_0 is the distance between the mode source injection point at $x = 0$ and the end of the cylindrical part of the wire at $x = 2985\,\mathrm{nm}$, and Γ is the complex reflection coefficient obtained by fitting the simulated standing wave pattern of the electric near-field intensity 5 nm away from the wire surface with Eq. (7.3). This yields Γ as the only fit parameter. Since the mode reflection is very sensitive to the exact condition of the wire termination [272, 273], the nanorod coupled via the nanosized gap can alter the reflection coefficient and the standing wave pattern drastically. Fig. 7.2 b shows two distinctively different exemplary near-field standing wave patterns corresponding to the absence of a nanorod (left panel) and a specifically chosen rod length (right panel) to be discussed below. In absence of an adjacent nanorod a pronounced standing wave pattern is observed, corresponding to a high reflectivity ($|\Gamma| = 95\,\%$). For a nanorod length of 346 nm, nearly zero reflectivity is observed, accompanied by strong energy localization on the nanorod. The absence of the reflection corresponds to perfect impedance matching between the nanowire (transmission line) and the gap-nanorod termination (load) and suggests an effective scheme to locally drive the nanorod antenna via a single-wire transmission line. In optical nanocircuitry, the characteristic impedance is determined by the electromagnetic fields of the guided mode on the nanowire. The degree of impedance matching, described by the complex reflectivity Γ, can be evaluated by characterizing the standing waves of the optical near-field around the nanowire waveguide termination. Once the characteristic impedance of the guided mode and the reflectivity at a given termination are known (not shown here), the impedance of the load, i. e., the nanoantenna, can be calculated using the complex reflectivity Γ [51].

7.3 Semi-analytical models for the wire-rod reflectivity

In this section we model the wire plasmon reflectivity at a single nanrod attached to a semi-infinite wire via a small gap in two equivalent notations. Both are based on a semi-analytical approach: It is demonstrated that the reflectivity of an attached nanorod can be obtained by only considering reflections at the open end of an infinite wire, propagation along the wire, as well as the reflection and transmission at a gap in an infinite wire. First we present the more intuitive power series ansatz and then move on to a transfer matrix algorithm which is particularly able to treat more complex terminations of the wire in an abstract way. Finally, we compare these model calculations with full FDTD simulations and demonstrate excellent agreement.

7.3.1 Power series ansatz

This ansatz explicitly considers the interference effects of the direct reflection at the nanogap and the fields which are fed back to the wire across the gap after having undergone an infinite number of Fabry-Pérot oscillations on the nanorod [11, 75, 110, 111] as visualized in Fig. 7.3 a. In principle, this builds upon the model introduced in Sec. 3.3.2, where resonances of isolated nanorods were determined. The coherent superposition of the aforementioned contributions result in the total reflection Γ,

$$\Gamma = R_g + \frac{T_g^2}{R_g} \cdot \sum_{k=1}^{n} [R_e R_g e^{2(-\alpha+\mathrm{i}\beta)L_{\mathrm{net}}}]^k. \tag{7.4}$$

Here, R_g and T_g are reflectivity at and transmission across the gap in an infinitely long wire, respectively. R_e denotes the reflectivity at the end of a semi-infinite wire open to vacuum. All these fundamental coefficients also include radiation losses which is essential to find generalized CPA conditions. R_g, T_g, and R_e are determined numerically by FDTD simulations with a mode source and the application of rigorous eigenmode expansion calculations in compliance with Sec. 4.4.2. Simulation domain boundaries are chosen such that the nanowire extends through the PML to mimic a semi-infinite geometry (cf. Sec. 4.2). The required electromagnetic field profiles are recorded at the end of each cylindrical section in the plane perpendicular to the wire axis (see vertical dashed lines in Fig. 7.3 b). This means that the hemispherical end caps are considered part of the gap in the modeling approaches. Nevertheless, we denote a gap size by the width of the air interstice (cf. Fig. 7.3 a).

As mentioned above, the guided TM_0 eigenmode is characterized by its propagation constant β and attenuation constant α. Exemplary values of all these fundamental coefficients are plotted in Sec. 7.3.3. L_{net} is defined as in Sec. 3.3.2, i. e., the net length of the cylindrical part of the nanorod without the hemispherical end caps and n represents the number of oscillation roundtrips on the nanorod. In order to capture all possible roundtrips, we consider the case $n \to \infty$ and simplify the sum in Eq. (7.4), using the limit of the geometric series [274]:

$$\Gamma = R_g + \frac{T_g^2}{R_g} \cdot \left[\frac{1}{1 - R_e R_g e^{2(-\alpha+\mathrm{i}\beta)L_{\mathrm{net}}}} - 1 \right]. \tag{7.5}$$

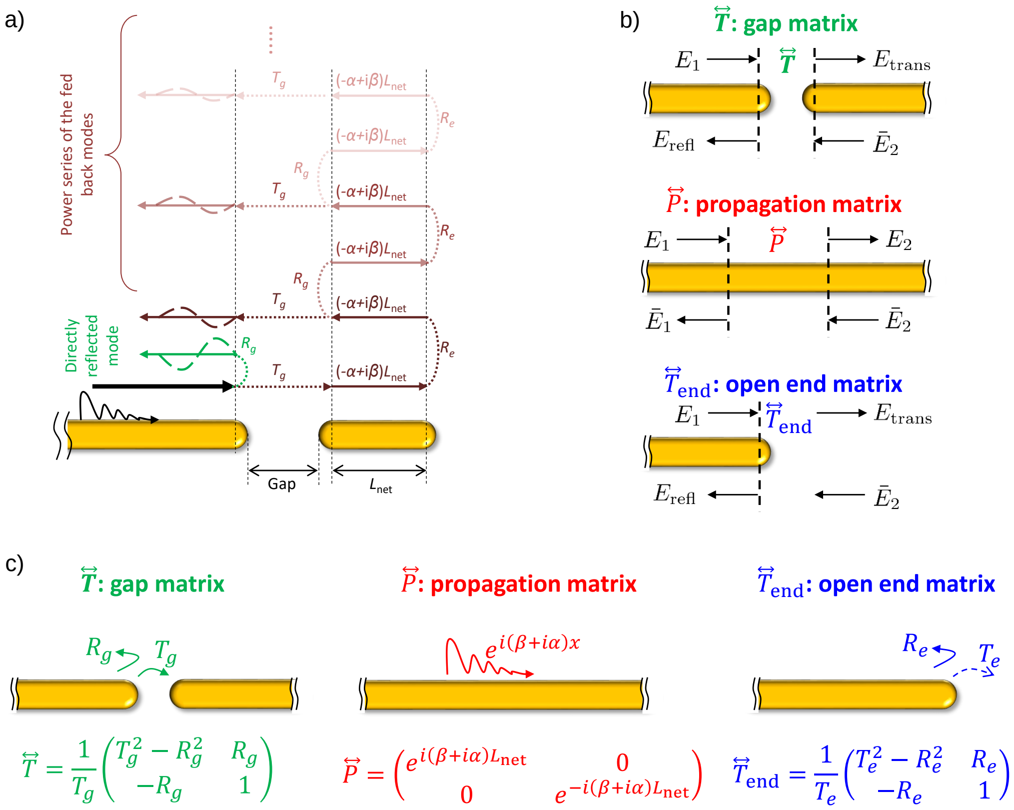

Figure 7.3 – Synopsis of definitions in the power series ansatz and the transfer matrix algorithm. a) Schematic illustration of the interference between the direct reflection and the power series of the fed back modes from the nanorod. **b)** Definition of input and output quantities for the transfer matrices $\overleftrightarrow{T}$ (reflection/transmission at gap), $\overleftrightarrow{P}$ (propagation along cylindrical section), and $\overleftrightarrow{T}_{\text{end}}$ (reflection/transmission at open end). **c)** Schematic illustrations of the gap matrix, propagation matrix, and open end matrix. Adapted from [266].

7.3.2 Transfer matrix algorithm

The second approach summarizes the properties of gap, open end, and regular cylindrical propagation section in transfer matrices [52], connecting the modes left and right of the corresponding object as illustrated in Fig. 7.3 b. As explained above, we choose the subset of incoming and outgoing wire plasmons as basis while radiation into free space is treated as loss mechanism. Then the defining equations of the transfer matrices for a gap ($\overleftrightarrow{T}$), propagation ($\overleftrightarrow{P}$), and open end ($\overleftrightarrow{T}_{\text{end}}$) read

$$\begin{pmatrix} E_{\text{trans}} \\ \bar{E}_2 \end{pmatrix} = \overleftrightarrow{T} \begin{pmatrix} E_1 \\ E_{\text{refl}} \end{pmatrix}, \tag{7.6a}$$

$$\begin{pmatrix} E_2 \\ \bar{E}_2 \end{pmatrix} = \overleftrightarrow{P} \begin{pmatrix} E_1 \\ \bar{E}_1 \end{pmatrix}, \tag{7.6b}$$

$$\begin{pmatrix} E_{\text{trans}} \\ \bar{E}_2 \end{pmatrix} = \overleftrightarrow{T}_{\text{end}} \begin{pmatrix} E_1 \\ E_{\text{refl}} \end{pmatrix}. \tag{7.6c}$$

The elements of the input and output vectors are defined in Fig. 7.3 b. The transfer matrices are written out in terms of the fundamental coefficients in Fig. 7.3 c. In $\overleftrightarrow{T}_{\text{end}}$, the transmission at the open end, T_e, is not well defined since the guided mode does not exist in free space. It turns out that in the total reflectivity Γ this quantity cancels out. The entire gap-rod termination is characterized by the total transfer matrix

$$\overleftrightarrow{M} = \overleftrightarrow{T}_{\text{end}} \overleftrightarrow{P} \overleftrightarrow{T}, \tag{7.7}$$

which connects incoming and reflected fields E_1, E_{refl} on the left side with transmitted fields E_{trans} on the right side of the termination,

$$\begin{pmatrix} E_{\text{trans}} \\ \bar{E}_2 \end{pmatrix} = \begin{pmatrix} M_{11} & M_{12} \\ M_{21} & M_{22} \end{pmatrix} \begin{pmatrix} E_1 \\ E_{\text{refl}} \end{pmatrix}. \tag{7.8}$$

Since we consider a single-channel input from the left side, we have $\bar{E}_2 \equiv 0$. Solving this system of equations yields the complex-valued total reflection

$$\Gamma = \frac{E_{\text{refl}}}{E_1} = -\frac{M_{21}}{M_{22}} = R_g + \frac{T_g^2}{R_g} \cdot \left[\frac{1}{1 - R_e R_g \, e^{2(-\alpha + \mathrm{i}\beta) L_{\text{net}}}} - 1 \right], \tag{7.9}$$

which is equivalent to the result obtained via the power series ansatz (Eq. (7.5)) discussed above. Note, that the overall reflectivity also corresponds to the scattering "submatrix" of the system for the subset of guided modes which is a scalar (Γ corresponds to the entry r from Eq. (7.2)) for the 1D single-mode case considered here.

7.3.3 Fundamental coefficients and comparison to full FDTD simulations

In order to give an overview over some numbers that enter the power series and transfer matrix formula, we plot the numerically obtained fundamental coefficients in Figs. 7.4 a-d. Panel a and b depict the real and imaginary part of the complex wave number of the guided TM$_0$ wire mode. These are equivalent to the propagation constant β and attenuation constant α, respectively, and plotted as a function of frequency. β increases almost linearly with frequency[1], whereas α grows faster than linearly. The significant increase in damping is caused by the optical properties of gold where the interband transition near the green spectral range (cf. Sec. 3.1) is approached and by the fact that the modal fields become stronger localized inside the metal, accompanied by higher losses (cf. Sec. 3.2).

For each frequency point, an (α, β)-pair represents the dispersive characteristic of the mode. By eliminating the explicit frequency dependence, we alter the representation and span the complex wave vector plane with α and β as the two axes. On this plane, the modal relation $\alpha(\beta)$ describes a line as imaged in Fig. 7.4 c, with the frequency as a parameter. It should be mentioned that the complex wave vector plane is a

---

[1] The vacuum light line lies beyond the frequency range plotted in Fig. 7.4 a. For the β-range under consideration, the light line takes on frequency values between 586 THz and 1128 THz.

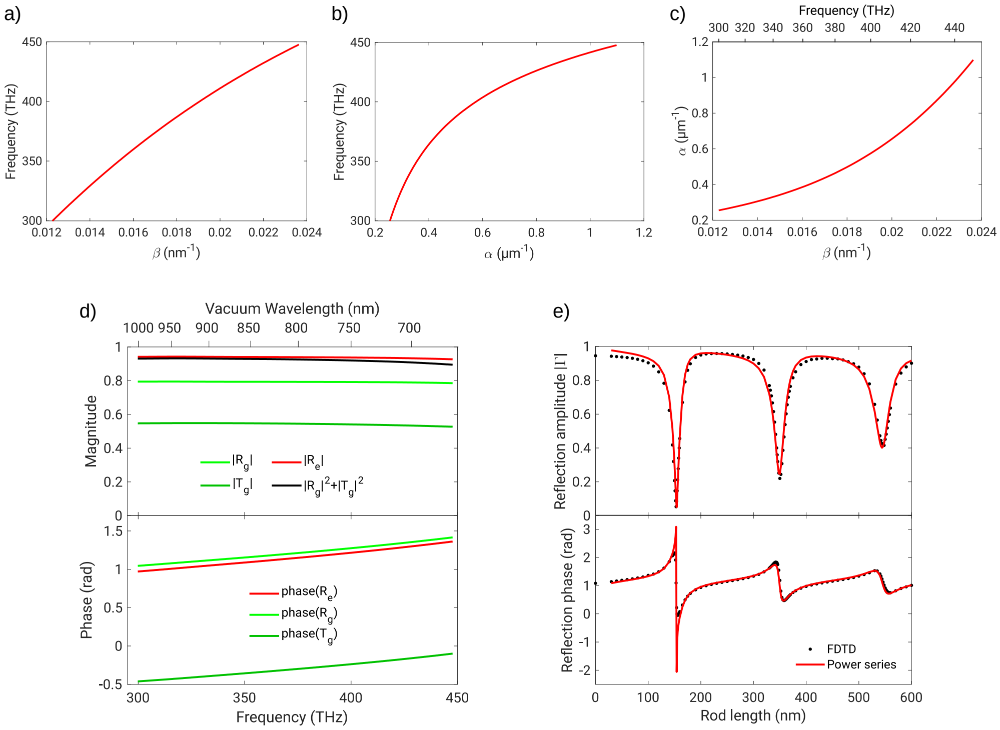

Figure 7.4 – Fundamental coefficients of the semi-analytical models and comparison of calculated and simulated reflectivity. The complex dispersion relation of the TM$_0$ mode is given by **a)** the propagation constant β and **b)** the attenuation constant α as a function of frequency, where $k = \beta + \mathrm{i}\alpha$. **c)** Parametric plot of the TM$_0$ mode within the complex wave vector plane spanned by β and α. Along the modal line (red), the frequency changes implicitly. **d)** Fundamental reflection and transmission coefficients for a fixed gap width of 10 nm as a function of frequency/vacuum wavelength. Upper and lower panel display magnitude and phase, respectively. Open end reflection data is drawn in red, gap reflection and transmission in light and dark green. The sum of reflected and transmitted intensity at the gap is plotted in black. **e)** Reflection amplitude $|\Gamma|$ (upper panel) and phase (lower panel) of the wire-rod system with 10 nm gap at 361 THz (830 nm), for varying rod length. Black data points represent results from full FDTD simulations. Transfer matrix/power series calculations are plotted as red solid line. The pronounced features in Γ are fully captured by the semi-analytic approaches. Panels a), b), c), and e) are adapted from [266].

useful theoretical construct, in which the scattering matrix of a resonating system can be neatly visualized.

The fundamental reflection/transmission coefficients R_g, T_g, and R_e, describing a gap and an open end, respectively, are plotted in Fig. 7.4 d. These quantities depend on the frequency and on the gap size. Here, a 10 nm gap is assumed. It is clearly seen that the open end reflection amplitude exceeds the gap reflection, which is intuitive because the near-fields can only couple back and form a counter-propagating wave. The gap reflection in turn exceeds the transmission across the gap. All magnitudes are almost constant over a large bandwidth and start to decrease slightly around

440 THz. As mentioned above, in our description the two hemispherical end caps belong to the gap. The increasing Ohmic dissipation inside those causes the magnitudes to decrease. Besides Ohmic losses, also radiative losses to the far-field occur at gaps and open ends because these represent discontinuities in the otherwise unperturbed waveguide geometry. This leads to a further reduction of the amplitudes. Note, that along the unperturbed cylindrical sections of nanowire and nanorod, however, the only dissipation mechanism is Ohmic damping, characterized by α. Since the β values of the TM_0 mode lie well below the light line of vacuum, the mode is fully guided and does not have leaky characteristics [275]. Additionally, we show the sum of reflected and transmitted intensity at the gap in Fig. 7.4 d, which should always be smaller than unity in a physically meaningful setting, as a consequence of the two loss channels. The lower panel of Fig. 7.4 d displays the phase values of the fundamental coefficients. In general, we encounter reflection phases close to $\pi/3$ and slightly negative values in transmission. It should be noted that for subnanometer gaps, more sophisticated methods might be needed to obtain R_g, T_g, and R_e under the influence of quantum effects [267, 268]. As along as these fundamental coefficients could be obtained, the formalism presented here would work in the same way.

When inserting the coefficients into Eq. (7.9), the total reflection amplitude and phase of a wire-rod system with arbitrary rod length and gap size at an arbitrary frequency can be computed analytically. In Fig. 7.4 e, we compare a calculation at fixed frequency 361 THz (wavelength 830 nm) and fixed 10 nm gap with varying rod length (red solid line) with full FDTD simulations in the same length range (black dots). Both approaches show excellent agreement in phase and amplitude. Little discrepancies in the amplitude may be attributed to numerical uncertainties in the fundamental coefficients, which stem from a finite thickness of mode expansion monitors in conjunction with the 0.5 nm mesh size. Moreover, very short rod lengths could be prone to mutual interactions between signals at the gap region and at the open end, which is not accounted for in the analytical models. Notably, we identify three subsequent Fabry-Pérot resonances, in the form of minima of $|\Gamma|$ and steep phase jumps, at the rod lengths 154, 349, and 544 nm, corresponding well with the three lowest resonance orders of an isolated nanorod that are found in Fig. 3.9 b. This connection is further discussed in Sec. 7.4 below. The excellent agreement also suggests, that the radiation losses are well included in the simulated coefficients which enter the power series and transfer matrices. Nevertheless, the lowest reflectivity observed here, at the first-order minimum, has a finite amplitude of about 5 %. Also the associated phase jump is quite steep, but still continuous. Thus, gCPA is not yet reached in the chosen wire-rod geometry.

7.4 Analysis of gCPA in the wire-rod system

So far, an algorithm that describes the reflectivity of a wire-rod system has been developed and validated. In this section we apply it to find gCPA conditions and characterize such a perfectly impedance-matched system. Perfect destructive interference, i. e., vanishing reflectivity, requires the directly reflected mode (green arrow in Fig. 7.3 a) and the transmitted mode, consisting of the infinite sum of transmitted waves over the gap (dark red arrows in Fig. 7.3 a), to have opposite phases and equal amplitudes. To accomplish this, the nanorod must provide just the right amount of loss and the gap must be chosen correctly to transmit a just sufficient portion of the mode for each round trip. In this regard, the length-dependent Ohmic losses of the plasmonic waveguide indeed become important and beneficial to enable unidirectional nanoscale gCPA.

Fig. 7.5 a shows the calculated reflectance (squared reflection amplitude, $|\Gamma|^2$) as a function of nanorod length at various frequencies for a fixed gap of 4 nm. Multiple local minima are obtained at different orders of nanorod resonances. Indeed, the second-order minimum reaches zero reflection, i. e., gCPA as we prove below. Interestingly, all the rod lengths for which reflection minima occur coincide with those of solitary nanorods showing a scattering resonance at that wavelength (cf. Sec. 3.3.2) as if the proximity of the nanowire did not perturb the resonance of the nanorod. To elucidate this effect, in Figs. 7.5 b, c we investigate the electric field at the rod termination for two gCPA scenarios based on the first and second order antenna resonances on the nano-rod. In both cases, the phase differences of the electric field across the gap are close to $\pi/2$, as opposed to the bonding and antibonding resonances of a two-wire antenna (cf. Sec. 3.3.3), where the phase jumps of the transverse field over the gap amount to π and zero, respectively. The $\pi/2$ phase shift ensures zero charge accumulation on the wire while the charge density is maximum at the rod ends, resulting in the absence of coupling between rod and feeding wire, i. e., a “nonbonding” condition. In other words, from the perspective of the guided mode on the semi-infinite wire, the wire appears to be infinite throughout. This nonbonding condition is fulfilled for all reflection minima observed in Fig. 7.5 a, including the one where gCPA occurs. The nonbonding condition with appropriate loss offers the necessary phase and amplitude for perfectly destructive interference of the reflected fields.

The small deviation of ideal gap width between calculations and full FDTD simulations (4 nm vs 5 nm), concerning the gCPA state based on the second-order antenna resonance, likely stem from little uncertainties in the numerically determined fundamental coefficients, such as errors introduced by the discretization, detrimental influence from reflections at the PML, or slow decay of energy in the simulation domain in connection with the threshold-based final time of Fourier integrals (cf. Sec. 4.2).

Another interesting feature is that gCPA is not associated with specific resonance orders. For instance, at 440 THz (681 nm) where the attenuation constant α is high, the smallest reflection occurs at the first-order resonance of the nanorod. At 360 THz (833 nm, white dashed line in Fig. 7.5 a), the nanorod’s second-order resonance leads to the lowest reflection intensity. This suggests the flexibility to accomplish gCPA with even and odd resonance orders and thus the possibility to select the dissipation channels, as will be discussed in Sec. 7.5.

To distinguish good absorption (local reflection minima) from gCPA, we investigate the continuity of the reflection phase. Fig. 7.5 d displays the reflectance and the reflection phase at 360 THz as a function of the nanorod length. The first reflectance dip, observed at nanorod length 153 nm, exhibits a narrow Lorentz-like line shape. The corresponding phase transition is steep but still continuous. The second reflection

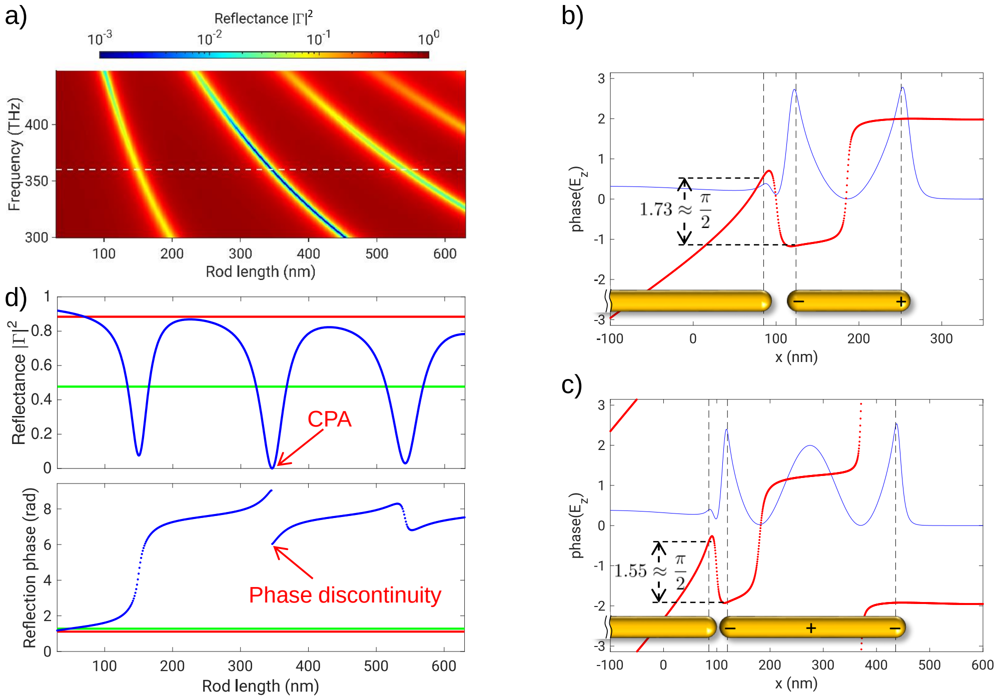

Figure 7.5 – Reflectivity spectra and phase of electric field at the termination. a) Calculated reflectance ($|\Gamma|^2$) as a function of the nanorod length and frequency. The gap is fixed at 4 nm. **b)** Phase of E_z (red dots), recorded 5 nm away from the wire surface for the dipolar resonance on a 157 nm long nanorod separated by a 9 nm gap at 354.5 THz (846 nm). The blue solid line depicts the total field intensity. The symmetry of charges is indicated on the structure outline. **c)** Same as b), but for the second-order antenna resonance on a 346 nm long nanorod separated by a 5 nm gap at 362.2 THz (828 nm). The phase jump across the gap is close to $\pi/2$ in both b) and c). **d)** Reflectance (upper panel) and reflection phase (lower panel) as a function of the nanorod length at 360 THz (833 nm), marked by the white dashed line in a). The red and green horizontal lines mark the reflectance and phase of a termination open to vacuum and a gap in an infinitely long wire, respectively. The CPA state at the second-order reflectance minimum and the phase discontinuity at the corresponding rod length 346 nm are labeled. Adapted from [266].

minimum at a rod length of 346 nm (see also Fig. 7.2 b, right panel) approaches zero, i. e., truly perfect absorption. The corresponding phase changes discontinuously. It is worth emphasizing that this phase jump does not originate from an irrelevant 2π jump. Furthermore, it turns out that the reflectance dips observed here mark a special case of Fano resonances, where the narrow nanorod resonance coherently interferes with the broadband background wave given by the guided TM_0 mode on the wire. By deliberately picking fundamental coefficient values that deviate from the natural set, arbitrary Fano line profiles can be created, yet accompanied by physically meaningless reflectance curves. This is discussed in appendix A.

To prove that we indeed observe a generalized version of CPA and to clarify the aforementioned connection between phase singularity position and guided mode dispersion line, in Fig. 7.6 a we plot the reflectance and reflection phase over the complex wave vector plane [52, 276], which is introduced in Sec. 7.3.3. A similar CPA description using a complex frequency plane has been established in previous reports [252, 277, 278]. For the selected range of frequencies, the reflectivity displays a zero and a pole of its amplitude accompanied by phase singularities in the positive and negative α range, respectively. Along a closed path around a singularity, a total phase of 2π is collected. Now it becomes evident that the phase discontinuity in Fig. 7.5 d is caused by the vortex-like phase singularity which accompanies the zero reflectance of the gCPA state. Further poles and zeros exist for each order of Fabry-Pérot resonances of the nanorod (not visible in Fig. 7.6 a). The plasmonic TM_0 mode dispersion relation is parametrically plotted as a white solid curve (SP mode) into the same complex wave vector plane (see also Fig. 7.4 c). The frequency varies implicitly along this curve. To accomplish vanishing reflection, the phase singularity corresponding to zero reflectivity must reside on this curve describing allowed α and β combinations of the mode [277], such as the case displayed in Fig. 7.6 a. The difference between a local minimum and a truly zero reflection because of gCPA is that true gCPA happens when the phase singularity hits the dispersion curve of the guided mode in the complex wave vector plane. If the phase singularity is close but does not exactly reside on the dispersion curve of the guided mode, the reflectance would merely be a local minimum with a smooth transition of phase. In numerical simulations, a finite reflectance is inevitable due to limited finite mesh size and frequency stepping. In reality, the resolution is limited by the diameter of an atom (the smallest spatial step) and the frequency bandwidth of the source. The narrow bandwidth of the gCPA dip implies that ultrashort pulsed excitation with broad bandwidth is not compatible with gCPA. Upon injecting a source field with broad bandwidth, one would observe a substantial intensity in reflection around the gCPA frequency, i. e. a non-negligible background signal.

By changing the geometry of the termination, such as the gap size and nanorod length, the position of the phase singularities can be moved freely within the complex wave vector plane. Fig. 7.6 b shows the trajectories of the phase singularities of the first-order and second-order resonances of the nanorod upon increasing the gap size and the rod length. While increasing the nanorod length shifts the phase singularities towards lower propagation constant, increasing the gap size mainly moves the singularity towards smaller attenuation constants. Importantly, geometrical changes offer the possibility for a reflection zero and its associated phase singularity to cross the dispersion line of the guided mode, thereby traversing a gCPA state when residing exactly on this line.

The effect of rod length changes can be intuitively understood as a change in the effective Fabry-Pérot resonance wavelength of the rod and thus as a control knob of the phase in the interference pattern of the back-transmitted waves onto the wire. The essential role of the gap, however, has been overlooked so far. During preliminary studies, length scans with fixed gap were performed, yielding low, but nonzero reflection amplitudes and continuous reflection phase profiles (cf. Fig. 7.4 e), thus no gCPA. One crucial and astonishing discovery in this thesis is that the gap width fulfills a task that complements the task of the rod length. The rod length determines the interfering phases, the gap controls the amplitudes of the interfering waves and thereby serves as a

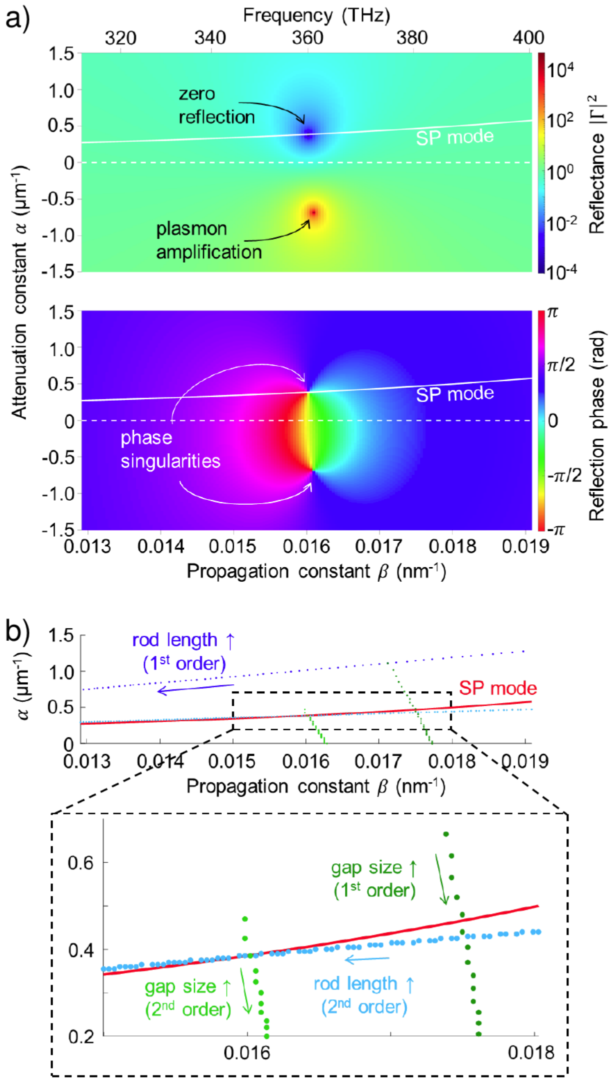

Figure 7.6 – Reflectivity and its dynamics in the complex wave vector plane. a) The reflectance (upper panel) and reflection phase (lower panel) plotted over the complex wave vector plane for a specific terminal condition (rod length 346 nm, gap 4 nm), at which one of the phase singularities hits the dispersion curve of the guided mode (white solid curve, same as red line in Fig. 7.4 c), leading to zero reflection for one specific value of β. β and α are the real and imaginary parts of the wave vector. Negative α represents gain. **b)** Upper panel: trajectories of the reflection phase singularities of the first-order and second-order nanorod resonances upon sweeping the gap size (increment 0.5 nm per dot) and nanorod length (increment 1 nm per dot). Dark blue and dark green dots mark the trajectories of the phase singularity of the first-order resonance upon increasing the rod length (126-187 nm) and gap size (4-19 nm), respectively. Light blue and light green dots mark the trajectories of the phase singularity of the second-order resonance upon sweeping the rod length (290-431 nm) and gap size (3-20 nm), respectively. The red solid curve depicts the dispersion of the guided mode. Lower panel: enlarged plot corresponding to the area marked by the dashed rectangle in the upper panel. Taken from [266].

control knob for the loss. Large gaps exhibit strong reflection and weak transmission, whereas small gaps give rise to the opposite effect. This is why the phase singularity mainly moves along the α-axis in the complex wave vector plane when the gap size is varied. Establishing a gCPA state at a well-defined frequency is only possible if both rod length and gap are carefully tuned and an appropriate guided mode dispersion is available. In this regard, gCPA is a highly sensitive feature, analogous to the triple point of water, at which its three thermodynamic phases coexist in thermal equilibrium, manifested by a unique point in the phase diagram spanned by temperature and pressure [279]. Here in the optical case, an "equilibrium" between loss and feeding is reached. Since gCPA is a single-frequency phenomenon, continuous wave (CW) driving at the gCPA frequency induces an infinite lifetime of the gCPA state. Consequently, perfect balancing between input power on one side, and absorption and radiative losses on the other side is achieved.

Within the experimentally accessible range of geometrical parameters, multiple singularities corresponding to different Fabry-Pérot resonance orders of the nanorod are available. This allows us to rationally design a wire-rod system to accomplish gCPA using super radiant or subradiant nanorod resonances (cf. Sec. 3.3.2), offering the opportunity to choose the dissipation mechanism for the absorbed energy. Thus, the gCPA analysis on the complex wave vector plane serves as a theoretical design tool for perfect impedance matching. The transfer matrix calculations yield fast results and avoid time-consuming numerical parameter sweeps. Another important feature seen in Fig. 7.6 a is the phase singularity point in the lower half of the complex plane, where the attenuation constant α is negative. This phase singularity is associated with a reflectivity pole. For $\alpha < 0$ the guided mode is amplified, suggesting the possibility of surface plasmon amplification by stimulated emission [76, 258, 280].

7.5 Exemplary applications of single-port gCPA

The gCPA approach developed in this thesis offers a broad range of applications. In principle, it can be applied to study the coupling of any guided mode into lossy cavities where the total loss may include radiative channels. In particular, structures consisting of discrete elements are straightforward to treat as they are composed of elementary reflection and transmission events. In the following, we will discuss two applications of gCPA in plasmonic nanocircuitry, (i) driving super- or subradiant nanoantenna modes with perfectly matched impedance and (ii) background-free nanoscale sensing.

Fig. 7.7 a shows the efficiency of radiative and nonradiative losses of a unidirectional gCPA-driven single nanorod in the first and second-order resonance. The same quantities of the open end of a semi-infinite nanowire are also plotted for reference. The data are obtained in FDTD simulations where the Poynting vector is integrated over a transmission box according to Eq. (2.9). The simulation setup is sketched in the inset of Fig. 7.7 a. After subtracting the power flow passing through the red region where the input near-field of the guided mode enters the box, the scattered power is normalized to that input power. According to the symmetry of the currents on the nanorod, the first-order and second-order resonances are superradiant and subradiant, respectively. Therefore, gCPA based on the first-order resonance (rod length 157 nm and gap 9 nm) results in 50 % far-field radiation efficiency, whereas gCPA achieved with the second-order resonance (rod length 346 nm, gap 5 nm) leads to 85 % nonradiative energy dissipation into heat. The freedom to select multiple resonance orders offers the opportunity to control the branching ratio of the absorbed power to either far-field radiation or local absorption at the rod termination.

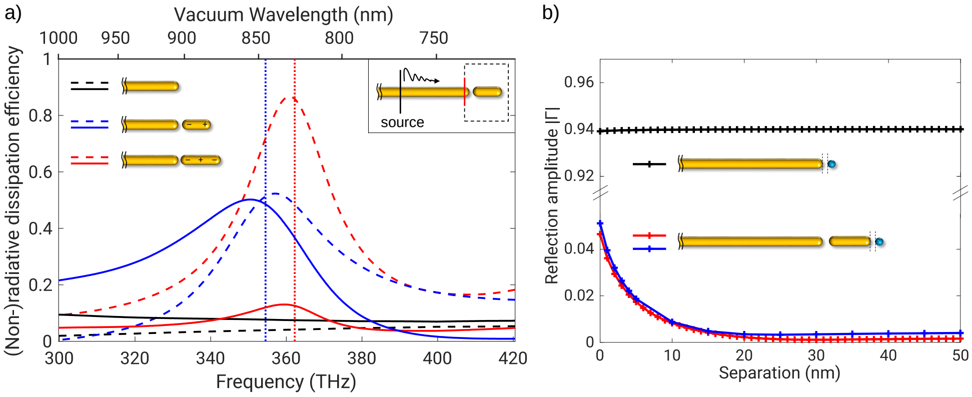

Figure 7.7 – **Selective driving of antenna modes and background-free sensing as applications of gCPA in a wire-rod system. a)** Radiative (solid lines) and nonradiative (dashed lines) dissipation efficiency of a gCPA-driven nanorod at the first-order (blue) and second-order resonances (red). The radiative and nonradiative dissipation efficiencies of the open end of a semi-infinite wire are also plotted for reference (black). The vertical dotted lines indicate the gCPA frequencies for first and second order resonances. The legends in the top left corner include the charge distribution on the nanorods for first-order and second-order resonances. The inset in the top right corner schematically depicts the simulation setup with a transmission box around the termination. **b)** Comparison of the reflection amplitude to a local perturbation (approaching dielectric sphere, diameter 20 nm) of a simple wire sensor (black) compared to a gCPA wire-rod sensor (red: calculation via transfer matrix algorithm; blue: full FDTD simulation). For the latter, a pronounced change in reflection amplitude is observed for separations below 10-20 nm. Adapted from [266].

For sensing applications, we use the subradiant nanorod resonance (rod length 346 nm, gap 5 nm) to achieve gCPA. Tiny perturbations of the nanorod's terminal conditions will shift the phase singularity in the complex k-plane and lead to the destruction of gCPA. As a result, a finite reflection against a completely dark background can be detected with high signal-to-background contrast, similar to the case of dark-field scattering or single-molecule fluorescence detection [281]. Assuming that the major source of noise in an experiment is shot noise, which is proportional to the square root of the signal intensity, the signal-to-noise (S/N) ratio is proportional to the amplitude of the reflection. It should be noted, though, that the amplitude cannot be increased arbitrarily by increasing the input intensity due to local heating of the nanorod. Fig. 7.7 b compares the change of the reflection amplitude upon local perturbations of a wire-rod system with that of a bare single wire probe. A perturbation is introduced by approaching a tiny dielectric glass nanosphere (diameter $= 20$ nm, $n = 1.52$) to the termination (see inset of Fig. 7.7 b).

In order to calculate the total wire-rod reflectivity Γ including the glass sphere, a new set of fundamental coefficients involving the modified open end of a semi-infinite wire, R_e, has to be numerically simulated first, with the technique presented in Secs. 4.4.2 and 7.3. As a matter of fact, this fundamental coefficient exactly describes the performance of a simple wire probe under the presence of the scatterer. Therefore, these data are plotted in black in Fig. 7.7 b and reveal that the reflection amplitude changes hardly, even if the glass nanosphere is moved extremely close to the wire's end cap along the wire axis. Subsequent transfer matrix calculations modeling the wire-rod sensor, plotted in red, indicate a rapid increase of the reflection amplitude as the glass nanosphere approaches the nanorod to a distance less than 20 nm. A pronounced nonlinear increase in the reflection amplitude is obtained when the separation is below 10 nm, showing ultimate sensitivity to perturbations in close vicinity of the probe. The analytically predicted reflectivity increase of the wire-rod sensor is perfectly reproduced by full FDTD simulations, plotted in blue. We conceive that even attachment or detachment of single proteins should be detectable as a notable increase in reflectivity [282–284].

7.6 Two-port gCPA: coherent control of nanoantenna radiation

Two-port CPA using photonic modes with dielectric or plasmonic resonators has been used to demonstrate coherent control of light with light without using nonlinear effects [251, 256, 262, 263]. Guided plasmons on two plasmonic nanowires sandwiching one nanorod resonator can also be used to realize two-port gCPA [285]. Such a system with two identical gaps, sketched in Fig. 7.8 a, leads to the total transfer matrix

$$\overleftrightarrow{M} = \overleftrightarrow{T}\,\overleftrightarrow{P}\,\overleftrightarrow{T}\,. \tag{7.10}$$

Generalizing the concept of two-port CPA according to Sec. 7.1, the subset of incoming and outgoing guided plasmons is investigated. Contrary to the single-port structure, here the scattering matrix is not a scalar anymore. While the transfer matrix is defined via waves left and right of an obstacle as basis vectors (cf. Eqs. (7.6)), the scattering matrix rigorously connects incoming and outgoing waves. Thus the definition of the scattering submatrix connecting the guided plasmon modes in Fig. 7.8 a reads

$$\begin{pmatrix} E_{\mathrm{out,l}} \\ E_{\mathrm{out,r}} \end{pmatrix} = \overleftrightarrow{S} \begin{pmatrix} E_{\mathrm{in,l}} \\ E_{\mathrm{in,r}} \end{pmatrix}. \tag{7.11}$$

After applying some algebraic steps, $\overleftrightarrow{S}$ can be calculated from the entries of the total transfer matrix in Eq. (7.10) via the basis transformation

$$\overleftrightarrow{S} = \begin{pmatrix} S_{11} & S_{12} \\ S_{21} & S_{22} \end{pmatrix} = \begin{pmatrix} -M_{21}/M_{22} & 1/M_{22} \\ M_{11} - M_{12}M_{21}/M_{22} & M_{12}/M_{22} \end{pmatrix}. \tag{7.12}$$

For a two-port excitation of equal intensities and tunable relative phase ϕ_{in}, the input vector reads

$$\begin{pmatrix} E_{\text{in,l}} \\ E_{\text{in,r}} \end{pmatrix} = \begin{pmatrix} 1 \\ e^{\mathrm{i}\phi_{\text{in}}} \end{pmatrix}. \tag{7.13}$$

The output intensity obtained from Eqs. (7.10)-(7.13) is defined as

$$I_{\text{out}} = \frac{|E_{\text{out,l}}|^2 + |E_{\text{out,r}}|^2}{|E_{\text{in,l}}|^2 + |E_{\text{in,r}}|^2} = \frac{|E_{\text{out,l}}|^2 + |E_{\text{out,r}}|^2}{2}. \tag{7.14}$$

Zero eigenvalues of $\overleftrightarrow{S}$, i. e. zero output intensity is found for specific sets of rod length, gap width, and frequency, either for symmetric input ($\phi_{\text{in}} = 0$; eigenvector (1,1)) or antisymmetric input ($\phi_{\text{in}} = \pi$; eigenvector (1,−1)).

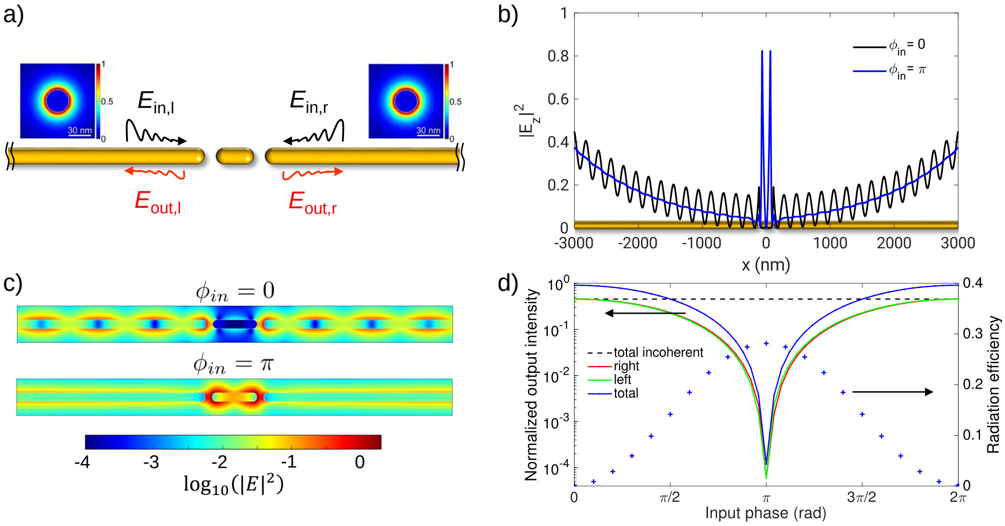

Figure 7.8 – **Two-port gCPA in a wire-rod-wire system.** **a)** Sketch of the symmetric wire-rod-wire system where two-port gCPA is realized, i. e., E_{out} vanishes on both sides. Insets show field distributions of the guided TM_0 mode used for excitation. **b)** Simulated intensity of the main electric field component (E_z) along the structure, 5 nm above the surface of the wire. The black line shows the case of symmetric input ($\phi_{\text{in}} = 0$) with constructive interference of input and output waves. The antisymmetric input case ($\phi_{\text{in}} = \pi$) is plotted as a blue line. The latter yields gCPA on the nanorod and destructive interference along the wires (rod length 154 nm, gap width 23 nm, frequency 361 THz, wavelength 830 nm). **c)** Corresponding maps of the total field intensity in logarithmic color scale. **d)** Calculated normalized output intensities versus relative input phase ϕ_{in} on the left side (green), right side (red) and the sum of both (blue) under coherent input. The simulated radiation efficiency of the nanorod as a function of input phase is plotted with blue plus signs (scale to the right). With an input phase of π, gCPA with output intensities on the wires as low as 10^{-4} is obtained, accompanied by strong far-field radiation from the dipolar mode on the nanorod. The horizontal black dashed line depicts the incoherent sum of the squared transmission amplitudes on left and right side. Taken from [266].

In Fig. 7.8 b, simulated electric field patterns 5 nm above a wire-rod-wire system with rod length 154 nm, gap size 23 nm on both sides at a frequency of 361 THz (wavelength 830 nm) are presented. The z-component field intensity is displayed for symmetric and antisymmetric input. Fig. 7.8 c provides maps of the total electric field intensity in the vicinity of the nanorod. With symmetric input ($\phi_{\mathrm{in}} = 0$), the outgoing waves interfere constructively, leading to a pronounced standing wave along the two wires ("superscattering"). Simultaneously, the fields around the nanorod are highly suppressed. Therefore, the energy can hardly enter the nanorod and the antenna is "off". In contrast, with antisymmetric input ($\phi_{\mathrm{in}} = \pi$), the interference of the transmission and reflection is perfectly destructive, leading to perfect absorption of the input power by the nanorod and highly enhanced field intensity on the nanorod. In this case, the dipole antenna is "turned on" and perfectly driven by the two wires.

The relative input phase ϕ_{in} constitutes an additional degree of freedom within the two-port scheme, compared to the wire-rod system. It is an external parameter that can be adjusted e. g. by interferometric pathways, thereby enabling coherent control of light by light without using any nonlinear effect. Generalized CPA, superscattering, and any absorption state in between these extreme cases can be reached by tuning ϕ_{in}. At gCPA, the output intensity of the wire plasmons defined in Eq. (7.14) can be suppressed by four orders of magnitude, as plotted in Fig. 7.8 d (blue line). Taking merely the incoherent sum of the right and left outgoing signals while disregarding their phases results in a normalized intensity of about 0.45 for the present geometry (black dashed line). In the all-plasmonic system studied here, a further aspect comes into play. Making use of a radiative dipolar antenna mode, the control of the input phase ϕ_{in} allows to coherently control the radiation of the plasmonic nanorod, i. e. to control the emission of a locally plasmon-driven transmitting optical nanoantenna by surface plasmons. Fig. 7.8 d shows the radiation efficiency of the nanorod with varying relative phases. At $\phi_{\mathrm{in}} = 0$, the rod is in an "off" state because no radiation is observed. When ϕ_{in} approaches π, the radiation increases up to 30 % of the overall injected power. As a benefit of coherence in the absorption process, a nonlinear mechanism is not required for such switching and deep modulation.

7.7 Rod dimer antenna driven under gCPA

This section straightforwardly builds on the single-port gCPA analysis developed in Sec. 7.4 by aligning a second nanorod next to the first via a second gap. This system is sketched in Fig. 7.9 a. As the guided wire mode is identical on all particles, the total reflectivity can be directly calculated using the fundamental coefficients and the total transfer matrix

$$\overleftrightarrow{M} = \overleftrightarrow{T}_{\mathrm{end}} \overleftrightarrow{P}_2 \overleftrightarrow{T}_2 \overleftrightarrow{P}_1 \overleftrightarrow{T}_1, \tag{7.15}$$

with the indices denoting the respective rod/gap.

Thereby, the reflectance $|\Gamma|^2$ is computed over the complex wave vector plane, revealing two pole-zero pairs appearing at different β. As in the prior sections, the zeros are found for $\alpha > 0$ while the poles reside in the gain region where $\alpha < 0$. The two pairs are expected because the double rod structure hosts two resonances that have been introduced in Sec. 3.3.3. Indeed, the rod dimer geometries used in Fig. 3.10 have first been determined with a gCPA analysis and later been simulated as isolated dimers in FDTD. This method of analytically determining antenna geometries hosting a certain resonance order at a certain wavelength works much faster than lengthy brute-force parameter sweeps in FDTD simulations, demonstrating the power of the here developed approach. A necessary criterion for employing the analytical framework is that the fundamental coefficients are known.

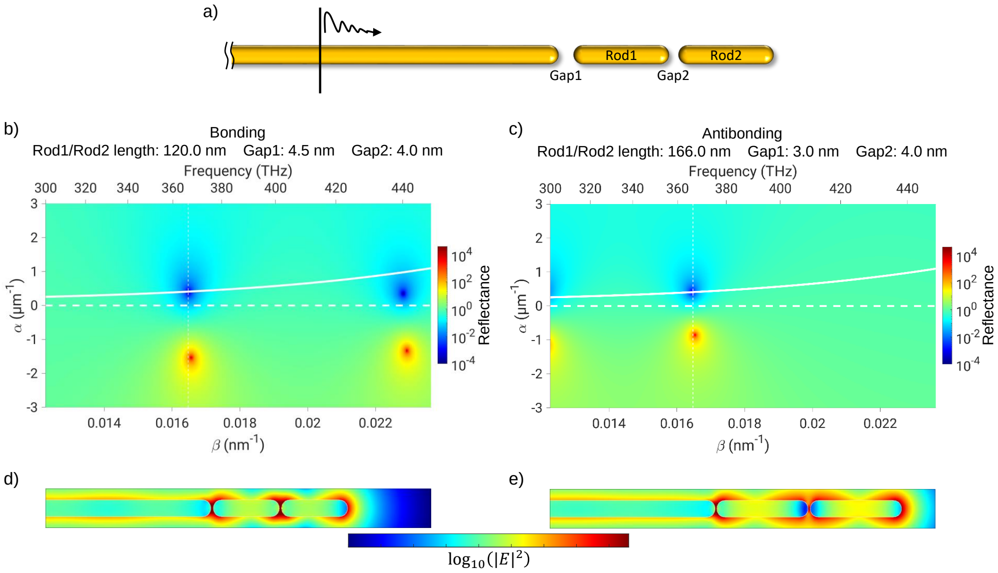

Figure 7.9 – **Wire-rod-rod system and its gCPA states.** **a)** Sketch of the structure with two equally long nanorods and generally distinct gaps. **b)** Reflectance $|\Gamma|^2$ in the complex wave vector plane, where the reflection minimum residing on the dispersion curve of the guided mode (white solid line) corresponds to the bonding resonance of the rod dimer. This gCPA state arises at 366 THz (818 nm). The calculated geometry (rod lengths, gap sizes) is given. **c)** Same as in b), but with the reflectance zero on the guided mode dispersion corresponding to the antibonding resonance of the rod dimer. **d)** Near-field intensity map of the bonding mode driven under gCPA. **e)** Near-field intensity map of the antibonding mode driven under gCPA. Panels d) and e) share the same logarithmic color scale.

Fig. 7.9 b displays the bonding mode of the double rod structure driven under gCPA. Therefore the associated reflectance zero coincides with the guided mode dispersion at 366 THz (818 nm). The reflectance minimum emerging at a higher frequency corresponds to the antibonding mode of the rod dimer. Since it is displaced from the guided mode dispersion line, it does not show gCPA at any frequency. This is a general observation with gCPA being a single-frequency effect. By enlarging the rod length and decreasing the width of the gap between wire and first rod, we move the antibonding mode onto the dispersion curve at 366 THz where it shows gCPA in Fig. 7.9 c. During the geometry change the pole-zero pair of the bonding resonance nearly moved outside of the plot range of the complex k-plane. It is worth mentioning that the gap between wire and first rod ("gap1") controls the loss, i. e. the α value under which the extrema appear, analogous to the gap in the single rod case (cf. Sec. 7.4). The gap width between the nanorods ("gap2"), in turn, controls the distance between the pole-zero pairs along the β-axis in the complex wave vector plane, which is in agreement with the gap dependent splitting strength between bonding and antibonding mode shown in Fig. 3.10.

Near-field intensity maps of these hybrid modes are presented in Figs. 7.9 d, e, confirming the expected field distributions. While the antibonding mode exhibits its highest field intensities at the dimer ends and moderate near-field in the gap region, the bonding mode features an electric field hotspot in the gap and considerable parts of the near-field also penetrate the gold end caps in this region. The hotspot could be harnessed as a platform for enhanced light-matter interaction when a single emitter is placed in the gap of the rod dimer. Moreover, these results once again show that also subradiant antenna modes can be directly addressed by this local near-field driving mechanism via surface plasmons on a nanowire.

7.8 Nanorod chains driven under gCPA: towards topological plasmonic Su-Schrieffer-Heeger chains

Beyond dimer antennas, the gCPA toolbox developed in this thesis allows modeling even more complex plasmonic antenna systems featuring rich modal structures. Here we consider one-dimensional chains whose building blocks are gold nanorods. A configuration with two alternating gap sizes along the chain is of particular interest because it resembles the backbone of *trans*-polyacetylene, the simplest conjugated polymer, with its staggered single and double bonds between adjacent carbon atoms. Both systems are imaged in Fig. 7.10 a. One can identify a unit cell containing two carbon atoms (two gold nanorods) as basis, giving rise to A and B sublattices. The double and single bonds are characterized by the hopping amplitudes t_1 and t_2, where $|t_1| > |t_2|$. These properties are transferred onto the plasmonic chain by choosing a small and a large gap size, resulting in stronger and weaker Coulomb interaction between neighboring nanorods, respectively.

In their seminal work in 1979, Su, Schrieffer, and Heeger predicted the existence of topological solitons on such dimerized polymers, located on the separate A and B sublattices [265]. The tight-binding Su-Schrieffer-Heeger (SSH) model is therefore the simplest showcase where topologically nontrivial modes are expected. Since the latter do not necessitate the non-commutative laws governing quantum mechanics, topology has reached out into various branches of classical physics, such as mechanics [286, 287], acoustic systems [288], photonic metamaterials [289, 290], microwave cavities and networks [291, 292], and electric circuitry [293–296]. Many of these examples rely on equal footing, namely a periodic sample with a boundary or interface across which a topological invariant of the band structure, e. g. the Berry phase [297, 298], changes. Consequently, energy bands cannot be smoothly connected. The band gap closes and reopens during a topological phase transition, in conjunction with the formation of topologically nontrivial edge or interface states which lie energetically in the middle of the band gap. It is worth mentioning that also the SPPs at metal/dielectric interfaces (cf. Sec. 3.2) can be thought of as a special case of topological edge states [299].

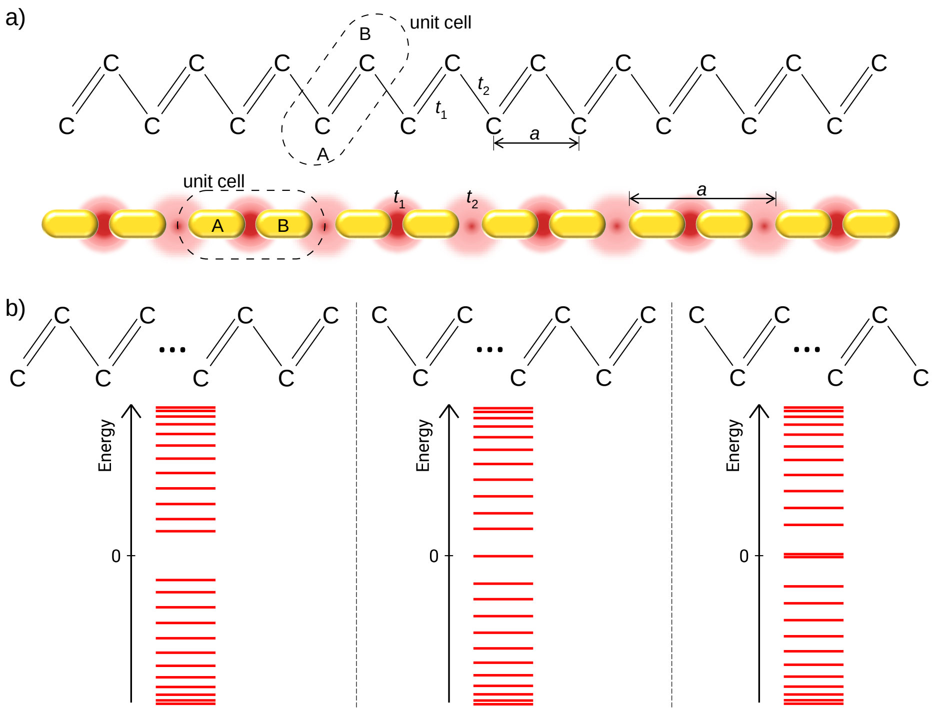

Figure 7.10 – Su-Schrieffer-Heeger (SSH) chains and the emergence of midgap states. a) Molecular structure of the backbone of *trans*-polyacetylene, on which the SSH model is based, and its plasmonic counterpart, a chain of identical gold nanorods separated by alternating gaps. These lead to strong (dark red spots) and weak (light red spots) Coulomb coupling of neighboring particles, mimicking the chemical double and single bonds. Unit cell, lattice constant a, sublattices A and B, as well as the hopping terms t_1 and t_2 are indicated. **b)** Approximate band structure of SSH chains with different terminations. Left: 24-site chain ending in two intact unit cells, i. e. two double bonds. Two symmetric bulk bands separated by a band gap around zero are obtained. Middle: By removing the leftmost C-atom, the left edge features a broken unit cell and an edge state forms. Energetically, it lies in the middle of the band gap. Right: 24-site chain ending in two single-bonded C-atoms. Two midgap edge states belonging to left and right edge arise. For the calculations, $t_1 = 1.3$ and $t_2 = 1$ is used.

SSH chains exhibit topological midgap edge states depending on the terminal conditions. The Hamiltonian of this system with open boundary conditions can be written as

$$\hat{H} = \left(c^\dagger_{1,\mathrm{A}},\, c^\dagger_{1,\mathrm{B}},\, c^\dagger_{2,\mathrm{A}},\, c^\dagger_{2,\mathrm{B}},\, \cdots \right) \overleftrightarrow{t} \begin{pmatrix} c_{1,\mathrm{A}} \\ c_{1,\mathrm{B}} \\ c_{2,\mathrm{A}} \\ c_{2,\mathrm{B}} \\ \vdots \end{pmatrix}, \tag{7.16}$$

with $c_{n,\mathrm{A/B}}, c^\dagger_{n,\mathrm{A/B}}$ the particle annihilation and creation operators for A/B sublattices in the n-th unit cell, and $\overleftrightarrow{t}$ the hopping matrix which conveys the nearest neighbor hopping interactions. We first consider the case of topologically trivial chain boundaries as seen in the left panel of Fig. 7.10 b. The hopping matrix then reads

$$\overleftrightarrow{t} = \begin{pmatrix} 0 & t_1 & 0 & 0 & \cdots \\ t_1 & 0 & t_2 & 0 & \cdots \\ 0 & t_2 & 0 & t_1 & \cdots \\ 0 & 0 & t_1 & 0 & \cdots \\ \vdots & \vdots & \vdots & \vdots & \ddots \end{pmatrix}. \tag{7.17}$$

By numerically diagonalizing the hopping matrix we obtain the approximate band structure[2], exhibiting a band gap around zero energy and symmetric upper and lower bulk band. Next, we eliminate the leftmost C-atom so that the chain ends in a single bond on the left side, as drawn in the middle panel of Fig. 7.10 b. As a result, an eigenstate appears in the middle of the band gap. This is associated with a state localized at the left edge of the chain. Finally, by interchanging the hopping amplitudes t_1 and t_2 from the original setting, we conceive a chain with two single bond boundaries (right panel of Fig. 7.10 b), and accordingly with two nearly degenerate midgap states which can be attributed to the two topologically nontrivial edges. Due to the finite size of the chain, the degeneracy of the zero energy midgap states is lifted. Nevertheless, we infer that the regimes of trivial and nontrivial topology are distinguished by the presence of midgap states and expect a similar behavior for gold nanorod chains under appropriate geometrical parameters.

Plasmonic waveguide arrays assembled in SSH configurations with topological defect centers or trivial/nontrivial interfaces were theoretically and experimentally investigated and found to host defect/interface localized states residing in photonic band gaps [300–303]. Chains of closed plasmonic nanoparticles have been theoretically studied, mainly with *ab initio* approaches to define Hamiltonians and topological invariants, including retardation and loss (non-Hermitian) mechanisms [304–307]. An experimental study of edge states in zigzag arranged plasmonic nanodisk chains was carried out as well, where SNOM measurements were employed to map spatial near-field distributions [308]. However, the plasmon resonances of disk-shaped particles are hardly tunable and less pronounced than the longitudinal mode of elongated rods and the dipole-dipole coupling behavior between adjacent disks depends on the excitation polarization, which might overshadow the topological origin of the observed near-field profiles.

The nanorod chain proposed here offers a more appealing design in this regard. Besides using a neat single-mode plasmonic system based on the longitudinal first-order resonance of the nanorods, two degrees of freedom guarantee great flexibility and tunability in generating topologically nontrivial edge states. The rod length determines the frequency around which photonic band gap and edge states emerge, while the gap width serves as a control knob for the Coulomb interaction between nearest neighbors.

---

[2] The exact bulk band structure is only obtained if periodic boundary conditions are invoked, but edge states would not exist in this setting. Conversely, the hopping matrix (7.17) which contains open boundary conditions, i. e. physical edges, can only be diagonalized approximately. In this context it is assumed that for long, but finite chains the exact boundary conditions have negligible impact on the bulk band structure.

This also constitutes a clear advantage over the original *trans*-polyacetylene chain because the nanorod coupling can be adjusted over a very wide range, as opposed to the fixed energies of chemical single and double bonds in conjugated polymers. In comparison to topolectric circuits, ultra-high frequency topological plasmonics necessitate the full treatment of Maxwell's equations beyond Kirchhoff's circuit laws and enable a new paradigm of light localization at the nanoscale.

7.8.1 gCPA based analysis of SSH chains

In view of the electrical network analyzing approach adopted in topolectrical circuitry, where band structures are read out via impedance measurements [294–296], we deem gCPA analysis a promising route to find edge states *in situ*, based on the reflectivity response of nanorod chains, as an alternative to first principle calculations. This is based on the following idea: Nanorod chains are fed by a semi-infinite nanowire that supports the fundamental guided TM_0 surface plasmon mode. The wire is subsequently used to obtain the reflectivity of the chain as a function of frequency, rod length, and gap sizes. Three exemplary systems with 12 nanorods, assembled in topologically trivial, homogeneous (constant gap width), and nontrivial phases, are sketched in Fig. 7.11 a. A band gap would imply that for a certain range of frequencies no power can be fed into the chain, giving rise to a maximum in reflection amplitude. The energy is then mostly retained on the feeding wire. This behavior is expected in the trivial phase. Conversely, the topological phase features localized edge states, which should be able to absorb the power from the feeding wire attached to the left end of the SSH chain. If the driven edge state shows the sought-after midgap resonance, a decrease in the reflection amplitude is expected in the frequency range where the band gap was found with the trivial conformation. We therefore establish the reflectivity as network analyzing quantity in plasmonic SSH chains and apply the gCPA analysis to elucidate the occurrence of edge states.

So far, gCPA analysis has been carried out using cylindrically symmetric structures placed in vacuum. Since a more realistic experimental setting would involve a substrate, we here include a glass halfspace ($n = 1.52$) in the calculations and simulations and adapt wire and rod shapes to be sharply cut at the air-glass interface and rounded at the top. Width and height are set to 50 nm. Updating the physical structure also requires a recalculation of all fundamental coefficients (cf. Sec. 7.3.3), including the complex dispersion relation of the guided mode, via full FDTD and FDFD simulations. The resulting field profile of the TM_0 mode is imaged in Fig. 7.11 b. Near-field maxima occur near the air-glass interface and inside the higher index medium. From the updated dispersion relation of the propagation constant β depicted in Fig. 7.11 c it can be seen that the mode lies below the light lines in both air and glass for the considered frequency interval. Therefore, the mode is again neatly guided and free of leakage losses. At any rate, the gCPA analysis using the transfer matrix algorithm can be applied in the same way.

Fig. 7.11 d provides results of semi-analytical transfer matrix calculations and full FDTD simulations, comparing reflection amplitude spectra for the three chain config-

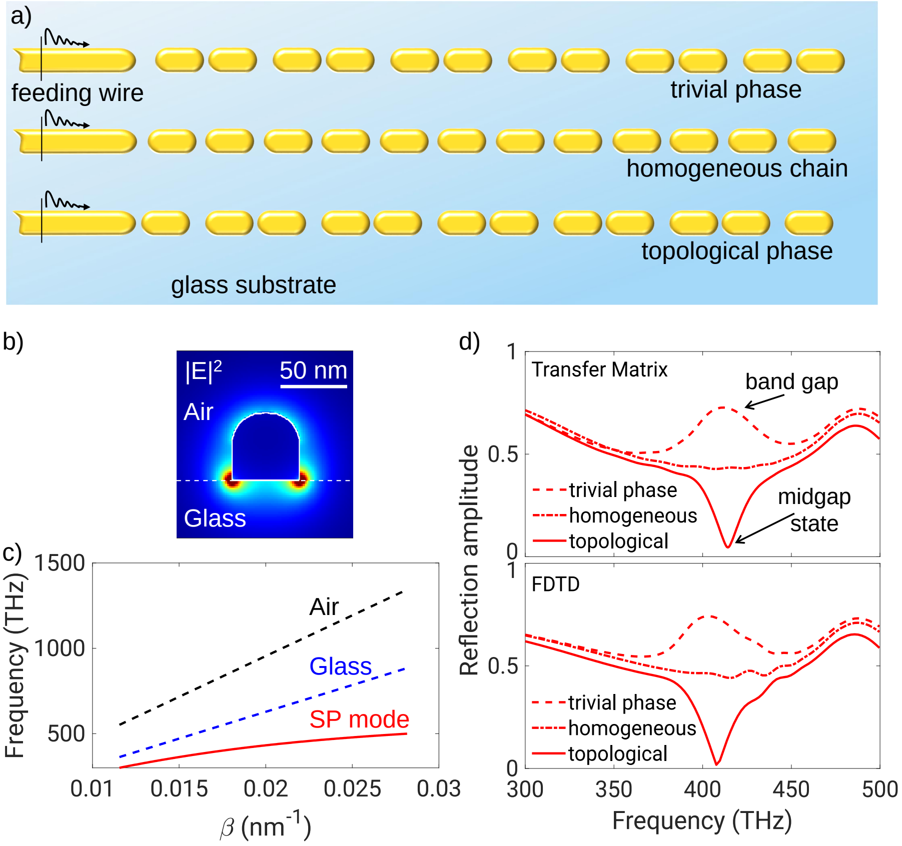

Figure 7.11 – 12-particle plasmonic SSH chains and reflectivity spectra. a) Top view sketch of topologically trivial, homogeneous, and nontrivial chain geometries, achieved by interchanging gap width configurations. The chains are fed by a guided surface plasmon on a semi-infinite feeding wire. **b)** Cross-sectional near-field intensity profile of the guided TM_0 mode. The wire is placed on an air/glass interface where the fields are seen to be concentrated. **c)** Dispersion of β of the guided mode compared to light lines in air (black) and glass (blue). **d)** Reflection amplitude spectra for the three chain configurations obtained from transfer matrix calculations (upper panel) and full FDTD simulations (lower panel). All nanorods have 120 nm length. The homogeneous chain consists of 14 nm gaps throughout. Small/big gaps in the topologically (non)trivial phase are 8 nm/20 nm. Both methods show very good agreement for all configurations. A plasmonic band gap as well as a deep reflection dip, indicating coupling to a midgap edge state at about 415 THz (722 nm), is clearly visible.

urations. All nanorods share a length of 120 nm to operate at visible to near-infrared wavelengths. The dimerization is achieved by gap sizes of 8 nm/20 nm in the topologically (non)trivial chains, while the homogeneous layout features a constant 14 nm gap. The latter shows reflectivities around 50 %. As expected, a broad reflection maximum is observed in the trivial phase, covering 380 THz (789 nm) to 430 THz (697 nm). In the center of this band gap region, a pronounced reflection dip close to zero amplitude occurs when the topologically nontrivial phase is considered. Physically, this means that at 415 THz, the vast majority of the input power from the guided plasmon mode is transferred onto the chain and dissipated there. Since the power is fed from the edge itself, we attribute this midgap reflectivity minimum to the presence of a topological edge state, in accordance with the tight-binding calculations in Fig. 7.10 b. These results also suggest that edge states can be driven under gCPA, i. e. completely vanishing reflection. All in all, transfer matrix and FDTD results show very good agreement for all chain configurations. Only some minor differences of the curves and a little spectral deviation of the reflection minima and maxima exist, probably due to higher-order effects such as next nearest neighbor interaction which is not accounted for in the transfer matrix formulas.

To gain deeper insight into the modal structure supported by the nanorod chains, we analyze the reflectivity on the complex wave vector plane. Similar to the behavior in Figs. 7.9 b-c, a homogeneous chain produces pole-zero pairs appearing along the β-axis and depending on the number of nanorods, which corresponds to a gapless spectrum where the topological transition between trivial and nontrivial regime takes place. Indeed, when the gaps in a homogeneous chain are increased substantially, the pairs move close towards each other, confirming the reduction of Coulomb coupling. The limiting case of infinite gaps corresponds to the “atomic limit” where all pairs collapse into one at the single rod resonance frequency. The reflectance of a trivial SSH chain is plotted in Fig. 7.12 a. For the chosen gap configuration of 7.5 nm/20.5 nm, a band gap opens, in agreement to the spectra shown in Fig. 7.11 d. Pole-zero pairs are absent in this region. All pairs reside in the gain region where $\alpha < 0$. We conclude that these extremal points belong to the bulk modes of the chain. These can only be addressed when gain is added to the system.

When shrinking the big gaps and growing the narrow gaps we traverse the homogeneous chain and end up in the topologically nontrivial regime imaged in Fig. 7.12 b. Here we fix the width of the gap between wire and first nanorod, which is not part of the SSH system and solely acts as feed gap, to 10 nm. The poles and zeros at the band edges undergo intriguing dynamics until one reflectance zero is pushed towards the loss region ($\alpha > 0$) and eventually traverses the dispersion line of the guided plasmon mode, so that a gCPA condition is satisfied. This happens in the middle of the band gap. The midgap state is therefore driven under gCPA and the reflected intensity on the feeding wire cancels out. Simultaneously, the corresponding reflectance pole is pushed towards more negative α.

Moreover, another pole and zero meet in the band gap and eventually annihilate in the gain region. This is particularly evident in the reflection phase plot of Fig. 7.12 c. The double phase singularity becomes infinitely small in the complex wave vector plane while its immediate neighborhood is governed by a constant phase value. Presumably, this second pole-zero pair can be associated with the right chain termination which is also in the nontrivial regime but on the far side of the feeding wire. Annihilation is only observed for phase singularities of opposite winding. This is supported by the fact that each zero and pole in the complex wave vector plane can be interpreted as a topological defect [254]. Then a topological charge of $+1$ (-1) can be attributed to counterclockwise (clockwise) winded phase singularities or intensity zeros (poles), respectively. When two oppositely charged defects coincide, they are able to coalesce

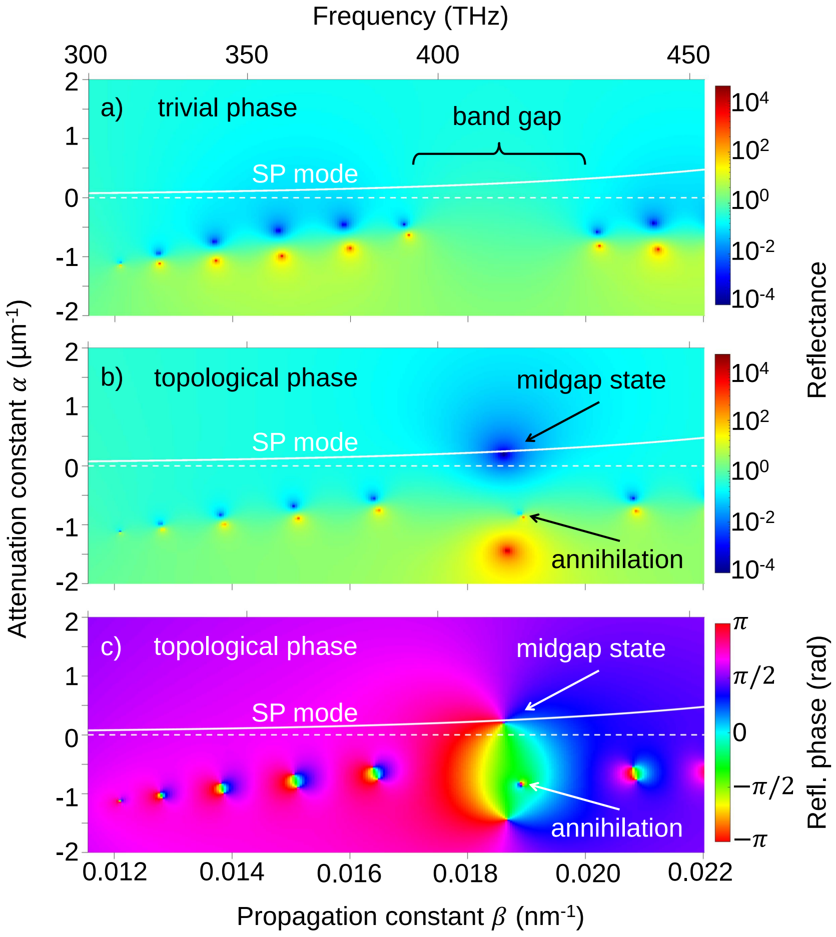

Figure 7.12 – Reflectivity of 12-particle SSH chains in the complex wave vector plane. **a)** Reflectance of an SSH chain in its topologically trivial phase, with 7.5 nm/20.5 nm gaps and 120 nm rod length. An energy gap without pole-zero pairs is visible. **b)** Reflectance of the SSH chain in its topologically nontrivial phase with interchanged gap sizes. The feed gap between wire and first rod is held at 10 nm for both phases. A reflection zero resides on the dispersion line of the guided mode in the middle of the band gap, indicating that a midgap state is driven under gCPA. In the gain region ($\alpha < 0$), a pole and a zero move towards each other and annihilate eventually. **c)** Reflection phase of the nontrivial configuration where the annihilation between pole and zero can be visualized better.

into zero topological charge. In a Hermitian system, this exotic phenomenon has been termed bound state in the continuum (BIC) if the coalescence happens on the real frequency axis ($\alpha = 0$). As a result, one would obtain a radiationless state with diverging quality factor [277].

While the transfer matrix algorithm has been shown to uncover edge states in plasmonic SSH chains by evaluating their reflectivity, it remains elusive whether topological invariants such as the Berry phase can be deduced from this formalism. One could then clearly distinguish the topological regimes via distinct values for the invariants.

7.8.2 Near-field distributions of SSH chains

With the help of a semi-infinite wire it is possible to identify midgap edge states by analyzing the reflectivity spectrum of a plasmonic SSH chain. Here we propose the visualization of these states upon a purely optical excitation of the chains, which provides an independent access besides the network analyzing approach. In FDTD simulations, we illuminate the system from the air side with a normal incidence plane wave source polarized along the chain axis. A side view of this setup is sketched in Fig. 7.13 a, where a near-field monitor 5 nm above the gold structure is used to map the electric near-field intensity.

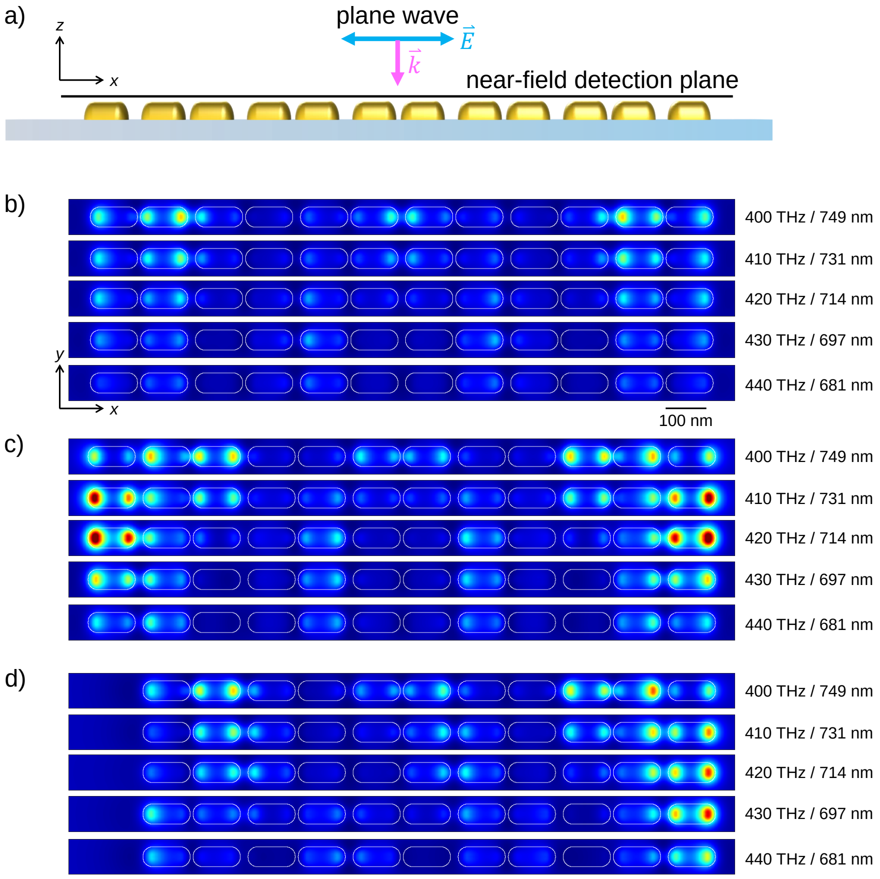

Figure 7.13 – **Near-fields of SSH chains under optical excitation.** **a)** Side view of the simulated geometry with gold nanorod chain on glass substrate, plane wave illumination from the air halfspace, and near-field monitor 5 nm above the chain. **b)** Electric near-field intensity maps in the xy-plane (top view) of a trivial SSH chain for different frequencies. Note that although the field monitor does not intersect the nanorods, their shape is outlined in white. Rod length and gap sizes are 120 nm, 8 nm, and 20 nm, respectively. **c)** Same as in b), but for a topologically nontrivial chain. The edge states are accompanied by highly enhanced fields at the corresponding frequency. **d)** Same as in c), but with the leftmost nanorod removed, so that this 11-particle chain features a trivial termination on the left and a nontrivial termination on the right. Only on the right side a localized edge state with enhanced near-fields is observed.

An SSH chain with topologically trivial configuration produces rather weak near-fields at the frequency window around 420 THz (714 nm), as imaged in Fig. 7.13 b, hinting once more towards a spectrally forbidden region. The picture changes drastically in Fig. 7.13 c, where a chain with topologically nontrivial ends is considered. Here, near-field hotspots arise above the terminal rods at the midgap frequency. The edge states are thus highly localized by a collective Coulomb coupling mechanism along the entire chain. The dominating field component at the monitor position is E_z, i. e., pointing out of plane. In order to demonstrate once more the topological origin of the localized edge state we conceive a plasmonic SSH chain with only one “defect” by removing the leftmost nanorod. Then the gap periodicity is such that a topologically trivial end appears on the left side while on the right side the nontrivial end is retained. The resulting near-field distributions are depicted in Fig. 7.13 d. As expected, highly enhanced near-fields are still encountered above the rightmost nanorod, albeit slightly blue-shifted, whereas no edge state is visible on the left end of the chain. From this near-field study we conclude that the topologically nontrivial chain geometries identified through the gCPA-based reflectivity analysis from Sec. 7.8.1 indeed support localized midgap edge states with enhanced optical near-fields. It implies that the quick and semi-analytical transfer matrix algorithm allows detecting the presence of edge states.

7.9 Concluding and prospective remarks

In summary, at the example of a semi-infinite plasmonic nanowire terminated by a gold nanorod, we present a new type of nanoscale, near-field energy transfer and perfect absorption based on a generalized CPA concept. Using gCPA is necessary for systems in which radiative losses may occur, e. g., plasmonic nanoresonators and quantum emitters. The generalization causes a breakdown of the equivalence between time-reversed lasing at threshold and CPA, although a SPASER condition (reflectivity pole) is still predicted if the loss on the nanorod is turned into gain. The reflectivity of the wire-rod system, the key figure that vanishes when a gCPA condition is met, is calculated in a semi-analytical way by mathematically lightweight, yet rigorous power series and transfer matrix formalisms accounting for a series of Fabry-Pérot oscillations on the nanorod. These models are supplied with numerically obtained fundamental coefficients of reflected and transmitted guided plasmon waves as a function of frequency and gap width. Not only spectra, but also 2D datasets over the complex wave vector plane are calculated on short computation time scales. With this we demonstrate that tuning the geometry of the nanorod can be used to deterministically move the reflectivity phase singularity in the complex wave vector plane. This allows us to find zero eigenvalue conditions for the selected subset of guided plasmonic modes of the scattering matrix. The respective zero eigenvalue must then reside on the dispersion curve of the guided input plasmon.

Since for gCPA no reflection occurs, the condition also corresponds to perfect impedance matching of the guided surface plasmon w. r. t. the nanorod antenna. The gCPA condition completely cloaks the wire termination and virtually decouples the nanorod from the feeding structure, i. e., a nonbonding condition. Thus gCPA allows injecting power to an optical nanoantenna to compensate the loss so that the antenna resonates continuously without damping, offering infinite quality factor at the resonant frequency. Distinct antenna resonance orders, incorporating superradiant and subradiant behavior, can be driven under gCPA and therefore perfect impedance matching. We further demonstrate that the gCPA condition is very sensitive to changes in the local environment and thus useful for background-free ultrasensing. We also achieve the coherent control of nanoantenna radiation using two-port gCPA.

More complex antenna systems can be treated equally well with the gCPA toolbox developed in this chapter. A straightforward extension is a rod dimer system whose modal structure is given by a bonding and an antibonding resonance. Both resonances are shown to be driven under gCPA with the associated reflectance minimum located on the dispersion line of the guided mode. Since the bonding mode offers highly enhanced near-fields and ultrasmall mode volumes in the dimer gap such a plasmonic cavity is a promising candidate for enhanced light-matter interaction studies. For the matter part, a single quantum emitter can be modeled as a two-level system whose population dynamics are described by semi-classical Maxwell-Bloch equations [309]. Placing such a quantum emitter model using certain parameter sets (dephasing rate, transition frequency, dipole moment) inside a Yee cell in the dimer gap within an FDTD simulation [310], one obtains the temporal evolution of a coupled light-matter system from which the reflection can also be calculated.

Fig. 7.14 displays reflectance spectra of a cylindrically shaped wire-rod-rod system embedded in vacuum with quantum emitter in the dimer gap. These data were obtained by Yiming Lai[3]. It turns out that the reflection dip splits and two dressed states emerge at room temperature, stemming from the mixing of bonding plasmon and emitter resonance via strong coupling. With gCPA being a single frequency phenomenon, one dressed state at a time can be neatly driven with a CW input at the gCPA frequency, causing vanishing reflection and thus upholding the “plexcitonic” light-matter state for infinite time spans by perfectly compensating its radiative and nonradiative losses. The remaining dressed state at finite reflectance manifests itself as a saddle point in the spectrum. Around 450 THz another dip is visible, which corresponds to the antibonding mode of the plasmonic dimer resonator and does not participate in the coupling scheme. We infer that gCPA establishes a new paradigm of macroscopically preparing and sustaining strongly coupled light-matter quantum states. In this way it enables a new type of “quantum endurance”.

On the plasmonics side, the reflection/transmission coefficient space entering the transfer matrices can be expanded by using more versatile types of wire/rod endings. For instance, completely flat or tip-shaped end caps with altered transfer properties can be considered. With these, also the near-field landscape in gaps can be adjusted for improved coupling experiments. Likewise, instead of entirely cut-through gaps, the usage of V-shaped grooves allows access to obstacles with increased transmission and reduced reflection of a guided wire mode. Technically, the fundamental coefficients of such discontinuities can be computed numerically in analogy to the method presented in this thesis. With the groove bearing several parameters (depth, width, cutting angle),

---

[3] Trinity College Dublin, University of Dublin, Dublin 2, Ireland

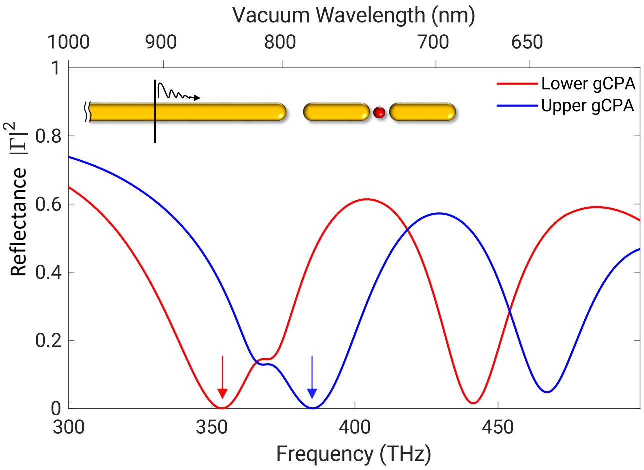

Figure 7.14 – Wire-rod-rod system with quantum emitter. Reflectance spectra with gCPA conditions of the lower dressed state (red, rod length 121 nm) and upper dressed state (blue, rod length 107 nm) are plotted. The gCPA dips are indicated by the arrows, while the non-gCPA dressed states appear as saddle points. The reflectance dips near 450 THz correspond to the antibonding plasmon mode of the rod dimer. The inset illustrates the simulated structure. Both gaps have 3 nm width. The quantum emitter is approximated as two-level system with transition frequency 366 THz (818 nm), dipole moment 20 D, and dephasing rate 6.3 THz (26 meV). These data were obtained by Yiming Lai.

a vast playground opens and new gCPA geometries can be discovered by combining multiple obstacle designs within a chain or circuit network.

Regarding plasmonic nanocircuitry, we demonstrated that a perfectly impedance matched far-field transmitter can be realized by selecting the superradiant first-order resonance on a single nanorod and that a thermal nanoradiator can be conceived with its subradiant second-order resonance at gCPA. Similarly, other functionalities are observed in specific wire-rod compounds. For example, the wire-rod-wire structure drawn in Fig. 7.1 with single-port guided mode feeding exhibits largely suppressed reflection and high transmissivity at a specific frequency if the rod length and gaps are optimized. Therefore, it acts as a plasmonic notch filter in reflection and narrow bandpass filter in transmission. This offers a platform for elaborating functional elements of advanced plasmonic nanocircuitry.

Subsequently, we adopted the gCPA toolbox to more sophisticated nanoantenna systems. Attaching a feeding nanowire to a collinear rod dimer enables locally driving both bonding and antibonding resonances in a perfectly impedance matched fashion. Additionally, we extended our analysis on chains of nanorods separated by alternating gaps. The chains possess multiple modes seen as reflectivity extremal points in the complex wave vector plane, accompanied by phase singularities. Upon geometry changes these extrema undergo intriguing trajectories and can even annihilate each other. Astonishingly, the chains under study represent a classical version of 1D Su-Schrieffer-Heeger chains which support two distinct topological regimes and localized midgap states at topologically nontrivial endings. In the nanoplasmonic SSH analog, hopping amplitudes and resonance behavior are easily tunable by varying the gap and particle geometries. Midgap states are detected by a reflectance zero crossing the dispersion line of the guided plasmon mode, i. e., they create a gCPA condition inside the band gap, and their edge localization is corroborated by FDTD simulated optical near-field distributions.

The SSH chains on glass substrate discussed here are readily producible by the aforementioned focused ion-beam milling technique from monocrystalline gold flakes. A suitable microscopy scheme, such as SNOM [4, 5] or photoemission electron microscopy (PEEM) [311–313], allows recording optical signals from which topography and near-field distributions can be deduced. The results from different topological regimes can then be compared against each other. A nanocircuitry experiment with the goal of measuring reflectivities is an alternative route towards revealing edge states and performing experimental gCPA in general. Here, enhanced optical spin-orbit interaction in metallic nanostructures [314–316] may facilitate launching a unidirectional plasmon on a nanowire and retrieving the reflected signal that propagates in the opposite direction. Both experimental approaches are currently under investigation.

8

Conclusion and outlook

While in their infancy, optical antennas were used as standalone structures and excited solely by optical instruments from bulky setups. A tremendous development in nanofabrication as well as theoretical studies have put antennas in the focus of integrated plasmonic nanocircuitry which allows driving the resonators locally, e. g. via nanoelectrodes [209]. This strategy bridges the gap between nanoelectronics, the fundament of modern hardware technology for more than five decades, and photonics with its enormous data bandwidth. Due to the noticeable size of wiring elements within metallic nanostructures, it is in general challenging to build functional plasmonic devices whose optical performance remains unaffected by the presence of wires. Distorted spectral signatures, broadening, and reduced radiation efficiency may become observable effects in wired resonators compared to solitary resonators. Three systems of locally driven nanoantennas were presented in the last chapters, consisting of wire-rod composites. Proper designs, aided by numerical simulations, allowed compiling complex antenna systems with advanced emission properties that remained unaltered by the presence of nanowires.

Thereby, the first in-plane electrically driven optical Yagi-Uda antenna was realized in Chap. 5. Several key aspects were addressed for a successful demonstration. First, the nanoscale light generation relies on inelastic tunneling of electrons across a 1 nm gap that was created by moving a passivated spherical gold particle into a larger prefabricated interstice using dielectrophoresis. Second, the connection wires have to ensure electrical access of the feed element while leaving its resonance unperturbed and allowing the placement of nearby parasitic elements, i. e. reflector and directors. Kinked connectors are found to satisfy these demands and even contribute to a forward directional emission, which is the central figure of merit of Yagi-Uda antennas. Third, the Yagi-Uda working principle has to be implemented by optimizing the resonance and positioning of the parasitic elements. This ensures a narrow phase-coherent emission beam in forward direction caused by constructive interference. An analytic dipole interaction model offers a quick optimization procedure, but it also contains inevitable simplifications. More detailed numerical optimizations account for particle shapes found in experiments, a glass substrate, and fully retarded treatment of Maxwell's equations. Based on the optimal geometry parameters, Yagi-

Uda antennas emitting around 870 nm could be reproducibly fabricated. The devices showed highly directional electroluminescence with forward-to-backward ratios up to 6.5 dB, determined within a conservative evaluation technique. This value is superior to previously published Yagi-Uda approaches in nano-optics [32, 157–159]. Interestingly, some concepts of macroscopic antenna theory can be transferred to the optical regime. For instance, enlarging the director number in numerical simulations leads to an increase in forward gain and to a narrowing of the beam angle. A fundamental limitation is given by the Ohmic dissipation in plasmonic nanostructures, which lowers the gain compared to radiofrequency Yagi-Uda arrays. Nevertheless, employing plasmonic materials with reduced losses, e. g. silver, holds promise for similar performance. Furthermore, dielectric layer structures with suitable refractive index profiles provide a platform for even higher gains because the emitted light beam is subsequently narrowed and confined to the antenna plane. In order to measure this emission behavior, near-field optical techniques such as SNOM might be used for acquiring in-plane radiation patterns. Owing to their high forward-to-backward emission ratio, Yagi-Uda antennas are possible candidates for electro-optic interconnects in future microprocessor architectures, featuring high data transfer rates and fast modulation speeds. Narrow beam angles minimize cross-talk between adjacent transmitters and receivers on a common chip, allowing for a high integration density. Current challenges to overcome for a broad deployment comprise the efficiency of the inelastic tunneling process as well as the rectifying capabilities of nanoantenna systems, as discussed in Sec. 5.5. Also, novel fabrication means suitable for mass-production on a common substrate need to be explored.

A second area where electrically driven optical antennas can unfold their potential are subwavelength-sized diodes. Chap. 6 introduced a color-switchable proof-of-concept device which combines a pair of connected nanoantennas with a single organic semiconductor thin film. These so-called organic light-emitting antennas, OLEA, are placed on a common glass substrate such that a lateral gold-organic-gold junction forms. The antennas fulfill multiple tasks in this architecture. First, via the electrical leads they supply the charge carriers to be injected into the organic material zinc phthalocyanine (ZnPc). Second, they enhance the recombination rate of nearby excitons by providing near-field hotspots. The two rod antennas, separated by a 50 nm gap, differ in length, giving rise to independent resonances (800 nm and 920 nm) at the two electrodes. In contrast to conventional stacked OLEDs equipped with planar electrodes, here excitons couple to superradiant plasmon modes, which is a desired effect. Third, the antenna electrodes couple the light efficiently into the far-field. They are also responsible for directional emission because the distinct resonances imply a Yagi-Uda like interference pattern. The most striking observation is that the electroluminescence spectrum does not consist of a superposition of the two electrode resonances, but resembles that of the cathode and therefore depends on the polarity of the applied voltage. The observed behavior is attributed to a higher injection barrier for electrons than for holes, leading to a recombination zone localized at the cathode antenna. The switching effect upon voltage polarity inversions also manifests itself as changes in the directionality of the angular far-field distribution, which is reproduced in numerical simulations. By depositing a planar gold reflector on top of the OLEA structure, the radiation pattern can be further optimized for emission towards the substrate direction. External quantum efficiencies of 10^{-7} to 10^{-6} indicate an emission enhancement by orders of magnitude compared to conventional stacked OLEDs made of ZnPc. All in all, the proof-of-principle study establishes an electrically driven switchable two-color point source, bearing the potential to be extended to RGB nanopixels when more sophisticated material compounds and advanced OLED engineering steps are taken into consideration. This is described in more detail in Sec. 6.8. In the future, such nanopixels may accompany the ongoing digitalization and become an ingredient in ultrasmall digital devices.

Optical antennas can also be locally driven by an impinging near-field, e. g. from a guided surface plasmon on a nanowire transmission line which is attached via a gap. Chap. 7 thoroughly investigated how perfect impedance matching is accomplished in such plasmonic wire-rod nanocircuits. The matching implies that no power is reflected back onto the feeding wire, but fully absorbed by the antenna. The rod is thus virtually decoupled from the wire. Borrowed from a generalized concept of coherent perfect absorption (gCPA), two semi-analytical approaches for computing the reflectivity of the input surface plasmon are stated and employed to identify configurations with vanishing reflection, benefiting from low computational effort. It turns out that the gCPA scenario relies on an intricate coexistence of radiative losses, nonradiative dissipation, and phase-sensitive interference effects between partially reflected and transmitted near-fields. Decisive parameters encompass the operating frequency, rod length and gap width, which all have to be exactly chosen at a time to achieve gCPA. This scheme is developed into a versatile analysis toolbox which allows to precisely track the modal structure of the antenna system under study. Besides coherent control of the radiation efficiency of a nanoantenna, further possible applications are explored through calculations and numerical simulations. Both superradiant and subradiant resonances can be driven under gCPA on a single rod. A gCPA-operated wire-rod sensor shows a steep increase in reflection upon disturbance of the gCPA condition from an otherwise dark background. More future directions are outlined in Sec. 7.9. In a final excursion, the gCPA toolbox is used to shed light on the modal structure of nanorod chains with alternating gap separations. These represent an optical version of the Su-Schrieffer-Heeger model known from quantum mechanics. The geometry dependent existence of topologically nontrivial edge-localized states, which appear in the middle of an energy band gap, is evidenced in the zero surface plasmon reflectivity as well as near-field distributions. Therefore, gCPA can streamline the design of topological photonic systems. This suggests a promising future for complex plasmonic antenna systems because topological matter constitutes, besides superconductors, the most exciting and appealing material class of the 21^{st} century.

A

The wire-rod system and Fano resonances

The reflectance dips of wire-rod structures for specific choices of rod length, gap size, and frequency can be regarded as a special case of Fano resonances. These emerge when a narrowband resonance (on the nanorod) interferes with a broadband background (the guided TM_0 mode on the nanowire) in a coherent way. Depending on the phase difference between the two signals, the resulting spectrum assumes different line shapes, from dips via asymmetric profiles to peaks [13, 317]. In this section we demonstrate that the same observations can in principle be made in the reflectance of the wire-rod system. Fig. A.1 a depicts the reflectance $|\Gamma|^2$ of the system already encountered in Fig. 7.5 d with varying rod length, where the second dip fulfills the gCPA condition. All values entering this calculation are derived from the fundamental coefficients in Sec. 7.3.3 so that the dip structure is reproduced. In principle, we are able to tune these coefficients freely and thereby deliberately abandon the values dictated by particle shapes and material properties. Here we manipulate the transmission phase over the gap while preserving all remaining fundamental coefficients. The resulting reflectance plots are displayed in Figs. A.1 b-d, with phase values $\pi/8$, $2\pi/5$, and $2\pi/3$, respectively. With increasing phase, the reflectance dips evolve into asymmetric line profiles, symmetric peaks, and again asymmetric features with opposite orientation. Hence, the characteristics of Fano resonances with varying Fano line shape parameter are observed.

In this regard, the reflectance dips arising for the natural choice of the transmission phase constitute a special case of all possible Fano line profiles that the system can potentially adopt. It must be emphasized, however, that only with the phase value dictated by nature a physically meaningful picture results from the calculation. As soon as the transmission phase is chosen artificially, we obtain $|\Gamma|^2 > 1$ for some rod lengths, implying that plasmon amplification is hypothetically achieved without applying a gain material, which is physically forbidden in a lossy system. With the modified transmission phase, a hypothetical constructive interference generates the reflectances exceeding unity, which becomes particularly apparent in the peak spectrum of Fig. A.1 c. It is interesting to see that even with artificial coefficients gCPA conditions can be satisfied, e. g. at a rod length of 130 nm in Fig. A.1 b. In the complex wave vector plane,

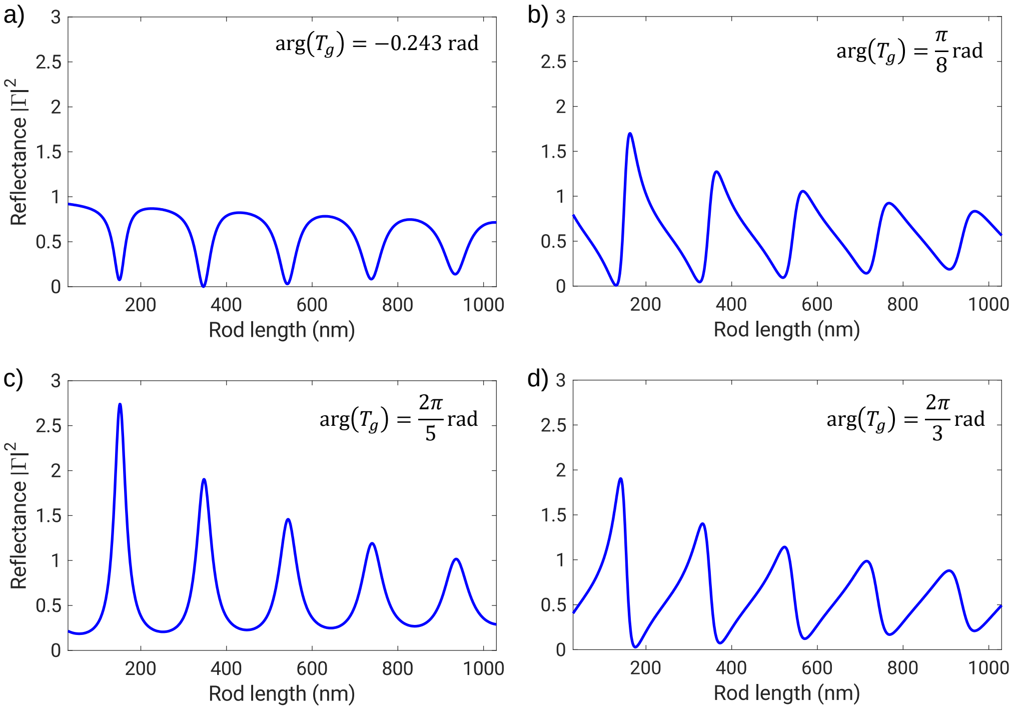

Figure A.1 – Reflectance of wire-rod system with different gap transmission phases. **a)** Calculated reflectance $|\Gamma|^2$ as a function of rod length of a wire-rod system at 833 nm with a 4 nm gap (same system as in Fig. 7.5 d), with the natural value of the transmission phase over a gap, indicated with $\arg(T_g)$. **b)-d)** Calculated reflectance with distinct, fixed values chosen for the transmission phase. Depending on its value, different Fano-like line shapes are obtained.

such asymmetric reflectance zeros with corresponding phase singularities would look different from those in Chap. 7. Instead of a circular shape, they would presumably manifest themselves as elongated, elliptic appearances.

Bibliography

[1] The Nobel Prize in Physics 1909. `https://www.nobelprize.org/prizes/physics/1909/marconi/lecture/` (2022).

[2] Hong, S. *Wireless: From Marconi's Black-Box to the Audion*. Transformations: Studies in the History of Science and Technology (MIT Press, Cambridge, Mass, 2001).

[3] Balanis, C. A. *Antenna Theory: Analysis and Design* (Wiley, New York, 1997), second edn.

[4] Pohl, D. W., Denk, W. & Lanz, M. Optical stethoscopy: Image recording with resolution $\lambda/20$. *Applied Physics Letters* **44**, 651–653 (1984).

[5] Dürig, U., Pohl, D. W. & Rohner, F. Near-field optical-scanning microscopy. *Journal of Applied Physics* **59**, 3318–3327 (1986).

[6] Greffet, J.-J., Laroche, M. & Marquier, F. Impedance of a Nanoantenna and a Single Quantum Emitter. *Physical Review Letters* **105**, 117701 (2010).

[7] Pohl, D. *Near Field Optics Seen as an Antenna Problem*, 9–21 (World Scientific, 2000).

[8] Mühlschlegel, P., Eisler, H.-J., Martin, O. J. F., Hecht, B. & Pohl, D. W. Resonant Optical Antennas. *Science* **308**, 1607–1609 (2005).

[9] Bharadwaj, P., Deutsch, B. & Novotny, L. Optical Antennas. *Advances in Optics and Photonics* **1**, 438 (2009).

[10] Novotny, L. & van Hulst, N. Antennas for light. *Nat Photon* **5**, 83–90 (2011).

[11] Biagioni, P., Huang, J.-S. & Hecht, B. Nanoantennas for visible and infrared radiation. *Reports on Progress in Physics* **75**, 024402 (2012).

[12] Agio, M. & Alù, A. (eds.) *Optical Antennas* (Cambridge University Press, Cambridge, 2013).

[13] Novotny, L. & Hecht, B. *Principles of Nano-Optics* (Cambridge University Press, Cambridge, 2012), second edn.

[14] Chikkaraddy, R. *et al.* Single-molecule strong coupling at room temperature in plasmonic nanocavities. *Nature* **535**, 127–130 (2016).

[15] Groß, H., Hamm, J. M., Tufarelli, T., Hess, O. & Hecht, B. Near-field strong coupling of single quantum dots. *Science Advances* **4**, eaar4906 (2018).

[16] Taylor, A. B. & Zijlstra, P. Single-Molecule Plasmon Sensing: Current Status and Future Prospects. *ACS Sensors* **2**, 1103–1122 (2017).

[17] Zhang, W., Fischer, H., Schmid, T., Zenobi, R. & Martin, O. J. F. Mode-Selective Surface-Enhanced Raman Spectroscopy Using Nanofabricated Plasmonic Dipole Antennas. *The Journal of Physical Chemistry C* **113**, 14672–14675 (2009).

[18] Höflich, K., Becker, M., Leuchs, G. & Christiansen, S. Plasmonic dimer antennas for surface enhanced Raman scattering. *Nanotechnology* **23**, 185303 (2012).

[19] Kildishev, A. V., Boltasseva, A. & Shalaev, V. M. Planar Photonics with Metasurfaces. *Science* **339**, 1232009–1232009 (2013).

[20] Lippitz, M., van Dijk, M. A. & Orrit, M. Third-Harmonic Generation from Single Gold Nanoparticles. *Nano Letters* **5**, 799–802 (2005).

[21] Kim, S. *et al.* High-harmonic generation by resonant plasmon field enhancement. *Nature* **453**, 757–760 (2008).

[22] Hanke, T. *et al.* Efficient Nonlinear Light Emission of Single Gold Optical Antennas Driven by Few-Cycle Near-Infrared Pulses. *Physical Review Letters* **103**, 257404 (2009).

[23] Sivis, M., Duwe, M., Abel, B. & Ropers, C. Extreme-ultraviolet light generation in plasmonic nanostructures. *Nature Physics* **9**, 304–309 (2013).

[24] IBM Unveils World's First 2 Nanometer Chip Technology, Opening a New Frontier for Semiconductors. `https://newsroom.ibm.com/2021-05-06-IBM-Unveils-Worlds-First-2-Nanometer-Chip-Technology,-Opening-a-New-Frontier-for-Semiconductors` (2022).

[25] Ayata, M. *et al.* High-speed plasmonic modulator in a single metal layer. *Science* **358**, 630–632 (2017).

[26] Haffner, C. *et al.* Low-loss plasmon-assisted electro-optic modulator. *Nature* **556**, 483–486 (2018).

[27] Dasgupta, A. *et al.* Optical wireless link between a nanoscale antenna and a transducing rectenna. *Nature Communications* **9**, 1992 (2018).

[28] Cai, W., Vasudev, A. P. & Brongersma, M. L. Electrically Controlled Nonlinear Generation of Light with Plasmonics. *Science* **333**, 1720–1723 (2011).

[29] Prangsma, J. C. *et al.* Electrically Connected Resonant Optical Antennas. *Nano Letters* **12**, 3915–3919 (2012).

[30] Kern, J. *et al.* Electrically driven optical antennas. *Nature Photonics* **9**, 582–586 (2015).

[31] Parzefall, M. & Novotny, L. Optical antennas driven by quantum tunneling: A key issues review. *Reports on Progress in Physics* **82**, 112401 (2019).

[32] Gurunarayanan, S. P. *et al.* Electrically Driven Unidirectional Optical Nanoantennas. *Nano Letters* **17**, 7433–7439 (2017).

[33] Parzefall, M. *et al.* Antenna-coupled photon emission from hexagonal boron nitride tunnel junctions. *Nature Nanotechnology* **10**, 1058–1063 (2015).

[34] Parzefall, M. *et al.* Light from van der Waals quantum tunneling devices. *Nature Communications* **10**, 292 (2019).

[35] Qian, H. *et al.* Efficient light generation from enhanced inelastic electron tunnelling. *Nature Photonics* **12**, 485–488 (2018).

[36] Rodwell, M. *et al.* Submicron scaling of HBTs. *IEEE Transactions on Electron Devices* **48**, 2606–2624 (2001).

[37] Grimm, P. *et al.* Color-Switchable Subwavelength Organic Light-Emitting Antennas. *Nano Letters* **22**, 1032–1038 (2022).

[38] Wolters, J. *et al.* Coupling of single nitrogen-vacancy defect centers in diamond nanocrystals to optical antennas and photonic crystal cavities. *physica status solidi (b)* **249**, 918–924 (2012).

[39] Bogdanov, S. I. *et al.* Ultrabright Room-Temperature Sub-Nanosecond Emission from Single Nitrogen-Vacancy Centers Coupled to Nanopatch Antennas. *Nano Letters* **18**, 4837–4844 (2018).

[40] Kern, J. *et al.* Nanoantenna-Enhanced Light–Matter Interaction in Atomically Thin WS $_2$. *ACS Photonics* **2**, 1260–1265 (2015).

[41] Kern, J. *et al.* Nanoscale Positioning of Single-Photon Emitters in Atomically Thin WSe $_2$. *Advanced Materials* **28**, 7101–7105 (2016).

[42] Hobson, P., Wedge, S., Wasey, J., Sage, I. & Barnes, W. Surface Plasmon Mediated Emission from Organic Light-Emitting Diodes. *Advanced Materials* **14**, 1393–1396 (2002).

[43] Koller, D. *et al.* Organic plasmon-emitting diode. *Nature Photonics* **2**, 684–687 (2008).

[44] Fusella, M. A. *et al.* Plasmonic enhancement of stability and brightness in organic light-emitting devices. *Nature* **585**, 379–382 (2020).

[45] Brütting, W. *Physics of Organic Semiconductors* (Wiley-VCH, Weinheim, 2005).

[46] Geffroy, B., le Roy, P. & Prat, C. Organic light-emitting diode (OLED) technology: Materials, devices and display technologies. *Polymer International* **55**, 572–582 (2006).

[47] Shi, X. *et al.* Large-area display textiles integrated with functional systems. *Nature* **591**, 240–245 (2021).

[48] Pozar, D. M. *Microwave Engineering* (Wiley, Hoboken, NJ, 2012), fourth edn.

[49] Geisler, P., Krauss, E., Razinskas, G. & Hecht, B. Transmission of Plasmons through a Nanowire. *ACS Photonics* **4**, 1615–1620 (2017).

[50] Engheta, N., Salandrino, A. & Alù, A. Circuit Elements at Optical Frequencies: Nanoinductors, Nanocapacitors, and Nanoresistors. *Physical Review Letters* **95** (2005).

[51] Huang, J.-S., Feichtner, T., Biagioni, P. & Hecht, B. Impedance Matching and Emission Properties of Nanoantennas in an Optical Nanocircuit. *Nano Letters* **9**, 1897–1902 (2009).

[52] Chong, Y. D., Ge, L., Cao, H. & Stone, A. D. Coherent Perfect Absorbers: Time-Reversed Lasers. *Physical Review Letters* **105**, 053901 (2010).

[53] Boriskina, S. V. *et al.* Losses in plasmonics: From mitigating energy dissipation to embracing loss-enabled functionalities. *Advances in Optics and Photonics* **9**, 775 (2017).

[54] Newton, I. *Philosophiae Naturalis Principia Mathematica* (Jussu Societatis Regiae ac Typis Joseph Streater, London, 1687), first edn.

[55] Maxwell, J. C. A dynamical theory of the electromagnetic field. *Philosophical Transactions of the Royal Society of London* **155**, 459–512 (1865).

[56] Jackson, J. D. *Classical Electrodynamics* (Wiley, New York, 1999), third edn.

[57] Einstein, A. Zur Elektrodynamik bewegter Körper. *Annalen der Physik* **322**, 891–921 (1905).

[58] Stratton, J. A. *Electromagnetic Theory*. International Series in Pure and Applied Physics (McGraw-Hill, New York, 1941).

[59] Griffiths, D. J. *Introduction to Electrodynamics* (Cambridge University Press, Cambridge, United Kingdom ; New York, NY, 2018), fourth edn.

[60] Bohren, C. F. & Huffman, D. R. *Absorption and Scattering of Light by Small Particles* (Wiley, 1998), first edn.

[61] Rebhan, E. *Mechanik, Elektrodynamik, spezielle und allgemeine Relativitätstheorie, Kosmologie*. No. Eckhard Rebhan ; Bd. 1 in Theoretische Physik (Spektrum Akad. Verl, Heidelberg, 2001), first edn.

[62] Abbe, E. Beiträge zur Theorie des Mikroskops und der mikroskopischen Wahrnehmung. *Archiv für Mikroskopische Anatomie* **9**, 413–468 (1873).

[63] Bozhevolnyi, S. I., Volkov, V. S., Devaux, E., Laluet, J.-Y. & Ebbesen, T. W. Channel plasmon subwavelength waveguide components including interferometers and ring resonators. *Nature* **440**, 508–511 (2006).

[64] Miyazaki, H. T. & Kurokawa, Y. Squeezing Visible Light Waves into a 3-nm-Thick and 55-nm-Long Plasmon Cavity. *Physical Review Letters* **96**, 097401 (2006).

[65] Huang, J.-S. *et al.* Atomically flat single-crystalline gold nanostructures for plasmonic nanocircuitry. *Nature Communications* **1**, 150 (2010).

[66] Wu, X., Kullock, R., Krauss, E. & Hecht, B. Single-crystalline gold microplates grown on substrates by solution-phase synthesis. *Crystal Research and Technology* **50**, 595–602 (2015).

[67] Krauss, E. *et al.* Controlled Growth of High-Aspect-Ratio Single-Crystalline Gold Platelets. *Crystal Growth & Design* **18**, 1297–1302 (2018).

[68] Olmon, R. L. *et al.* Optical dielectric function of gold. *Physical Review B* **86**, 235147 (2012).

[69] Vial, A., Grimault, A.-S., Macías, D., Barchiesi, D. & de la Chapelle, M. Improved analytical fit of gold dispersion: Application to the modeling of extinction spectra with a finite-difference time-domain method. *Physical Review B* **71**, 085416 (2005).

[70] Etchegoin, P. G., Le Ru, E. C. & Meyer, M. An analytic model for the optical properties of gold. *The Journal of Chemical Physics* **125**, 164705 (2006).

[71] Etchegoin, P. G., Le Ru, E. C. & Meyer, M. Erratum: “An analytic model for the optical properties of gold” [J. Chem. Phys. 125, 164705 (2006)]. *The Journal of Chemical Physics* **127**, 189901 (2007).

[72] Rioux, D. *et al.* An Analytic Model for the Dielectric Function of Au, Ag, and their Alloys. *Advanced Optical Materials* **2**, 176–182 (2014).

[73] Overcoming the Multi-wavelength FDTD Challenge. `https://www.lumerical.com/learn/whitepapers/overcoming-the-multi-wavelength-fdtd-challenge/` (2021).

[74] Yang, H. U. *et al.* Optical dielectric function of silver. *Physical Review B* **91** (2015).

[75] Ditlbacher, H. *et al.* Silver Nanowires as Surface Plasmon Resonators. *Physical Review Letters* **95**, 257403 (2005).

[76] Lu, Y.-J. *et al.* Plasmonic Nanolaser Using Epitaxially Grown Silver Film. *Science* **337**, 450–453 (2012).

[77] Schörner, C., Adhikari, S. & Lippitz, M. A Single-Crystalline Silver Plasmonic Circuit for Visible Quantum Emitters. *Nano Letters* **19**, 3238–3243 (2019).

[78] Razinskas, G. *Functional Plasmonic Nanocircuitry*. Ph.D. thesis, Julius-Maximilians-Universität Würzburg, Würzburg (2017).

[79] Otto, A. Excitation of nonradiative surface plasma waves in silver by the method of frustrated total reflection. *Zeitschrift für Physik A Hadrons and nuclei* **216**, 398–410 (1968).

[80] Kretschmann, E. Die Bestimmung optischer Konstanten von Metallen durch Anregung von Oberflächenplasmaschwingungen. *Zeitschrift für Physik A Hadrons and nuclei* **241**, 313–324 (1971).

[81] Zia, R., Selker, M. D., Catrysse, P. B. & Brongersma, M. L. Geometries and materials for subwavelength surface plasmon modes. *Journal of the Optical Society of America A* **21**, 2442 (2004).

[82] Dionne, J. A., Sweatlock, L. A., Atwater, H. A. & Polman, A. Planar metal plasmon waveguides: Frequency-dependent dispersion, propagation, localization, and loss beyond the free electron model. *Physical Review B* **72**, 075405 (2005).

[83] Halas, N. J., Lal, S., Chang, W.-S., Link, S. & Nordlander, P. Plasmons in Strongly Coupled Metallic Nanostructures. *Chemical Reviews* **111**, 3913–3961 (2011).

[84] Pitarke, J. M., Silkin, V. M., Chulkov, E. V. & Echenique, P. M. Theory of surface plasmons and surface-plasmon polaritons. *Reports on Progress in Physics* **70**, 1–87 (2007).

[85] Sarid, D. Long-Range Surface-Plasma Waves on Very Thin Metal Films. *Physical Review Letters* **47**, 1927–1930 (1981).

[86] Sarid, D. Long-Range Surface-Plasma Waves on Very Thin Metal Films. *Physical Review Letters* **48**, 446–446 (1982).

[87] Berini, P., Charbonneau, R., Lahoud, N. & Mattiussi, G. Characterization of long-range surface-plasmon-polariton waveguides. *Journal of Applied Physics* **98**, 043109 (2005).

[88] Boltasseva, A. *et al.* Integrated Optical Components Utilizing Long-Range Surface Plasmon Polaritons. *Journal of Lightwave Technology* **23**, 413 (2005).

[89] Berini, P. Long-range surface plasmon polaritons. *Advances in Optics and Photonics* **1**, 484 (2009).

[90] Zervas, M. N. Surface plasmon–polariton waves guided by thin metal films. *Optics Letters* **16**, 720 (1991).

[91] Dionne, J. A., Sweatlock, L. A., Atwater, H. A. & Polman, A. Plasmon slot waveguides: Towards chip-scale propagation with subwavelength-scale localization. *Physical Review B* **73**, 035407 (2006).

[92] Park, J. *et al.* Resonant tunneling of surface plasmon polariton in the plasmonic nano-cavity. *Optics Express* **16**, 16903 (2008).

[93] Yang, H., Li, J. & Xiao, G. Decay and propagation properties of symmetric surface plasmon polariton mode in metal–insulator–metal waveguide. *Optics Communications* **395**, 159–162 (2017).

[94] Mie, G. Beiträge zur Optik trüber Medien, speziell kolloidaler Metallösungen. *Annalen der Physik* **330**, 377–445 (1908).

[95] Kern, J. *Optical and Electrical Excitation of Nanoantennas with Atomic-Scale Gaps*. Ph.D. thesis, Julius-Maximilians-Universität Würzburg, Würzburg (2014).

[96] Brongersma, M. L. & Kik, P. G. (eds.) *Surface Plasmon Nanophotonics*. No. 131 in Springer Series in Optical Sciences (Springer, Dordrecht, 2007).

[97] Gans, R. Über die Form ultramikroskopischer Goldteilchen. *Annalen der Physik* **342**, 881–900 (1912).

[98] Gans, R. Über die Form ultramikroskopischer Silberteilchen. *Annalen der Physik* **352**, 270–284 (1915).

[99] Sun, L., Hao, Y., Chien, C.-L. & Searson, P. C. Tuning the properties of magnetic nanowires. *IBM Journal of Research and Development* **49**, 79–102 (2005).

[100] Rogobete, L., Kaminski, F., Agio, M. & Sandoghdar, V. Design of plasmonic nanoantennae for enhancing spontaneous emission. *Optics Letters* **32**, 1623 (2007).

[101] Tam, F., Goodrich, G. P., Johnson, B. R. & Halas, N. J. Plasmonic Enhancement of Molecular Fluorescence. *Nano Letters* **7**, 496–501 (2007).

[102] Wen, J. *et al.* Room-Temperature Strong Light–Matter Interaction with Active Control in Single Plasmonic Nanorod Coupled with Two-Dimensional Atomic Crystals. *Nano Letters* **17**, 4689–4697 (2017).

[103] Saute, B., Premasiri, R., Ziegler, L. & Narayanan, R. Gold nanorods as surface enhanced Raman spectroscopy substrates for sensitive and selective detection of ultra-low levels of dithiocarbamate pesticides. *The Analyst* **137**, 5082 (2012).

[104] Ou, Y. *et al.* Gold Nanorods as Surface-Enhanced Raman Spectroscopy Substrates for Rapid and Sensitive Analysis of Allura Red and Sunset Yellow in Beverages. *Journal of Agricultural and Food Chemistry* **66**, 2954–2961 (2018).

[105] Nie, S. Probing Single Molecules and Single Nanoparticles by Surface-Enhanced Raman Scattering. *Science* **275**, 1102–1106 (1997).

[106] Kühn, S., Håkanson, U., Rogobete, L. & Sandoghdar, V. Enhancement of Single-Molecule Fluorescence Using a Gold Nanoparticle as an Optical Nanoantenna. *Physical Review Letters* **97**, 017402 (2006).

[107] Knight, M. W., Sobhani, H., Nordlander, P. & Halas, N. J. Photodetection with Active Optical Antennas. *Science* **332**, 702–704 (2011).

[108] Raschke, G. *et al.* Gold Nanoshells Improve Single Nanoparticle Molecular Sensors. *Nano Letters* **4**, 1853–1857 (2004).

[109] Anker, J. N. *et al.* Biosensing with plasmonic nanosensors. *Nature Materials* **7**, 442–453 (2008).

[110] Dorfmüller, J. *et al.* Fabry-Pérot Resonances in One-Dimensional Plasmonic Nanostructures. *Nano Letters* **9**, 2372–2377 (2009).

[111] Taminiau, T. H., Stefani, F. D. & van Hulst, N. F. Optical Nanorod Antennas Modeled as Cavities for Dipolar Emitters: Evolution of Sub- and Super-Radiant Modes. *Nano Letters* **11**, 1020–1024 (2011).

[112] Novotny, L. & Hafner, C. Light propagation in a cylindrical waveguide with a complex, metallic, dielectric function. *Physical Review E* **50**, 4094–4106 (1994).

[113] Encina, E. R. & Coronado, E. A. Resonance Conditions for Multipole Plasmon Excitations in Noble Metal Nanorods. *The Journal of Physical Chemistry C* **111**, 16796–16801 (2007).

[114] Novotny, L. Effective Wavelength Scaling for Optical Antennas. *Physical Review Letters* **98**, 266802 (2007).

[115] Huang, J.-S. *et al.* Mode Imaging and Selection in Strongly Coupled Nanoantennas. *Nano Letters* **10**, 2105–2110 (2010).

[116] Myroshnychenko, V. *et al.* Modelling the optical response of gold nanoparticles. *Chemical Society Reviews* **37**, 1792 (2008).

[117] Bryant, G. W., García de Abajo, F. J. & Aizpurua, J. Mapping the Plasmon Resonances of Metallic Nanoantennas. *Nano Letters* **8**, 631–636 (2008).

[118] Prodan, E. A Hybridization Model for the Plasmon Response of Complex Nanostructures. *Science* **302**, 419–422 (2003).

[119] Rechberger, W. *et al.* Optical properties of two interacting gold nanoparticles. *Optics Communications* **220**, 137–141 (2003).

[120] Nordlander, P., Oubre, C., Prodan, E., Li, K. & Stockman, M. I. Plasmon Hybridization in Nanoparticle Dimers. *Nano Letters* **4**, 899–903 (2004).

[121] Novotny, L. Strong coupling, energy splitting, and level crossings: A classical perspective. *American Journal of Physics* **78**, 1199–1202 (2010).

[122] Fließbach, T. *Mechanik* (Springer Berlin Heidelberg, Berlin, Heidelberg, 2015).

[123] Funston, A. M., Novo, C., Davis, T. J. & Mulvaney, P. Plasmon Coupling of Gold Nanorods at Short Distances and in Different Geometries. *Nano Letters* **9**, 1651–1658 (2009).

[124] Kern, J. *et al.* Atomic-Scale Confinement of Resonant Optical Fields. *Nano Letters* **12**, 5504–5509 (2012).

[125] Wokaun, A., Lutz, H.-P., King, A. P., Wild, U. P. & Ernst, R. R. Energy transfer in surface enhanced luminescence. *The Journal of Chemical Physics* **79**, 509–514 (1983).

[126] Purcell, E. M. Spontaneous emission probabilities at radio frequencies. *Physical Review* **69**, 681 (1946).

[127] Hohenester, U. & Trügler, A. MNPBEM – A Matlab toolbox for the simulation of plasmonic nanoparticles. *Computer Physics Communications* **183**, 370–381 (2012).

[128] Ruppin, R. Decay of an excited molecule near a small metal sphere. *The Journal of Chemical Physics* **76**, 1681–1684 (1982).

[129] Anger, P., Bharadwaj, P. & Novotny, L. Enhancement and Quenching of Single-Molecule Fluorescence. *Physical Review Letters* **96**, 113002 (2006).

[130] Gallinet, B., Butet, J. & Martin, O. J. F. Numerical methods for nanophotonics: Standard problems and future challenges: Numerical methods for nanophotonics. *Laser & Photonics Reviews* **9**, 577–603 (2015).

[131] Aizpurua, J. *et al.* Optical Properties of Gold Nanorings. *Physical Review Letters* **90**, 057401 (2003).

[132] Taflove, A. & Hagness, S. C. *Computational Electrodynamics: The Finite-Difference Time-Domain Method*. Artech House Antennas and Propagation Library (Artech House, Boston, 2005), third edn.

[133] Yee, K. Numerical solution of initial boundary value problems involving maxwell's equations in isotropic media. *IEEE Transactions on Antennas and Propagation* **14**, 302–307 (1966).

[134] Lumerical Support. `https://support.lumerical.com/hc/en-us` (2021).

[135] Berenger, J.-P. A perfectly matched layer for the absorption of electromagnetic waves. *Journal of Computational Physics* **114**, 185–200 (1994).

[136] Chew, W. C. & Weedon, W. H. A 3D perfectly matched medium from modified maxwell's equations with stretched coordinates. *Microwave and Optical Technology Letters* **7**, 599–604 (1994).

[137] Gedney, S. D. & Zhao, B. An Auxiliary Differential Equation Formulation for the Complex-Frequency Shifted PML. *IEEE Transactions on Antennas and Propagation* **58**, 838–847 (2010).

[138] Sacks, Z., Kingsland, D., Lee, R. & Jin-Fa Lee. A perfectly matched anisotropic absorber for use as an absorbing boundary condition. *IEEE Transactions on Antennas and Propagation* **43**, 1460–1463 (1995).

[139] Ochs, M. *et al.* Nanoscale Electrical Excitation of Distinct Modes in Plasmonic Waveguides. *Nano Letters* **21**, 4225–4230 (2021).

[140] Zhu, Z. & Brown, T. Full-vectorial finite-difference analysis of microstructured optical fibers. *Optics Express* **10**, 853 (2002).

[141] Hung, Y.-T., Huang, C.-B. & Huang, J.-S. Plasmonic mode converter for controlling optical impedance and nanoscale light-matter interaction. *Optics Express* **20**, 20342 (2012).

[142] Dai, W.-H., Lin, F.-C., Huang, C.-B. & Huang, J.-S. Mode Conversion in High-Definition Plasmonic Optical Nanocircuits. *Nano Letters* **14**, 3881–3886 (2014).

[143] Using and understanding Mode Expansion Monitors. `https://optics.ansys.com/hc/en-us/articles/360034902433-Using-and-understanding-Mode-Expansion-Monitors` (2022).

[144] Snyder, A. W. & Love, J. D. *Optical Waveguide Theory*. No. 190 in Science Paperbacks (Chapman and Hall, London ; New York, 1983).

[145] Uda, S. High Angle Radiation of Short Electric Waves. *Proceedings of the IRE* **15**, 377–385 (1927).

[146] Yagi, H. Beam Transmission of Ultra Short Waves. *Proceedings of the IRE* **16**, 715–740 (1928).

[147] Alù, A. & Engheta, N. Wireless at the Nanoscale: Optical Interconnects using Matched Nanoantennas. *Physical Review Letters* **104**, 213902 (2010).

[148] Solís, D. M., Taboada, J. M., Obelleiro, F. & Landesa, L. Optimization of an optical wireless nanolink using directive nanoantennas. *Optics Express* **21**, 2369 (2013).

[149] Moore, G. Cramming More Components Onto Integrated Circuits. *Proceedings of the IEEE* **86**, 82–85 (1998).

[150] Kish, L. B. End of Moore's law: Thermal (noise) death of integration in micro and nano electronics. *Physics Letters A* **305**, 144–149 (2002).

[151] Maksymov, I. S., Staude, I., Miroshnichenko, A. E. & Kivshar, Y. S. Optical Yagi-Uda nanoantennas. *Nanophotonics* **1**, 65–81 (2012).

[152] Galal, H. & Agio, M. Highly efficient light extraction and directional emission from large refractive-index materials with a planar Yagi-Uda antenna. *Optical Materials Express* **7**, 1634 (2017).

[153] Hofmann, H. F., Kosako, T. & Kadoya, Y. Design parameters for a nano-optical Yagi–Uda antenna. *New Journal of Physics* **9**, 217–217 (2007).

[154] Li, J., Salandrino, A. & Engheta, N. Shaping light beams in the nanometer scale: A Yagi-Uda nanoantenna in the optical domain. *Physical Review B* **76**, 245403 (2007).

[155] Chen, X., Yu, W., Yue, W., Yao, P. & Liu, W. A design of nano-optical Yagi-Uda antenna with high forward directivity. *Microwave and Optical Technology Letters* **59**, 786–789 (2017).

[156] Kosako, T., Kadoya, Y. & Hofmann, H. F. Directional control of light by a nano-optical Yagi–Uda antenna. *Nature Photonics* **4**, 312–315 (2010).

[157] Curto, A. G. *et al.* Unidirectional Emission of a Quantum Dot Coupled to a Nanoantenna. *Science* **329**, 930–933 (2010).

[158] See, K.-M. *et al.* Photoluminescence-Driven Broadband Transmitting Directional Optical Nanoantennas. *Nano Letters* **18**, 6002–6008 (2018).

[159] Ho, J. *et al.* Highly Directive Hybrid Metal–Dielectric Yagi-Uda Nanoantennas. *ACS Nano* **12**, 8616–8624 (2018).

[160] Maksymov, I. S., Miroshnichenko, A. E. & Kivshar, Y. S. Actively tunable bistable optical Yagi-Uda nanoantenna. *Optics Express* **20**, 8929 (2012).

[161] Checcucci, S. *et al.* Beaming light from a quantum emitter with a planar optical antenna. *Light: Science & Applications* **6**, e16245–e16245 (2017).

[162] Bharadwaj, P., Bouhelier, A. & Novotny, L. Electrical Excitation of Surface Plasmons. *Physical Review Letters* **106**, 226802 (2011).

[163] Berndt, R., Gimzewski, J. K. & Johansson, P. Inelastic tunneling excitation of tip-induced plasmon modes on noble-metal surfaces. *Physical Review Letters* **67**, 3796–3799 (1991).

[164] Marquardt, C. W. *et al.* Electroluminescence from a single nanotube–molecule–nanotube junction. *Nature Nanotechnology* **5**, 863–867 (2010).

[165] Mueller, T. *et al.* Efficient narrow-band light emission from a single carbon nanotube p–n diode. *Nature Nanotechnology* **5**, 27–31 (2010).

[166] Freitag, M. *et al.* Hot Carrier Electroluminescence from a Single Carbon Nanotube. *Nano Letters* **4**, 1063–1066 (2004).

[167] Chen, J. *et al.* Bright Infrared Emission from Electrically Induced Excitons in Carbon Nanotubes. *Science* **310**, 1171–1174 (2005).

[168] Minot, E. D. *et al.* Single Quantum Dot Nanowire LEDs. *Nano Letters* **7**, 367–371 (2007).

[169] Le Moal, E. *et al.* Engineering the emission of light from a scanning tunneling microscope using the plasmonic modes of a nanoparticle. *Physical Review B* **93**, 035418 (2016).

[170] Cao, S. *et al.* Directional light beams by design from electrically driven elliptical slit antennas. *Beilstein Journal of Nanotechnology* **9**, 2361–2371 (2018).

[171] Kullock, R., Ochs, M., Grimm, P., Emmerling, M. & Hecht, B. Electrically-driven Yagi-Uda antennas for light. *Nature Communications* **11**, 115 (2020).

[172] Lambe, J. & McCarthy, S. L. Light Emission from Inelastic Electron Tunneling. *Physical Review Letters* **37**, 923–925 (1976).

[173] Gimzewski, J. K., Reihl, B., Coombs, J. H. & Schlittler, R. R. Photon emission with the scanning tunneling microscope. *Zeitschrift für Physik B Condensed Matter* **72**, 497–501 (1988).

[174] Février, P. & Gabelli, J. Tunneling time probed by quantum shot noise. *Nature Communications* **9**, 4940 (2018).

[175] Jones, T. B. *Electromechanics of Particles* (Cambridge University Press, Cambridge, GBR, 2009).

[176] Dewarrat, F., Calame, M. & Schönenberger, C. Orientation and Positioning of DNA Molecules with an Electric Field Technique. *Single Molecules* **3**, 189–193 (2002).

[177] Hohenester, U. Simulating electron energy loss spectroscopy with the MNPBEM toolbox. *Computer Physics Communications* **185**, 1177–1187 (2014).

[178] Hohenester, U. Making simulations with the MNPBEM toolbox big: Hierarchical matrices and iterative solvers. *Computer Physics Communications* **222**, 209–228 (2018).

[179] Waxenegger, J., Trügler, A. & Hohenester, U. Plasmonics simulations with the MNPBEM toolbox: Consideration of substrates and layer structures. *Computer Physics Communications* **193**, 138–150 (2015).

[180] Kullock, R., Grimm, P., Ochs, M. & Hecht, B. Directed emission by electrically-driven optical antennas. In Razeghi, M., Brown, G. J., Leo, G. & Lewis, J. S. (eds.) *Quantum Sensing and Nano Electronics and Photonics XV*, 37 (SPIE, San Francisco, United States, 2018).

[181] Hone, D., Mühlschlegel, B. & Scalapino, D. J. Theory of light emission from small particle tunnel junctions. *Applied Physics Letters* **33**, 203–204 (1978).

[182] Emerson, D. The gain of an endfire array. *ARRL Antenna Compendium* **5**, 87–95 (1996).

[183] Straw, R. D. & Hall, G. L. (eds.) *The ARRL Antenna Compendium. Vol. 5*, vol. 5 of *Radio Amateur's Library* (ARRL, Newington, Conn, 1996), first edn.

[184] Burke, G. J. & Pogio, A. J. Numerical Electromagnetics Code (NEC)-Method of Moments. A User-Oriented Computer Code for Analysis of the Electromagnetic Response of Antennas and Other Metal Structures. Part 1: Program Description-Theory. Part 2: Program Description-Code. Volume 1. Revised. Tech. Rep. UCID-18834, Lawrence Livermore National Lab CA (1981).

[185] Molteno, T. C. A. NEC2++: An NEC-2 compatible Numerical Electromagnetics Code. Electronics Technical Report 2014-3, University of Otago, Dunedin, New Zealand (2014).

[186] Boidin, R., Halenkovič, T., Nazabal, V., Beneš, L. & Němec, P. Pulsed laser deposited alumina thin films. *Ceramics International* **42**, 1177–1182 (2016).

[187] Parzefall, M. & Novotny, L. Light at the End of the Tunnel. *ACS Photonics* **5**, 4195–4202 (2018).

[188] Qian, H. *et al.* Highly-efficient electrically-driven localized surface plasmon source enabled by resonant inelastic electron tunneling. *Nature Communications* **12**, 3111 (2021).

[189] Sharma, A., Singh, V., Bougher, T. L. & Cola, B. A. A carbon nanotube optical rectenna. *Nature Nanotechnology* **10**, 1027–1032 (2015).

[190] Donchev, E. *et al.* The rectenna device: From theory to practice (a review). *MRS Energy & Sustainability* **1**, E1 (2014).

[191] Polman, A., Kociak, M. & García de Abajo, F. J. Electron-beam spectroscopy for nanophotonics. *Nature Materials* **18**, 1158–1171 (2019).

[192] Schilder, N. J., Agrawal, H., Garnett, E. C. & Polman, A. Phase-Resolved Surface Plasmon Scattering Probed by Cathodoluminescence Holography. *ACS Photonics* **7**, 1476–1482 (2020).

[193] Pavlov, R. S., Curto, A. G. & van Hulst, N. F. Log-periodic optical antennas with broadband directivity. *Optics Communications* **285**, 3334–3340 (2012).

[194] Das Portal zu Licht und Beleuchtung | licht.de. `https://www.licht.de/de/` (2022).

[195] Pope, M., Kallmann, H. P. & Magnante, P. Electroluminescence in Organic Crystals. *The Journal of Chemical Physics* **38**, 2042–2043 (1963).

[196] Helfrich, W. & Schneider, W. G. Recombination Radiation in Anthracene Crystals. *Physical Review Letters* **14**, 229–231 (1965).

[197] Williams, D. F. & Schadt, M. DC and Pulsed Electroluminescence in Anthracene and Doped Anthracene Crystals. *The Journal of Chemical Physics* **53**, 3480–3487 (1970).

[198] Chiang, C. K. *et al.* Electrical Conductivity in Doped Polyacetylene. *Physical Review Letters* **39**, 1098–1101 (1977).

[199] Chiang, C. K. *et al.* Electrical Conductivity in Doped Polyacetylene. *Physical Review Letters* **40**, 1472–1472 (1978).

[200] Tang, C. W. & VanSlyke, S. A. Organic electroluminescent diodes. *Applied Physics Letters* **51**, 913–915 (1987).

[201] Tang, C. W., VanSlyke, S. A. & Chen, C. H. Electroluminescence of doped organic thin films. *Journal of Applied Physics* **65**, 3610–3616 (1989).

[202] Burroughes, J. H. *et al.* Light-emitting diodes based on conjugated polymers. *Nature* **347**, 539–541 (1990).

[203] Müllen, K. & Scherf, U. *Organic Light Emitting Devices: Synthesis, Properties and Applications* (John Wiley & Sons, 2006).

[204] Okamoto, K. *et al.* Surface-plasmon-enhanced light emitters based on InGaN quantum wells. *Nature Materials* **3**, 601–605 (2004).

[205] Huang, K. C. *et al.* Antenna electrodes for controlling electroluminescence. *Nature Communications* **3**, 1005 (2012).

[206] Wang, H. *et al.* Nanoantennas Involved Optical Plasmonic Cavity for Improved Luminescence of Quantum Dots Light-Emitting Diodes. *ACS Applied Materials & Interfaces* **13**, 44760–44767 (2021).

[207] Ma, L. *et al.* Nanoantenna-Enhanced Light-Emitting Diodes: Fundamental and Recent Progress. *Laser & Photonics Reviews* **15**, 2000367 (2021).

[208] Brütting, W., Frischeisen, J., Schmidt, T. D., Scholz, B. J. & Mayr, C. Device efficiency of organic light-emitting diodes: Progress by improved light outcoupling: Device efficiency of OLEDs. *physica status solidi (a)* **210**, 44–65 (2013).

[209] Huang, K. C. Y. *et al.* Electrically driven subwavelength optical nanocircuits. *Nature Photonics* **8**, 244–249 (2014).

[210] Kolb, V. & Pflaum, J. Hybrid metal-organic nanocavity arrays for efficient light out-coupling. *Optics Express* **25**, 6678 (2017).

[211] Latscha, H. P., Kazmaier, U. & Klein, H. A. *Organische Chemie*. Springer-Lehrbuch (Springer Berlin Heidelberg, Berlin, Heidelberg, 2008).

[212] Mayer, T. *et al.* Silicon–organic pigment material hybrids for photovoltaic application. *Solar Energy Materials and Solar Cells* **91**, 1873–1886 (2007).

[213] Meiss, J. *et al.* Fluorinated Zinc Phthalocyanine as Donor for Efficient Vacuum-Deposited Organic Solar Cells. *Advanced Functional Materials* **22**, 405–414 (2012).

[214] Kasha, M. Characterization of electronic transitions in complex molecules. *Discussions of the Faraday Society* **9**, 14 (1950).

[215] Haken, H. & Wolf, H. *Molekülphysik und Quantenchemie* (Springer, Berlin, 2006).

[216] Barth, S. *et al.* Current injection from a metal to a disordered hopping system. III. Comparison between experiment and Monte Carlo simulation. *Physical Review B* **60**, 8791–8797 (1999).

[217] Fowler, R. H. & Nordheim, L. Electron emission in intense electric fields. *Proceedings of the Royal Society of London. Series A, Containing Papers of a Mathematical and Physical Character* **119**, 173–181 (1928).

[218] Forbes, R. G. Exact analysis of surface field reduction due to field-emitted vacuum space charge, in parallel-plane geometry, using simple dimensionless equations. *Journal of Applied Physics* **104**, 084303 (2008).

[219] Jensen, K. L., Lebowitz, J., Lau, Y. Y. & Luginsland, J. Space charge and quantum effects on electron emission. *Journal of Applied Physics* **111**, 054917 (2012).

[220] Bruder, I. *et al.* What determines the performance of metal phthalocyanines (MPc, M=Zn, Cu, Ni, Fe) in organic heterojunction solar cells? A combined experimental and theoretical investigation. *Organic Electronics* **11**, 377–387 (2010).

[221] Isago, H. *Optical Spectra of Phthalocyanines and Related Compounds*. NIMS Monographs (Springer Japan, Tokyo, 2015).

[222] Theisen, R. F., Huang, L., Fleetham, T., Adams, J. B. & Li, J. Ground and excited states of zinc phthalocyanine, zinc tetrabenzoporphyrin, and azaporphyrin analogs using DFT and TDDFT with Franck-Condon analysis. *The Journal of Chemical Physics* **142**, 094310 (2015).

[223] Feng, S., Wang, Y.-C., Ke, Y., Liang, W. & Zhao, Y. Effect of charge-transfer states on the vibrationally resolved absorption spectra and exciton dynamics in ZnPc aggregates: Simulations from a non-Makovian stochastic Schrödinger equation. *The Journal of Chemical Physics* **153**, 034116 (2020).

[224] Feng, S., Wang, Y.-C., Liang, W. & Zhao, Y. Vibrationally resolved absorption spectra and ultrafast exciton dynamics in α-phase and β-phase zinc phthalocyanine aggregates. *Physical Chemistry Chemical Physics* **24**, 2974–2987 (2022).

[225] Berger, O. *et al.* Studies on phase transformations of Cu-phthalocyanine thin films. *Journal of Materials Science: Materials in Electronics* **11**, 331–346 (2000).

[226] Heutz, S., Bayliss, S. M., Middleton, R. L., Rumbles, G. & Jones, T. S. Polymorphism in Phthalocyanine Thin Films: Mechanism of the $\alpha \to \beta$ Transition. *The Journal of Physical Chemistry B* **104**, 7124–7129 (2000).

[227] Hammer, S., Ferschke, T., v. Eyb, G. & Pflaum, J. Phase transition induced spectral tuning of dual luminescent crystalline zinc-phthalocyanine thin films and OLEDs. *Applied Physics Letters* **115**, 263303 (2019).

[228] Iwatsu, F., Kobayashi, T. & Uyeda, N. Solvent effects on crystal growth and transformation of zinc phthalocyanine. *The Journal of Physical Chemistry* **84**, 3223–3230 (1980).

[229] Dressel, M. *et al.* Kramers-Kronig-consistent optical functions of anisotropic crystals: Generalized spectroscopic ellipsometry on pentacene. *Optics Express* **16**, 19770 (2008).

[230] Wojdyła, M., Derkowska, B., Łukasiak, Z. & Bała, W. Absorption and photoreflectance spectroscopy of zinc phthalocyanine (ZnPc) thin films grown by thermal evaporation. *Materials Letters* **60**, 3441–3446 (2006).

[231] Brendel, M. *et al.* The Effect of Gradual Fluorination on the Properties of F_nZnPc Thin Films and F_nZnPc/C_{60} Bilayer Photovoltaic Cells. *Advanced Functional Materials* **25**, 1565–1573 (2015).

[232] Bruder, I. *et al.* Theoretical and experimental investigation on the influence of the molecular polarizability of novel zinc phthalocyanine derivatives on the open circuit voltage of organic hetero-junction solar cells. *Solar Energy Materials and Solar Cells* **94**, 310–316 (2010).

[233] Buret, M. *et al.* Spontaneous Hot-Electron Light Emission from Electron-Fed Optical Antennas. *Nano Letters* **15**, 5811–5818 (2015).

[234] Cazier, N. *et al.* Electrical excitation of waveguided surface plasmons by a light-emitting tunneling optical gap antenna. *Optics Express* **24**, 3873 (2016).

[235] Schlettwein, D. *et al.* Electronic Energy Levels in Individual Molecules, Thin Films, and Organic Heterojunctions of Substituted Phthalocyanines. *The Journal of Physical Chemistry B* **105**, 4791–4800 (2001).

[236] Opitz, A. *et al.* Mixed crystalline films of co-evaporated hydrogen- and fluorine-terminated phthalocyanines and their application in photovoltaic devices. *Organic Electronics* **10**, 1259–1267 (2009).

[237] Derry, G. N., Kern, M. E. & Worth, E. H. Recommended values of clean metal surface work functions. *Journal of Vacuum Science & Technology A: Vacuum, Surfaces, and Films* **33**, 060801 (2015).

[238] Gao, W. & Kahn, A. Electronic structure and current injection in zinc phthalocyanine doped with tetrafluorotetracyanoquinodimethane: Interface versus bulk effects. *Organic Electronics* **3**, 53–63 (2002).

[239] Fink, R. F. *et al.* Exciton Trapping in π-Conjugated Materials: A Quantum-Chemistry-Based Protocol Applied to Perylene Bisimide Dye Aggregates. *Journal of the American Chemical Society* **130**, 12858–12859 (2008).

[240] Hoche, J. *et al.* The mechanism of excimer formation: An experimental and theoretical study on the pyrene dimer. *Physical Chemistry Chemical Physics* **19**, 25002–25015 (2017).

[241] Baldo, M. A. *et al.* Highly efficient phosphorescent emission from organic electroluminescent devices. *Nature* **395**, 151–154 (1998).

[242] Adachi, C., Baldo, M. A., Thompson, M. E. & Forrest, S. R. Nearly 100% internal phosphorescence efficiency in an organic light-emitting device. *Journal of Applied Physics* **90**, 5048–5051 (2001).

[243] Endo, A. *et al.* Thermally Activated Delayed Fluorescence from Sn4+-Porphyrin Complexes and Their Application to Organic Light Emitting Diodes

- A Novel Mechanism for Electroluminescence. *Advanced Materials* **21**, 4802–4806 (2009).

[244] Uoyama, H., Goushi, K., Shizu, K., Nomura, H. & Adachi, C. Highly efficient organic light-emitting diodes from delayed fluorescence. *Nature* **492**, 234–238 (2012).

[245] To, W.-P., Cheng, G., Tong, G. S. M., Zhou, D. & Che, C.-M. Recent Advances in Metal-TADF Emitters and Their Application in Organic Light-Emitting Diodes. *Frontiers in Chemistry* **8**, 653 (2020).

[246] Kappaun, S., Slugovc, C. & List, E. Phosphorescent Organic Light-Emitting Devices: Working Principle and Iridium Based Emitter Materials. *International Journal of Molecular Sciences* **9**, 1527–1547 (2008).

[247] de Boer, B., Hadipour, A., Mandoc, M. M., van Woudenbergh, T. & Blom, P. W. M. Tuning of Metal Work Functions with Self-Assembled Monolayers. *Advanced Materials* **17**, 621–625 (2005).

[248] Baffou, G. & Quidant, R. Thermo-plasmonics: Using metallic nanostructures as nano-sources of heat: Thermoplasmonics. *Laser & Photonics Reviews* **7**, 171–187 (2013).

[249] Alù, A. & Engheta, N. Tuning the scattering response of optical nanoantennas with nanocircuit loads. *Nature Photonics* **2**, 307–310 (2008).

[250] Alù, A. & Engheta, N. Input Impedance, Nanocircuit Loading, and Radiation Tuning of Optical Nanoantennas. *Physical Review Letters* **101**, 043901 (2008).

[251] Wan, W. *et al.* Time-Reversed Lasing and Interferometric Control of Absorption. *Science* **331**, 889–892 (2011).

[252] Baranov, D. G., Krasnok, A., Shegai, T., Alù, A. & Chong, Y. Coherent perfect absorbers: Linear control of light with light. *Nature Reviews Materials* **2**, 17064 (2017).

[253] Pichler, K. *et al.* Random anti-lasing through coherent perfect absorption in a disordered medium. *Nature* **567**, 351–355 (2019).

[254] Sweeney, W. R., Hsu, C. W. & Stone, A. D. Theory of reflectionless scattering modes. *Physical Review A* **102**, 063511 (2020).

[255] Stone, A. D., Sweeney, W. R., Hsu, C. W., Wisal, K. & Wang, Z. Reflectionless excitation of arbitrary photonic structures: A general theory. *Nanophotonics* **10**, 343–360 (2020).

[256] Zhang, J., MacDonald, K. F. & Zheludev, N. I. Controlling light-with-light without nonlinearity. *Light: Science & Applications* **1**, e18–e18 (2012).

[257] Dutta-Gupta, S., Deshmukh, R., Venu Gopal, A., Martin, O. J. F. & Dutta Gupta, S. Coherent perfect absorption mediated anomalous reflection and refraction. *Optics Letters* **37**, 4452 (2012).

[258] Noh, H., Chong, Y., Stone, A. D. & Cao, H. Perfect coupling of light to surface plasmons by coherent absorption. *Physical Review Letters* **108**, 186805 (2012).

[259] Yoon, J. W., Koh, G. M., Song, S. H. & Magnusson, R. Measurement and Modeling of a Complete Optical Absorption and Scattering by Coherent Surface Plasmon-Polariton Excitation Using a Silver Thin-Film Grating. *Physical Review Letters* **109**, 257402 (2012).

[260] Bruck, R. & Muskens, O. L. Plasmonic nanoantennas as integrated coherent perfect absorbers on SOI waveguides for modulators and all-optical switches. *Optics Express* **21**, 27652 (2013).

[261] Jung, M. J., Han, C., Yoon, J. W. & Song, S. H. Temperature and gain tuning of plasmonic coherent perfect absorbers. *Optics Express* **23**, 19837 (2015).

[262] Roger, T. *et al.* Coherent perfect absorption in deeply subwavelength films in the single-photon regime. *Nature Communications* **6**, 7031 (2015).

[263] Fang, X., MacDonald, K. F. & Zheludev, N. I. Controlling light with light using coherent metadevices: All-optical transistor, summator and invertor. *Light: Science & Applications* **4**, e292–e292 (2015).

[264] Alaee, R., Vaddi, Y. & Boyd, R. W. Dynamic coherent perfect absorption in nonlinear metasurfaces. *Optics Letters* **45**, 6414 (2020).

[265] Su, W. P., Schrieffer, J. R. & Heeger, A. J. Solitons in Polyacetylene. *Physical Review Letters* **42**, 1698–1701 (1979).

[266] Grimm, P., Razinskas, G., Huang, J.-S. & Hecht, B. Driving plasmonic nanoantennas at perfect impedance matching using generalized coherent perfect absorption. *Nanophotonics* **10**, 1879–1887 (2021).

[267] Savage, K. J. *et al.* Revealing the quantum regime in tunnelling plasmonics. *Nature* **491**, 574–577 (2012).

[268] Scholl, J. A., García-Etxarri, A., Koh, A. L. & Dionne, J. A. Observation of Quantum Tunneling between Two Plasmonic Nanoparticles. *Nano Letters* **13**, 564–569 (2013).

[269] Zhang, S. *et al.* Chiral Surface Plasmon Polaritons on Metallic Nanowires. *Physical Review Letters* **107**, 096801 (2011).

[270] Rewitz, C. *et al.* Ultrafast Plasmon Propagation in Nanowires Characterized by Far-Field Spectral Interferometry. *Nano Letters* **12**, 45–49 (2012).

[271] Razinskas, G., Biagioni, P. & Hecht, B. Limits of Kirchhoff's Laws in Plasmonics. *Scientific Reports* **8**, 1921 (2018).

[272] Barnard, E. S., White, J. S., Chandran, A. & Brongersma, M. L. Spectral properties of plasmonic resonator antennas. *Optics Express* **16**, 16529 (2008).

[273] Feigenbaum, E. & Orenstein, M. Ultrasmall Volume Plasmons, yet with Complete Retardation Effects. *Physical Review Letters* **101**, 163902 (2008).

[274] Bronštejn, I. N., Semendjaev, K. A., Musiol, G. & Mühlig, H. *Taschenbuch der Mathematik* (Deutsch, Frankfurt am Main, 2008), seventh edn.

[275] Zia, R., Selker, M. D. & Brongersma, M. L. Leaky and bound modes of surface plasmon waveguides. *Physical Review B* **71**, 165431 (2005).

[276] Wegert, E. & Semmler, G. Phase Plots of Complex Functions: A Journey in Illustration. *Notices of the AMS* **58**, 768–780 (2011).

[277] Krasnok, A. *et al.* Anomalies in light scattering. *Advances in Optics and Photonics* **11**, 892 (2019).

[278] Krasnok, A. & Alu, A. Active Nanophotonics. *Proceedings of the IEEE* **108**, 628–654 (2020).

[279] Demtröder, W. *Experimentalphysik Bd. 1: Mechanik und Wärme*. Springer-Lehrbuch (Springer-Spektrum, Berlin Heidelberg, 2015), seventh edn.

[280] Oulton, R. F. *et al.* Plasmon lasers at deep subwavelength scale. *Nature* **461**, 629–632 (2009).

[281] Moerner, W. E. & Fromm, D. P. Methods of single-molecule fluorescence spectroscopy and microscopy. *Review of Scientific Instruments* **74**, 3597–3619 (2003).

[282] Ament, I., Prasad, J., Henkel, A., Schmachtel, S. & Sönnichsen, C. Single Unlabeled Protein Detection on Individual Plasmonic Nanoparticles. *Nano Letters* **12**, 1092–1095 (2012).

[283] Zijlstra, P., Paulo, P. M. R. & Orrit, M. Optical detection of single non-absorbing molecules using the surface plasmon resonance of a gold nanorod. *Nature Nanotechnology* **7**, 379–382 (2012).

[284] Dantham, V. R. *et al.* Label-Free Detection of Single Protein Using a Nanoplasmonic-Photonic Hybrid Microcavity. *Nano Letters* **13**, 3347–3351 (2013).

[285] Park, H., Lee, S.-Y., Kim, J., Lee, B. & Kim, H. Near-infrared coherent perfect absorption in plasmonic metal-insulator-metal waveguide. *Optics Express* **23**, 24464 (2015).

[286] Kane, C. L. & Lubensky, T. C. Topological boundary modes in isostatic lattices. *Nature Physics* **10**, 39–45 (2014).

[287] Süsstrunk, R. & Huber, S. D. Observation of phononic helical edge states in a mechanical topological insulator. *Science* **349**, 47–50 (2015).

[288] Yang, Z. *et al.* Topological Acoustics. *Physical Review Letters* **114**, 114301 (2015).

[289] Haldane, F. D. M. & Raghu, S. Possible Realization of Directional Optical Waveguides in Photonic Crystals with Broken Time-Reversal Symmetry. *Physical Review Letters* **100**, 013904 (2008).

[290] Lu, L., Joannopoulos, J. D. & Soljačić, M. Topological photonics. *Nature Photonics* **8**, 821–829 (2014).

[291] Poli, C., Bellec, M., Kuhl, U., Mortessagne, F. & Schomerus, H. Selective enhancement of topologically induced interface states in a dielectric resonator chain. *Nature Communications* **6**, 6710 (2015).

[292] Hu, W. *et al.* Measurement of a Topological Edge Invariant in a Microwave Network. *Physical Review X* **5**, 011012 (2015).

[293] Ningyuan, J., Owens, C., Sommer, A., Schuster, D. & Simon, J. Time- and Site-Resolved Dynamics in a Topological Circuit. *Physical Review X* **5**, 021031 (2015).

[294] Lee, C. H. *et al.* Topolectrical Circuits. *Communications Physics* **1**, 39 (2018).

[295] Imhof, S. *et al.* Topolectrical-circuit realization of topological corner modes. *Nature Physics* **14**, 925–929 (2018).

[296] Helbig, T. *et al.* Band structure engineering and reconstruction in electric circuit networks. *Physical Review B* **99**, 161114 (2019).

[297] Berry, M. V. Quantal phase factors accompanying adiabatic changes. *Proceedings of the Royal Society of London. A. Mathematical and Physical Sciences* **392**, 45–57 (1984).

[298] Zak, J. Berry's phase for energy bands in solids. *Physical Review Letters* **62**, 2747–2750 (1989).

[299] Yang, F., Ma, S., Ding, K., Zhang, S. & Pendry, J. B. Continuous topological transition from metal to dielectric. *Proceedings of the National Academy of Sciences* **117**, 16739–16742 (2020).

[300] Bleckmann, F., Cherpakova, Z., Linden, S. & Alberti, A. Spectral imaging of topological edge states in plasmonic waveguide arrays. *Physical Review B* **96**, 045417 (2017).

[301] Liu, C., Dutt, M. V. G. & Pekker, D. Robust manipulation of light using topologically protected plasmonic modes. *Optics Express* **26**, 2857–2872 (2018).

[302] Wang, L., Cai, W., Bie, M., Zhang, X. & Xu, J. Zak phase and topological plasmonic Tamm states in one-dimensional plasmonic crystals. *Optics Express* **26**, 28963 (2018).

[303] Fedorova, Z. *et al.* Limits of topological protection under local periodic driving. *Light: Science & Applications* **8**, 63 (2019).

[304] Poddubny, A., Miroshnichenko, A., Slobozhanyuk, A. & Kivshar, Y. Topological Majorana States in Zigzag Chains of Plasmonic Nanoparticles. *ACS Photonics* **1**, 101–105 (2014).

[305] Ling, C. W., Xiao, M., Chan, C. T., Yu, S. F. & Fung, K. H. Topological edge plasmon modes between diatomic chains of plasmonic nanoparticles. *Optics Express* **23**, 2021–2031 (2015).

[306] Pocock, S. R., Xiao, X., Huidobro, P. A. & Giannini, V. Topological Plasmonic Chain with Retardation and Radiative Effects. *ACS Photonics* **5**, 2271–2279 (2018).

[307] Ott, A. & Biehs, S.-A. Radiative heat flux through a topological Su-Schrieffer-Heeger chain of plasmonic nanoparticles. *Physical Review B* **102**, 115417 (2020).

[308] Sinev, I. S. *et al.* Mapping plasmonic topological states at the nanoscale. *Nanoscale* **7**, 11904–11908 (2015).

[309] Boyd, R. W. *Nonlinear Optics* (Elsevier, Academic Press, Amsterdam Heidelberg, 2008), third edn.

[310] Kongsuwan, N. *et al.* Suppressed Quenching and Strong-Coupling of Purcell-Enhanced Single-Molecule Emission in Plasmonic Nanocavities. *ACS Photonics* **5**, 186–191 (2018).

[311] Brüche, E. Elektronenmikroskopische Abbildung mit lichtelektrischen Elektronen. *Zeitschrift für Physik* **86**, 448–450 (1933).

[312] Razinskas, G. *et al.* Normal-Incidence PEEM Imaging of Propagating Modes in a Plasmonic Nanocircuit. *Nano Letters* **16**, 6832–6837 (2016).

[313] Hensen, M. *et al.* Spatial Variations in Femtosecond Field Dynamics within a Plasmonic Nanoresonator Mode. *Nano Letters* **19**, 4651–4658 (2019).

[314] Lefier, Y. & Grosjean, T. Unidirectional sub-diffraction waveguiding based on optical spin–orbit coupling in subwavelength plasmonic waveguides. *Optics Letters* **40**, 2890 (2015).

[315] Pan, D., Wei, H., Gao, L. & Xu, H. Strong Spin-Orbit Interaction of Light in Plasmonic Nanostructures and Nanocircuits. *Physical Review Letters* **117**, 166803 (2016).

[316] Krauss, E., Razinskas, G., Köck, D., Grossmann, S. & Hecht, B. Reversible Mapping and Sorting the Spin of Photons on the Nanoscale: A Spin-Optical Nanodevice. *Nano Letters* **19**, 3364–3369 (2019).

[317] Lovera, A., Gallinet, B., Nordlander, P. & Martin, O. J. Mechanisms of Fano Resonances in Coupled Plasmonic Systems. *ACS Nano* **7**, 4527–4536 (2013).

Acknowledgments

Throughout my time as a PhD student I had the opportunity to get in contact with numerous colleagues, also outside of Würzburg. Only with the continuous support of these people it was possible to complete the work presented in this dissertation. Here I would like to acknowledge the most important ones.

First, I would like to convey my gratitude to **Prof. Dr. Bert Hecht**. By giving me the opportunity to work on diverse projects over the years I was able to learn a lot and benefit from his precious input in any of the projects. Likewise, I thank **Prof. Dr. Jens Pflaum** and **Prof. Dr. Tobias Hertel**, the co-supervisors, for fruitful discussions, questions, and for sharing their expertise in the intersecting realms of physics and chemistry.

A special thanks goes to **Prof. Dr. Jer-Shing Huang**, who collaborated on the plasmonic coherent perfect absorber project and thereby triggered and steered the progress. I thank **Prof. Dr. Ortwin Hess** and his group with whom it was very interesting to examine CPA in the context of a strongly interacting single emitter. **Prof. Dr. Ronny Thomale** and his students are acknowledged for supplying me with the basics of the Su-Schrieffer-Heeger model. Here I also would like to mention the Würzburg-Dresden Cluster of Excellence *ct.qmat* which served as a platform to share and discuss the plasmonic Su-Schrieffer-Heeger chain project with many other scientists.

I appreciate the constant assistance and guidance of **Prof. Dr. Volker Behr** throughout the years regarding the administration of Linux server architectures, a fundamental pillar for numerical simulations.

I thank **Dr. René Kullock**, who served as a mentor over large parts of my PhD time and delivered invaluable results on the experimental side and setup development. We had plenty of instructive discussions about Yagi-Uda antennas and OLEA samples. **Maximilian Ochs** and **Stefan Zeißner** performed lots of high-quality measurements which are a considerable part of this thesis and the publications. I also thank the collaborators **Maximilian Rödel, Sebastian Hammer, Simon Wiegand, Verena Kolb, Monika Emmerling, Enno Schatz, Dr. Thorsten Feichtner**, and others for the prosperous teamwork, as well as **Dr. Daniel Clarke, Yiming Lai, Dr. Cheng Zhang, Tobias Hofmann**, and **Tobias Helbig** for further ongoing teamwork and exchange.

The quiet and comfortable working atmosphere was made possible by my part-time office mates **Gary Razinskas** and **Benedikt Schurr** with whom I had nice and useful conversations. **Hitrud Eaton** and **Sabine Voll** were very helpful in any secretary-related and organizational issue. Needless to say, I am grateful to the entire **Experimental Physics V** chair for the good working environment and also for the various social activities, such as excursion days, barbecue events, lunchtimes, cake sessions, and, most importantly, recording Christmas movies. Having been part of this team makes me really proud.

My thanks go to **Johanna Rank**, who proofread parts of this work concerning language aspects.

Of course I always relied on the perpetual support of my **family**. They have been indispensable to keep me grounded in tough periods, stood by my side, and furthermore provided premium cakes for several celebration events. Thank you for this!

Affidavit

I hereby confirm that my thesis entitled “Locally driven complex plasmonic nanoantenna systems” is the result of my own work. I did not receive any help or support from commercial consultants. All sources and / or materials applied are listed and specified in the thesis.

Furthermore, I confirm that this thesis has not yet been submitted as part of another examination process neither in identical nor in similar form.

Place, Date Signature

Eidesstattliche Erklärung

Hiermit erkläre ich an Eides statt, die Dissertation “Lokal angetriebene komplexe plasmonische Nanoantennen-Systeme” eigenständig, d.h. insbesondere selbständig und ohne Hilfe eines kommerziellen Promotionsberaters, angefertigt und keine anderen als die von mir angegebenen Quellen und Hilfsmittel verwendet zu haben.

Ich erkläre außerdem, dass die Dissertation weder in gleicher noch in ähnlicher Form bereits in einem anderen Prüfungsverfahren vorgelegen hat.

Ort, Datum Unterschrift